Thermoreponsive behaviour of AM(_2)O(_8) materials

Simon Allen

Abstract

Thermoreponsive Behaviour of AM_2O_8 Materials — Ph.D. Thesis

Simon Allen — 2003

This thesis investigates the synthesis and structural characterisation of AM_2O_8 phases, many of which show negative thermal expansion (NTE); relevant literature is reviewed in **Chapter One**.

Chapter Two describes the synthesis, structure solution, and mechanistic role of a new family of low-temperature (LT) orthorhombic AM_2O_8 polymorphs (A^{IV} = Zr, Hf; M^{VI} = Mo, W). These materials are key intermediates in the preparation of cubic AM_2O_8 phases from $AM_2O_7(OH)_2(H_2O)_2$. The structure of LT-AM_2O_8 has been elucidated by combined laboratory X-ray and neutron powder diffraction. Variable temperature X-ray diffraction (VTXRD) studies have shown LT-AMo_2O_8 phases exhibit anisotropic NTE. LT-$ZrMo_2O_8$ has been shown to undergo spontaneous rehydration, allowing preparation of $ZrMo_2O_7(OD)_2(D_2O)_2$ and assignment of D_2O/OD positions within the structure by neutron diffraction. Using this result, a reversible topotactic dehydration pathway from $AM_2O_7(OH)_2(H_2O)_2$ to LT-AM_2O_8 is proposed.

Chapter Three investigates the order-disorder phase transition with concurrent oxygen mobility in cubic AM_2O_8 materials; studies include comprehensive VT neutron diffraction of cubic $ZrMo_2O_8$ to reveal a static to dynamic transition at 215 K, and novel quench-anneal/quench-warm variable temperature/time diffraction experiments on $ZrWMoO_8$ which lead to an activation energy of 40 kJmol^{-1} for oxygen migration.

In **Chapter Four** ^{17}O-labelled cubic ZrW_2O_8 has been prepared to understand the oxygen migration process by VT MAS NMR. *In situ* hydrothermal studies of cubic $ZrMo_2O_8$ using synchrotron radiation have shown direct hydration to $ZrMo_2O_7(OH)_2(H_2O)_2$.

In **Chapter Five** VTXRD of trigonal α-AMo_2O_8 phases reveals a previously unknown second-order phase transition at 487 K (A = Zr) or 463 K (A = Hf) from $P\bar{3}1c$ to $P\bar{3}m1$. Rigid-body Rietveld refinements have shown this is due to alignment of apical Mo–O groups with the c axis in the high-temperature, α' phase.

Thermoresponsive Behaviour of AM_2O_8 Materials

Simon Allen M.Chem (Oxon)
University of Durham

Supervisor: Dr. John S. O. Evans

A thesis submitted in partial fulfilment of the requirements
for the degree of Doctor of Philosophy.

Department of Chemistry
University of Durham
2003

List of Contents

Declaration

The work described in this thesis is entirely the work my own, except where I have acknowledged help from a named person *or* given a reference to a published source or a thesis.

The research presented was performed in the Department of Chemistry, University of Durham between October 1999 and September 2002, the results of which have not been submitted for a degree in this or any other university.

This thesis conforms to the word limit set out in the Degree Regulations. It contains 65,400 words including appendices and footnotes but excluding references, or experimental data included on the CD-R located at the rear of the thesis.

Date: 13/8/03 Signature: 

Statement of Copyright

Acknowledgements

John Evans – thank you for being a reliable wall of knowledge, being understanding at my lack of... understanding at times, for all the great ideas and support since undergraduate days, for help on HRPD, all things *TOPAS* and premium grade proof-reading. Thanks also to Ivana for proof-reading tips and discussions. Much gratitude go to the following people for their invaluable assistance:-

Richard Gover – used his powers to obtain neutron time and flew half way round the world to collect data on D_2O precursor, for the "been there done it" discussions, Sunday roasts, and the stereo. Thanks for having time for me. A big thanks also due to Tad Matsumura (for assisting Richard), Ryoji Kanno (for funding the trip) and Takashi Kamiyama (data collections at KEK) in Japan.

Ian King – for the ^{17}O VT MAS NMR work in France, discussions and for being a legend of a housemate 2 years running. Also thanks to Prof. Dominique Massiot and Dr. Franck Fayon for assisting Ian, and thanks to Dr. David Apperley for recording the room temperature ^{17}O ZrO_2 NMR spectrum.

Neil Withers – resident Mr Fix It, for constructing and maintaining the glovebox from a pile of junk (so I could do the ^{17}O work) and Schlenk lines (ditto), showing me how to seal quartz tubes & being "in-the-know" for Powerpoint. A deserved University Challenge Captain. Thanks also to Brian Hall for sharing glovebox construction duties with Neil, and for dry ether supplies.

Clare Crossland – assistance at Daresbury especially at 4 a.m., putting up with the toast stench, secret Word functions, spherical harmonic discussions and help with Maple. Good luck in your final year!

Nick Warmingham – the highly efficient $AM_2O_7(OH)_2(H_2O)_2$ precursor processing machine.

Lara Turner for performing the non-standard EI Mass Spectrometry experiment. Dr. Richard Ibberson for assistance with HRPD data collections, and to Dr. Wuzong Zhou and Prof. Russell Morris at St. Andrews for performing electron diffraction.

Aural stimulation and inspiration for those late nights spent writing up: Guy and co., Richard Green and Tiny, and all at Blue Apple Café, Beccy Owen and many more.

Non-research based help and friends for endless support throughout:- Gemma (for your high spirits and for taking me away to another place), Angela and Ian (for 5* hotel service and many uplifting times), Sandra (care, understanding and also for Sandar), George and Dr. Neil (for their omnipresence, time and for putting me up in Liverpool/Oxford), Françine (for 'toons, tunes, budino, and guidance throughout), Kelly (for advice), Debbie (for her bubbly visits to the office), Amber (for the 40% ABV Xmas cake), and to David (for being the real fount of all knowledge science-wise). Last and most definitely not least, Mum, Dad and Anna; and Pam for immense belief, love, encouragement and understanding. Thanks also to EPSRC, the Department of Chemistry and ICI for funding and scholarships.

'... behind every shadow is light'

R. Green, *Floodlit World*, 1997.

Glossary of Abbreviations

^{i}Pr = isopropyl, $(CH_3)_2CH_2$-

R = alkyl or aryl group

THF = tetrahydrofuran

VT = variable temperature

VTXRD = variable temperature (powder) X-ray diffraction

PV = pseudo-Voigt (peak function)

RT = room temperature

NTE = negative thermal expansion

FWHM = full width at half maximum

ESD = estimated standard deviation

MAS NMR = magic-angle spinning nuclear magnetic resonance

RMM = relative molecular mass

Chapter One: Negative Thermal Expansion and AM_2O_8 Phases

1.1 The Phenomenon of Negative Thermal Expansion (NTE)

1.1.1 Introduction

This thesis describes a range of studies on members of the AM_2O_8 ($A = Zr^{IV}$, Hf^{IV}; $M = Mo^{VI}$, W^{VI}) family of solid-state materials, which exhibit unusual thermoresponsive behaviour. The thermoresponsive behaviour of a material describes the effect of temperature upon its bulk expansion properties. For example, the volume of normal substances increases when they are heated at constant pressure. Several AM_2O_8 compounds exhibit the opposite effect and shrink when heated. This introductory chapter contains background theory on thermal expansion, information on why some framework materials can actually contract on heating, and a detailed review of the structural chemistry of AM_2O_8 phases, which form the main focus of this work.

Most solid materials expand on heating owing to the anharmonic nature of the normal vibrations of a chemical bond. These vibrations arise from the asymmetric potential well that connects two bonded atoms due to interatomic repulsions dominating attractive forces at short distances. As temperature increases, higher vibrational energy levels are populated forcing an increase in bond length and bulk expansion of the material.

The thermal expansion of a material is mathematically derived from its linear strain relative to a reference cell parameter, a_0, as in Equation 1.1.

$$Strain = \int_{a_0}^{a} \frac{da}{a} = \ln\left(\frac{a}{a_0}\right) = \ln[1 + (\delta a / a_0)] \qquad (1.1)$$

The derivative of the strain with respect to temperature is known as the linear coefficient of expansion, defined as,

$$\alpha_l = (\partial \ln a / \partial T)_P = \left(\frac{1}{a}\right)\left(\frac{\partial a}{\partial T}\right)_P \tag{1.2}$$

A formal definition of the mean linear expansion coefficient between two temperatures is given by Equation 1.3.

$$\alpha_l = \int_{T_0}^{T} \alpha(T)dT/(T - T_0) = \ln(a/a_0)/(T - T_0) \tag{1.3}$$

However, it is more common to quote the expression in Equation 1.4.

$$\alpha_l = \frac{((a - a_0)/a_0)}{T - T_0} \tag{1.4}$$

Whenever a mean linear expansion coefficient is quoted in this thesis, it refers to the expression given in Equation 1.4. For materials displaying anisotropic expansion it is common to quote $\alpha_l = \frac{1}{3}\alpha_V$, where α_V is the mean volumetric expansion coefficient. Materials have been broadly classified into three groups depending on their coefficient of thermal expansion: high ($\alpha_l > 8 \times 10^{-6}$ K^{-1}), intermediate ($2 < \alpha_l < 8 \times 10^{-6}$ K^{-1}), or very low ($0 \leq \alpha_l < 2 \times 10^{-6}$ K^{-1}).[1]

The formal relationship between lattice vibrations and thermal expansion was established by Grüneisen. He observed that the ratio of the thermal expansion coefficient to the isobaric heat capacity of a number of metals was approximately independent of temperature over a large temperature range.[2] Grüneisen later applied Einstein's quantum model to phonons in order to quantify the above experimental observation. The model included $3N$ independent harmonic vibrations with the same frequency ν. It was assumed atoms were subject to a simple interatomic potential set up by their neighbours. The volume, V, dependence of the frequency was described by the Grüneisen parameter, γ, in Equation 1.5.

$$\gamma = \frac{-d\ln v}{d\ln V} \tag{1.5}$$

From Equation 1.5, expressions for the Helmholtz and internal energies, and volume of a system, Grüneisen derived Equation 1.6, where α_V is the volumetric expansion coefficient (defined by replacing a by V in Equation 1.4), κ_T is the isothermal compressibility ($= -(1/V)(\partial V/\partial P)_T$) and C_V is the isovolumetric heat capacity. The significance of Equation 1.6 is that γ is independent of temperature and only a function of volume. It can be seen that γ is crucial in determining whether a material expands or contracts. A positive γ requires a positive α; a negative γ implies a negative α.

$$\gamma = \frac{\alpha_V V}{\kappa_T C_V} \tag{1.6}$$

Of course Grüneisen's theory only strictly applies to simple systems and cannot be applied to materials that display anisotropic expansion. In reality, a range of phonons are available to a solid which are of different energies and are thus populated at different temperatures. A mean Grüneisen parameter must therefore be considered, $\gamma_m = \Sigma w_i\gamma_i / \Sigma w_i$ where w_i is the weight of the ith vibrational mode that contributes to the overall heat capacity, and overall thermal expansion of the material.

Some common materials actually contract on heating over certain temperature ranges. These include solids with the diamond structure (*e.g.* silicon) at low temperature,[3] ice below 73 K,[4] and β-quartz at high temperature.[5] These shrinking materials possess lattice vibrations which overcome the normal expansive vibrations and permit the phenomenon of negative thermal expansion (NTE), *i.e.* the dimensions of the lattice are reduced with increasing temperature.[6] Such vibrational modes are generally transverse in their nature as opposed to normal longitudinal vibrations. Figure 1.1 illustrates the effect of transverse vibrations in a two-dimensional lattice containing two different cations bridged by oxygen atoms.

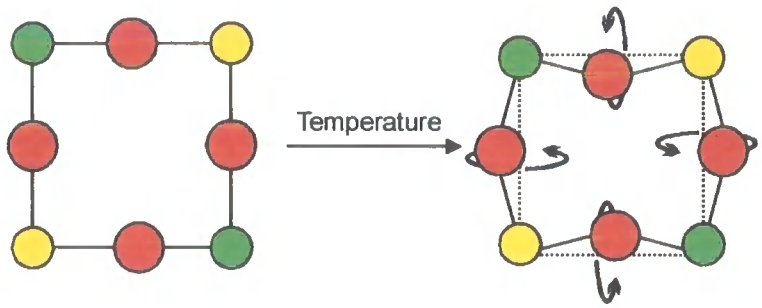

Figure 1.1. The effect of transverse vibrations on a series of *M*–O–*M′* bonds. The dashed line shows that as transverse vibrations occur the *M*···*M′* distance is reduced, thus contracting the area of the lattice (or the volume, in three dimensions).

Equations 1.5 and 1.6 offer a simple explanation of thermal expansion. Consider a single *M*–O–*M′* bond: if the frequency of a phonon decreases as a function of decreasing volume (a so-called soft vibrational mode), there will be a negative Grüneisen parameter and therefore α_V must also be negative by Equation 1.6.[7,8] This is the origin of NTE. For normal longitudinal vibrations, the frequency decreases as volume increases, implying the opposite scenario; such phonons tend to have a positive Grüneisen parameter and lead to positive thermal expansion. In general, transverse vibrations are of lower energy than their longitudinal counterparts and tend to dominate at low temperatures.

Consider the thermal expansion of silicon. At temperatures approaching 0 K the thermal expansion tends to zero due to the absence of any populated vibrational energy levels. The temperature dependence of the expansion coefficient between 4 and 340 K has been accurately measured by dilatometry by Lyon *et al.* as shown in Figure 6.10. The expansion is weakly positive between 6 to 18 K, negative between 18 and 125 K and then positive above 125 K.[9] In the 18 to 125 K region, transverse vibrations have the largest weighting of the density of states meaning a negative mean Grüneisen parameter exists. These modes dominate the expansion and give rise to NTE. At other temperatures normal expansive vibrations dominate.

The Einstein model of heat capacity can be combined with the Grüneisen relationship such that the unit cell parameters of a crystalline solid can be modelled as a function of temperature using Equation 1.7.[10,11]

$$\ln a_{calc} = \ln a_0 + \sum_i \frac{c_i \theta_i}{\exp(\theta_i / T) - 1} \qquad (1.7)$$

Whilst Equation 1.7 is a convenient expression for the magnitude of thermal expansion that captures some aspects of the underlying physics, the model of the vibrational density of states it assumes (Einstein; all oscillators have the same frequency) is an extreme one. Refinable parameters such as the Einstein temperature parameter, $\theta_i = h\upsilon_i/k_B$ where υ_i is the vibrational frequency, give some idea of the energy scale of the vibrations involved, but detailed interpretation should be performed with caution.

1.1.2 Rigid Unit Modes

Figure 1.1 shows that during the course of a transverse vibration, if an *M*–O distance remains constant, the *M*···*M′* distance will decrease and NTE will occur. This only holds for relatively strong (stiff) *M*–O covalent bonds, *e.g.* where *M* is Si, P or a highly charged metal cation. NTE thus occurs in lattices that contain relatively rigid polyhedra with relatively flexible bridging links.

In the case of silicon above, NTE is only observed at low temperatures. However NTE is not always a low-temperature phenomenon. The structure of the material directly determines the relative importance of different vibrational modes and thus the temperature at which NTE is seen to occur. In fact, many materials undergo NTE at high temperatures after a phase transition has occurred. For example β-quartz undergoes near-zero or weak negative thermal expansion above the α to β phase transition temperature, T_c of 846 K.[5] It is typical of framework materials like quartz to undergo a displacive order-disorder phase transition - an artefact of the relatively rigid polyhedra, which unfold in the low-temperature α phase such that they attain the correct geometric arrangement required to undergo transverse vibrations. Dove *et al.* have coined the term Rigid Unit Modes (RUMs) to describe low-frequency phonons that allow motion of, but not distortion of, polyhedral groups in a framework material. The transverse modes that operate in the high-temperature β form of quartz have been classed as RUMs;[12] Hammonds *et al.* have introduced and developed the theory such that the RUM density of states of any framework structure can be calculated.[13]

On a simple level, to ascertain whether a framework structure has available RUMs, one compares the number of degrees of freedom to the number of polyhedral constraints. If the number of degrees of freedom (F) is greater than the number of constraints (C) then RUMs may exist. The degrees of freedom can be calculated simply from the number of dimensions in which objects are free to rotate and translate (six per polyhedron). The constraints are related to the number of shared vertices each polyhedron has (*e.g.* for an octahedron sharing all 6 vertices, it is constrained in 3 dimensions at each vertex so the number of constraints = $6 \times 3 = 18$). This simple model tends to overestimate the number of constraints, as some will be symmetry related. Systems such as β-quartz which have zero degrees of freedom for RUMs ($F = 6$ and $C = 3 \times 2 = 6$, as two vertices of each tetrahedron are constrained) should be considered as potentially flexible. A set of RUMs have been reported for β-quartz by Hammonds.[14] In addition, it is often possible for the polyhedra to rotate with only a small distortion, which is termed a quasi-rigid unit mode, or qRUM.

1.2 Examples of NTE in Framework Materials

There has been considerable work reported in the literature on negative thermal expansion in framework materials such as ice, zeolites, silicates, $A_2(MO_4)_3$ and AM_2O_7 phases. Some examples are given below, however the main focus is on cubic AM_2O_8 materials - the first family of phases to show isotropic NTE that included room temperature, as well as other interesting thermoresponsive effects. These are described in Section 1.3.

1.2.1 Ice

The thermal expansion of hexagonal ice was measured by dilatometry in 1929 and was shown to exhibit NTE below 70 K.[15] Full confirmation of the thermoresponsive behaviour was not given until an X-ray synchrotron diffraction study was reported in 1994,[4] in which it was shown that ice displays virtually isotropic NTE from 10 to 73 K, since the a / c cell parameter ratio is almost constant. Above this temperature positive expansion is shown. Similar behaviour is mirrored in other tetrahedrally bonded structures with similar topologies such as Si and InSb.[16]

1.2.2 Zeolites

Zeolites or aluminosilicates are a large family of materials consisting of vertex sharing SiO_4 and AlO_4 tetrahedra and are thus candidates as materials displaying NTE. It has been shown that chabazite, a purely siliceous zeolite, has one of the largest negative coefficient of linear expansion known for any material, $\frac{1}{3}\alpha_V$ varying from -0.5×10^{-6} to -16.7×10^{-6} K^{-1} between 293 and 873 K.[17] The fact that the expansion coefficient varies considerably with temperature and the lattice symmetry is non-cubic (hexagonal), implies the expansion is anisotropic and such a material would be of limited use in controlled expansion applications. However faujasite, another pure silica framework material, displays isotropic NTE over a temperature range of 25 to 573 K ($\alpha_l = -4.2 \times 10^{-6}$ K^{-1}).[18] Couves *et al.* have performed variable temperature free-energy calculations and confirmed NTE in zeolites such as faujasite.[19] Aluminophosphate frameworks, which are made up from tetrahedral AlO_4 and PO_4 units also share the property of NTE, *e.g.* hexagonal AlPO-17 contracts anisotropically between 18 and 300 K ($\frac{1}{3}\alpha_V = -11.7 \times 10^{-6}$ K^{-1}).[20] Zeolites and aluminophosphates tend to possess large expansion coefficients owing to their higher degree of openness and flexibility, relative to β-quartz, for example.

1.2.3 AM_2O_7 Phases

The family of AM_2O_7 (A = Zr, Hf; M = P, V) materials with the zirconium phosphate structure also display negative thermal expansion.[21,22] They contain AO_6 octahedra and MO_4 tetrahedra, which share all vertices; there are no terminal oxygen atoms and so this type of structure is inherently more rigid than cubic AM_2O_8 phases which contain terminal M–O bonds (Section 1.3).

The cubic structure of Figure 1.2 is in fact only the ideal structure, which was reported as early as 1935 for ZrP_2O_7,[23] and 1942 for ZrV_2O_7.[24] The room temperature powder XRD pattern of ZrP_2O_7 can be approximately indexed on this simple 7.94 Å cell (space group $Pa\bar{3}$). However this cell would require the presence of unreasonably short P–O–P bond lengths.

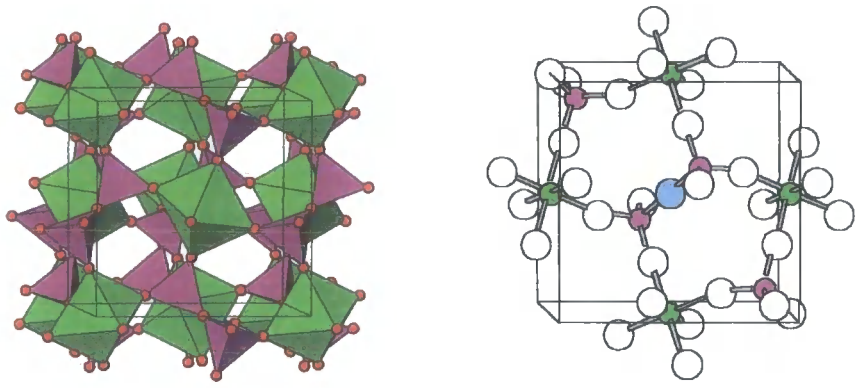

Figure 1.2. Two representations of the structure of cubic AM_2O_7 phases; the polyhedral view (*left*) shows vertex-linked AO_6 octahedra to M_2O_7 groups. The ball and stick view (*right*) highlights part of the unit cell, in particular, the location of a M_2O_7 group (*i.e.* a pair of vertex-bonded MO_4 tetrahedra) along a three-fold axis consistent with $Pa\bar{3}$ lattice symmetry.

Many members of the AM_2O_7 family are thus actually distorted at room temperature. For example, ZrV_2O_7, ZrP_2O_7 and TiP_2O_7 all undergo a phase transition on cooling to give a lower symmetry $3 \times 3 \times 3$ super-cell, which allows for non-linear M_2O_7 groups.[25]

Zirconium vanadate shows positive expansion below 345 K. At 345 K a phase transition occurs from the $3 \times 3 \times 3$ super-cell,[26] to an incommensurate structure with non-integral super-lattice peak positions. At 375 K, it exists as a simple cubic lattice of cell edge, a. The librational RUMs dominate in the simple cubic structure and thus cause NTE ($\alpha_l = -7.1 \times 10^{-6}$ K^{-1} between 400 and 500 K). At low temperatures, positive expansion results from the unfolding of the polyhedra in the super-cell. The incommensurate phase possibly results because there are several energy minima, due to various arrangements of 108 ZrO_6 octahedra and 216 VO_4 tetrahedra in the 26.3 Å × 26.3 Å × 26.3 Å cube being allowed, while still retaining all the lattice topology and space group symmetry.[27] Further details of AM_2O_7 phases are described in detail elsewhere.[28]

1.2.4 $A_2M_3O_{12}$ Phases

$A_2(MO_3)_4$ phases show strong anisotropic thermal expansion. The first member of the family to be structurally investigated was $Sc_2(WO_4)_3$.[29] The structure contains ScO_6 and WO_4 corner-shared regular polyhedra. It is an orthorhombic phase in which NTE is displayed in the a and c directions and positive expansion occurs along b. Thus the

mean expansion coefficient, $\frac{1}{3}\alpha_V$ is quite low at -2.2×10^{-6} K^{-1} between 10 and 450 K. A variety of other $A_2M_3O_{12}$ phases have been prepared and characterised.[30] Substitution of larger A^{III} cations tends to increase the magnitude of the negative thermal expansion coefficient. For example, $Lu_2(WO_4)_3$[†] shows anisotropic NTE along all three orthorhombic edges with a mean expansion coefficient, $\frac{1}{3}\alpha_V = -6.8 \times 10^{-6}$ K^{-1} (400 – 900 K).[31]

1.3 Isotropic NTE and Phase Transitions in Cubic $ZrW_{2-x}Mo_xO_8$ Phases

1.3.1 Cubic ZrW_2O_8

1.3.1.1 Synthesis and Properties of ZrW_2O_8

ZrW_2O_8 was first reported as a ternary phase in 1959 by Graham *et al.*,[32] who were intending to stabilize cubic ZrO_2 by doping with higher-valent W^{VI} and annealing at temperatures ranging from 1273 to 1673 K. However through their work they instead provided basic preparations of impure samples of ZrW_2O_8 from the binary oxides ZrO_2 and WO_3 for a range of compositions. They reported that the new ZrW_2O_8 phase was not observed below 1423 K; and that samples had to be quenched in water or air from high temperature. Slow-cooling simply led to decomposition to the starting materials, highlighting the metastability of this phase. The room temperature X-ray powder pattern was indexed by Graham on a cubic unit cell, with $a = 9.154$ Å. In 1967, Chang *et al.* reported that the material melts at 1530 K to ZrO_2 and a liquid.[33] The preparation of pure ZrW_2O_8 by Chang involved prolonged (> 24 hours) heating of ZrO_2 and WO_3 contained in a Pt tube at 1473 K under a nitrogen atmosphere, followed by a quench in water.

The phase diagram for ZrO_2-WO_3 was also reported by Chang and the only ternary phase in the system was the cubic polymorph of ZrW_2O_8, thermodynamically stable between 1380 and 1530 K. Early syntheses of ZrW_2O_8 were restricted to such high

---

[†] Comparison of effective ionic radii, $r(Lu^{III}) = 0.861$ Å; $r(Sc^{III}) = 0.745$ Å.

temperatures and for prolonged annealing times until 1998 when Closmann *et al.* reported that ZrW_2O_8 could made phase pure *via* the thermal treatment of a hydrated zirconium tungstate precursor, $ZrW_2O_7(OH)_2(H_2O)_2$ at 873 K for 10 hours. This precursor was made using a similar sol-gel route to that employed by Clearfield to prepare $ZrMo_2O_7(OH)_2(H_2O)_2$,[34] and $ZrW_2O_7(OH)_2(H_2O)_2$ in the 1970s.[35] The temperature employed to dehydrate the precursor and form ZrW_2O_8 is in the region where the product is presumably only kinetically stable. For further details of these hydrated precursor phases see Sections 1.3.2.1 and 1.3.3.1; extensive studies of their dehydration pathways are performed Chapter 2.

The property of negative thermal expansion in ZrW_2O_8 was first reported in 1968 using dilatometry between room temperature and 973 K.[36] Expansion data could not be acquired above ~ 1073 K owing to the thermal decomposition to ZrO_2 and WO_3. The unique property of ZrW_2O_8 to display isotropic negative thermal expansion went unnoticed until the mid-1990s. The room temperature structure was solved by powder X-ray and neutron methods by Mary *et al.*,[37] and also, independently, using neutron diffraction by Auray *et al.*.[38] Mary and co-workers had previously investigated the $ZrP_{2-x}V_xO_7$ family of phases which showed negative thermal expansion above 373 K and are structurally related to cubic ZrW_2O_8 (see Section 1.3.1.2). In addition to the room temperature structure of ZrW_2O_8 they reported its variable temperature behaviour between 0.3 and 693 K; the room temperature to 693 K diffraction derived cell parameters showed excellent agreement to the dilatometer data.[36]

1.3.1.2 Room Temperature Structure of ZrW_2O_8

The room temperature structure of zirconium tungstate, α-ZrW_2O_8 (or α-$Zr(WO_4)_2$) was indexed on a cubic unit cell in the acentric space group $P2_13$ and consists of ZrO_6 and WO_4 polyhedra (Figure 1.3). Each ZrO_6 octahedron is vertex-linked to six other WO_4 tetrahedra; three of the vertices of any given WO_4 tetrahedron are shared with three ZrO_6 octahedra leaving one of the W–O vertices as a non-bridging atom. Evans *et al.* suggested the unfavourable bonding arrangement around the non-bridging oxygen in ZrW_2O_8 could be the reason for the metastability of the phase.[39] Although unusual, mono-coordinate oxygen atoms in the solid state are not without precedence - trigonal polymorphs of ZrM_2O_8 where M = W,[40] Mo,[41,42] also feature MO_4 moieties containing

one terminal O atom (Sections 1.4.2 and 5.1; see also new orthorhombic phases in Chapter 2). The layered V_2O_5 structure also possesses one mono-coordinate O atom per pyramidally-coordinated VO_5 group; the V···O interlayer bond length is ~ 2.8 Å and thus cannot viewed as a real covalent bond.[43] Materials such as Li_2TiOMO_4 (M = Si, Ge),[44] and the mineral fresnoite $Ba_2TiOSi_2O_7$,[45] also contain five-coordinate titanyl groups with apical O atoms.

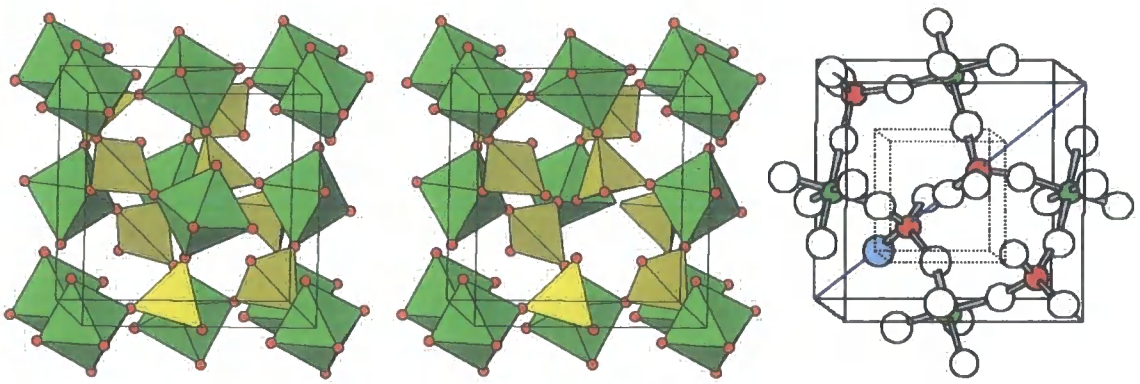

Figure 1.3. Polyhedral representation of the unit cell of cubic ZrW_2O_8 at room temperature (*left*). Removing the front "face-centred" ZrO_6 octahedron for clarity reveals the proximity of two weakly bonded WO_4 tetrahedra along the body diagonal (*centre*). The diagram on the right highlights a portion of the unit cell where the O(4)O_3W(1)···O(3)W(2)O_3 interaction along the body diagonal is more apparent. Note the apical O(4) atom highlighted in blue at ~ (0.23, 0.23, 0.23).

Figure 1.3 shows the existence of the mono-coordinate oxygen atoms that are located along the body diagonal (three-fold axis) of the cubic unit cell. The two WO_4 groups point along same direction of the body diagonal, giving rise to the acentric symmetry of the unit cell. A weak interaction does exist between the "mono-coordinate" O(3) atom at (~ 0.49, ~ 0.49, ~ 0.49) and the neighbouring W(1); the bond length is ~ 2.4 Å at room temperature, compared to the bridging W–O distances of 1.78 to 1.80 Å or non-bridging distance of 1.71 to 1.73 Å. O(4), on the other hand, is strictly mono-coordinate with the nearest metal ~ 3.6 Å away. The contribution to the total atom valence of a central atom, M can be calculated empirically from the surrounding ligand to M bond lengths.[46,47] Such bond valence calculations show that approximately 5% of the total bonding about W(1) and 15% of that of O(3) are accounted for by the long W(1)···O(3) interaction, *i.e.* O(3) can be described as "partially two-coordinate".

The room temperature structure of α-ZrW_2O_8 is similar to that of AM_2O_7 materials at high temperature, which tend to adopt the centric $Pa\bar{3}$ space group. Comparing Figures 1.3 and 1.2 shows the axially symmetric $[O_3MOMO_3]^{4-}$ moiety present in AM_2O_7 phases lies along the body-diagonal, in place of two weakly bonded WO_4^{2-} polyhedra in ZrW_2O_8. The asymmetry of the two WO_4^{2-} groups lowers the symmetry from $Pa\bar{3}$ to $P2_13$ through loss of the inversion centre.

1.3.1.3 Thermoresponsive Behaviour of ZrW_2O_8

Evans, Mary and Sleight discovered the full extent of the unusual thermoresponsive properties of ZrW_2O_8.[37,39] Figure 1.4 shows the results of neutron diffraction and dilatometry which were used to show that ZrW_2O_8 continually contracts from 2 K to 1050 K, only showing a slight interruption in the smooth cell parameter curve at around 448 K due to an order-disorder phase transition.[48] ZrW_2O_8 remains cubic throughout this temperature range and thus the contraction is isotropic. ZrW_2O_8 was the first example of a material to display isotropic NTE over such a large temperature range, which also included room temperature. Such a discovery prompted a variety of investigations on this material and other AM_2O_8 materials that will be discussed in the remainder of this chapter.

Early NTE materials were reported to display anisotropic behaviour, which would lead to micro-cracking and failure of composite materials. No such problems would be envisaged for ZrW_2O_8 and it has thus been of significant interest for use in a variety of technological applications. Also, the coefficient of thermal expansion from 0 – 350 K, $\alpha_l = -9.1 \times 10^{-6}\ K^{-1}$,[48] is comparable to the expansion of regular ceramic materials like alumina and silicon, with $\alpha_l = 7.8 \times 10^{-6}\ K^{-1}$,[50] and $2.5 \times 10^{-6}\ K^{-1}$,[51] respectively. Another reason for the commercial interest is the fact that the contraction is effectively constant over the operating temperature range of electronic components. This leads to the idea of matching or controlling the expansion of composite materials. Examples of such applications of NTE materials are outlined in Section 1.5.

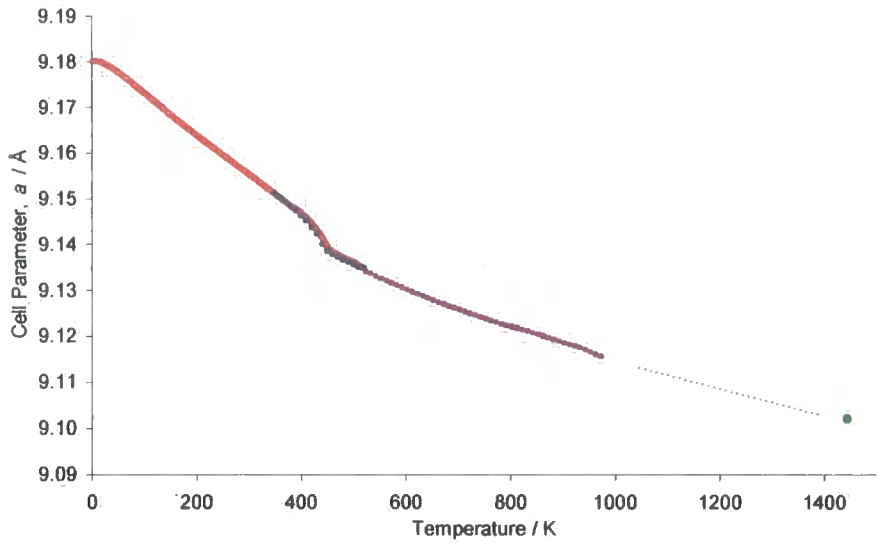

Figure 1.4. The cubic cell parameter of ZrW_2O_8 as a function of temperature obtained from neutron diffraction upon warming (2 – 520 K) and cooling (520 – 350 K),[48] dilatometry (298 – 973 K),[39] and very high temperature neutron diffraction at 1443 K.[49] The region of instability of the material is highlighted by the dashed line between ~ 1050 to 1380 K. Isotropic NTE is shown throughout; an order-disorder phase transition in the material is manifested by the hump at ~ 448 K. Cell parameter hysteresis through the phase transition is discussed in Section 3.5.2.

Figure 1.4 shows reduced expansion above the α to β phase transition temperature of 448 K ($\alpha_l = -6.5 \times 10^{-6}$ K^{-1} between 454 and 520 K). The structure of the high temperature form or β phase is reported to be a higher symmetry $Pa\bar{3}$ structure as in the case of AM_2O_7 phases. Structural Rietveld refinement showed that the phase transition is due to the disordering of W and O atoms along the body diagonal (Figure 1.5).[52]

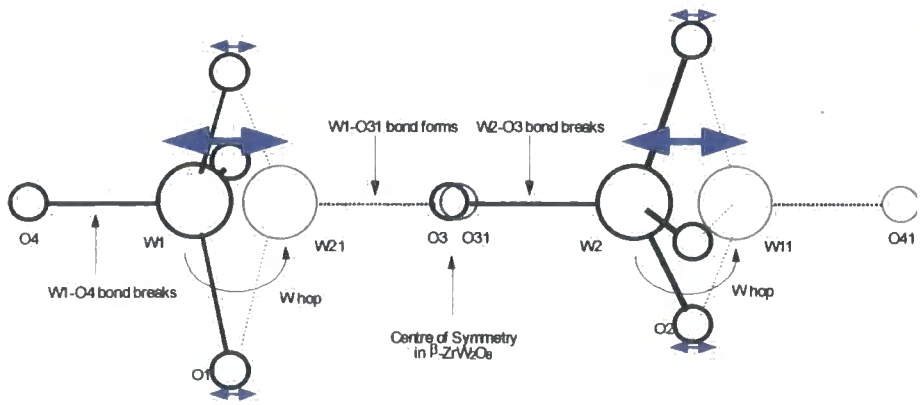

Figure 1.5. A schematic of the WO_4^{2-} group inversion in the order-disorder phase transition of ZrW_2O_8. In the α phase, W1, W2, O1, O2, O3 and O4 are fully occupied (bold bonds), whereas in the β form W11, W21, O31, and O41 become half occupied as well (bold and dashed bonds). Figure taken from Evans *et al.*.[39]

The order-disorder phase transition is manifested by loss of (*hk0*) $h \neq 2n$ peaks in the diffraction patterns of β-ZrW_2O_8, consistent with the gain of a centre of symmetry for a $P2_13$ to $Pa\bar{3}$ transformation. The model used in the Rietveld refinement of the data shown in Figure 1.4 is schematically represented in Figure 1.5. The bold lines show the two tungstate groups pointing in the same direction in the α form (along the three-fold axis). At high temperature, the data are consistent with a disordering of these groups such that they can both point along [111] or $[\bar{1}\bar{1}\bar{1}]$ with equal probability, through a dynamic inversion-type motion. The extent of ordering is refined using a site occupancy parameter, *frac* which equals 0 or 1 for fully ordered (α-ZrW_2O_8), or 0.5 for fully disordered WO_4 groups (β-ZrW_2O_8). It is noteworthy that the tetrahedra can be modelled to move independently but the coordination number of each W atom is always four. Refinements using two *frac* parameters (one per WO_4) made no noticeable improvement to the quality of the refinements and it was presumed that the process was best described as cooperative rather than independent inversion of WO_4 groups. Figure 1.6 shows the temperature variation of the fractional occupancy parameter; this can be used to monitor directly the course of the phase transition.

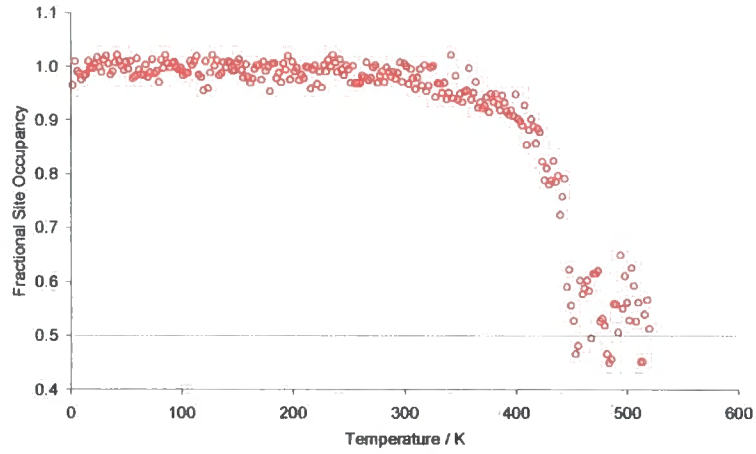

Figure 1.6. Refined O(4) fractional occupancy parameter as a function of temperature from neutron diffraction data of ZrW_2O_8.[48] The *frac* values of approximately one half (*i.e.* 50% disordering between the O(4) and O(41) sites) above 448 K confirms the complete disordering of WO_4 moieties. At 300 K and below, *frac* = 1.0 implying complete ordering of WO_4 (*i.e.* 100% occupancy of site O(4) and 0% of site O(41)).

Highly covalent *M*–O bonds *i.e.* relatively stiff polyhedra, and flexible Zr–O–W links are responsible for NTE in cubic ZrW_2O_8. Cooperative librations such as those displayed in Figure 1.1 lead to a reduction of the unit cell in all three dimensions.[37]

Pryde *et al.* have since quantified this observation by performing RUM calculations on ZrW_2O_8 and have confirmed the existence of a family of low-energy transverse vibrations in the structure.[53,54] Further evidence comes from low-temperature specific heat capacity measurements; below 200 K a dominant low-energy phonon (~ 5 meV or 40.3 cm^{-1}) exists, with a negative Grüneisen parameter.[55] Ernst *et al.* have measured the phonon density of states of ZrW_2O_8 by inelastic neutron scattering and shown five modes exist up to the energy of 8.5 meV with a large negative Grüneisen parameter.[56] David *et al.* also confirmed the presence of a low-energy vibrational mode (~ 3.3 meV or 27 cm^{-1}) with a negative Grüneisen parameter by fitting the cell parameter trend derived from neutron diffraction (that of Figure 1.4) using a combined Einstein-Debye model of the internal energy.[57] They also reconstructed the form of the density of states from the observed lattice parameters to give an low-energy phonon of ~ 4.7 meV (38 cm^{-1}). The above analyses have justified the existence of a low-energy 40 cm^{-1} band observed in the vibrational Raman spectrum recorded by Evans,[39] and confirm the origin of NTE in ZrW_2O_8.

Cao *et al.*, however, have recently argued that the RUM model in α-ZrW_2O_8 is not entirely valid.[58] They have performed variable temperature XAFS (X-ray absorption fine structure) measurements to probe the local environment of the W and Zr atoms. They suggest the low-energy vibrational mode in ZrW_2O_8 is not solely due to transverse O motion but rather heavy atom motion as well. They suggest that there are significant distortions of Zr–O distances between 20 and 300 K such that the ZrO_6 octahedra can only be considered as stiff rather than rigid; WO_4 are, however, much stiffer. They also imply that W–O–Zr units were relatively rigid between 20 to 160 K with only a minor distortion up to 300 K. As a consequence of these observations they formulated an alternative model where correlated vibrations of a rigid WO_4 and the three bonded, less rigid ZrO_6 groups occur in a plane perpendicular to the [111] axis (Figure 1.3, *left*). The W···Zr linkage remains rigid causing the Zr···Zr distance to decrease, which in turn gives rise to contraction of the unit cell (since a is determined by the Zr···Zr distance as in Figure 1.3). Cao's justification for this model over the purely rigid unit model was that in the latter model, the amplitude of the W–O–Zr transverse vibration required to give the observed coefficient of expansion would imply a large change in W···Zr distance. It should be noted, however, that these conclusions are contrary to Evans' crystallographic studies,[48] and (unpublished) neutron total scattering experiments.[59]

A consequence of the order-disorder transition in ZrW_2O_8 at 448 K is the onset of oxygen migration in the material.[48] For example, O(4) in Figure 1.5 becomes mobile; it leaves the original (0.23, 0.23, 0.23) site and becomes randomly distributed over the two symmetry related sites in $Pa\bar{3}$ of (0.23, 0.23, 0.23) and (0.77, 0.77, 0.77). These can be seen in Figure 1.7 where disordering occurs over the two opposite corner sites represented by the dashed cube. Mary *et al.* have reported the ionic conductivity of β-ZrW_2O_8 as comparable to that of cubic stabilised ZrO_2.[37] The room temperature α phase exhibited conductivity characteristic of an insulator.

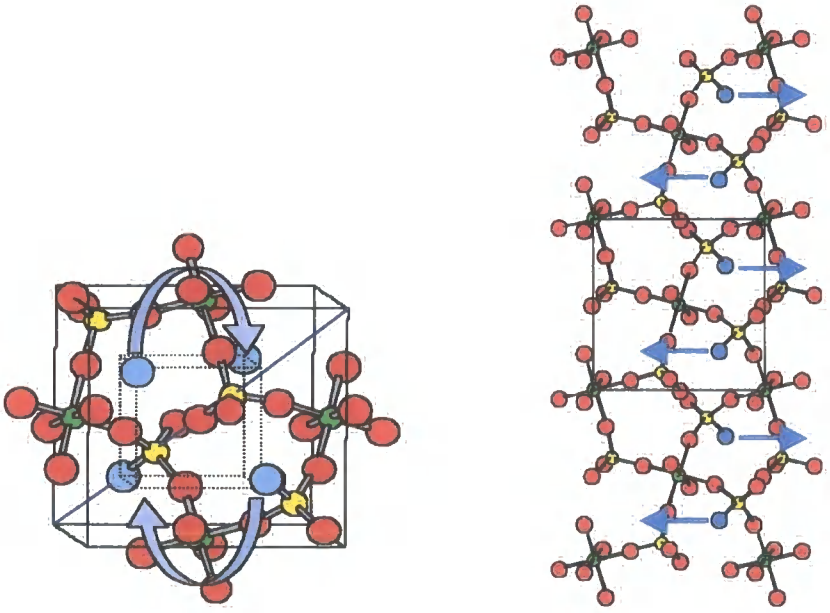

Figure 1.7. Oxygen disorder and migration in the unit cell of cubic ZrW_2O_8 (*left*) and throughout its lattice above 448 K (*right*). At the order-disorder phase transition, apical O(4) atoms migrate from their WO_3O groups to the rear face of neighbouring WO_4 groups, in nucleophilic substitution-like attack. In total, oxygen disorder occurs over eight sites in the unit cell shown by the corners of the inner cube in the left hand figure. An animated graphic of the migration process is available for visualisation purposes.[60]

Identical thermoresponsive behaviour has also reported in cubic HfW_2O_8 by Mary and Evans.[37,39] It had been known since 1967 that HfW_2O_8 is isostructural with ZrW_2O_8 owing to the similarity of their powder patterns.[61] However, Mary and Evans revealed that not only do both these materials possess the property of isotropic NTE over a large temperature range, but also the order-disorder phase transition occurs at the same temperature. The identity of the A^{IV} cation seems to have little effect on the thermal expansion of cubic AM_2O_8 phases. This is consistent with the observation that NTE is

not determined directly by the nature of the cation but rather by the existence of flexible *A*–O–*M* bridges.

1.3.2 Cubic $ZrMo_2O_8$

1.3.2.1 Synthesis of $ZrMo_2O_8$

Despite the similarity of the general chemistry of Mo and W, the existence of cubic $ZrMo_2O_8$ was only reported relatively recently.[62] Unlike ZrW_2O_8, the cubic molybdate analogue does not seem to occur as a thermodynamically stable phase in the ZrO_2-MO_3 system. Instead, the dominant ternary phase above ~ 873 K is a trigonal polymorph of $ZrMo_2O_8$ (see Section 1.4.2 and Chapter 5).[63] Extended annealing at 873 K can give rise to a monoclinic polymorph of $ZrMo_2O_8$.[64]

Cubic $ZrMo_2O_8$ cannot be prepared from the binary oxides below ~ 1070 K, and annealing at higher temperatures as in the preparation of ZrW_2O_8 cannot be achieved owing to higher volatility of MoO_3 compared to WO_3 (T_{melt} = 1068 and 1746 K, respectively). Lind and co-workers were the first to prepare pure cubic $ZrMo_2O_8$ by careful dehydration of a "hydrated precursor", $ZrMo_2O_7(OH)_2(H_2O)_2$.[62] The so-called precursor (referred to throughout this thesis) was first prepared by a sol-gel route and characterised in 1972 by Clearfield and Blessing.[34] Prolonged heating of the precursor gives rise to the thermodynamic trigonal product and so care has to be taken to stop the dehydration at the cubic stage (Figure 1.12). However, Lind's synthesis was difficult to reproduce. Many attempts at dehydrating the precursor using a variety of conditions were performed by Hanson but a pure sample of cubic $ZrMo_2O_8$ proved elusive.[65] A ~ 78% pure sample was eventually prepared and used in a neutron diffraction study by Evans, Hanson and co-workers (Section 1.3.2.2).[66]

Lind provided a modified synthesis of cubic $ZrMo_2O_8$ *via* $ZrMo_2O_7(OH)_2(H_2O)_2$ in 2001.[67] A variety of Zr sources were reacted with ammonium *para*-molybdate in solution to prepare a number of $ZrMo_2O_7(OH)_2(H_2O)_2$ precursors, each of which was dehydrated with the aim of obtaining pure cubic $ZrMo_2O_8$. For example, it was found that preparing $ZrMo_2O_7(OH)_2(H_2O)_2$ from $ZrO(ClO_4)_2$ in $HClO_4$ using a 63 – 70%

excess of Zr over a 1 : 2 ratio of Zr : Mo consistently led to pure samples of cubic $ZrMo_2O_8$ when heated between 638 and 678 K. A typical preparation of a precursor is outlined in Section 7.2. An excess of Zr was necessary to avoid co-precipitation of amorphous MoO_3 during the preparation of the precursor. When the Zr source and acid were replaced by $ZrOCl_2$ in HCl (as originally described by Clearfield and in Lind's first paper) followed by heating between 628 to 683 K, majority cubic $ZrMo_2O_8$ with small amounts of trigonal in some samples were obtained. In comparison to the above "perchlorate route", this "chloride route" is less satisfactory. Other routes to the precursor were also investigated using acetates and sulphates although these did not yield cubic $ZrMo_2O_8$ but rather only the trigonal phase or amorphous materials. It was noted that the perchlorate and chloride-derived precursors only gave pure cubic $ZrMo_2O_8$ *via* an unidentified "low-temperature" polymorph of $ZrMo_2O_8$ (denoted as LT-$ZrMo_2O_8$) which formed as an intermediate at ~ 410 K (Figure 1.12). However, the role of the LT phase in the precursor to cubic transformation as well as its structure were not known. They are investigated in Chapter 2 for the first time.

Lind suggested that the different dehydration behaviour of $ZrMo_2O_7(OH)_2(H_2O)_2$ prepared from different reagents was due to sample crystallinity and sample morphology, although these were essentially empirical observations. The perchlorate precursor was the most crystalline product of all the precursors and this favoured the formation of the cubic phase. Chloride-derived precursors were generally less crystalline and generally led to impure samples of cubic $ZrMo_2O_8$. The particle shape of the precursors was dependent on the Zr source anion; rod-like particles were obtained for perchlorate derived precursors whereas grain-like particles were observed for chloride derived samples. Sample morphology did not change during dehydration. Particle agglomeration also varied from precursor to precursor; chloride derived samples (and subsequent samples of cubic $ZrMo_2O_8$) were agglomerated whereas perchlorate derived samples were the least aggregated.

1.3.2.2 Structure and Thermal Expansion Properties of $ZrMo_2O_8$

The room temperature structure of cubic $ZrMo_2O_8$ was shown to be essentially isomorphous with that of cubic ZrW_2O_8.[62] The chief difference was the choice of space group owing to the orientation of the tetrahedral MO_4 groups (Section 1.3.1.3).

Diffraction data were consistent with the adoption of the high-temperature $Pa\bar{3}$ β-ZrW_2O_8 structural model for $ZrMo_2O_8$ at room temperature. The thermal expansion was studied by variable temperature X-ray and neutron diffraction by Lind and co-workers and is shown in Figure 1.8. Isotropic negative thermal expansion was observed between 11 and 573 K.

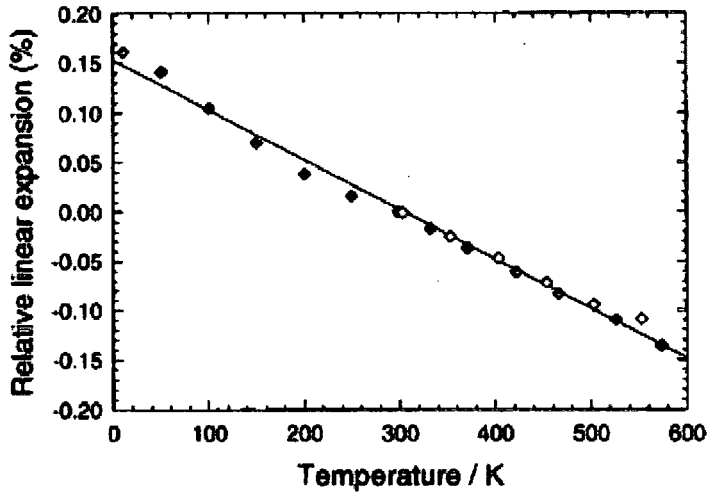

Figure 1.8. Thermal expansion of $ZrMo_2O_8$ between 11 and 573 K according to Lind and co-workers.[62] Relative linear expansion is defined as $100(a_T - a_{298})/a_{298}$ where a_{298} = 9.1304 (2) Å. Refined neutron and X-ray data are represented by closed and open points, respectively.

Lind reported there was a lack of a discontinuity in the cell parameter as a function of temperature and concluded no order-disorder phase transition was apparent in cubic $ZrMo_2O_8$ (contrast the form of the plot in Figure 1.8 to the equivalent Figure 1.4 for ZrW_2O_8). It seemed that the same disordered β phase prevailed throughout the temperature range considered.

The above work prompted further investigation by Evans and co-workers in 2000 to obtain more definitive variable temperature data.[66] Those shown in Figure 1.8 were not entirely conclusive owing to the slight curvature of the trend at low temperature and the fact that only one data point per ~ 50 K was collected. Evans and co-workers' efforts were slightly hampered by the problem of repeating Lind's first synthesis in order to prepare a large bulk sample of pure cubic $ZrMo_2O_8$ as mentioned in Section 1.3.2.1. Nevertheless more complete thermal expansion data were derived using a sample containing ~ 22% trigonal impurity. Their main result is shown in Figure 1.9.

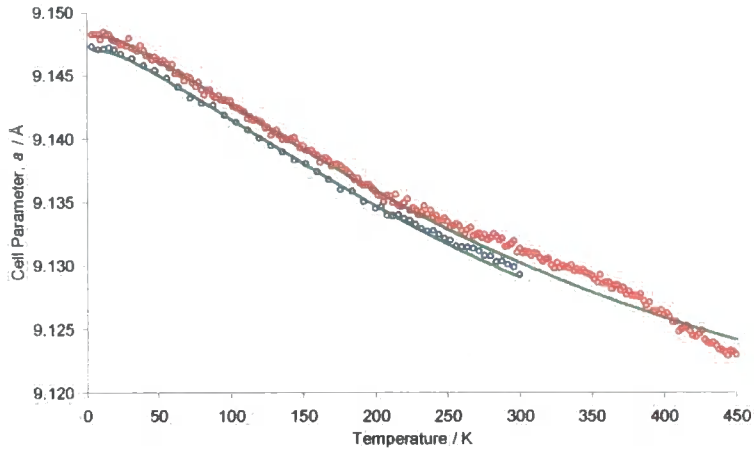

Figure 1.9. The cubic lattice parameter of $ZrMo_2O_8$ upon warming and cooling according to Evans' reported variable temperature neutron diffraction experiment.[66] The solid lines denote the thermal expansion of using a two-coefficient Einstein model (Equation 1.7; $i = 2$). ESDs are typically smaller than the size of the data points.

Figure 1.9 shows significant thermal history in the cell parameter of cubic $ZrMo_2O_8$. The sample was initially quench-cooled from room temperature to 4 K and diffraction data collected upon warming up to 450 K (red data in the figure). The sample was then slow-cooled from 300 back to 4 K (blue data). Confirmation of the disordered β structure was obtained at all temperatures, however, the hysteretic behaviour between warming and cooling is significant. A beam-loss enforced anneal at 196 K upon warming led to a change in the thermal expansion properties. A further change in gradient at ~ 380 K could not be explicitly justified. Evans did suggest that oxygen-ordering could also be important in cubic $ZrMo_2O_8$, though it seems the effect is on a much more subtle level than ZrW_2O_8 or $ZrWMoO_8$ (Sections 1.3.1.3 and 1.3.3.2). Overall, it was concluded that the disordered structure is entropically favoured although a justification for the difference in behaviour to ZrW_2O_8 remains open to question. Ideally further studies had to be performed on a pure sample and these are presented in Chapter 3.

1.3.3 Cubic $ZrWMoO_8$

1.3.3.1 Synthesis of $ZrWMoO_8$

Closmann and Sleight reported that members of the cubic $ZrW_{2-x}Mo_xO_8$ family with $x \leq 1.5$ could be prepared *via* the decomposition of the corresponding $ZrW_{2-x}Mo_xO_7(OH)_2(H_2O)_2$ hydrated phase.[68] Higher members of the family were presumably subject to trigonal impurities. The so-called precursor to cubic $ZrWMoO_8$, $ZrWMoO_7(OH)_2(H_2O)_2$ was prepared from zirconium oxychloride, ammonium *meta*-tungstate and ammonium molybdate. Again this was based on Clearfield's $ZrM_2O_7(OH)_2(H_2O)_2$ syntheses;[34,35] the chief difference was that sodium molybdate/tungstate was replaced by ammonium molybdate/*meta*-tungstate. Solutions of these reagents were refluxed in HCl for 2 days, dried and calcined at 723 K for 10 hours.

1.3.3.2 Thermoresponsive Behaviour of $ZrWMoO_8$

Evans employed Closmann's synthesis to prepare a ~ 13 g sample of cubic $ZrWMoO_8$ in order to compare the thermal expansion and oxygen-ordering to other $ZrW_{2-x}Mo_xO_8$ phases.[66] A comprehensive variable temperature neutron diffraction experiment was performed. Like $ZrMo_2O_8$, the disordered β structure was adopted at room temperature.

For the variable temperature experiment, the sample was quench-cooled from 300 to 2 K in 82 minutes. Diffraction data were recorded upon warming every 2 K from 2 to 640 K, and upon slow-cooling from 639 to 99 K, with a final data collection at 2 K. The refined cubic cell parameter at these temperatures shows an interesting trend (Figure 1.10). Very different behaviour is shown between warming a quenched sample compared to a subsequent slow cool. Initially, the "high temperature" dynamically disordered β phase was trapped by the relatively rapid cool to base temperature. This was manifested by the cell parameter which closely follows the lower curve since the disordered β phase has a smaller cell parameter than that of the ordered α form. The quenched structure was now in a statically disordered β state - insufficient thermal energy was present to allow rapid ordering of the WO_4 or MoO_4 groups. However as the temperature was slowly increased, the material gained enough energy to begin to order

these groups, with the onset of oxygen migration. Evans quoted the linear expansion coefficient as -7.7×10^{-6} K^{-1} between 2 and 200 K, slightly smaller than that of ZrW_2O_8 under the same conditions (-8.9×10^{-6} K^{-1}). The disorder-order process begins at ~ 200 K in Figure 1.10; a hump in the cell parameter exists as the system tries to revert to the ordered α phase. However, the system cannot fully revert since at ~ 250 K the disordered phase becomes thermodynamically stable, meaning the system then reverts back to the β form (complete by 280 K) and remains up to high temperature (> 640 K). Note there is a slight offset between the observed quench-warmed cell parameter and that predicted by the Einstein model. This is because the quench was not infinitely fast (it took 82 minutes to cool) and so partial ordering occurred and therefore some α form was present.

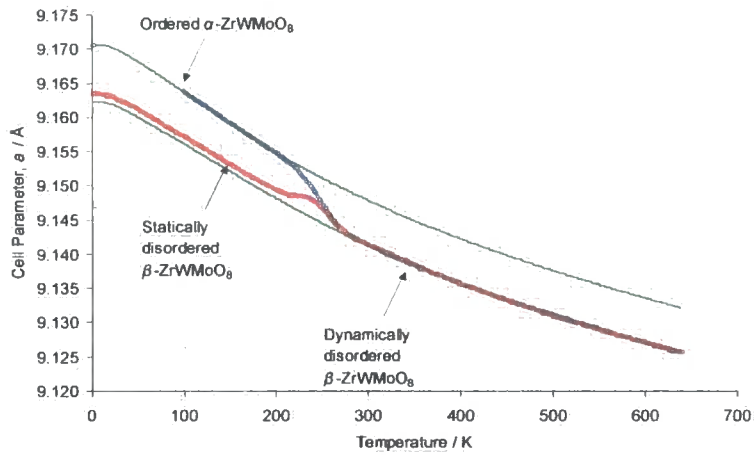

Figure 1.10. Cubic cell parameter of $ZrWMoO_8$ reported by Evans for a quenched sample upon warming from 2 to 640 K *i.e.* the thermal expansion properties of a kinetically stabilised β form. Subsequent slow-cooling data of the β form are also shown from 639 to 99 K, and at 2 K, allowing formation of the low-temperature thermodynamically stable α form at 270 K.[66] Calculated thermal expansion curves of the α and β forms are shown as upper and lower green lines. These curves were calculated using Equation 1.7.

Under slow cooling conditions, $ZrWMoO_8$ begins in its high temperature β state at 639 K; the cell parameter on cooling is very close to that of the quench-warmed sample between 638 and 300 K. However, due to the β to α transition at 270 K, a striking departure from the lower cell parameter curve (of the quenched β form) is observed (Figure 1.10). The linear expansion of the slow-cooled phase is slightly greater than the quench-warmed phase between 200 and 2 K; a value of -8.7×10^{-6} K^{-1} was quoted by

Evans. The phase transition was again monitored *via* the fractional occupancy parameter in the variable temperature Rietveld refinements. As for ZrW_2O_8, the O(4) fractional site occupancy ("*frac*") is ~ 0.50 above the phase transition temperature (compare Figure 1.6). However between 270 and 200 K there is an increase in *frac* to ~ 0.80 (compare 1.0 for the tungstate). Complete oxygen ordering was not observed in $ZrWMoO_8$ unlike in ZrW_2O_8. Evans suggested frustration in the ordering process could result from the different local and neighbouring environments that were possible with combinations of pairs of WO_4 or MoO_4 groups. Further studies on the oxygen ordering in $ZrWMoO_8$ by slower cooling experiments were necessary and are given in Chapter 3.

The most striking consequence of the apparent lowering of the phase transition temperature in $ZrWMoO_8$ relative to ZrW_2O_8 is the onset of oxygen mobility at temperatures as low as 200 K. Evans *et al.* suggested there were no other known electrical insulators that show this property at such low temperatures. AC impedance measurements were performed on $ZrWMoO_8$ confirming the property of ionic conduction albeit at higher temperatures; the conductivity was measured to be ~ 10^{-6} Ω^{-1} cm^{-1} at 700 K.[66] This compares to values for Y_2O_3-doped ZrO_2 of ~ 10^{-4} Ω^{-1} cm^{-1},[69] and ~ 10^{-5} Ω^{-1} cm^{-1} for ZrW_2O_8.[39] The ionic conductivity was measured between ~ 575 and 970 K; a linear Arrhenius plot gave an activation energy of 65 (1) $kJmol^{-1}$ at high temperature.

A value for the activation energy was also determined at low temperature, in the region of the phase transition itself. The form of the hump in the red cell parameter curve in Figure 1.10 contains kinetic information about the β to α process. Evans *et al.* analysed the excess cell parameter due to the α phase over the cell parameter of the disordered β phase as a function of temperature. Assuming the extent of oxygen ordering was proportional to the square root of the excess cell parameter, the extent of ordering could be related to the rate constant and a value for the activation energy could be derived. A similar analysis is employed in Section 3.4.3 except that data are extracted from fractional occupancy parameters instead of cell parameters. Evans obtained a value of 22 (5) $kJmol^{-1}$; quite different to that obtained by impedance; they suggested the discrepancy could be due to the fact that the low-temperature derived value describes a short-range migration whereas high-temperature impedance describes a longer-range

effect. Also, it was stated that activation energies of oxygen mobility were often temperature dependent.

As a result of its low-temperature oxygen mobility, $ZrWMoO_8$ potentially could be used in low-temperature gas sensing, catalysis or in alternative fuel cells. It could also be used as a component of a controlled-expansion composite below 200 K or above 300 K as it shows strong isotropic NTE. The phase transition just below room temperature, however, could cause problems in composites due to a change in the thermal expansion coefficient in this region.

1.3.4 Other Cubic $ZrW_{2-x}Mo_xO_8$ Phases

Studies of cubic $ZrW_{2-x}Mo_xO_8$ phases with non-integer values of x are more sparse in the literature. Closmann and co-workers have prepared samples with $x = 0.4$, 0.6, 0.7, 1.2, 1.4 and 1.5 although the variable temperature behaviour of each of these has not been given.[68] They did, however, note that the $x = 0.4$ and 0.6 phases could be prepared from their precursors at 873 K, and had room temperature structures consistent with ordered α-ZrW_2O_8 ($P2_13$). For $x = 0.7 - 1.5$, products could be prepared at 723 K and these were consistent with the disordered β-ZrW_2O_8 ($Pa\bar{3}$) structure at room temperature. It seemed that the introduction of Mo into the ZrW_2O_8 framework lowered the phase transition temperature (T_c), and thus presumably the onset of oxygen migration. Closmann briefly confirmed this observation by noting for $ZrW_{1.6}Mo_{0.4}O_8$, T_c was 393 K,[68] compared to 448 K for ZrW_2O_8,[48] and 270 K for $ZrWMoO_8$.[66] Cell parameters of $ZrW_{2-x}Mo_xO_8$ showed a decrease with increasing Mo substitution levels at room temperature; for $x = 0$ and 0.6, the cell parameter is between 9.16 and 9.15 Å; in the $x = 0.7$ to 1.5 materials, cell parameters were 9.05 to 9.03 Å. Not only was the smaller size of Mo^{VI} versus W^{VI} presumed responsible for the decrease in cell parameter with increasing Mo levels but also the fact that the β structure is smaller than the α phase (as in Figure 1.10). In their $ZrWMoO_8$ paper, Evans and co-workers suggested that although unusual, the decrease in cell parameter from α to β forms was due to the gain in entropy in going from the ordered MO_4 to disordered MO_4 configuration. A negative volume change can be expected with a positive increase in entropy, for

materials with a negative expansion coefficient, following the thermodynamic argument shown in Equation 1.8.[70]

$$\alpha_V = \frac{1}{V}\left(\frac{\partial V}{\partial T}\right)_P = \kappa_T\left(\frac{\partial P}{\partial T}\right)_V = \kappa_T\left(\frac{\partial S}{\partial V}\right)_T \qquad (1.8)$$

Variable temperature studies have been briefly reported for other $ZrW_{2-x}Mo_xO_8$ phases although in a far less thorough manner to the studies by Evans *et al.*. Chinese workers reported that T_c for $ZrW_{1.6}Mo_{0.4}O_8$ was somewhere between 343 and 383 K,[71] compared to 393 K according to Closmann. They also reported that $ZrW_{0.8}Mo_{1.2}O_8$ retained the disordered oxygen model between 293 and 773 K although refinements were only performed at six different temperatures. On a qualitative level they confirmed Closmann's observation that the increase in Mo substitution favoured the disordered structure at lower temperatures. Their refined cell parameters as a function of temperature, however, seemed poorly determined and did not agree with those given by Closmann for $x = 0.4$ and 1.2.

Although the precursor route to $ZrW_{2-x}Mo_xO_8$ seems the most widely used, it is not very efficient owing to long reflux times involved in preparing the precursor itself. Closmann stated that if the reflux time was shortened from 48 hours then monophasic final products were not observed. Closmann found the reflux stage could, however, be replaced by hydrothermal synthesis for 4 hours at 473 K.[68] Kameswari has reported a variety of other syntheses of these materials.[72] For example, a combustion type route led to the successful formation of *e.g.* $ZrW_{1.5}Mo_{0.5}O_8$ in 15 minutes at 773 K. Nitric acid was added to stoichiometric masses of zirconium oxynitrate, ammonium *meta*-tungstate, molybdic acid, and urea (as a fuel) and placed in a preheated furnace at 773 K. The mixture decomposed evolving large quantities of NH_3 and NO_x gas followed by spontaneous combustion, causing the furnace temperature to rise to 1325 K in 2 – 3 seconds. After a few minutes the temperature stabilised back to 773 K and a slightly impure sample was recovered. Pure phase products could be obtained following brief heating to 1423 K. Although this combustion route is faster than the precursor route, it is potentially dangerous and probably not suited to large-scale industrial syntheses.

1.4 First-order Phase Transitions in Other AM_2O_8 Phases

1.4.1 Temperature and Pressure Dependence of ZrW_2O_8 Polymorphs

It was mentioned in Section 1.3.1.1 that cubic ZrW_2O_8 is the only ternary phase that appears in the ZrO_2-WO_3 phase diagram at ambient pressure.[33] Nevertheless, while exploring new sol-gel routes to cubic ZrW_2O_8, a trigonal modification of the structure was recently reported by Wilkinson *et al.*.[40] It was prepared using non-hydrolytic sol-gel chemistry as described in Section 5.1.1. Crystallisation of the resulting amorphous gels to temperatures around 1013 K led to formation of the new trigonal phase, which had a similar diffraction pattern to trigonal $ZrMo_2O_8$ (Section 1.4.2 and Chapter 5),[41] or to the MRe$_2$O$_8$ (M = Mn, Co, Ni, Zn) family of materials.[73] A full discussion of trigonal AMo$_2$O$_8$ (A = Zr, Hf) phases and their relation to the MRe$_2$O$_8$ phases is presented in Chapter 5. Wilkinson reported that trigonal ZrW_2O_8 underwent conversion to the cubic polymorph at ~ 1473 K.

The application of pressure to AM_2O_8 phases has been well documented in the literature following the work of Evans, Mary and Sleight on the unique expansion properties of cubic ZrW_2O_8 (Section 1.3.1). The prime area of study has been the pressure-dependent behaviour of cubic ZrW_2O_8 such that potential problems during the processing of tailored-expansion ZrW_2O_8-containing composites could be determined. Component materials can be exposed to high pressures during manufacture of composites; potential candidates must therefore be resistant to pressure-induced phase transitions.

Evans *et al.* performed variable pressure studies on cubic ZrW_2O_8 up to 0.6 GPa. At relatively low pressure (0.2 GPa, which can be achieved with a laboratory pellet press for example) the cubic structure converted to a new orthorhombic (γ) polymorph of ZrW_2O_8, the structure of which was solved by powder neutron diffraction.[74,75] The first-order phase transition was reported to be irreversible at room temperature and involved a 5% reduction in unit cell volume. The lowering in symmetry from cubic to orthorhombic arises from the changes in W environment; the three-fold axes along which the 2 WO_4 groups are aligned in the cubic phase are lost. Six unique W sites are

present in γ-ZrW_2O_8, resulting from the pressure-induced distortion of the W···O–W angle from 180 °. A consequence of these polyhedral tilts is a tripling of the cell parameter along the orthorhombic *b* direction. Cell parameters along the *a* and *c* directions remain similar although slightly reduced compared to that of the cubic form. Figure 1.11 shows the unit cell of the high-pressure phase of ZrW_2O_8.

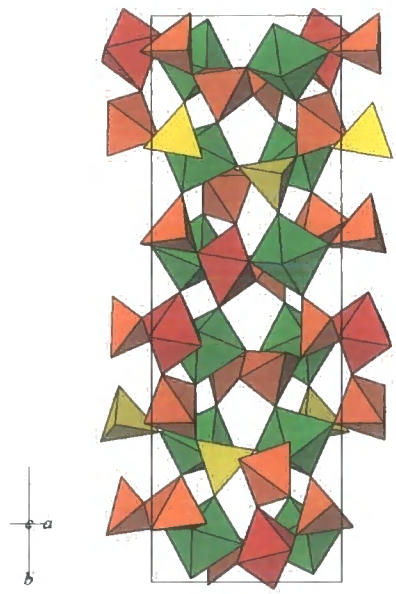

Figure 1.11. The orthorhombic unit cell of γ-ZrW_2O_8 which consists of ZrO_6 polyhedra, vertex linked to WO_n polyhedra (n = 4, 5, 6; bonds shown for distances ≤ 2.3 Å). γ-ZrW_2O_8 shows a tripling of the *b* cell parameter relative to cubic α-ZrW_2O_8 in Figure 1.3. Unlike the cubic phase there are no apical O atoms as such; additional W–O bonds relative to cubic form are, however, long (~ 2.3 Å).

Evans showed that although orthorhombic γ-ZrW_2O_8 could be quenched at ambient pressure, it readily converts back to cubic α-ZrW_2O_8 upon annealing at 393 K and 1 bar. Perrotoni and da Jornada have reported the amorphisation of α-ZrW_2O_8 between applied pressures of 1.5 and 3.5 GPa.[76] The amorphous phase could be recovered on release of pressure, and the cubic form re-crystallised by annealing at 923 K. Grezechnik *et al.* furthered these investigations by performing *in situ* high pressure-high temperature X-ray synchrotron experiments.[77] A sample of ZrW_2O_8 was heated at 2.2 – 2.5 GPa just after the pressure-induced amorphisation had occurred; below 1000 K no structural transformations were detected. However, at 1042 K a new crystalline polymorph of ZrW_2O_8 formed, which was recoverable upon the release of pressure. This new phase was found to be stable up to ~ 1100 K at ambient pressure, *i.e.* similar to the

decomposition temperature reported for cubic ZrW_2O_8.[36] The observed unit cell volume reduction relative to α-ZrW_2O_8 was 42%. The structure was solved by powder methods and shown to be similar to hexagonal α-U_3O_8. In this structure Zr^{IV} and W^{VI} are statistically distributed along chains of highly distorted, vertex-shared MO_6 octahedra, with an additional, very weak M–O interaction at a displacement of 2.85 (6) Å.

The thermal expansion behaviour of orthorhombic γ-ZrW_2O_8 was also reported by Evans *et al.*.[74,78] Although some of the flexibility of the cubic phase had been lost due to supplementary W–O bonding, γ-ZrW_2O_8 still displayed negative thermal expansion albeit with a reduced expansion coefficient of $\frac{1}{3}\alpha_V = -2 \times 10^{-6}$ K^{-1} (4 - 150 K).[74] Evans suggested the increase in bonding would permit a greater contribution to normal expansive phonons and a smaller contribution to the contractive librations, manifesting itself by a smaller expansion coefficient than for α-ZrW_2O_8. Near 225 K, α_V of γ-ZrW_2O_8 is reduced to zero, becoming positive above room temperature and up to 400 K.[74,75] Evans suggested the cause of this change in expansion above room temperature was related to a change in the ordering of WO_4 groups as the α phase begins to reform.[74] A direct analogy to the marked change in cell parameter during the α- to β-ZrW_2O_8 transition was made.

In conclusion, the pressure-induced transition of cubic ZrW_2O_8 at 0.2 GPa could pose initial problems if used in the manufacture of controlled expansion composites (Section 1.5). However, the cubic phase can be easily recovered by heating to 393 K. High-pressure studies of other AM_2O_8 materials are described in Sections 1.4.2 and 1.4.3.

1.4.2 Temperature and Pressure Dependence of $ZrMo_2O_8$ Polymorphs

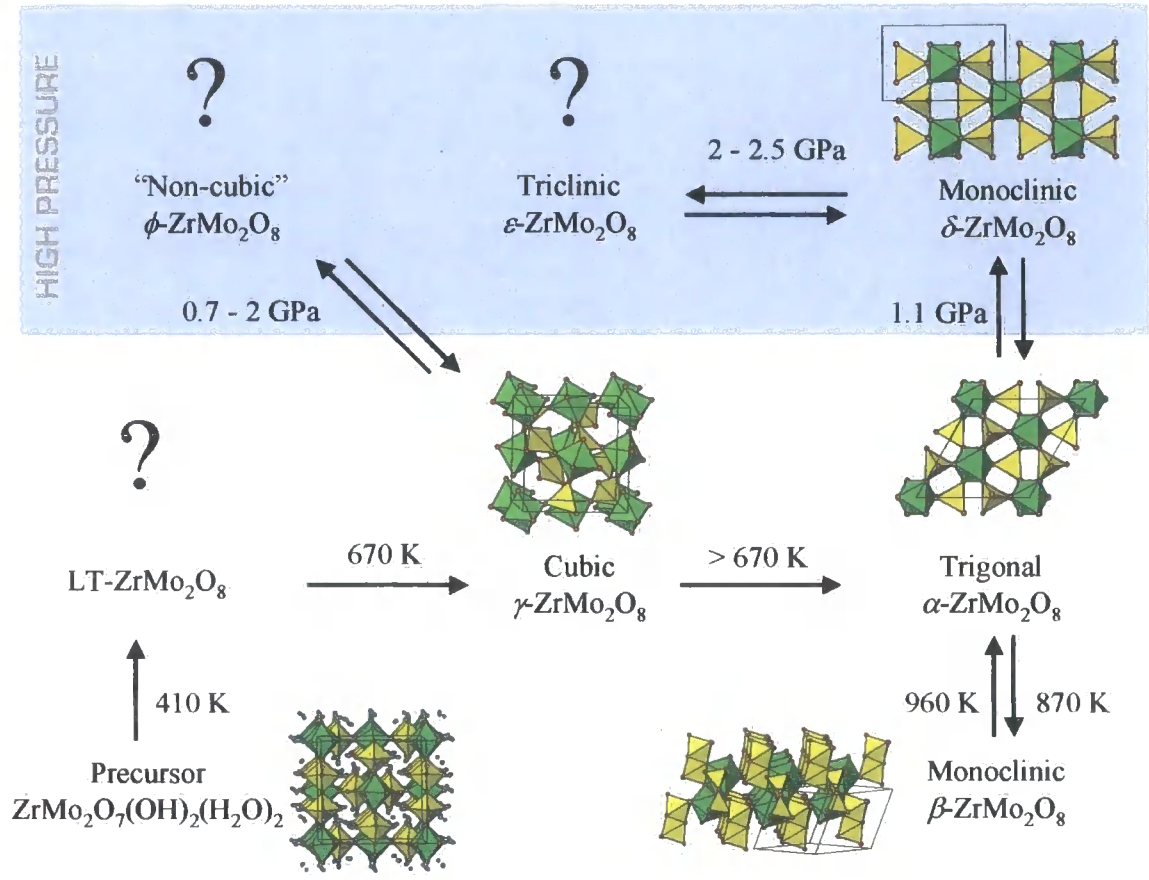

Figure 1.12. Known $ZrMo_2O_8$ and related phases under conditions of varying temperature or pressure.

An outline of the literature of $ZrMo_2O_8$ phases is given in Section 5.1.1, which leads into the studies of trigonal α-$ZrMo_2O_8$. This phase has been known since the late 1960s to crystallise in the $P\bar{3}1c$ space group,[61,63,79] although its atomic structure was not correctly reported until twenty years later (Section 5.1.1).[41,42] It is the thermodynamically stable product when ZrO_2 and MoO_3 are heated in a 1 : 2 molar ratio at high temperature and is a layered structure consisting of the same polyhedra that make up the cubic ZrW_2O_8-structure type; ZrO_6 octahedra vertex linked to MoO_4 tetrahedra, with one vertex unshared (Figures 1.12 and 5.1). Layers are held together by van der Waals interactions. Prior to 1989, this trigonal polymorph was the only known $ZrMo_2O_8$ polymorph. This is in direct contrast to ZrW_2O_8 where only the cubic phase was known until 1999.

The β (second) phase of $ZrMo_2O_8$, reported in 1989 by Russian workers, crystallises in the monoclinic *C*2/*c* space group and consists of infinite chains of edge-sharing ZrO_8 capped pentagonal bipyramids interspaced by pairs of edge-sharing MoO_5 square pyramids (Figure 1.12). French workers also reported identical lattice dimensions and symmetry at the same time, although a complete structural analysis was not given.[80] It is a more condensed phase than the trigonal polymorph ($\rho_{mono} = 4.8$ gcm^{-3}; $\rho_{trig} = 3.9$ gcm^{-3}). The Russian group prepared single crystals of monoclinic $ZrMo_2O_8$ from a solution of potassium polymolybdates, whereas the French group initially combined the binary oxides and annealed them at 873 K for 24 hours, followed by hydrothermal treatment of the resulting powder at 973 K to prepare their single crystals. The monoclinic form could be converted to the trigonal phase by annealing at ~ 960 K.[81] The reverse reaction could only be achieved by heating for several days below this temperature, implying a kinetically controlled reaction to the thermodynamically more stable monoclinic form.[64,81]

The third reported (γ) phase, cubic $ZrMo_2O_8$ was reported in 1998 and is discussed in Section 1.3.2 and Chapter 3.[62] It possesses the β-ZrW_2O_8 structure type, is of lower density than both the trigonal and monoclinic polymorphs and metastable at all temperatures. It undergoes a first-order phase transition at ~ 660 – 770 K to trigonal $ZrMo_2O_8$ (Figure 1.12); the exact temperature being dependent on the nature of the precursor to cubic $ZrMo_2O_8$ and its morphology.[67] Kinetic studies have implied that cubic $ZrMo_2O_8$ will not, however, convert to the less-desired trigonal phase at temperatures below 553 K over a period of several years.[82] This should be borne in mind as an upper stability limit for potential use in a NTE-containing composite material. In contrast cubic ZrW_2O_8 is kinetically stable up to 1050 K presumably as a result of the absence of a trigonal phase under normal conditions.[37,39]

The behaviour of cubic and trigonal $ZrMo_2O_8$ under applied pressure have been reported; the three known high-pressure phases are shown in Figure 1.12, although little structural information on two of these phases is known. For cubic γ-$ZrMo_2O_8$ studies up to 0.6 GPa were initially performed by Lind *et al.* in 1998; a lack of a phase transition was noted in comparison to ZrW_2O_8 (Section 1.4.1).[62] They presumed that $ZrMo_2O_8$ was a better candidate for use in composites owing to a lack of both a pressure- and a

thermal-induced phase transition. Further studies in 2001 also by Lind, however, revealed that under quasi-hydrostatic conditions a first-order transition with an 11% relative volume reduction over the range of 0.7 to 2.0 GPa was observed.[83] Strong peak broadening and overlap barred the structural elucidation of this high pressure phase, although it was thought likely to be non-cubic. Grzechnik and Crichton termed this phase φ-$ZrMo_2O_8$ and referred to its lattice symmetry as "monoclinic" without justification. They presented diffraction studies of quenched cubic $ZrMo_2O_8$ following high pressure and temperature treatment.[84] Following compression to 1.3 GPa, the cubic γ phase was recovered at 298 K, a mixture of trigonal α and monoclinic β obtained after heating to 663 K, and pure monoclinic β at 818 K and above. Reversibility of the phase transition (albeit with hysteresis) and its higher pressure onset relative to ZrW_2O_8 still makes cubic $ZrMo_2O_8$ a potentially important material. However, under conditions of non-hydrostatic pressure both cubic $ZrMo_2O_8$ and $HfMo_2O_8$ begin to amorphise at significantly lower pressures of ~ 0.3 GPa, in contrast to 1.5 GPa for ZrW_2O_8.[76]

Two high-pressure forms of $ZrMo_2O_8$ can be derived from the atmospheric pressure trigonal α phase (Figure 1.12): compression to 1.06 – 1.11 GPa allows reversible conversion to a monoclinic δ phase in which the ZrO_6 and MoO_4 polyhedra are tilted to allow a 5% volume reduction through a decrease in interlayer separation.[85] This phase prevails up to a pressure range of 2.0 – 2.5 GPa, where conversion to a triclinic ε phase of unknown structure occurs.[86] A unit cell volume decrease of 10% is observed during the δ to ε transition and again this transition is reversible. Compression up to 9.5 GPa reveals increased broadening of Bragg reflections and ε-$ZrMo_2O_8$ becomes semi-amorphous. After exposure to these very high pressures trigonal α-$ZrMo_2O_8$ could not be recovered after the release of pressure.

1.4.3 Temperature and Pressure Dependence of $HfMo_2O_8$ Polymorphs

Variable temperature and pressure work on $HfMo_2O_8$ is less well documented in the literature. Trigonal $HfMo_2O_8$ is described in Chapter 5 and it has been known since 1967 that there is an isostructural relationship with $ZrMo_2O_8$.[61,79] However the correct structure was only reported accurately twenty years later.[64] Synthesis of cubic $HfMo_2O_8$

was mentioned in passing by Lind in 1998 although its thermal expansion behaviour was not reported.[62] Chapter 3 includes such studies. No other temperature dependent phases have been published.

Variable pressure work has also been carried out on cubic $HfMo_2O_8$ by Lind *et al.*;[83] similar behaviour to the Zr analogue was observed as a first order transition to an undetermined non-cubic structure was apparent. It seems so far that $ZrMo_2O_8$ and $HfMo_2O_8$ phases show similar structural changes with varying thermal and high-pressure conditions. One distinct difference was reported only very recently;[87] a high pressure-high temperature study of trigonal α-$HfMo_2O_8$ revealed a phase transition to a new phase with the ambient monoclinic β-$ZrMo_2O_8$ structure type. β-$HfMo_2O_8$ could be prepared by applying pressure of 2.15 GPa for 30 minutes, followed by brief heating to 833 K whilst still under pressure. This is analogous behaviour to cubic $ZrMo_2O_8$;[84] high pressure-high temperature studies on trigonal $ZrMo_2O_8$ are not available for comparison. This is the only reported route to the dense monoclinic β-$HfMo_2O_8$ polymorph. High pressure-room temperature treatment of trigonal $HfMo_2O_8$ failed to induce a phase transition even at pressures of 7 GPa. This is markedly different behaviour to isostructural trigonal $ZrMo_2O_8$, which converts to monoclinic δ structure at 1.1 GPa.[85,86]

1.5 Applications of NTE Materials

Why are materials that shrink with temperature of interest? A whole host of potential uses can be envisaged for cubic AM_2O_8 phases and some have already been explored as a result of the highly attractive property of isotropic NTE. Mixed in the correct ratio with a positively expanding material, the expansion of composite materials can be tuned as required. The role as a temperature compensator is a key property for use in electronic, ceramic, optical and structural engineering applications. For example, the matching of components in the semiconductor industry, and null-expansive supports of filters and thin film mirrors in astronomical optics requires a controlled expansion over their operating temperatures. Patents on zero-expansion composites containing AM_2O_8 (A = Zr, Hf; M = Mo, W) and BMX_4 (B = Mg, Ca, Sr, Ba; X = O, S) components have been accepted.[88] The application of ZrW_2O_8 as a temperature compensating support for

Bragg reflection gratings in optical fibres,[89] has also been patented.[90] Biomedical applications can also be found; artificial joints and dental fillings must possess the same expansion properties as bones and teeth, respectively, if they are to last 20 years without causing pain, or falling out. ZrW_2O_8 also has potential for use in gas sensing or catalysis as a result of the observed oxygen mobility, meaning that it is effectively a low temperature ionic conductor.

ZrW_2O_8 has been incorporated into asphalt concrete to explore ways of reducing thermal expansion and cracking under temperature fluctuations of everyday weather conditions. A 60% by weight addition has been shown to reduce the bulk thermal expansion coefficient to zero.[91] The obvious disadvantage, however, is the large quantity of relatively expensive ZrW_2O_8 that would be required for this application.

Preliminary investigations into the processing of ZrW_2O_8 with copper in a low expansion, high conduction composite have been performed. Bulk expansion can be tailored to that of silicon or alumina and giving potential application as heat sinks for electronic components. Exposing ZrW_2O_8-Cu matrix to harsh conditions of 873 K and 0.10 GPa to process the matrix led to reaction of the two materials, while heat treatment under vacuum at 873 K led to oxygen loss in the material.[92] Pressing of the matrix at lower temperatures led to successful conversion of a dense composite containing 50 – 60% ZrW_2O_8 by volume. Dilatometry studies actually revealed overall positive expansion, with considerable hysteresis and time dependent recovery during thermal cycling.[93] These properties were attributed to the partial formation of the high-pressure phase of ZrW_2O_8 during cycling. Considerable residual stress was also present owing to the large difference in thermal expansion of the two components. Other cubic AM_2O_8 phases have not yet been investigated in the same way. The example above illustrates the need for an isotropic NTE material with the absence of a pressure-induced phase transition.

The study of the thermoresponsive behaviour of AM_2O_8 (A = Zr, Hf; M = W, Mo) phases is both technologically important and academically appealing. It is hoped that this thesis gives further insight into the synthesis, structure and properties of this fascinating family of materials.

1.6 References

1. R. Roy, D. K. Agrawal, H. A. McKinstry, *Ann. Rev. Mater. Sci.*, **19**, 1989, 59-81.
2. E. Grüneisen, *Ann. Phys.*, **26**, 1908, 393-402.
3. R. H. Carr, R. D. McCammon, G. K. White, *Philos. Mag.*, **12**, 1965, 157-163.
4. K. Röttger, A. Endriss, J. Ihringer, S. Doyle, W. F. Kuhs, *Acta Cryst.*, **B50**, 1994, 644-648.
5. D. Taylor, *Br. Ceram. Trans. J.*, **83**, 1984, 129-134.
6. G. K. White, *Contemp. Phys.*, **34**, 1993, 193-204.
7. M. Blackman, *Proc. Phys. Soc.*, **B70**, 1957, 827.
8. T. H. K. Barron, *Ann. Phys.*, **1**, 1957, 77.
9. K. G. Lyon, G. L. Salinger, C. A. Swenson, G. K. White, *J. Appl. Phys.*, **48**, 1977, 865-869.
10. R. R. Reeber, *Phys. Status Solidi*, **A32**, 1975, 321-331.
11. K. Wang, R. R. Reeber, *Appl. Phys. Lett.*, **76**, 2000, 2203-2204.
12. M. T. Dove, V. Heine, K. D. Hammonds, *Miner. Mag.*, **59**, 1995, 629-639.
13. K. D. Hammonds, M. T. Dove, A. P. Giddy, V. Heine, *Am. Mineral.*, **79**, 1994, 1207-1209.
14. K. D. Hammonds, M. T. Dove, A. P. Giddy, V. Heine, B. Winkler, *Am. Mineral.*, **81**, 1996, 1057-1079.
15. M. Jakob, S. Erk, *Wiss. Abh. Phys. Techn. Reichsanst.*, **12**, 1929, 302-316.
16. D. F. Gibbons, *Phys. Rev.*, **112**, 1952, 136-140.
17. D. A. Woodcock, P. Lightfoot, L. A. Villaescusa, M. -J. Diaz-Cabanas, M. A. Camblor, D. Engberg, *Chem. Mater.*, **11**, 1999, 2508-2514.
18. M. P. Attfield, A. W. Sleight, *Chem. Commun.*, 1998, 601-602.
19. J. W. Couves, R. H. Jones, S. C. Parker, P. Tschaufeser, C. R. A. Catlow, *J. Phys.: Condens. Mater.*, **5**, 1993, L329-L332.
20. M. P. Attfield, A. W. Sleight, *Chem. Mater.*, **10**, 1998, 2013-2019.
21. V. Korthuis, N. Khosrovani, A. W. Sleight, N. Roberts, R. Dupree, W. W. Warren, *Chem. Mater.*, **7**, 1995, 412-417.
22. N. Khosrovani, A. W. Sleight, T. Vogt, *J. Solid State Chem.*, **132**, 1997, 355-360.
23. G. R. Levi, G. Peyronel, *Z. Kristallogr.*, **92**, 1935, 190-209.

24. G. Peyronel, *Gazz. Chim. Ital.*, **72**, 1942, 83-88.
25. H. Vollenke, A. Wittmann, H. Novotny, *Monatsh. Chemie*, **94**, 1963, 956-963.
26. J. S. O. Evans, J. C. Hanson, A. W. Sleight, *Acta. Cryst.*, **B54**, 1998, 705-713.
27. J. S. O. Evans, *J. Chem. Soc., Dalton Trans.*, 1999, 3317-3326.
28. I. J. King, Ph.D. Thesis, University of Durham, 2003.
29. J. S. O. Evans, T. A. Mary, A. W. Sleight, *J. Solid State Chem.*, **137**, 1998, 148-160.
30. A. K. Tyagi, S. N. Achary, M. D. Matthews, *J. Alloys Comp.*, **339**, 2002, 207-210.
31. P. M. Forster, A. Yokochi, A. W. Sleight, *J. Solid State Chem.*, **140**, 1998, 157-158.
32. J. Graham, A. D. Wadsley, J. H. Weymouth, L. S. Williams, *J. Am. Ceram. Soc.*, **42**, 1959, 570.
33. L. L. Y. Chang, M. G. Scroger, B. Phillips, *J. Am. Ceram. Soc.*, **50**, 1967, 211-215.
34. A. Clearfield, R. H. Blessing, *J. Inorg. Nucl. Chem.*, **34**, 1972, 2643-2663.
35. A. Clearfield, R. H. Blessing, *J. Inorg. Nucl. Chem.*, **36**, 1974, 1174-1176.
36. C. Martinek, F. A. Hummel, *J. Am. Ceram. Soc.*, **51**, 1968, 227-228.
37. T. A. Mary, J. S. O. Evans, T. Vogt, A. W. Sleight, *Science*, **272**, 1996, 90-92.
38. M. Auray, M. Quarton, M. Leblanc, *Acta Cryst.*, **C51**, 1995, 2210-2213.
39. J. S. O. Evans, T. A. Mary, T. Vogt, M. A. Subramanian, A. W. Sleight, *Chem. Mater.*, **8**, 1996, 2809-2823.
40. A. P. Wilkinson, C. Lind, S. Pattanaik, *Chem. Mater.*, **11**, 1999, 101-108.
41. M. Auray, M. Quarton, P. Tarte, *Acta Cryst.*, **C42**, 1986, 257-259.
42. V. N. Serezhkin, V. A. Efremov, V. K. Trunov, *Russ. J. Inorg. Chem*, **32**, 1987, 1568-1570.
43. R. Enjalbert, J. Galy, *Acta Cryst.*, **C42**, 1986, 1467-1469.
44. T. J. Bastow, G. A. Botton, J. Etheridge, M. E. Smith, H. J. Whitfield, *Acta Cryst.*, **A55**, 1999, 127-132.
45. R. Masse, J. -C. Grenier, A. Durif, *Bull. Soc. Fr. Minéral. Crystallogr.*, **90**, 1967, 20-23.
46. I. D. Brown, D. Altermatt, *Acta. Cryst.*, **B41**, 1985, 244-247.
47. N. E. Brese, M. O'Keeffe, *Acta. Cryst.*, **B47**, 1991, 192-197.
48. J. S. O. Evans, W. I. F. David, A. W. Sleight, *Acta Cryst.*, **B55**, 1999, 333-340.

49. N. Duan, U. Kameswari, A. W. Sleight, *J. Am. Chem. Soc*, **121**, 1999, 10432-10433.
50. Multilab Ltd., *Expansion coefficient for Alsint® (99.7% alumina)*, Newcastle upon Tyne, 1999.
51. Y. Okada, Y. Tokumaru, *J. Appl. Phys.*, **56**, 1984, 314-320.
52. H. M. Rietveld, *J. Appl. Cryst.*, **2**, 1969, 65-71.
53. A. K. A. Pryde, K. D. Hammonds, M. T. Dove, V. Heine, J. D. Gale, M. C. Warren, *J. Phys. Condens. Matter*, **8**, 1996, 10973-10982.
54. A. K. A. Pryde, K. D. Hammonds, M. T. Dove, V. Heine, J. D. Gale, M. C. Warren, *Phase Transit.*, **61**, 1997, 141-153.
55. A. P. Ramirez, G. R. Kowach, *Phys. Rev. Lett.*, **80**, 1998, 4903-4906.
56. G. Ernst, C. Broholm, G. R. Kowach, A. P. Ramirez, *Nature*, **396**, 1998, 147-149.
57. W. I. F. David, J. S. O. Evans, A. W. Sleight, *Europhys. Lett.*, **46**, 1999, 661-669.
58. D. Cao, F. Bridges, G. R. Kowach, A. P. Ramirez, *Phys. Rev. Lett.*, **89**, 2002, 215902.
59. J. S. O. Evans, M. G. Tucker, M. T. Dove, unpublished work, 2000.
60. J. S. O. Evans, *http://www.dur.ac.uk/john.evans/webpages/invert.htm*, 1999.
61. V. K. Trunov, L. M. Kovba, *Russ. J. Inorg. Chem*, **12**, 1967, 1703-1704.
62. C. Lind, A. P. Wilkinson, Z. B. Hu, S. Short, J. D. Jorgensen, *Chem. Mater.*, **10**, 1998, 2335-2337.
63. J. Thoret, *Rev. Chim. Miner.*, **11**, 1974, 237-261.
64. M. Auray, M. Quarton, P. Tarte, *Powder Diffr.*, **2**, 1987, 36-38.
65. P. A. Hanson, M.Sci. Thesis, University of Durham, 1999.
66. J. S. O. Evans, P. A. Hanson, R. M. Ibberson, U. Kameswari, N. Duan, A. W. Sleight, *J. Am. Chem. Soc.*, **122**, 2000, 8694-8699.
67. C. Lind, A. P. Wilkinson, C. J. Rawn, E. A. Payzant, *J. Mater. Chem.*, **11**, 2001, 3354-3359.
68. C. Closmann, A. W. Sleight, J. C. Haygarth, *J. Solid State Chem.*, **139**, 1998, 424-426.
69. B. C. H. Steele, *Solid State Ionics*, **75**, 1995, 157-165.
70. L. D. Landau, E. M. Lifshitz, *Statistical Physics*, Pergamon Press, 1958.

71. S. Y. Zhang, X. H. Zhao, H. Ma, X. Y. Wu, *Chinese J. Chem.*, **18**, 2000, 571-575.

72. U. Kameswari, A. W. Sleight, J. S. O. Evans, *Int. J. Inorg. Mat.*, **2**, 2000, 333-337.

73. A. Butz, G. Miehe, H. Paulus, P. Strauss, H. Fuess, *J. Solid State Chem.*, **138**, 1998, 232-237.

74. J. S. O. Evans, J. Jorgensen, R. M. Ibberson, W. I. F. David, A. W. Sleight, *Phys. Rev. B*, **60**, 1999, 14643-14648.

75. J. D. Jorgensen, Z. Hu, S. Teslic, D. N. Argyriou, S. Short, J. S. O. Evans, A. W. Sleight, *Phys. Rev. B*, **59**, 1999, 215-225.

76. C. A. Perottoni, J. A. H. Da Jornada, *Science*, **280**, 1998, 886-889.

77. A. Grzechnik, W. A. Crichton, K. Syassen, P. Adler, M. Mezouar, *Chem. Mater.*, **13**, 2001, 4255-4259.

78. J. S. O. Evans, Z. Hu, J. D. Jorgensen, D. N. Argyriou, S. Short, A. W. Sleight, *Science*, **275**, 1997, 61-65.

79. W. Freundlich, J. Thoret, *Compt. Rend. Acad. Sci. Paris*, **C265**, 1967, 96-98.

80. M. Auray, M. Quarton, P. Tarte, *Powder Diffr.*, **4**, 1989, 29-30.

81. R. F. Klevtsova, L. A. Glinskaya, E. S. Zolotova, P. V. Klevtsov, *Sov. Phys. Dokl.*, **34**, 1989, 185-187.

82. C. Lind, A. P. Wilkinson, C. J. Rawn, E. A. Payzant, *J. Mater. Chem.*, **12**, 2002, 990-994.

83. C. Lind, D. G. VanDerveer, A. P. Wilkinson, J. Chen, M. T. Vaughan, D. J. Weidner, *Chem. Mater.*, **13**, 2001, 487-490.

84. A. Grzechnik, W. A. Crichton, *Solid State Sci.*, **4**, 2002, 1137-1141.

85. A. M. Krogh Andersen, S. Carlson, *Acta Cryst.*, **B57**, 2001, 20-26.

86. S. Carlson, A. M. Krogh Andersen, *Phys. Rev. B*, **61**, 2000, 11209-11212.

87. S. N. Achary, G. D. Mukherjee, A. K. Tyagi, B. K. Godwal, *Phys. Rev. B*, **66**, 2002, 184106.

88. T. Suzuki, O. Atsushi, J. Kuwata, *Zero Thermal Expansion Material by Mixture of Negative and Positive Thermal Expansion Tungstates or Molybdates for High Precision Component Parts*, European Patent No. 1277712, Matsushita Electric Industrial Co. Ltd., Japan, 2003.

89. L. M. Sheppard, *http://www.photonics.com/spectra/tech/read.asp?techid=593*, 1999, Photonics Technology.

90. D. A. Fleming, D. W. Johnson, G. R. Kowach, P. J. Lemaire, *Manufacture of Isotropic Negative Thermal Expansion Ceramics for Thermal Compensators*, U.S. Patent No. 6258743, Agere Systems Guradian Corp., USA, 2001.

91. M. Kofteros, S. Rodriguez, V. Tandon, L. E. Murr, *Scripta Mater.*, **45**, 2001, 369-374.

92. C. Verdon, D. C. Dunand, *Scripta Mater.*, **36**, 1997, 1075-1080.

93. H. Holzer, D. C. Dunand, *J. Mater. Res.*, **14**, 1999, 780-789.

Chapter Two: Low Temperature Synthesis, Characterisation and Thermal Properties of a New Family of AM_2O_8 Polymorphs

2.1 Introduction

Cubic $ZrW_{2-x}Mo_xO_8$ phases are a family of solid-state materials displaying isotropic negative thermal expansion (NTE) over a broad temperature range. It is important to possess detailed knowledge of the syntheses of these materials so they can be made more efficiently in industry for possible use in controlled expansion composites and optical materials. The most studied member of the family is cubic ZrW_2O_8 which displays isotropic NTE between 0.3 – 1050 K (see Chapters 1 and 3).[1,2] It is typically prepared *via* a traditional high temperature route by mixing stoichiometric quantities of ZrO_2 and WO_3 with *e.g.* an anneal at 1448 K and a subsequent rapid quench in air (Section 7.5.2).[3] It is only thermodynamically stable at this high temperature while at lower temperatures it is unstable with respect to the denser ZrO_2 and WO_3 starting materials.[4] Cubic ZrW_2O_8 is, however, kinetically stable meaning a quenched sample can be obtained at room temperature although this is difficult to accomplish on large samples. The high temperatures involved and the quenching problem mean that economical bulk industrial production would be difficult. A second potential problem with practical applications of ZrW_2O_8 is it undergoes two types of phase transitions: an order-disorder phase transition at around 448 K,[5] and also a pressure-induced transition at about 0.2 GPa which might limit its use in composite materials under more extreme circumstances.[6] Such drawbacks have to be taken into account even though the remarkable property of isotropic NTE over a ~ 1050 K temperature range is a very attractive property of cubic ZrW_2O_8.

Cubic $ZrMo_2O_8$ poses different problems in its synthesis. Direct combination of the binary oxides leads to the formation of the thermodynamically stable trigonal polymorph of $ZrMo_2O_8$ instead of the cubic. A structural investigation of trigonal $ZrMo_2O_8$ is presented in Chapter 5. It is a more condensed phase than the cubic (density

of trigonal is 3.93 gcm^{-3} versus 3.59 gcm^{-3} for cubic). Conversely, no reported preparation of trigonal ZrW_2O_8 from WO_3 and ZrO_2 exists *via* traditional high temperature routes.

Cubic $ZrMo_2O_8$ was first prepared as a pure phase in 1998 by Lind *et al. via* the decomposition of a hydrated precursor,[7] $ZrMo_2O_7(OH)_2(H_2O)_2$, which itself was first characterised in 1972 by Clearfield and Blessing.[8] Initial variable temperature and pressure work carried out by Lind showed that neither an order-disorder transition nor a pressure induced transition (up to 0.6 GPa) occurred in cubic $ZrMo_2O_8$ (unlike in ZrW_2O_8). The material displays isotropic NTE but data are not as detailed as for ZrW_2O_8.[5] It is envisaged that cubic $ZrMo_2O_8$ could be a more reliable component in composite materials if more extreme conditions of temperature and pressure are employed. Lind's synthetic route proved, however, problematic when Evans *et al.* repeated it in 2000 as the best samples obtainable contained ~ 22% trigonal impurity.[9]

Previous reports have been unsuccessful in elucidating the actual decomposition path and subsequent formation of the cubic phase from the hydrated precursor. A previously recognised, but unidentifiable low temperature (LT) polymorph was reported although its structure and role in the decomposition path were not understood.[10] Lind *et al.* reported the results of a series of dehydrations of $ZrMo_2O_7(OH)_2(H_2O)_2$ precursors synthesised using a variety of Zr sources. A range of synthetic preparations were attempted and cubic $ZrMo_2O_8$ was only observed when dehydration of the precursor proceeded *via* the unidentified, dehydrated LT phase. This suggests the LT phase plays an important role in the process.

This chapter aims to clarify the missing link between the precursor phase $ZrMo_2O_7(OH)_2(H_2O)_2$ and the cubic $ZrMo_2O_8$ phase by investigating the structure and mechanistic role of the so-called LT intermediate.

Further details on individual ZrM_2O_8 phases that have been documented in the literature are described in Chapter 1. A reaction scheme of the above $ZrMo_2O_8$ phases and their relationship to one another are displayed in Figure 1.12.

2.2 Thermal Decomposition Study of $ZrMo_2O_7(OH)_2(H_2O)_2$

2.2.1 Formation of LT-$ZrMo_2O_8$

$ZrMo_2O_7(OH)_2(H_2O)_2$ (sample i.d. NRW001, ~ 6.7 g) was prepared using $ZrOCl_2$ as the Zr source by Nick Warmingham,[11] following the method of Lind *et al.*,[10] and is detailed in Section 7.1. A 65% excess of Zr over the 1 : 2 Zr : Mo ratio was used for the starting materials.

In situ variable temperature X-ray diffraction (VTXRD) decomposition data on the $ZrMo_2O_7(OH)_2(H_2O)_2$ precursor were collected using a Bruker d8 diffractometer equipped with an Anton Parr HTK1200 high temperature furnace (Section 6.1). VT data consisting of 35 measurements were collected in the programmed temperature range 303 – 983 K (every 20 K, 21 minutes each, with a 0.043 Ks^{-1} ramp rate, a 2θ range of 10 – 70 ° and a standard step size of 0.0144 ° 2θ). The powdered sample was sieved onto an amorphous SiO_2 disc and adhered using vacuum grease. A 1 degree divergence slit was used (all HTK1200 refinements throughout this chapter used the same fixed slit). The 35 diffraction patterns that comprise the measurement d8_01386 are shown in Figure 2.1.

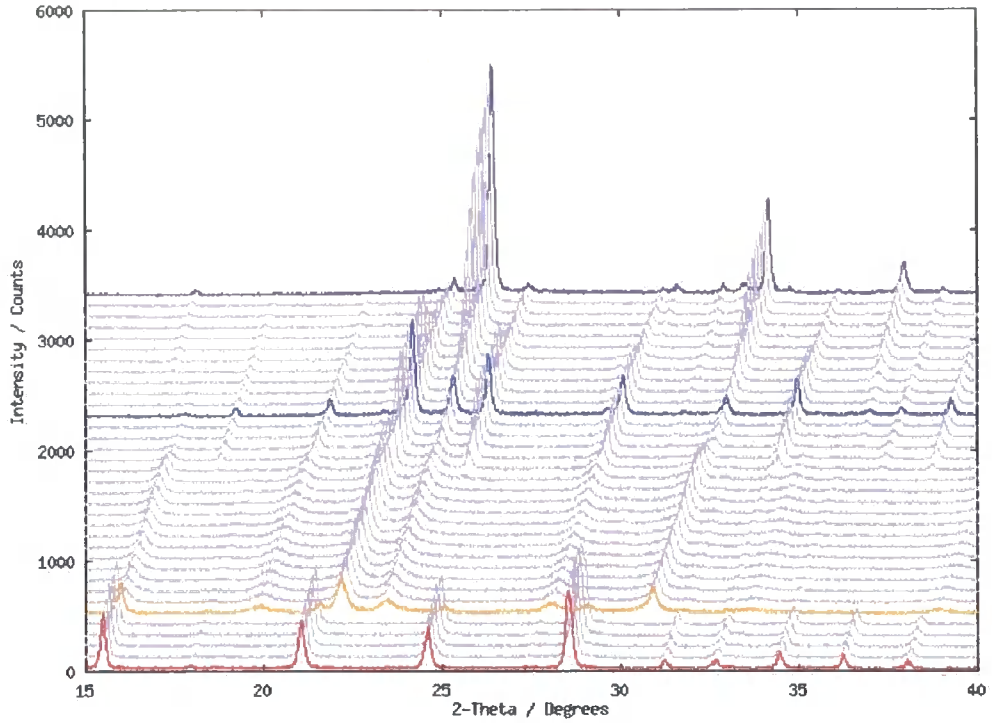

Figure 2.1. Variable temperature X-ray diffraction data for the decomposition of $ZrOCl_2$-derived $ZrMo_2O_7(OH)_2(H_2O)_2$ (NRW001, d8_01386) to various $ZrMo_2O_8$ polymorphs - Low Temperature 'LT', cubic and trigonal. Powder patterns are shown from 303 K (base of the figure) to 983 K (top of the figure) in 20 K steps, and are offset by 0.1 ° 2θ for clarity.

The precursor rapidly dehydrates to a new phase with a mixture of broad and sharper peaks between 388 and 435 K. This is the unknown low temperature (LT) polymorph of $ZrMo_2O_8$ and it remains the sole phase between 435 and 653 K at which point the cubic polymorph is observed albeit with a trigonal impurity (note the major peak at ~ 23.0 ° 2θ in the cubic powder patterns in Figure 2.1). At around 800 K the fraction of cubic begins to diminish and eventually only trigonal $ZrMo_2O_8$ exists at 983 K. Above this temperature, decomposition to ZrO_2 and amorphous MoO_3 occurs. The *in situ* diffraction study in Figure 2.1 illustrates that pure cubic $ZrMo_2O_8$ cannot be synthesised from this particular $ZrOCl_2$-derived precursor and there is always an inherent trigonal impurity. Quantitative details are given in Section 2.2.5. It is intriguing that this series of decompositions is very hard to monitor simply by observing the intensity of individual peaks in the diffraction data, as almost every 2θ peak of one phase is "accidentally" also present in another phase. The peak at ~ 15.5 ° 2θ, for example, is the (*020*) peak of the precursor material, but very close in 2θ to a peak of LT-$ZrMo_2O_8$; the peak at ~ 23.0 ° is the (*112*) of trigonal $ZrMo_2O_8$ but an LT peak also exists at this 2θ

value. Similar observations hold for many other peaks in the data. In fact it was initially difficult to tell if the LT form was actually a true single phase because of the coincidence of all of its Bragg reflections with those of the precursor, cubic and trigonal $ZrMo_2O_8$ phases.

2.2.2 Structure Solution of LT-$ZrMo_2O_8$

To solve the structure of polycrystalline LT-$ZrMo_2O_8$, the unknown intermediate between the precursor and cubic $ZrMo_2O_8$, a good quality powder X-ray pattern was recorded at 473 K on the d8 diffractometer. *Multiindex*, a local modification of the ITO code by Visser,[12] was used to obtain a unit cell from X-ray data of LT-$ZrMo_2O_8$. 15 peaks were indexed using an orthorhombic cell, with cell parameters $a = 5.865$, $b = 7.264$, $c = 9.103$ Å (figure of merit of 21). The resulting cell volume was ~ 388 Å^3, almost exactly half of that of cubic $ZrMo_2O_8$ (761 Å^3). Assuming the structure had similar building blocks to the cubic polymorph with a similar density of 3.59 gcm^{-3}, this implied the number of formula units per cell, $Z = 2$. The resulting unit cell contents would be $Zr_2Mo_4O_{16}$. A "simulated annealing" structure solution using initial unit cell contents of six heavy (Zr) atoms was thus performed using *TOPAS* (Section 6.1.11).[13] The simulated annealing technique involves repeated cycles of a random choice of atomic positions,[14-16] followed by a full Rietveld refinement,[17] distinguishable from Monte Carlo methods which give random-path structure solutions only. Since the diffraction data were too poor to obtain any reliable indication as to the space group symmetry from systematic absences, initial attempts at solution were performed in the simplest space group $P1$. The X-ray scattering power of Zr and Mo are similar and so it was valid to model the structure purely with Zr atoms in this first stage. After repeating 100000 cycles of annealing/refining, a set of atomic coordinates which resembled the rutile structure were obtained, with a weighted profile R-factor of 19.6%. Four rigid-body MoO_4 tetrahedra were then employed in a subsequent anneal/refinement to try and improve the model, as it was suspected that LT-$ZrMo_2O_8$ would contain similar groups to its cubic and trigonal analogues. The MoO_4 groups were permitted to rotate freely in the unit cell in several thousand different orientations. The chosen solution with the lowest weighted profile R-factor (16.1%) contained approximately octahedrally coordinated Zr. The space group of this model was identified as $Pmn2_1$ using *Cerius2*.[18]

Although this model gave a reasonable fit to the X-ray data, there were still major problems in describing the broadness of some peaks as in Figure 2.2 (*e.g.* the major peaks such as (*111*) and (*121*) at 21.8 and 30.6 ° 2θ, respectively).

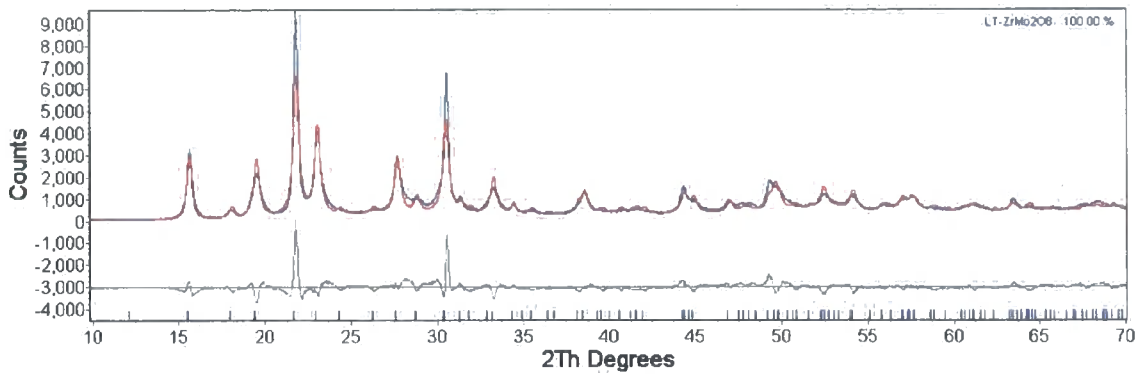

Figure 2.2. Initial rigid-body X-ray Rietveld refinement of LT-$ZrMo_2O_8$ in the *Pmn*2_1 space group. The calculated pattern is shown by the red trace, observed pattern shown by the blue trace. The difference curve is shown in grey. The widths of many of the Bragg peaks are modelled incorrectly.

As described above, only a relatively poor Rietveld fit was obtained in the initial X-ray refinement of the LT form using a standard pseudo-Voigt (PV) peak function. Several broad peaks could not be modelled adequately with a single Gaussian/Lorentzian function as used under normal circumstances. Since the LT phase is formed at low temperatures (precursor to LT transformation occurs at 388 K), it was presumed that anisotropic strain could be the origin of this *hkl*-dependent broadening. LT-$ZrMo_2O_8$ cannot be annealed at high temperature due to the conversion to cubic at ~ 650 K. The strain seemingly arises from significant distortions that occur following the destructive dehydration of the precursor phase. To account for the inherent strain and resulting anisotropic peak broadening, a spherical harmonic (SH) function was invoked.[19] A SH function is a 3D function that obeys the point group symmetry of the crystal and has an *hkl* dependence whereas a PV function does not. A sixth-order spherical harmonic function was used to describe the *hkl*-dependent FWHM in the strained LT form by appending an extra term to the standard PV peak shape (Equation 2.1), which consists of a scale factor and 10 spherical harmonic coefficients (Equation 2.2),

$$\text{pv\_fwhm} = pv_1 + pv_2 \tan\theta + pv_3 / \cos\theta + \boldsymbol{p\ sh\ \tan\theta} \qquad (2.1)$$

where, $pv_{1\text{-}3}$ terms describe the pseudo-Voigt peak width as a function of θ, $\boldsymbol{p}$ is the scale factor of the spherical harmonic and,

$$\boldsymbol{sh} \equiv Y_{ijp}(\theta,\varphi) = \sum_{ij} C_{ij} P_i^j(\theta,\varphi) \qquad (2.2)$$

where, C_{ij} are spherical harmonic coefficients that can be refined, P_i^j are standard Legendre polynomials. Y_{ijp} are the spherical harmonics displayed in Table 2.1.

For an orthorhombic cell, Laue class *mmm*, the selection rules for the indices of symmetrised spherical harmonic functions, $Y_{ijp}(\theta, \varphi)$ are $i = 0, 2, 4...$; $j = 0, 2, 4...$ with even parity, p only.[19] Hence the spherical harmonics corresponding to the Laue class *mmm* of LT-$ZrMo_2O_8$ are given in Table 2.1.

ijp	$Y_{ijp}(\theta, \varphi)$
00	1
20	$0.5(3\cos^2\theta-1)$
22+	$\sin^2\theta\cos2\varphi$
40	$0.125(35\cos^4\theta-30\cos^2\theta+3)$
42+	$0.77778(7\cos^2\theta-1)\sin^2\theta\cos2\varphi$
44+	$\sin^4\theta\cos4\varphi$
60	$0.0625(231\cos^6\theta-315\cos^4\theta+105\cos^2\theta-5)$
62+	$0.64549(33\cos^4\theta-18\cos^2\theta+1)\sin^2\theta\cos2\varphi$
64+	$0.81675(11\cos^2\theta-1)\sin^4\theta\cos4\varphi$
66+	$\sin^6\theta\cos6\varphi$

Table 2.1 Spherical harmonic indices *ijp* and their corresponding symmetrised functions, $Y_{ijp}(\theta, \varphi)$ of even order for an orthorhombic space group. Y_{00} is a normalising coefficient and thus not refined.

Higher order terms could be included but only cause subtle effects and a sixth-order spherical harmonic was considered sufficient for these data. The same functions are

used in quantum mechanics to describe what are commonly known *s*, *p*, *d*, *f*, *etc.* orbitals.

The description of a complex strain-broadened phase such as this from laboratory X-ray data is, of course, questionable. Better quality X-ray and neutron diffraction data were therefore obtained to confirm the structural model. A bulk sample of LT-$ZrMo_2O_8$ was obtained by heating $ZrMo_2O_7(OH)_2(H_2O)_2$ (NRW001) at 573 K for 8 hours (Section 7.1.1); 3.00 g of powdered sample, peach in colour were loaded into a 11 mm vanadium can and room temperature neutron diffraction data were collected on the High-Resolution Powder Diffractometer (HRPD) at the ISIS neutron spallation source of the Rutherford Appleton Laboratory, UK. Data were obtained from three detector banks: 168 ° (back-scattering), 90 ° and 30 ° (low-angle), over a time-of-flight range of 40000 – 116000, 37000 – 125000, and 40000 – 118000 μs respectively, for a count time of ~ 3 hours (total beam current ~ 116 μA).

A superior quality X-ray dataset was collected at room temperature under dynamic vacuum using a Bruker d8 diffractometer with an Anton Parr HTK1200 furnace as described in Section 7.1.1. A 13 hour powder pattern was obtained between 10 – 90 ° 2θ (d8_01665).

A combined X-ray and 3-bank HRPD Rietveld refinement was then performed. Data quality was sufficient that rigid MoO_4 groups were not required. 102 parameters were refined in total; a global set of 19 atomic coordinates, 5 temperature factors and 9 spherical harmonic coefficients were refined with slightly different lattice parameters to fit X-ray and neutron data. For the X-ray data the following were refined: twelve Chebyshev polynomial coefficients to model the background function, a histogram scale factor, sample displacement correction, three cell parameters, six pseudo-Voigt peak profile parameters and a SH scale factor. For each bank of the neutron data, nine background terms, a histogram scale factor, an absorption correction (modelled as $exp(-2fixb(sin\theta/\lambda)^2)$, two peak shape parameters (FWHM and Lorentzian terms) and a SH scale factor were refined. Three cell parameters were refined for the whole neutron dataset. The key refinement details are given in Tables 2.2 and 2.3; the four Rietveld plots are given in Figure 2.4. The overall weighted profile *R*-factor, $_wR_p = 5.10\%$, and the overall $\chi^2 = 0.600$ (small due to a large contribution by the background in the

neutron diffraction patterns). Full refinement details are located in the *TOPAS* input file in the Electronic Appendix (e-Appendix).

	X-ray, d8_01665	Neutron, 168 °	Neutron, 90 °	Neutron, 30 °
Cell parameter a / Å	5.87926 (5)		5.87953 (1)	
Cell parameter b / Å	7.32918 (20)		7.31599 (4)	
Cell parameter c / Å	9.12978 (16)		9.13920 (4)	
Cell volume V / Å^3	393.404 (13)		393.118 (3)	
R_{Bragg} ($\equiv R_{F^2}$)	0.0350	0.0164	0.0188	0.0185
${}_wR_p$	0.108	0.0512	0.0672	0.0464

Table 2.2 Refined cell parameters and residual factors for the combined X-ray and neutron refinement of LT-$ZrMo_2O_8$.

	x	y	z	B_{iso} / Å^2
Zr	½	0.25883 (5)	½	1.56 (2)
Mo(1)	½	0.94896 (5)	0.17991 (5)	2.73 (2)
O(11)	½	0.77290 (8)	0.29729 (5)	5.40 (2)
O(12)	½	0.15225 (6)	0.27996 (7)	3.29 (2)
O(13)	0.75603 (5)	0.91406 (5)	0.07397 (5)	3.29 (2)
Mo(2)	½	0.42378 (5)	0.89130 (5)	2.73 (2)
O(21)	½	0.21216 (9)	–0.01251 (7)	4.48 (2)
O(22)	½	0.37234 (7)	0.70605 (6)	3.29 (2)
O(23)	0.74276 (5)	0.55982 (4)	0.94697 (5)	3.29 (2)

Table 2.3. Combined X-ray and neutron refined atomic coordinates of LT-$ZrMo_2O_8$.

Table 2.3 shows the five refined independent temperature factors used to give a stable refinement; those of the two Mo atoms and of the four bridging oxygen atoms O(12), O(13), O(22) and O(23) were equated. Allowing these temperature factors to differ led to no significant improvement in the refinements. The terminal oxygen atoms, O(11)

and O(21) were allowed to refine freely. It is interesting to note that the terminal oxygen atoms, like those in cubic ZrW_2O_8 show a higher temperature factor than the Zr–O–Mo bridging oxygens.

The refined spherical harmonic coefficients are given in Table 2.4; they represent the extent to which each of the 10 SH functions contribute to the overall model of the strain in the crystal. The overall function (and hence the strain) can be visualised using *Maple*.[20] It is plotted in Figure 2.3 where the relative magnitude of the strain along three Cartesian axes is apparent. The relevance of the topology of the spherical harmonic is explained in Section 2.2.7.

ijp	$Y_{ijp}(\theta, \varphi)$
00	1
20	–0.2873 (52)
22+	–3.9826 (55)
40	2.8403 (59)
42+	3.8853 (49)
44+	0.6548 (48)
60	–0.3121 (8)
62+	–0.1527 (44)
64+	1.0403 (32)
66+	0.4278 (35)

Table 2.4. Refined spherical harmonic coefficients for LT-$ZrMo_2O_8$.

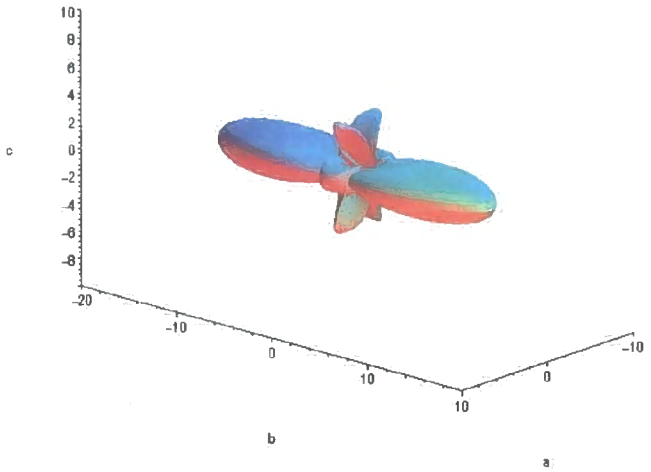

Figure 2.3. Visualisation of the sixth-order spherical harmonic used to describe the strain in LT-$ZrMo_2O_8$.

The Rietveld plots (Figure 2.4) show a very good agreement between the $Pmn2_1$ model of LT-$ZrMo_2O_8$ especially since most of the reflections are so broad. At the outset of this work on LT phases, it was envisaged that solving and refining the structure would be an almost unrealistic task. Minor discrepancies between observed and calculated patterns remain. However given the extreme broadening of some reflections and the relative simplicity of the SH function used to model this, it is believed that this is the best structural model currently obtainable. The inclusion of the spherical harmonic in the refinement improved the ${}_wR_p$ by around 5% in the X-ray fit alone.

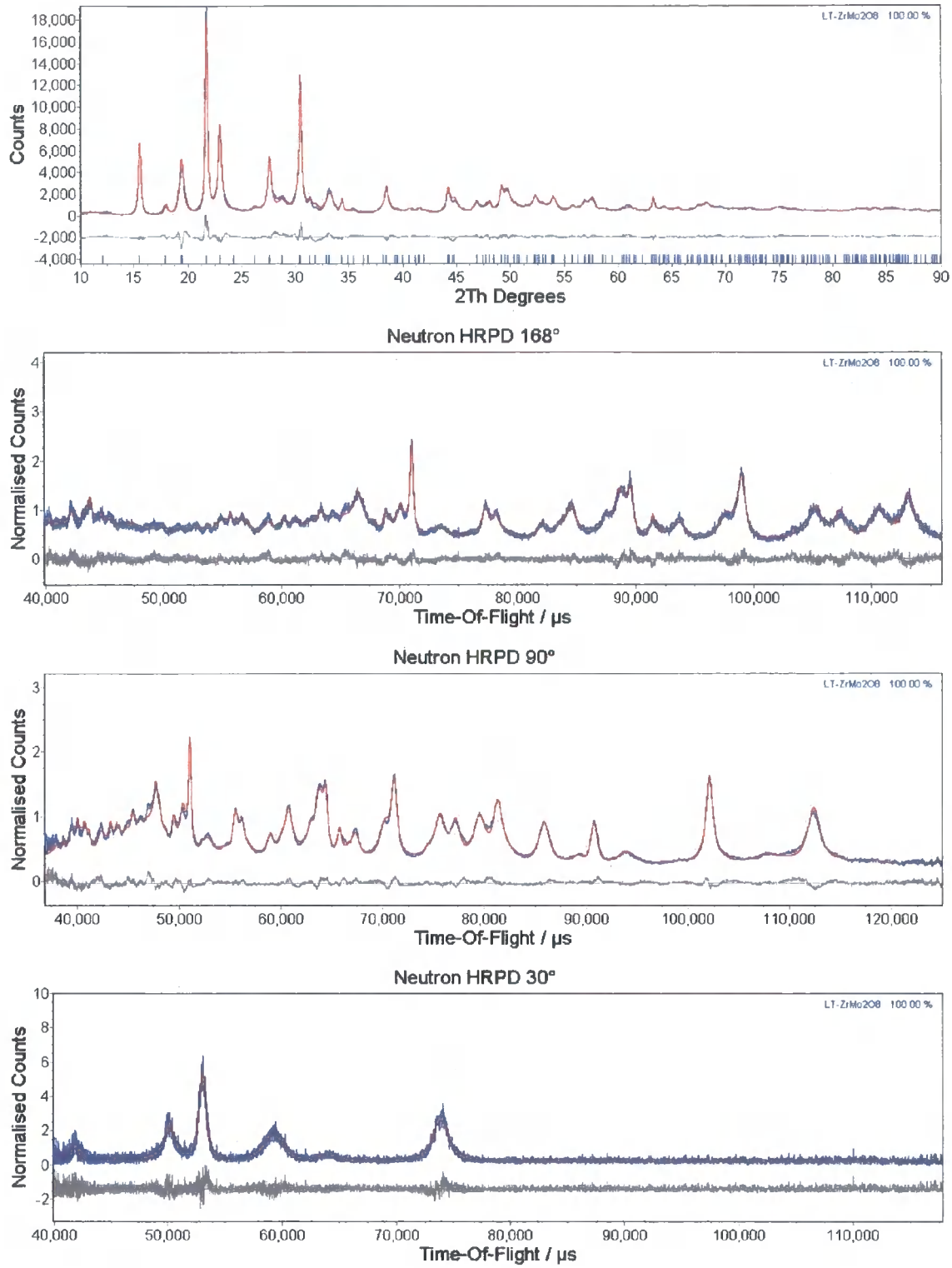

Figure 2.4. X-ray (*top*, d8_01665, d = 8.84 – 1.09 Å), and 168 ° (*below*, d = 0.83 – 2.40 Å), 90 ° (d = 1.06 – 3.59 Å) and 30 ° (d = 3.09 – 9.13 Å) bank neutron Rietveld refinement plots for LT-$ZrMo_2O_8$.

2.2.3 Electron Diffraction of LT-$ZrMo_2O_8$

Electron diffraction was kindly performed by Dr. Wuzong Zhou and Prof. Russell Morris at the University of St. Andrews. The technique was used as a confirmatory check of the unit cell dimensions obtained for LT-$ZrMo_2O_8$ *via* X-ray and neutron diffraction studies in Section 2.2.2. The electron diffraction patterns in various crystallographic directions are shown in Figure 2.5.

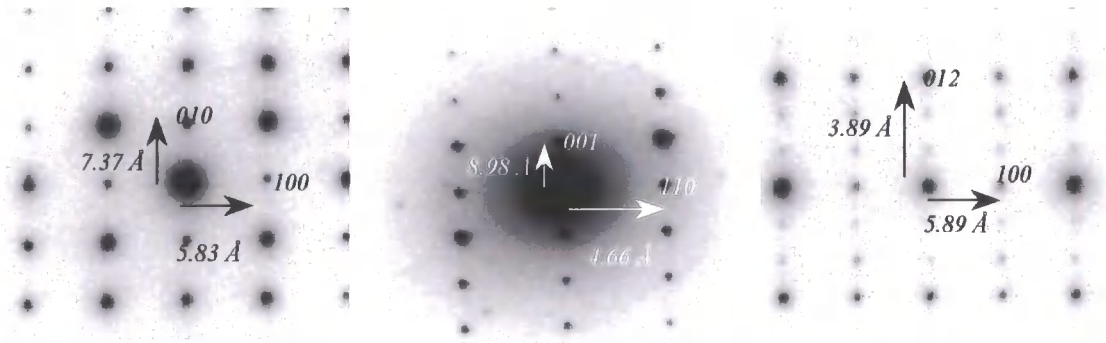

Figure 2.5. Electron diffraction patterns of LT-$ZrMo_2O_8$. The important *d*-spacings obtained are 5.89 Å for [100], 7.37 Å for [010] and 8.98 Å for [001]. The diffractogram on the right shows a tripling of the unit cell along the [012] direction.

The unit cell parameters obtained by electron diffraction are $a = 5.89$ Å, $b = 7.37$ Å, $c = 8.98$ Å confirming the structure presented in Section 2.2.2. Figure 2.5 (*right*) gives some indication that there may be a subtle tripling of the simple cell parameter used above. However, no evidence for this could be observed in the powder data. The unit cell dimensions are in approximate agreement with those obtained by electron diffraction for a recently reported but only partially characterised new polymorph of $ZrW_{1.6}Mo_{0.4}O_8$ by Zhao *et al.*.[21] They reported a unit cell of $a = 8.969$ (7), $b = 7.011$ (8), and $c = 5.96$ (1) Å for a metastable orthorhombic phase, which was prepared by dehydrating $ZrW_{1.6}Mo_{0.4}O_7(OH)_2(H_2O)_2$. However, a definitive space group was not given and a structure solution of this 'LT' phase was not attempted. The similarity of the powder pattern for orthorhombic $ZrW_{1.6}Mo_{0.4}O_8$ and LT-AM_2O_8 phases in this thesis, however, implies an isostructural relationship.

2.2.4 Structural Description of LT-$ZrMo_2O_8$

The structure of LT-$ZrMo_2O_8$ is shown in Figure 2.6; it consists of a three-dimensional array of vertex-shared ZrO_6 octahedra and MoO_4 tetrahedra with a singly coordinated O atom, as in cubic or trigonal $ZrMo_2O_8$. Ordered pairs of MoO_4 tetrahedra point in the same direction, for example, along [011] in Figure 2.6 (*right*). From Table 2.5, the Mo(1)···O(21) distance is 2.61 Å which suggests a weak bonding interaction and its bond valence contribution is ~ 10% of the Mo(1)–O(12) bond. A similar situation exists in trigonal $ZrMo_2O_8$ at room temperature as reported by Serezhkin *et al.* (and referred to in Chapter 5),[22] where neighbouring Mo···O contacts are present although at larger separations of 3.1 Å and above.

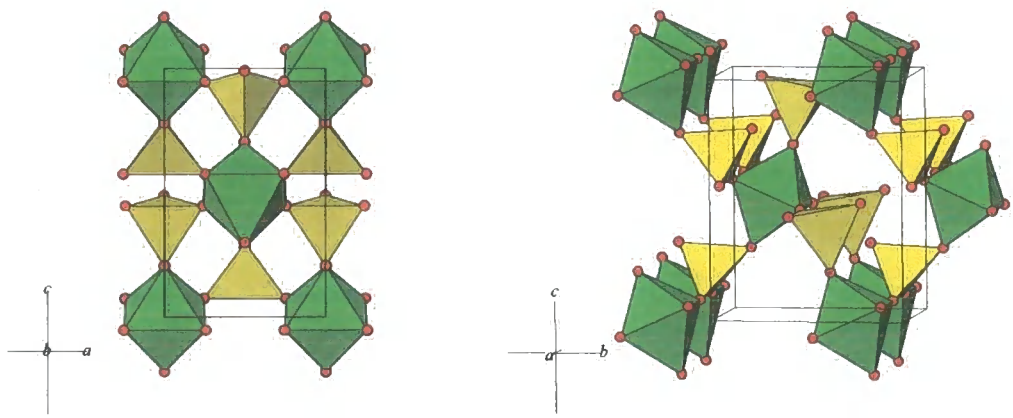

Figure 2.6. Polyhedral representations of orthorhombic LT-$ZrMo_2O_8$ comprised of ZrO_6 and MoO_4 tetrahedra. A terminal O atom resides on one of the tetrahedral vertices.

Figure 2.7 shows that LT-$ZrMo_2O_8$ is structurally related to the rutile structure type. This is visualised by replacing MoO_4 by trigonally coordinated O atoms, and ZrO_6 with octahedral Ti. The LT structure can hence be described as a "decorated" rutile structure.

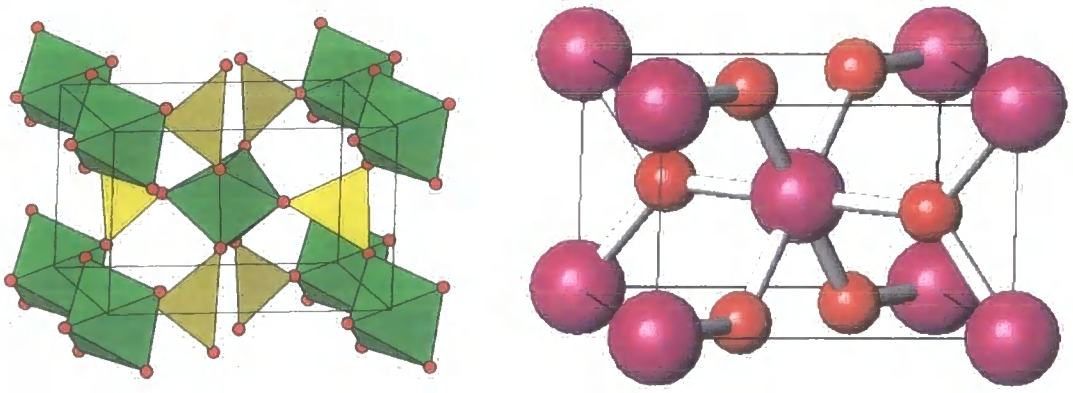

Figure 2.7. LT-$ZrMo_2O_8$ (*left*) in comparison to rutile, TiO_2 (*right*). Terminal O atoms have been omitted from the MoO_4 groups in the LT structure for clarity. A different LT unit cell has been chosen to show the similarity with rutile.

Bond lengths and bond valence values for LT-$ZrMo_2O_8$ are shown in Table 2.5. For any given atom in the structure, the contribution to the total atom valence made by each of the bonded atoms can be calculated.[23,24] In other words, the oxidation state of the atoms in the structure can be approximated from the refined bond lengths, which is a useful way to verify the structural model. The total valence V_i of an atom i is defined as the sum of all valence contributions of the bonded atoms j, $V_i = \Sigma v_{ij}$. The expression used to calculate bond valences, v_{ij} between two atoms i and j is, $v_{ij} = exp[(R_{ij}-d_{ij})/0.37]$, where d_{ij} is the bond length and R_{ij} is the bond valence parameter between i and j atoms in a crystal. R_{ij} is an empirically determined constant derived from bond lengths in literature crystal data and depends on the identity and oxidation state of the atoms. The relevant values here are 1.937 for Zr^{IV} and 1.907 Mo^{VI} oxides.

Atom pair	Bond length / Å	Bond valence, v_{ij}	Total valence, V_i
Zr–O(12)	2.1561 (6)	0.5531	
Zr–O(13)	2.0304 (4)	0.7769	
Zr–O(13)	2.0304 (4)	0.7769	
Zr–O(22)	2.0564 (5)	0.7243	
Zr–O(23)	2.0699 (3)	0.6983	
Zr–O(23)	2.0699 (3)	0.6983	Zr = 4.23
Mo(1)–O(11)	1.6762 (7)	1.8662	O(11) = 1.87
Mo(1)–O(12)	1.7472 (6)	1.5402	O(12) = 2.09
Mo(1)–O(13)	1.8066 (4)	1.3118	O(13) = 2.09
Mo(1)–O(13)	1.8066 (4)	1.3118	
Mo(1)–O(21)	2.6101 (8)	0.1495	Mo(1) = 6.18
Mo(2)–O(21)	1.7321 (5)	1.6045	O(21) = 1.75
Mo(2)–O(22)	1.7823 (4)	1.4009	O(22) = 2.13
Mo(2)–O(23)	1.8144 (3)	1.2845	O(23) = 1.98
Mo(2)–O(23)	1.8144 (3)	1.2845	Mo(2) = 5.57

Table 2.5. Relevant refined bond lengths for LT-$ZrMo_2O_8$ and calculated atom valences.

Judging from the structure of LT-$ZrMo_2O_8$ and its similarity to cubic ZrM_2O_8 phases in terms of polyhedral units and their connectivity, it would be envisaged that the structure would be flexible enough to possess low energy rigid unit modes and thus display negative thermal expansion. The structure has been elucidated here and the thermal expansion of LT-$ZrMo_2O_8$ is investigated in Section 2.2.8.

2.2.5 *In situ* Variable Temperature X-ray Diffraction of $ZrMo_2O_7(OH)_2(H_2O)_2$

The successful solution of the structure of LT-$ZrMo_2O_8$ in Section 2.2.2 permits a quantitative analysis of the VTXRD data for the decomposition of the chloride-derived $ZrMo_2O_7(OH)_2(H_2O)_2$ precursor illustrated in Figure 2.1. As structural details of the

four phases involved (precursor; LT, cubic and trigonal $ZrMo_2O_8$), are now known, the fraction of each phase at each temperature can be determined from multiple Rietveld refinements.

A *TOPAS* seed file was generated containing Rietveld refinement parameters for each of the four phases observed in the d8_01386 VT run and it is shown in the e-Appendix. A total of 29 variables were used for the refinements. Above 983 K, decomposition to amorphous MoO_3 and monoclinic ZrO_2 occurred and these refinements are not shown. 12 Chebyshev background terms and a global sample height correction were refined. Atomic positions were fixed for each phase to room temperature values. One single isotropic temperature factor for all atoms in all phases was refined as were four phase scale factors. The lattice parameters for all four phases were allowed to refine (8 in total) along with a single peak profile parameter for each of the precursor, cubic and trigonal phases. For the LT phase, a combined pseudo-Voigt and sixth-order spherical harmonic (SH) function was used to describe the excess sample strain. The SH coefficients and scale factor were fixed at values obtained in the combined neutron/X-ray refinements. The pseudo-Voigt peak shape coefficients for the LT phase were refined for one range then subsequently fixed for the VT refinement. Temperatures extracted for the HTK1200 furnace were corrected using a previously derived temperature profile function using α-Al_2O_3 as outlined in Section 6.1.3. Such a function is applied to all furnace VTXRD refinements in this chapter. Full results of the 35 refinements are collated in an *Excel* sheet given in the e-Appendix, while the most important details are discussed below.

The refined phase fractions were extracted from the VT refinements and their temperature-dependence is shown in Figure 2.8.

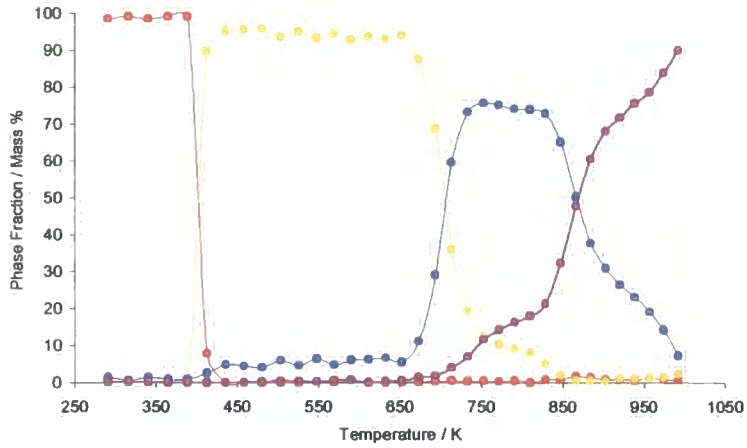

Figure 2.8. The phase fraction of zirconyl chloride-derived $ZrMo_2O_7(OH)_2(H_2O)_2$ and its dehydrated products, LT-$ZrMo_2O_8$, cubic $ZrMo_2O_8$ and trigonal $ZrMo_2O_8$, every 20 K between 303 and 983 K (d8_01386). Actual temperatures were calibrated *via* an external α-Al_2O_3 standard (Section 6.1.3) and range between 291 K and 992 K.

Figure 2.8 illustrates in detail the qualitative observations of Figure 2.1. The $ZrOCl_2$-derived precursor dehydrates to LT-$ZrMo_2O_8$ between 388 and 435 K. Between 653 and 733 K, the LT phase disappears and the fraction of the cubic polymorph rises. However it can be seen that the thermodynamic trigonal phase also begins to crystallise at 713 K, and the desired cubic phase always exists with a trigonal impurity. The maximum amount of the desired cubic phase that can be prepared is ~ 76% at 752 K. Interestingly, a sample of cubic $ZrMo_2O_8$ of approximately this purity was the best sample that could be prepared by Evans *et al.* for use in a HRPD VT study in 2000 (Section 1.3.2.2).[9] Above 828 K it can be seen that cubic $ZrMo_2O_8$ is no longer stable and it slowly converts to the denser trigonal form. Above 990 K, decomposition to the binary oxides occurs. The ~ 6% of cubic $ZrMo_2O_8$ that is apparently present between 400 and 650 K is probably an artefact due to the difficulty of accurately fitting the broad peaks of the LT phase from 20 minute diffraction patterns.

In order to determine whether the precursor to LT-$ZrMo_2O_8$ phase transition occurs between crystalline phases or *via* amorphous intermediates the above VTXRD study was repeated with a known amount of crystalline α-Al_2O_3 added to the precursor material as an intensity standard (Section 7.1).

An analogous VTXRD dehydration study of $ZrMo_2O_7(OH)_2(H_2O)_2$/α-Al_2O_3 was performed from 303 – 983 K in 20 K steps (d8_01422). The same 29 variables were

refined as in the d8_01386 run, except that 5 additional parameters were used to describe α-Al_2O_3 (a scale factor, two cell parameters, one peak shape parameter and a single isotropic temperature factor). The *TOPAS* seed input file and the results spreadsheet are both given in the e-Appendix. Figure 2.9 gives the phase fraction versus temperature plot.

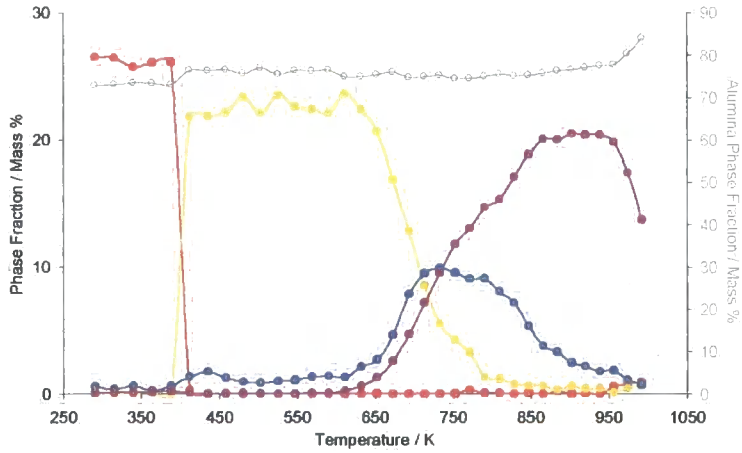

Figure 2.9. The variation of the phase fraction of zirconyl chloride-derived $ZrMo_2O_7(OH)_2(H_2O)_2$ and of the subsequent LT-$ZrMo_2O_8$, cubic $ZrMo_2O_8$ and trigonal $ZrMo_2O_8$ phases (d8_01422). Also shown is α-Al_2O_3 added as an internal intensity standard.

Figure 2.9 shows that there is no marked change in the refined phase fraction of α-Al_2O_3 at any stage of the experiment. If an amorphous intermediate existed, the fraction of α-Al_2O_3 would increase significantly at around 400 K. Such an increase is, however observed at decomposition point of trigonal $ZrMo_2O_8$, presumably due to amorphous MoO_3 and crystalline ZrO_2 at ~ 956 K. With regard to the precursor and LT-$ZrMo_2O_8$, it seems that the transformation is crystalline to crystalline, hinting that there could be a concerted, topotactic relationship between these two phases. A possible mechanism for the precursor to LT transformation is described in Section 2.2.7. It is worth noting that in Figure 2.9 (compared to Figure 2.8) that there is a reduced proportion of cubic $ZrMo_2O_8$ throughout, despite the fact that the same heating rate was employed. Also the trigonal phase begins to form and subsequently decompose at lower temperatures (653 K and 956 K respectively) in this particular experiment.

In 2001, Lind *et al.* published the preparation of $ZrMo_2O_7(OH)_2(H_2O)_2$ derived from $ZrO(ClO_4)_2$ as opposed to $ZrOCl_2$, from which pure cubic $ZrMo_2O_8$ could be made

more easily.[10] This preparation was repeated by Nick Warmingham and synthetic details are given in Section 7.2. A ~ 15.7 g powdered sample of light green-coloured, perchlorate-derived $ZrMo_2O_7(OH)_2(H_2O)_2$ (sample i.d. NRW036) was prepared. This material is visually distinct to $ZrOCl_2$-derived $ZrMo_2O_7(OH)_2(H_2O)_2$, which is lavender in colour.

A VTXRD study of perchlorate-derived $ZrMo_2O_7(OH)_2(H_2O)_2$ was performed to establish the best conditions required to form a bulk sample of pure cubic $ZrMo_2O_8$ for a detailed neutron diffraction investigation of its thermal expansion (Section 3.2). A sample of perchlorate-derived precursor was mounted in the HTK1200 furnace in the usual way. An initial scan at 318 K was performed with subsequent 30 minute scans every 10 K between 323 and 983 K, although these temperatures were corrected with α-Al_2O_3 in the normal way. The diffraction data are displayed in Figure 2.10; 29 variables were used in the seed refinement, as for chloride-derived precursor (d8_01386) above. Full results of the four-phase variable temperature Rietveld refinement are given in the e-Appendix (d8_01612); the phase fraction plot is given in Figure 2.11. Figures 2.10 and 2.11 show a large, clear window between ~ 740 – 880 K in which the cubic form is the dominant phase with very little (< 5%) trigonal present. The near-absence of the large trigonal peak at 23 ° 2θ in the highlighted cubic powder pattern is noteworthy. The onset of formation of trigonal $ZrMo_2O_8$ is at a significantly higher temperature than previously observed (~ 860 K for the perchlorate precursor versus ~ 710 K for the chloride analogue). This permits the complete conversion of LT to cubic at around 670 – 700 K without co-crystallisation of the trigonal impurity in the perchlorate case. The explanation for this is not very clear, but Lind illustrated that the ability of various precursors (formed from different Zr sources) to form pure cubic $ZrMo_2O_8$ could be correlated their sample morphology which remain unchanged throughout the phase transformations.[10]

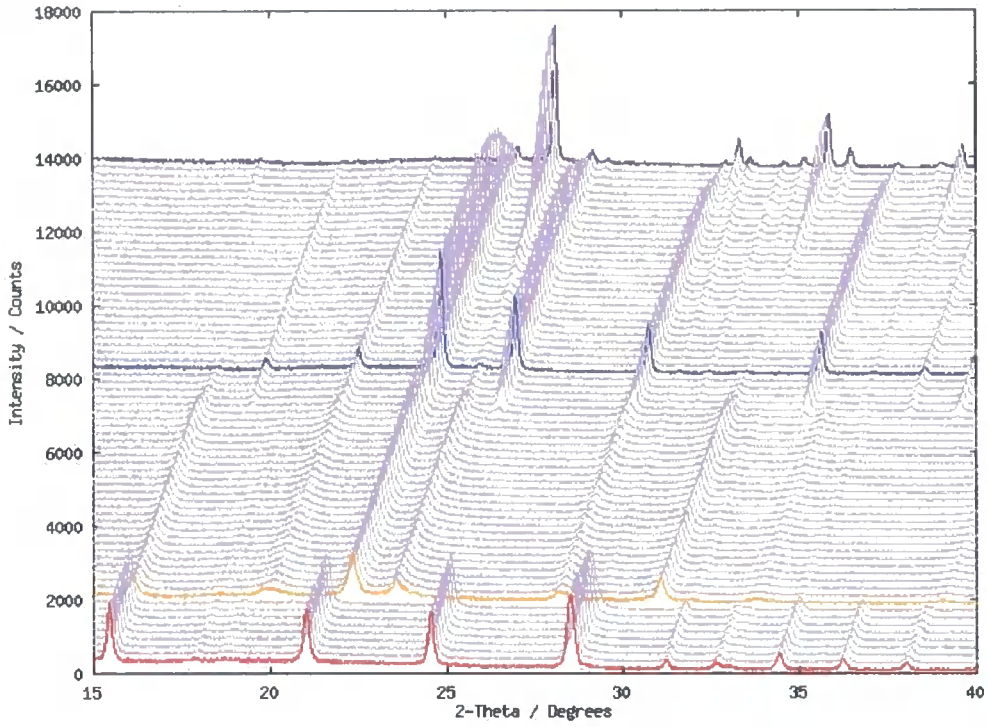

Figure 2.10. *In situ* diffraction patterns of perchlorate-derived $ZrMo_2O_7(OH)_2(H_2O)_2$ and its decomposition products, LT-$ZrMo_2O_8$, cubic $ZrMo_2O_8$ and trigonal $ZrMo_2O_8$ (d8_01612). A high background exists due to the absence of radial sollers from the PSD detector in this experiment (compare to Figure 2.1).

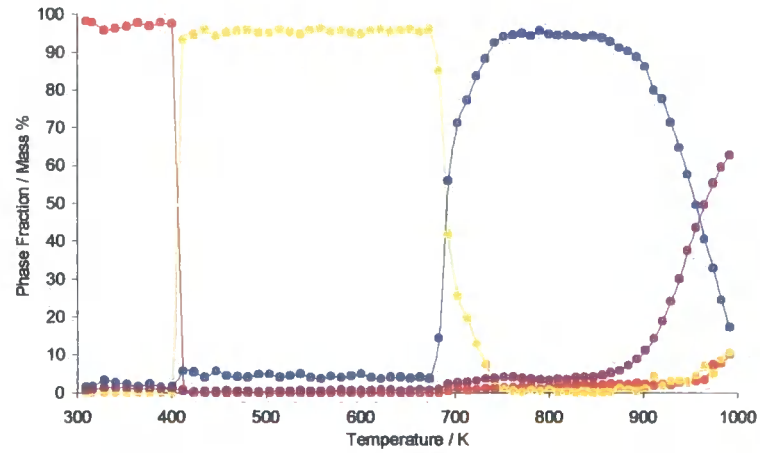

Figure 2.11. Phase fraction of zirconyl perchlorate-derived $ZrMo_2O_7(OH)_2(H_2O)_2$, LT-$ZrMo_2O_8$, cubic $ZrMo_2O_8$ and trigonal $ZrMo_2O_8$ phases (d8_01612).

The above VTXRD analysis permitted the successful preparation of a ~ 13.8 g pure sample of cubic $ZrMo_2O_8$ for use in neutron diffraction studies, by heating perchlorate-derived $ZrMo_2O_7(OH)_2(H_2O)_2$ to 723 K. Section 7.2.1 gives the full synthetic

conditions employed to prepare cubic $ZrMo_2O_8$ (SA97B), while Section 3.2 describes the thermal expansion properties of this material.

Temperatures extracted from the HTK1200 furnace in the above VT runs were back-calibrated against an external Al_2O_3 standard. A maximum temperature error inherent with the HTK1200 furnace of 30 K at ~ 700 K was observed and hence calibration performed (Section 6.1.3).

2.2.6 Rehydration of LT-$ZrMo_2O_8$

It was noticed that upon exposure to air, a freshly prepared sample of LT-$ZrMo_2O_8$ (peach/beige colour, made *via* chloride-derived $ZrMo_2O_7(OH)_2(H_2O)_2$) would turn grey in a few hours. The X-ray pattern of the grey sample showed new broad peaks at roughly the same 2θ values as the most intense peaks of the precursor phase. However, when an LT-$ZrMo_2O_8$ sample had been left in a vial for around 1 year, complete conversion to lavender $ZrMo_2O_7(OH)_2(H_2O)_2$ with a sharp diffraction pattern was surprisingly observed. When exposed to a warm moist atmosphere, the rehydration process could be accelerated and over 6 days the peach LT form turned first to grey and then to lavender $ZrMo_2O_7(OH)_2(H_2O)_2$.

The spontaneous rehydration of the LT polymorph highlights its metastability; this property has not previously been reported in the literature. The reversibility of the hydration process again suggests that a topotactic precursor-LT relationship exists as was first mentioned in Section 2.2.2. More details are given in Section 2.2.7.

In Clearfield's original single crystal work on $ZrMo_2O_7(OH)_2(H_2O)_2$, only provisional hydrogen positions were assigned *via* hydrogen bond arguments.[8] If actual OH/H_2O positions could be determined accurately this might enable the description of a precursor to LT dehydration mechanism. The reversible relationship of the precursor to LT transformation was therefore exploited in order to prepare a deuterated precursor, "$ZrMo_2O_7(OD)_2(D_2O)_2$" (ideal formula). Deuteration rather than regular hydration was highly preferential so that powder neutron diffraction could be performed since of the two isotopes, protium scatters neutrons incoherently causing problems with structural

analysis due to a large background. There is also little hope of locating hydrogen atoms in the presence of heavy metal atoms in powder X-ray analysis.

Deuteration of LT-$ZrMo_2O_8$ was carried out in conjunction with Nick Warmingham by simple hydrothermal treatment of LT-$ZrMo_2O_8$ with D_2O at 373 K (Section 7.1.2). Dr. Richard K. B. Gover and Tadaaki Matsumura kindly collected room temperature neutron diffraction data on Vega and Sirius, the high-resolution powder diffractometers at the KEK pulsed spallation neutron scattering facility (KENS), National Laboratory for High Energy Physics, Tsukuba, Japan. 1.43 g of "$ZrMo_2O_7(OD)_2(D_2O)_2$" were contained in a standard vanadium can and an ~ 18 hour diffraction pattern recorded between 5000 and 50000 μs on Vega and a ~ 15 hour pattern between 14000 and 50000 μs on Sirius. In both cases data were from acquired from back-scattering detector banks. Brief details of Vega and Sirius are given in Section 6.2.2. A laboratory Rietveld quality X-ray powder pattern was obtained using a Siemens d5000 diffractometer (instrument details of which are given in Section 6.1.9); a sample of $ZrMo_2O_7(OD)_2(D_2O)_2$ was sieved on a silicon wafer and an ~ 11 hour data collection obtained between 10 – 90 ° 2θ with a step size of 0.02 ° 2θ.

A combined neutron and X-ray Rietveld refinement was performed using *TOPAS* and a total of 88 variables were refined. For each of the two neutron histograms, a histogram scale factor, six background terms, an absorption correction coefficient (modelled as $exp(-2fixb(sin\theta/\lambda)^2)$; for Sirius only), two cell parameters and two peak shape terms (FWHM and Lorentzian coefficients) were employed. For the X-ray dataset, a similar absorption coefficient, an axial divergence parameter, a histogram scale factor, nine background terms, a sample height correction, two cell parameters and six PV terms were used to describe the precursor phase.

Initial studies suggested that each of the Mo sites was in fact disordered over two sites, which is presumably related to disorder in the positions of the H_2O molecules, *i.e.*, a mixture of $H_2O\cdots Mo{=}O$ and $O{=}Mo\cdots OH_2$. Hence six Mo atomic coordinates (for Mo(1) and Mo(1a)), as well as a fractional occupancy parameter, and seven O coordinates of the metal-only bonded oxygens were refined. The remaining O atomic positions were involved in bonding to D and accounted for by rigid bodies as discussed below. Nine isotropic temperature factors were refined: one for Zr, one for Mo (Mo(1) being equated

to Mo(1a)), six for O and one for all D atoms. Four rigid bodies were employed to model two unique water molecules disordered over Mo(1)/Mo(1a), and two disordered hydroxyls (two O(5)–D groups which bridge Zr and Mo). For each rigid-body, three rotational angle parameters were refined to describe the orientation of the D_2O/OD moieties, giving 12 refined *rot* values in all. Nine translational values (equivalent to *abc* coordinates) were refined for the three rigid-body bearing O atoms.

Preliminary refinements showed that temperature factors for the D sites were too large ($B_{iso} \approx 7$ Å^2) and a relatively high background (Figure 2.12, *lower*) suggested some incoherent scattering by hydrogen was present. It is possible that $D_2O \leftrightarrow H_2O$ exchange may have occurred during the final stages of the synthesis or during transit. EI Mass Spectrometry was used to measure the proportion of deuterium versus hydrogen in the sample; the value of x in $D_xH_{2-x}O$ was rather low at only 1.24. The neutron scattering power of deuterium ($b_D = 0.6671$) was readjusted to account for the presence of hydrogen ($b_H = -0.3739$) to give an average scattering length of 0.2736. The D : H ratio calculation is described in Appendix A1.1.

The Vega and Sirius refinements had to include a second phase to account for the vanadium sample can. The following structural parameters were refined then fixed for the final cycle: one histogram scale factor, cubic cell parameter, a single temperature factor and the two usual peak profile terms.

The combined Rietveld refinement plots are displayed in Figure 2.12. Good agreement between the experimental and calculated diffraction patterns of $ZrMo_2O_7(OD)_2(D_2O)_2$ is observed. The deuterated (rehydrated) precursor shows sharp Bragg reflections in the first plot in the figure as in the case of the original precursor (base of Figure 2.1). In fact the powder pattern of an as-synthesised precursor and a dehydrated/rehydrated precursor seem identical bar a different signal : noise ratio. This rules out the possibility of small particle size as the effect of broadening the reflections in the intermediate LT phase, since the size of the particles would not change throughout this transformation.

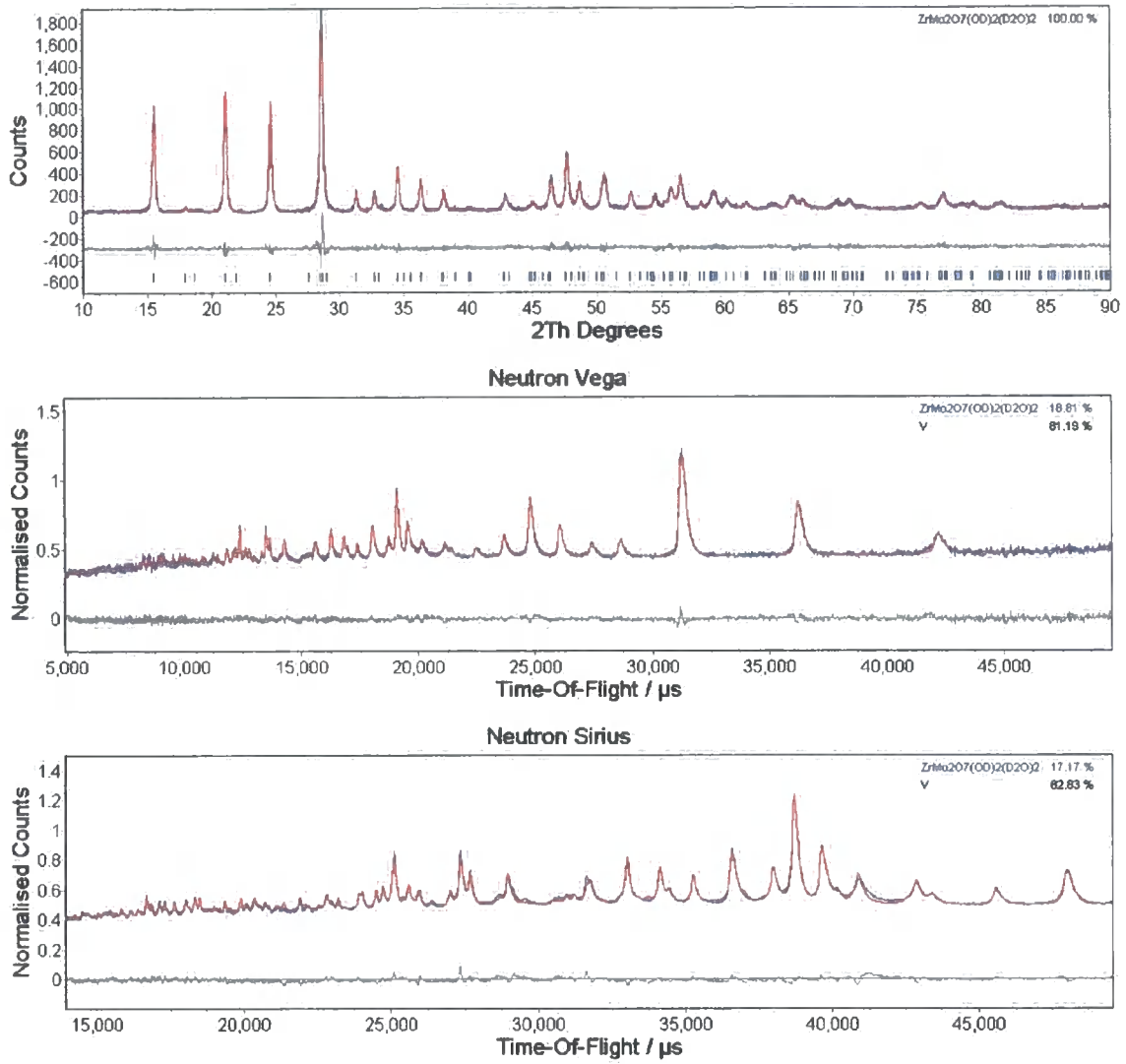

Figure 2.12. Combined X-ray (*top*, d5_02941) and back-scattering neutron (*below*) Rietveld refinement plots for $ZrMo_2O_7(OD)_2(D_2O)_2$. The corresponding *d*-spacing ranges are d = 8.84 –1.09 Å (X-ray), 0.50 – 5.00 Å (Vega) and 0.69 – 2.47 Å (Sirius). The V can gives rise to small peaks at ~ 21300 (Vega) and 43400 μs (Sirius) amongst others, barely visible on this scale. Note: the high background in the neutron patterns caused by the incoherent scattering by H atoms.

Cell parameters and atomic parameters extracted from the *TOPAS* $ZrMo_2O_7(OD)_2(D_2O)_2$ file are presented in Tables 2.6 and 2.7, respectively while full details are set out in the e-Appendix. Reasonable agreement between the refined and literature tetragonal cell parameters exist in Table 2.6. The overall weighted profile *R*-factor, $_wR_p$ = 3.39%, and the overall χ^2 = 0.214, which are small and reflect the large proportion of the total scattering contributed by the background.

	X-ray, d5_02941	Neutron, Vega	Neutron, Sirius	Clearfield single crystal
Cell parameter a / Å	11.45529 (9)	11.46671 (4)	11.48486 (4)	11.45 (1)
Cell parameter c / Å	12.48477 (11)	12.49724 (7)	12.51642 (7)	12.49 (1)
Cell volume V / Å^3	1638.30 (3)	1643.20 (2)	1650.94 (1)	1637 (4)
R_{Bragg} ($\equiv R_{F^2}$)	0.0278	0.00719	0.00937	0.037
${}_wR_p$	0.114	0.0286	0.0295	N/A

Table 2.6. Combined refined cell parameters of $ZrMo_2O_7(OD)_2(D_2O)_2$ versus those for the single crystal values of the hydrated analogue reported by Clearfield.

	x	y	z	B_{iso} / Å^2
Zr	0	0	0	0.454 (1)
Mo(1)	0.02971 (15)	0.16780 (18)	0.23482 (20)	0.329 (2)
Mo(1a)	–0.01189 (19)	0.15980 (20)	0.23124 (22)	0.329 (2)
O(1)	0.17450	0.16591	0.24661	2.55 (4)
D(11)	0.23440	0.10313	0.24014	1.23 (3)
D(12)	0.22074	0.23922	0.25537	1.23 (3)
O(2)	0.82641	0.16287	0.22362	1.25 (3)
D(21)	0.80047	0.11977	0.28884	1.23 (3)
D(22)	0.78808	0.24079	0.22969	1.23 (3)
O(3)	0.17253 (8)	0.99669 (15)	0.99352 (10)	0.0716 (17)
O(4)	–0.01224 (8)	0.11942 (6)	0.86490 (9)	–0.590 (5)
O(5)	0.00140	0.16796	0.06447	1.35 (2)
D(51)	–0.05811	0.22802	0.04515	1.23 (3)
D(52)	0.04366	0.24088	0.04395	1.23 (3)
O(6)	0	0	0.17930 (14)	0.625 (2)

Table 2.7. Refined positional and thermal motion parameters for $ZrMo_2O_7(OD)_2(D_2O)_2$ from a combined X-ray and neutron study. ESD values are absent for D/O atoms involved in rigid-bodies *e.g.* water-bearing O(1)/O(2) and hydroxyl-bearing O(5), and their deuterium atoms.

Examination of the temperature factors in Table 2.7 imply that the refinements are not of particularly high quality but are the best that could be achieved with the current data. The structure of $ZrMo_2O_7(OD)_2(D_2O)_2$ is represented in Figure 2.13.

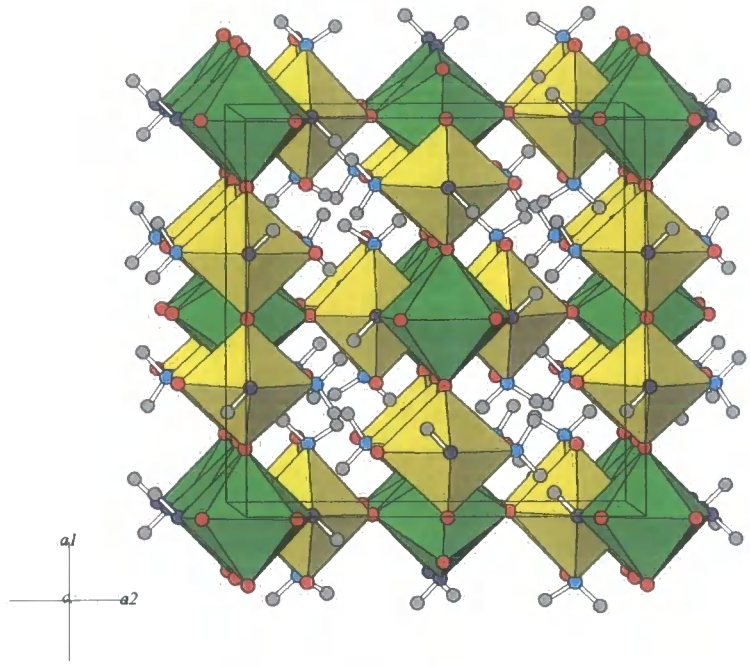

Figure 2.13. Polyhedral representation of $ZrMo_2O_7(OD)_2(D_2O)_2$. Only one unique Mo site/D_2O molecule is shown for clarity; D_2O are statistically distributed over Mo(1) and Mo(1a).

The D_2O species seem to be equally disordered over the Mo(1) and Mo(1a) sites as shown by the refined fractional occupancy value of 0.565 (3), *i.e.* around a half; only one site is shown in Figure 2.13 for clarity. The refined location of the hydroxyl-D is on the bridging oxygen O(5), which links the distorted $MoO_4(OH)(H_2O)$ octahedron to the pentagonal $ZrO_5(OH)_2$ bipyramid. These observations are identical to the tentative assignments of H coordination made by Clearfield on bond angle and bond length arguments.[8]

The presence of two Mo sites and the statistical distribution of D_2O in the above refinement were absent from Clearfield's structural refinement. This could be the result of the low temperature rehydration route. Presumably the H_2O and terminal O sites are ordered down an individual channel of the structure but different channels are disordered with respect to each other as a result of crystal stacking faults. Significantly

worse fits were obtained using only one Mo site and so the disordered, two Mo model was favoured. The resulting Mo(1)–O(1) and Mo(1)–O(2) mean bond lengths here are 1.667 (17) and 2.337 (24) Å respectively, comparable to Clearfield's values of 1.72 and 2.31 Å. For Mo(1a)–O(1) and Mo(1a)–O(2), the mean distances are 2.147 (17) and 1.857 (27) Å, respectively.

The orientation of the hydroxyl group in Figure 2.13 is noteworthy; it would be expected to lie in the trigonal plane with the Mo–O(5)–Zr moiety, however the O–D vector lies out of this plane in these refinements.

2.2.7 Topotactic Relationships Between $ZrMo_2O_7(OH)_2(H_2O)_2$, LT-$ZrMo_2O_8$ and Cubic $ZrMo_2O_8$

In Section 2.2.5 it was noted that no change in the total amount of crystalline phases occurs during conversion of the $ZrMo_2O_7(OH)_2(H_2O)_2$ precursor to dehydrated LT-$ZrMo_2O_8$. The reversibility between the precursor and LT form was established in Section 2.2.6. These aspects of the precursor and LT suggest a topotactic relationship between the two structures, that is the structure of the product in the reaction is determined by that of the reactant and *vice versa.*

Using the results of the refined structure of the precursor obtained in Section 2.2.6 a possible mechanistic pathway to the LT form can be suggested. The structure of the precursor is redisplayed in Figure 2.14 and is schematically segregated into infinite chains for ease of visualisation.

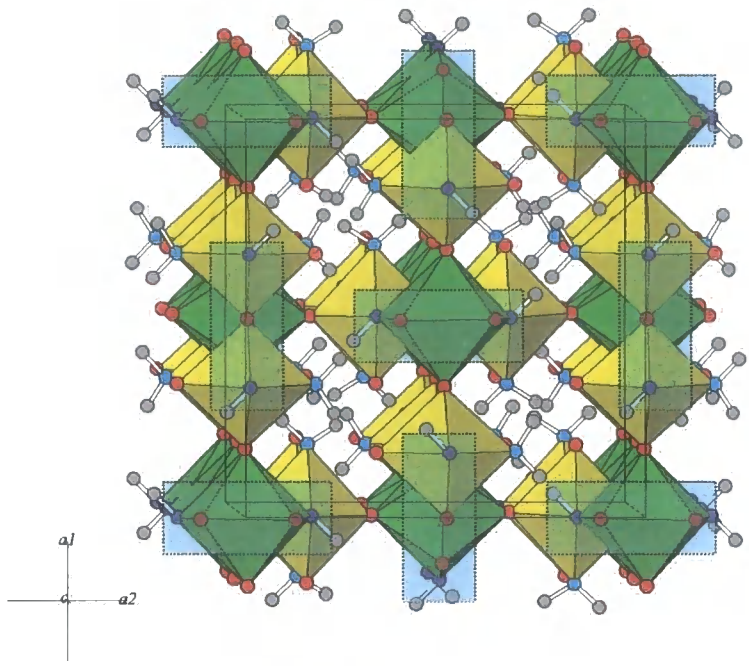

Figure 2.14. The structure of $ZrMo_2O_7(OH)_2(H_2O)_2$ can be visualised as a series of interlinked infinite chains running along the [001] direction as highlighted by the shaded rectangles.

One of the chains of precursor from Figure 2.14 is displayed in Figure 2.15, where it is dissected piece by piece eventually to give the corresponding LT-$ZrMo_2O_8$ chain. It illustrates a possible topotactic mechanism for the transformation.

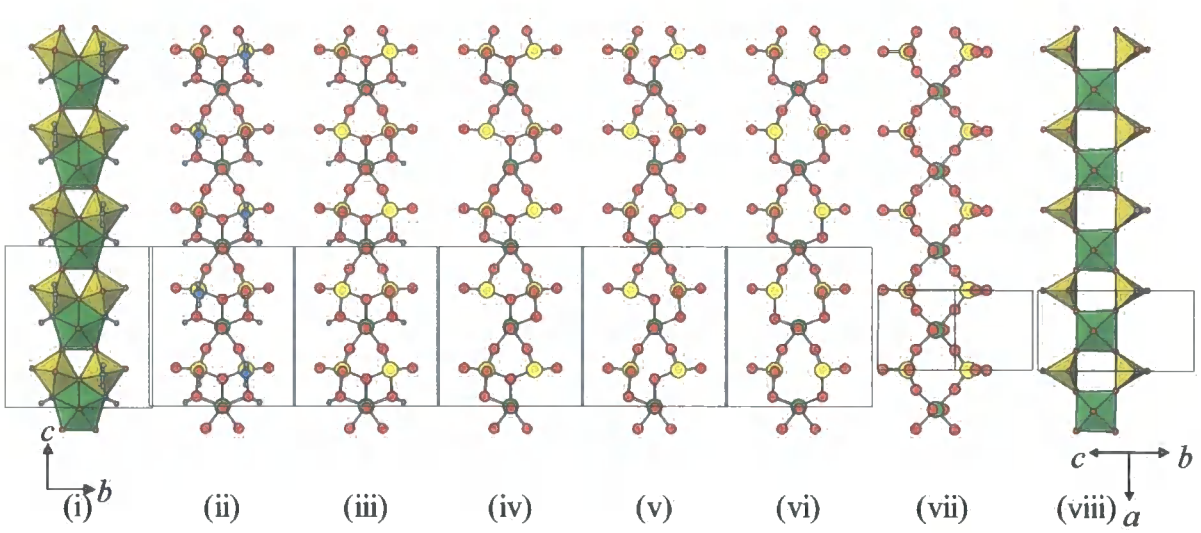

Figure 2.15. A schematic for the dehydration process of a $ZrMo_2O_7(OH)_2(H_2O)_2$ precursor chain (shown in (i)/(ii)) to LT-$ZrMo_2O_8$ (shown in (vii)/(viii)). Loss of 2 × H_2O, is shown to give (iii) followed by loss of OH/H in (iv), cleavage of a Mo–O bond leads to (v), subsequent rotation about the free Zr–O–Mo link to give (vi) and finally, relaxation of the polyhedra to give the LT dehydrate structure in (vii)/(viii).

Figure 2.15 sets out a plausible mechanism for the loss of 3 water molecules from the $ZrMo_2O_7(OH)_2(H_2O)_2$ structure. The first two waters that are lost are from the top and rear face of the precursor chain (the latter H_2O is not visible in Figure 2.15(ii)). These waters make up part of the $MoO_4(OH)(H_2O)$ coordination octahedron. A further water molecule is removed from the unit cell by loss of a proton and a hydroxide group. By breaking a Mo–O bond, the atom connectivities of the LT form are achieved. The $ZrO_5(OH)_2$ pentagonal bipyramids and $MoO_4(OH)(H_2O)$ octahedra that existed in the precursor now find themselves as highly-distorted ZrO_6 and MoO_4 moeities. All that is required to transform to the LT structure is the regularisation of the coordination polyhedra. Since this regularisation must happen at low temperature (~ 400 K), this is potentially the cause of the significant amount of strain broadening observed in the structure.

The form of the refined spherical harmonic in LT-$ZrMo_2O_8$ given in Figure 2.3 (and redisplayed in Figure 2.16) can be rationalised in terms of the directionality of the strain caused by the polyhedral rearrangement of the above mechanism. It can be seen that the major atom shifts to get from step (vi) to (vii) occur in the *bc* plane, whereas minimal displacements occur parallel to the *a* direction (*i.e.* the strain is minimal parallel to the

chains). This is reflected by the magnitude of the lobes in the spherical harmonic plot; they are larger in the *c* and *b* directions and minimal along *a*. It therefore seems likely that the anisotropic strain can be directly related to the topotactic pathway.

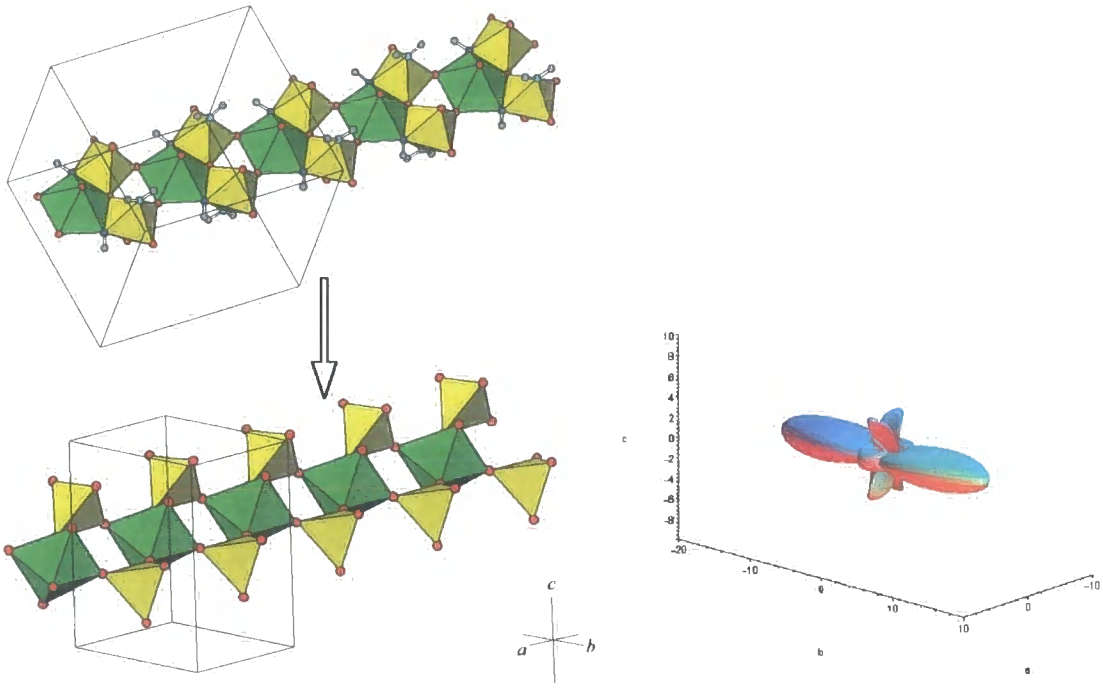

Figure 2.16. Precursor (*top*) and LT-$ZrMo_2O_8$ (*below*) structures and the corresponding strain in LT (*right*).

When comparing the structures of LT and cubic $ZrMo_2O_8$, a relationship between the two is apparent, albeit at a more local level than between the precursor and LT phases (Figure 2.17).

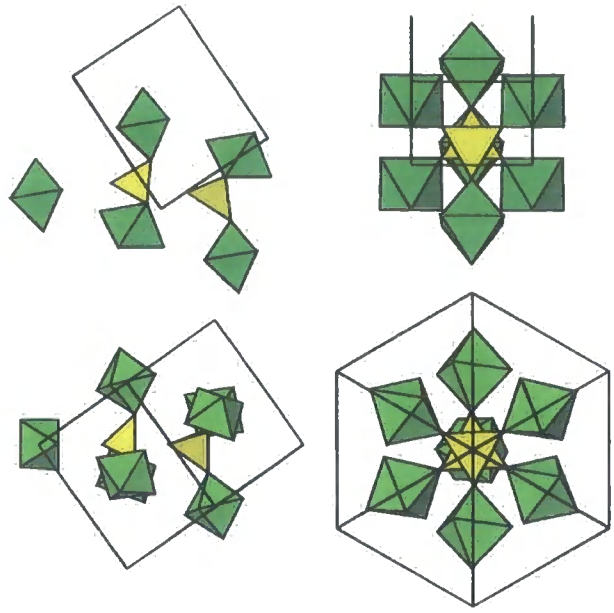

Figure 2.17. Comparable polyhedral views of LT (*top*) and cubic (*below*) $ZrMo_2O_8$ illustrating their structural similarity. Segments of corner sharing polyhedra have been chosen in each case.

Large sections of the polyhedral connectivities are the same in LT and cubic; both phases contain, for example, pairs of MoO_4 groups that point in the same direction. The fact that large segments of the cubic structure are "preformed" in the LT phase most likely means that the kinetically controlled LT to cubic phase transition can occur more rapidly than the formation of the thermodynamic trigonal phase.

There is a clear structural pathway from the precursor phase *via* the LT structure to cubic $ZrMo_2O_8$. This structural pathway is presumably crucial in allowing the formation of the desired pure cubic material. Interestingly, preliminary investigations (see Section 4.2.3 for *in situ* hydrothermal studies) suggest that there may also be a reverse structural pathway directly from cubic $ZrMo_2O_8$ to the precursor phase. This will be discussed later.

2.2.8 Thermal Expansion Properties of LT-$ZrMo_2O_8$

An initial investigation of the thermal expansion properties of LT-$ZrMo_2O_8$ was performed using the VTXRD methodology employed throughout this thesis. Data were collected using a Bruker d8 X-ray diffractometer with an Anton Paar TTK450

cryofurnace. A dynamic vacuum was employed in order to prevent any rehydration of the LT sample. Due to poor crystallinity, large anisotropic strain broadening in the sample and the necessity to collect rapid individual scans over a large temperature range, the data were of relatively poor quality. Whilst detailed structural refinement as a function of temperature were not attempted, reasonable values for the temperature dependence of the cell parameters could be obtained.

Data were collected every 10 K from 550 – 90 K; each scan collected for ~ 30 minutes, between 12 – 70 ° 2θ and a heat rate of 0.2 Ks^{-1} was employed between the scans (run number: d8_01687). An α-Al_2O_3 internal standard was employed to correct the temperature profile of the cryofurnace (details of sample i.d. SA99A are in Section 7.1.1). Full details of the specific temperature calibration of this run are given elsewhere (Section 6.1.4 and the e-Appendix).

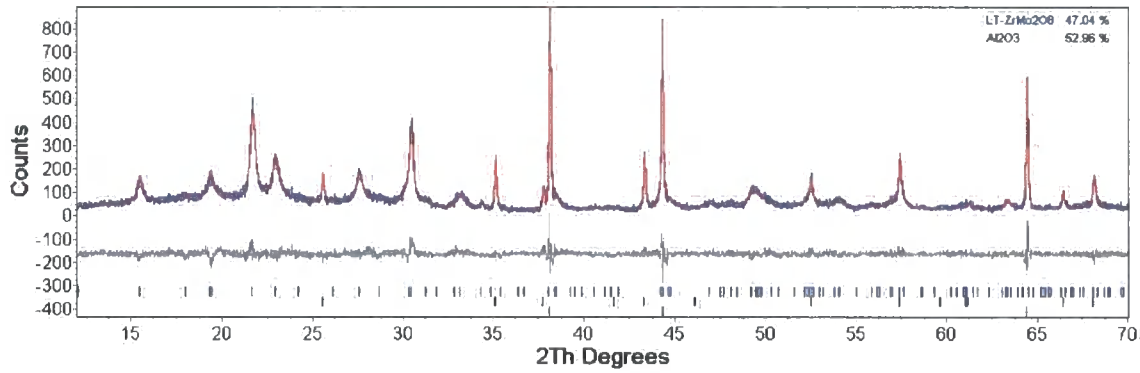

Figure 2.18. Seed Rietveld refinement for the VT LT-$ZrMo_2O_8$ study with an α-Al_2O_3 internal standard (black tick marks) at "550 K" (SA99A, d8_01687). Note the broad nature of the LT peaks (shown by upper blue calculated tick marks). The positions of the three intense Al sample holder peaks are shown by the lower blue tick marks.

A total of 36 parameters were refined for the seed "550 K" measurement (true temperature, 487 K) for the three phases present. The Rietveld refinement is displayed in Figure 2.18. For LT-$ZrMo_2O_8$, a cell-only refinement was performed with the minimum number of variables: a histogram scale factor, three cell parameters, sample height correction, and one isotropic temperature factor. All atomic coordinates, the pseudo-Voigt peak shape and spherical harmonic parameters were fixed throughout. For the α-Al_2O_3 phase, one scale factor, two rhombohedral cell parameters, one peak shape term, two atomic coordinates and two temperature factors were refined. The Al sample

holder was also modelled as an atomic fit because peak overlap at some temperatures led to correlations between the Al cell parameters and those of the LT phase (normally a structure-less Pawley fit is sufficient for Al).[25] Thus a scale factor, a sample height correction, a cubic cell parameter, six PV peak terms and a temperature factor were refined for Al. Twelve Chebyshev background terms were also employed. The *TOPAS* input file is given in the e-Appendix.

The cell parameters of LT-$ZrMo_2O_8$ are shown below in Figure 2.19; overall anisotropic negative thermal expansion is observed between ~ 100 – 500 K, with a mean linear expansion coefficient of α_l (= ⅓α_V) = -1.6×10^{-6} K^{-1}. This value is calculated from $\alpha_l = \frac{1}{3}[(V_T - V_0)/V_0(T - T_0)]$ between 100 and 500 K.

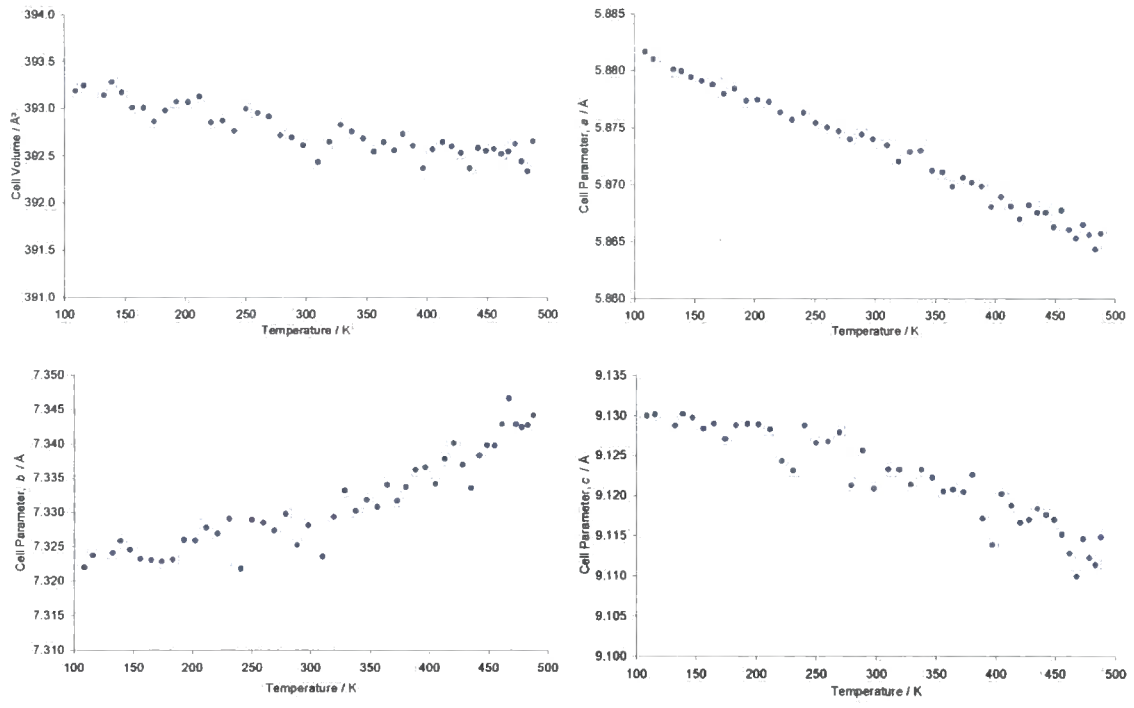

Figure 2.19. Refined unit cell parameters of LT-$ZrMo_2O_8$ as a function of temperature, corrected by an α-Al_2O_3 internal standard (SA99A, d8_01687).

The individual mean expansion coefficients derived from the above unit cell parameter plots are: $\alpha_a = -7.2 \times 10^{-6}$ K^{-1}, $\alpha_b = +7.5 \times 10^{-6}$ K^{-1}, $\alpha_c = -5.1 \times 10^{-6}$ K^{-1}. The negative thermal expansion along a and c in LT-$ZrMo_2O_8$ is comparable to that of the cubic polymorph ($\alpha_l = -9.1 \times 10^{-6}$ K^{-1}). However the overall expansion coefficient is smaller since positive expansion occurs in b. It is not surprising that overall, the property of negative thermal expansion is exhibited by LT-$ZrMo_2O_8$ as in cubic $ZrMo_2O_8$, since

both structures contain the same relatively rigid vertex-sharing ZrO_6 and MoO_4 polyhedra with seemingly flexible, bridging Zr–O–Mo links.

2.3 Thermal Decomposition Study of $HfMo_2O_7(OH)_2(H_2O)_2$

2.3.1 Introduction and Synthesis of $HfMo_2O_7(OH)_2(H_2O)_2$

To gather further evidence for the existence of the low-temperature (LT) polymorph of $ZrMo_2O_8$ described in Section 2.2, it was decided to investigate the related Hf^{IV} phase. The analogous $HfMo_2O_7(OH)_2(H_2O)_2$ precursor material was reported in 1978 by Loboda *et al.*,[26] *via* a similar synthesis to Clearfield's Zr precursor,[8] except that $ZrOCl_2$ was replaced by $HfOCl_2$.

Outline thermal decomposition studies of $HfMo_2O_7(OH)_2(H_2O)_2$ were performed by Loboda; a thermogravimetric analysis showed the presence of three exotherms at ~ 440, 750 and 830 K although a full assignment of these phase transitions was not be made. Nothing was known of the various polymorphs of $HfMo_2O_8$ at that time apart from the trigonal phase, which had been reported by Freundlich *et al.* in 1967.[27] The exotherm at 820 K was thus attributed to trigonal $HfMo_2O_8$. Interestingly, Loboda noted two types of water were present and a stepwise dehydration of $HfMo_2O_7(OH)_2(H_2O)_2$ at ~ 440 K which subsequently could be dehydrated further at ~ 510 K to give an "amorphous" $HfMo_2O_8$ material. No further details were given but this perhaps suggests that the semi-crystalline LT polymorph was present. Loboda also stated that at ~ 750 K, a $HfMo_2O_8$ phase of unknown structure formed (presumably the cubic phase), whereas heating the precursor to ~ 820 K gave the trigonal phase.

Bearing in mind Lind *et al.* had optimised Clearfield's preparation of $ZrMo_2O_7(OH)_2(H_2O)_2$ (by using a 63% excess of Zr over the 1 : 2 ratio which happened to avoid the co-precipitation of amorphous MoO_3) it made sense to simply replace $ZrOCl_2$ with $HfOCl_2$ and use their method to prepare the Hf analogue.[10] The synthesis of pure $HfMo_2O_7(OH)_2(H_2O)_2$ (i.d. NRW027) was performed by Nick Warmingham as described in Section 7.3. The actual Hf : Mo ratio employed was 1.71 : 2, after gravimetric analyses of the hydrated starting materials were accounted for. In other

words, the reaction used a 71% excess over the stoichiometric 1 : 2 ratio used by Loboda's preparation. A ~ 7 g pale cream sample of $HfMo_2O_7(OH)_2(H_2O)_2$ was prepared and its identity confirmed by powder X-ray diffraction.

2.3.2 Dehydration of $HfMo_2O_7(OH)_2(H_2O)_2$

A sample of $HfMo_2O_7(OH)_2(H_2O)_2$ was mounted in the HTK1200 furnace of the d8 diffractometer in the usual manner in order to perform an *in situ* decomposition study of the Hf precursor material. Diffraction patterns were each recorded in the 2θ range of 10 – 70 ° for 25 minutes, and in 20 K intervals between 308 and 1068 K (d8_01539). A close-up of the diffraction patterns is shown in Figure 2.20. It is immediately apparent when comparing this to Figure 2.1 or Figure 2.10, that $HfMo_2O_7(OH)_2(H_2O)_2$ undergoes the same phase transitions as the Zr analogue, although there is difference in the stability region of the various $HfMo_2O_8$ phases. Quantitative phase fractions are described in Section 2.3.4 following the description of the LT phase.

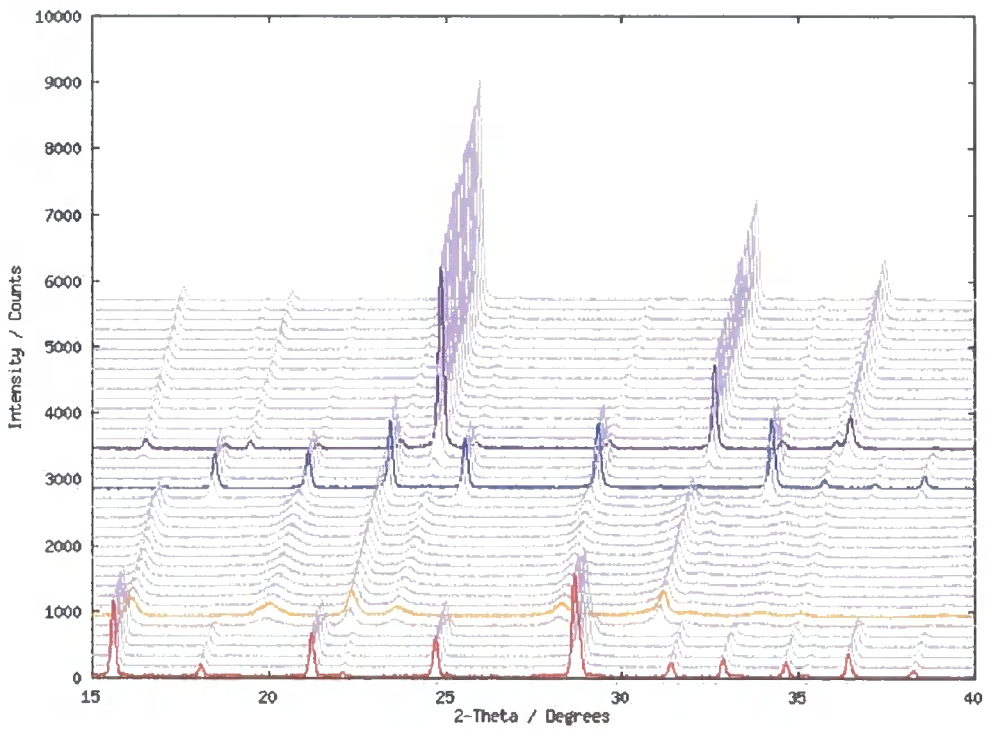

Figure 2.20. VTXRD patterns of $HfMo_2O_7(OH)_2(H_2O)_2$ and its dehydrated products: LT-$HfMo_2O_8$, cubic $HfMo_2O_8$ and trigonal $HfMo_2O_8$ (NRW027, d8_01539). Powder patterns are shown from 308 K (base of the figure) to 1068 K (top) in 20 K steps.

2.3.3 Rietveld Refinement of LT-$HfMo_2O_8$

Figure 2.20 gives evidence of a diffraction pattern at ~ 400 K which consists of broad Bragg reflections characteristic of the LT polymorph described in Section 2.2. A good quality X-ray pattern of this material was obtained by heating a portion of the precursor in a furnace at 573 K as described in Section 7.3.1. The resulting material was bright orange when freshly removed from the furnace (sample i.d. SA100B). A small amount was sprinkled onto a grease-coated silica disc and quickly mounted in the HTK1200 furnace of the d8 diffractometer and held at room temperature under dynamic vacuum. A ~ 8 hour scan in the 2θ range, 13 – 90 ° was recorded (d8_01866). Room temperature powder neutron diffraction was also performed on the High-Resolution Powder Diffractometer (HRPD) at the ISIS pulsed neutron facility of the Rutherford Appleton Laboratory, UK. 2.27 g of freshly dehydrated LT-$HfMo_2O_8$ were packed into a 5 mm vanadium can and data were collected in the usual three detector banks: 168 °, 90 ° and 30 °, over a time-of-flight range of 40000 – 116000, 38500 – 125000, and 40000 – 118000 μs respectively, with a count time of ~ 2 hours (corresponding total beam current of ~ 65 μA; around half that collected in the Zr case).

Data were refined in the same manner as in the combined neutron/X-ray LT-$ZrMo_2O_8$ case. The same 102 variables were employed, including a sixth-order spherical harmonic as in Section 2.2.2. The *TOPAS* input file can be found in the e-Appendix with the main refinement details are given in Tables 2.8, 2.9 and 2.10; the four Rietveld plots are given in Figure 2.22. The overall weighted profile *R*-factor, $_wR_p$ = 5.38%, and the overall χ^2 = 0.455 (again, small due to a large contribution to the scattering from the background in the neutron diffraction patterns).

	X-ray, d8_01866	Neutron, 168 °	Neutron, 90 °	Neutron, 30 °
Cell parameter a / Å	5.85222 (6)		5.84226 (1)	
Cell parameter b / Å	7.30601 (20)		7.28226 (8)	
Cell parameter c / Å	9.07306 (17)		9.07668 (7)	
Cell volume V / Å^3	387.931 (14)		386.167 (5)	
R_{Bragg} ($\equiv R_{F^2}$)	0.0395	0.0152	0.0128	0.0374
${}_wR_p$	0.105	0.0538	0.0941	0.0422

Table 2.8 Refined cell parameters and residual factors for the combined room temperature X-ray and neutron refinement of LT-$HfMo_2O_8$.

Comparison of Tables 2.8 and 2.2 show that, as is the case with other AM_2O_8 phases (*e.g.* cubic phases in Chapter 3, or trigonal phases in Chapter 5), the unit cell volume of the Hf compound is slightly less than that of Zr (< 2% here).

	x	y	z	B_{iso} / Å^2
Hf	½	0.25728 (8)	½	1.27 (2)
Mo(1)	½	0.94750 (8)	0.17927 (8)	2.22 (2)
O(11)	½	0.78334 (16)	0.30053 (12)	7.50 (4)
O(12)	½	0.15478 (9)	0.27919 (14)	2.06 (2)
O(13)	0.75382 (10)	0.92009 (11)	0.07850 (8)	2.06 (2)
Mo(2)	½	0.42611 (8)	0.89196 (7)	2.22 (2)
O(21)	½	0.22184 (17)	0.00671 (14)	3.66 (3)
O(22)	½	0.38422 (12)	0.69684 (10)	2.06 (2)
O(23)	0.75107 (11)	0.56059 (8)	0.95071 (8)	2.06 (2)

Table 2.9. Combined X-ray and neutron refined atomic positions and thermal parameters of LT-$HfMo_2O_8$.

As for the Zr case, the terminal O atoms have larger temperature factors than the bridging oxygens (which were equated as previously). There is little difference between

the observed coordinates in Tables 2.9 (Hf) and 2.3 (Zr). The Hf analogue seems to be isostructural with the previously reported LT-$ZrMo_2O_8$ structure.

ijp	$Y_{ijp}(\theta, \varphi)$ for $HfMo_2O_8$	$Y_{ijp}(\theta, \varphi)$ for for $ZrMo_2O_8$
00	1	1
20	–0.8188 (89)	–0.2873 (52)
22+	–4.29437 (93)	–3.9826 (55)
40	3.03053 (96)	2.8403 (59)
42+	3.57892 (81)	3.8853 (49)
44+	0.5473 (80)	0.6548 (48)
60	–0.3525 (12)	–0.3121 (8)
62+	–1.10447 (72)	–0.1527 (44)
64+	0.5800 (52)	1.0403 (32)
66+	0.5568 (63)	0.4278 (35)

Table 2.10. Comparison of refined spherical harmonic coefficients for LT-AMo_2O_8 (A = Hf, Zr).

The low (up to fourth) order terms of the refined spherical harmonic are essentially the same in both LT forms of $ZrMo_2O_8$ and $HfMo_2O_8$ (Table 2.10). The higher order terms do vary, but they generate a smaller contribution in comparison. The two functions can be compared in Figure 2.21.

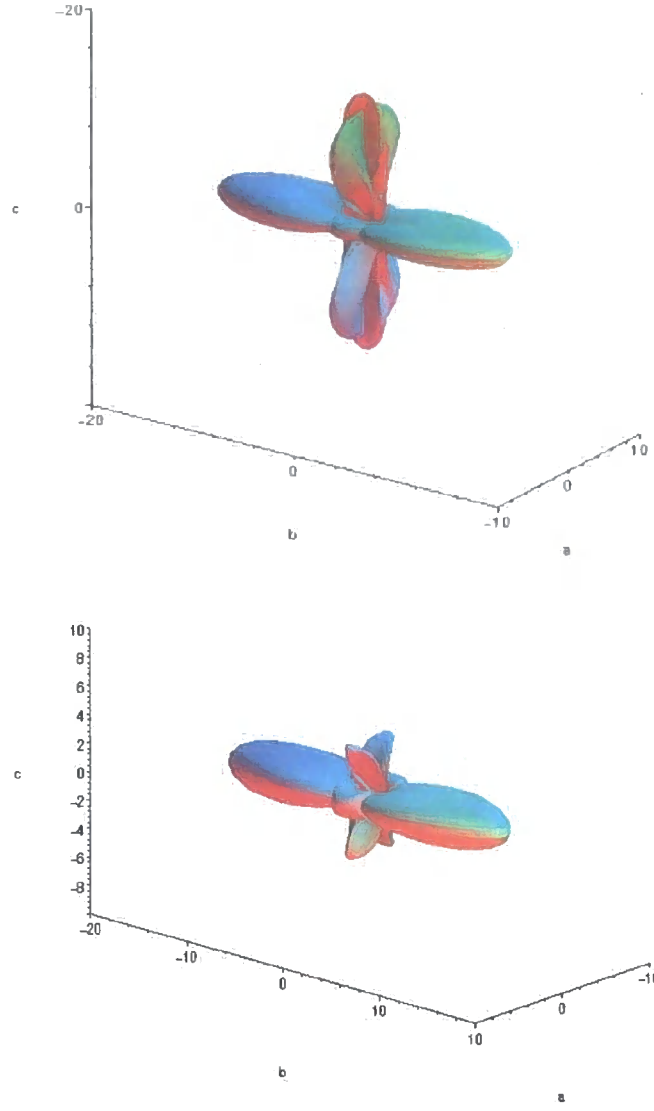

Figure 2.21. Comparison of the refined spherical harmonic functions in LT-$HfMo_2O_8$ (*top*) and LT-$ZrMo_2O_8$ (*lower*).

The shape of the spherical harmonics in Figure 2.21, which represent the directionality of the strain, is similar in both instances and is encouraging support for the mechanism. The function for LT-$HfMo_2O_8$ has a larger magnitude of strain along *c*, but more importantly strain is minimal along *a* in both instances.

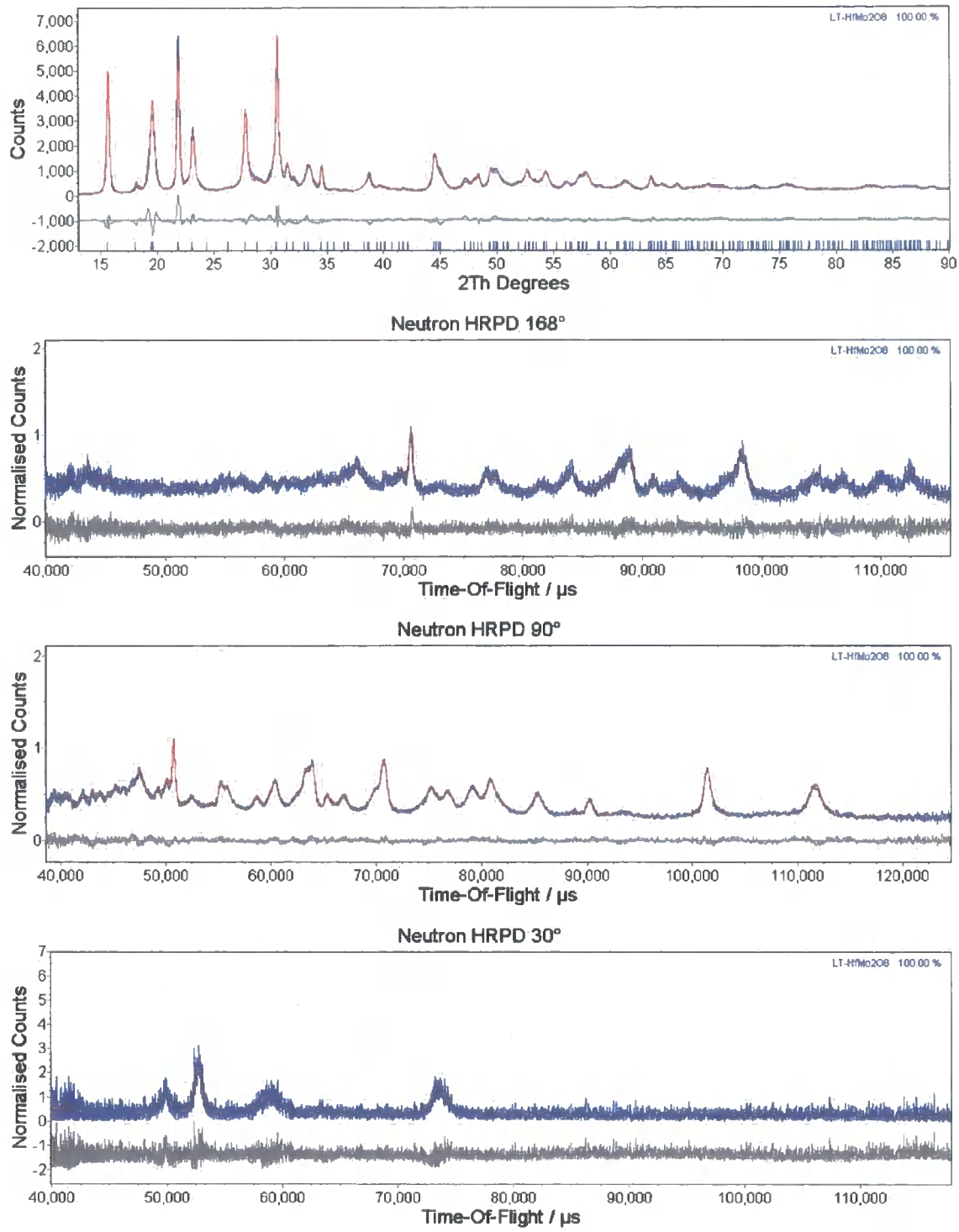

Figure 2.22. X-ray (*top*, d8_01866, $d = 6.81 - 1.09$ Å), and 168 ° (*lower*, $d = 0.83 - 2.40$ Å), 90 ° ($d = 1.11 - 3.59$ Å) and 30 ° ($d = 3.09 - 9.13$°Å) bank neutron Rietveld refinement plots for LT-$HfMo_2O_8$.

The Rietveld fits of LT-$HfMo_2O_8$ (Figure 2.22) are convincing despite a poorer signal : noise ratio due to around 50% counting times compared to those of LT-$ZrMo_2O_8$ (Figure 2.12). The confirmation of the structure of LT-$HfMo_2O_8$ permits

the multi-phase refinement of $HfMo_2O_7(OH)_2(H_2O)_2$ and its dehydrated products, as outlined in Section 2.3.4.

2.3.4 Quantitative VT X-ray Analysis of $HfMo_2O_7(OH)_2(H_2O)_2$

To quantify the observations visualised in Figure 2.20, a four-phase *TOPAS* input file was prepared using the Zr case as a template; in fact the same 29 parameters were included in the refinement as outlined in Section 2.2.5. The seed input file and the resulting spreadsheet of refined parameters at all temperatures are given in the e-Appendix.

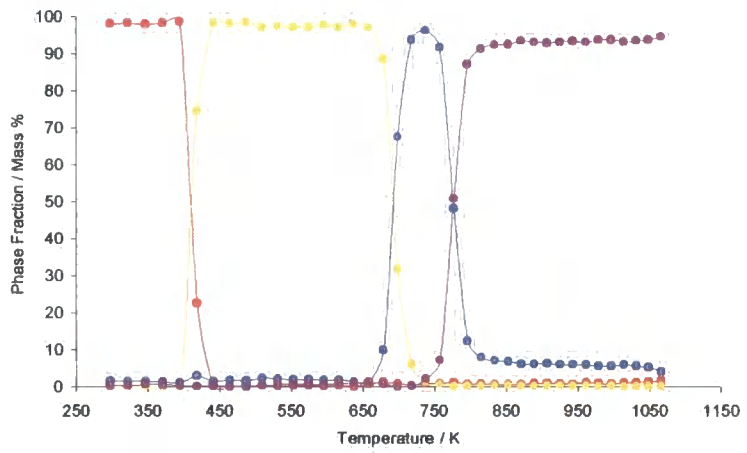

Figure 2.23. Refined phase fractions of LT-$HfMo_2O_8$, cubic $HfMo_2O_8$ and trigonal $HfMo_2O_8$, derived from $HfMo_2O_7(OH)_2(H_2O)_2$ as a function of temperature between 308 and 1068 K (d8_01539).

Figure 2.23 illustrates the stability regions of the hydrated precursor, and the subsequently dehydrated LT, cubic and trigonal polymorphs of $HfMo_2O_8$. Firstly the precursor dehydrates at around 394 K to give the now-familiar LT polymorph. Subsequent conversion to the cubic form occurs, although this phase only exists over a limited temperature range (718 – 757 K) albeit pure phase. Contrast this to the behaviour of the chloride-derived Zr precursor, where only a cubic/trigonal mixture can be prepared. The trigonal phase forms at 757 K and remains as the sole phase until decomposition above ~ 1066 K (not shown). The above study now simplifies the task of determining the optimal conditions required to prepare cubic $HfMo_2O_8$ as a pure phase; an otherwise time-consuming task. More details on the *ex situ* preparation and

expansion properties of cubic and trigonal $HfMo_2O_8$ are presented in Sections 3.3 and 5.2, respectively.

2.3.5 Rehydration Properties of LT-$HfMo_2O_8$

After the observations and conclusions made in Section 2.2, it was not surprising to find that LT-$HfMo_2O_8$ was also susceptible to rehydration. Even under ambient conditions, a sample would darken to a deep orange colour within one week and the powder diffraction pattern clearly showed partial conversion to the hydrated precursor. Within two weeks under a moist atmosphere, full rehydration to a crystalline sample of the $HfMo_2O_7(OH)_2(H_2O)_2$ precursor occurs, again as confirmed by powder X-ray diffraction. The implication of the similar behaviour between the Hf and Zr cases is that the choice of the A^{IV} metal site seems to be irrelevant to the underlying $AMo_2O_7(OH)_2(H_2O)_2$ precursor to LT-AMo_2O_8 relationship in terms of its reversibility and topotacticity.

2.3.6 Thermal Expansion of LT-$HfMo_2O_8$

Three VTXRD experiments upon two samples of LT-$HfMo_2O_8$ were performed using a Bruker d8 diffractometer equipped with an Anton Paar TTK450 cryofurnace under dynamic vacuum. The initial data collection (d8_01521) on sample NRW032 (see Section 7.3.1 for synthetic details), consisted of a warm every 10 K between set temperatures of 100 and 550 K (corrected temperatures: 109 K – 516 K), for 30 minutes at each temperature. After each individual powder pattern was recorded, the sample was heated in the cryofurnace at a rate of 0.2 Ks^{-1}. Data were collected from 10 – 70 ° 2θ. A basic *TOPAS* refinement of LT-$HfMo_2O_8$ at 100 K was carried out in which HRPD-derived atomic coordinates and the spherical harmonic strain function from Section 2.3.3 were used. The only refined parameters were twelve background terms, a sample height correction, a histogram scale factor, three cell parameters and one global temperature factor. This refinement (plotted in Figure 2.24) was used as a seed for all other temperatures in the usual way *via MultiTOPAS*. The input file is located in the e-Appendix. A more detailed refinement was not feasible bearing in mind the poor crystallinity of the LT polymorph. The trend in LT-$HfMo_2O_8$ cell parameters versus

temperature were extracted from the *Excel* sheet in the e-Appendix and are plotted in Figure 2.25.

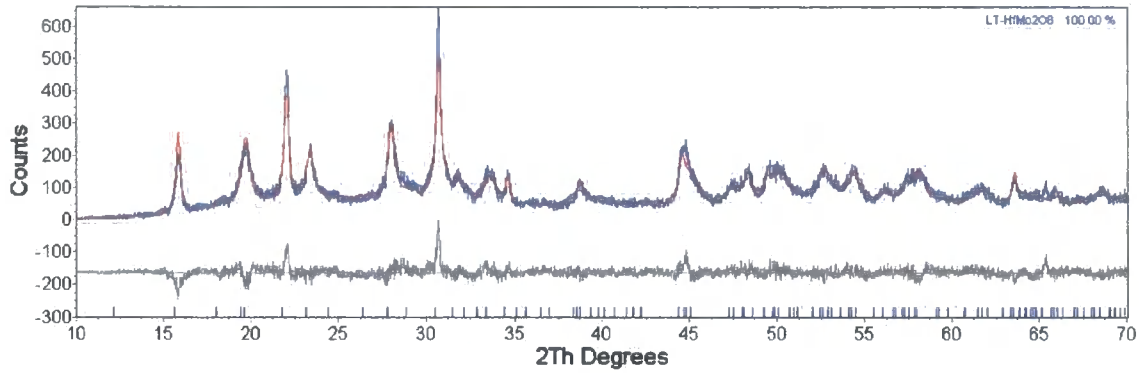

Figure 2.24. Seed Rietveld refinement plot at 100 K for LT-$HfMo_2O_8$. (NRW032, d8_01521).

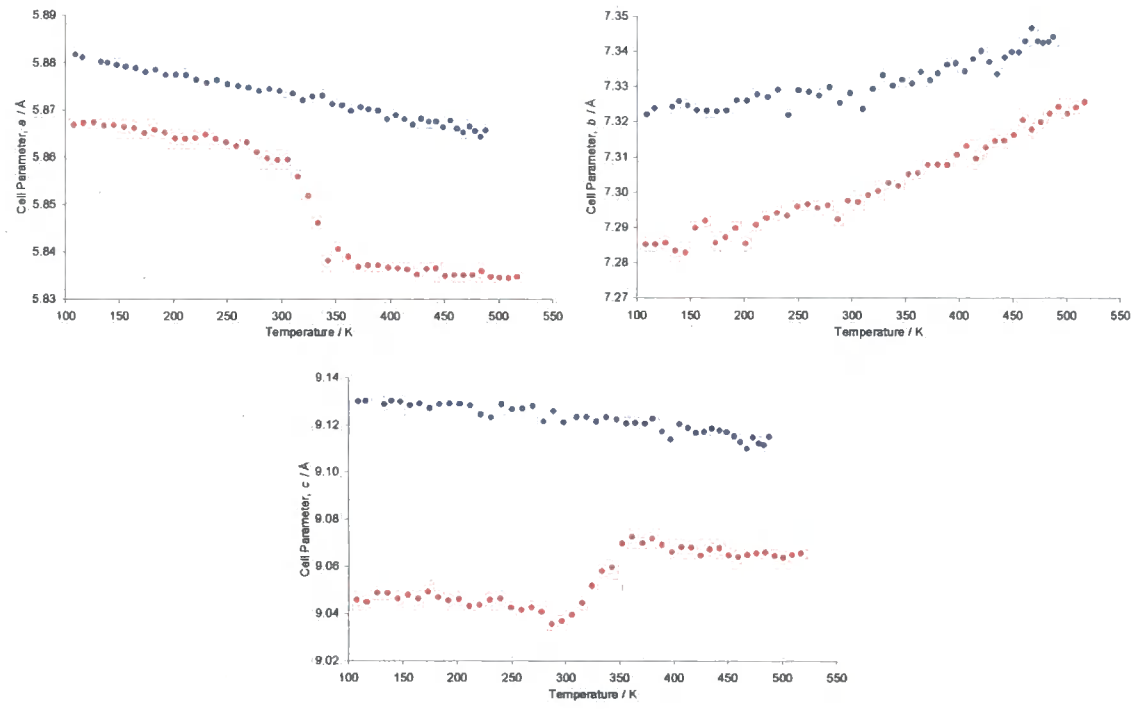

Figure 2.25. The temperature dependent behaviour of the orthorhombic cell parameters of LT-AMo_2O_8 (A = Hf (d8_01521), Zr (d8_01687)). Temperatures were back-calibrated *via* α-Al_2O_3.

Initially it was thought that the discontinuities in the a and c cell parameters in Figure 2.25 suggested the possibility of a first-order phase transition in LT-$HfMo_2O_8$. However it was noted that the discontinuity occurred over ~ 300 – 370 K and close inspection of the refined powder pattern in Figure 2.24 showed an onset of shouldering on the ~ 29 °

2θ peak, due to a trace amount of the precursor phase. This implied that this particular sample is partially hydrated. Otherwise overall similar behaviour is apparent in the Hf and Zr counterparts; NTE is apparent in the *a* and *c* directions whereas positive expansion occurs along *b*.

The thermal expansion of LT-$HfMo_2O_8$ was re-investigated on sample SA99B (details in Section 7.3.1) to verify the above proposition regarding rehydration. More rigorous dehydration procedures were performed on SA99B than on NRW032. An α-Al_2O_3 reference was also present to double check the temperature profile of the cryofurnace. Two VTXRD experiments were performed between 100 and 550 K. Prior to the first VT run on SA99B (d8_01802), the sample was preheated under vacuum at 343 K for 15 minutes in the cryofurnace. For the second run, the sample was heated for 2.5 hours at 473 K in the cryofurnace prior to the start of the data collection (d8_01809). Three phase VT refinements were performed using *TOPAS* with the seed "100 K" refinement consisting of 26 variables in total as presented in the e-Appendix. For the LT phase and background, the same 18 variables were employed as in the above d8_01521 refinement; in addition the Al_2O_3 phase was modelled by refining a histogram scale factor, two cell parameters and one temperature factor. The Al sample holder gave rise to its own powder pattern and was modelled with its own sample height correction, scale factor, cubic lattice parameter and temperature factor. A fixed pseudo-Voigt peak shape was used for each phase to avoid the correlation of cell parameters in the refinement at certain temperatures. The lattice parameters of LT-$HfMo_2O_8$ were found to vary with temperature as shown in Figure 2.26 and in the *Excel* spreadsheets located in the e-Appendix.

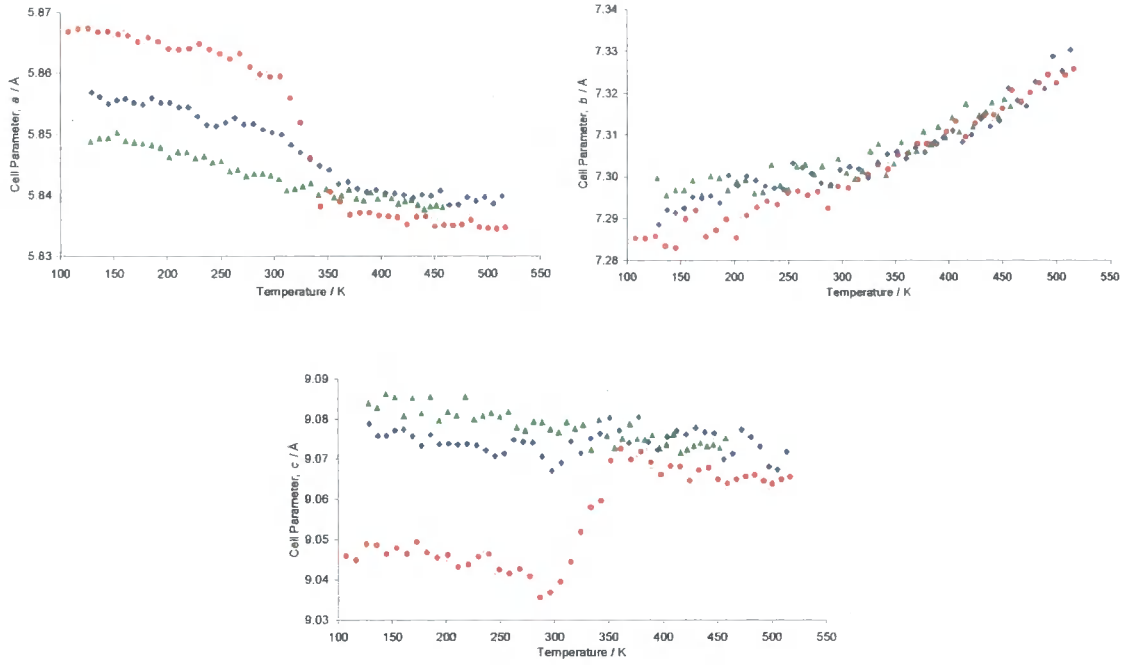

Figure 2.26. Temperature dependence of the cell parameters of LT-$HfMo_2O_8$ in 3 VT experiments. Red circles are data for the partially rehydrated NRW032 sample (d8_01521). Blue diamonds represent data from sample SA99B previously heated to 343 K for 15 mins (d8_01802). Green triangles are also for SA99B with heating to 473 K for 2.5 hours (d8_01809).

It can be seen in Figure 2.26 that the discontinuity in the *a* and *c* data is reduced when the sample is briefly preheated to 70 K and disappears completely upon extended preheating at 473 K, which confirms partial rehydration is responsible for this effect. Interestingly this was never a major problem with LT-$ZrMo_2O_8$ as rehydration was not apparent within the ~ 5 minute time period between removing a bulk sample from a furnace, sprinkling it on an Al plate, loading it into the evacuated cryofurnace and beginning the diffraction measurement. The hump in the cell parameters of the "wet sample" is presumably due to the dehydration of an intermediate phase between the LT and precursor. This speculated "LT-$HfMo_2O_8.xH_2O$" phase has different *a* and *c* cell parameters compared to pure dehydrated LT-$HfMo_2O_8$, as highlighted in Figure 2.26 by comparing data shown by filled circles and triangles, respectively.

Linear expansion coefficients for the rigorously dried sample of LT-$HfMo_2O_8$ derived from the gradients of the unit cell parameter plots are: $\alpha_a = -6.5 \times 10^{-6}\ K^{-1}$, $\alpha_b = +8.7 \times 10^{-6}\ K^{-1}$, $\alpha_c = -4.1 \times 10^{-6}\ K^{-1}$ (d8_01809, Figure 2.26). The mean linear

expansion α_l ($= \frac{1}{3}\alpha_V$) $= -2.0 \times 10^{-6}$ K^{-1} (see d8_01809 *Excel* sheet in the e-Appendix). These values are comparable to those of LT-$ZrMo_2O_8$.

The above study assisted the collation of accurate HRPD neutron diffraction data in Section 2.3.3 where it was ensured that spontaneous rapid rehydration of the LT-$HfMo_2O_8$ was avoided. The freshly dehydrated sample was loaded into its vanadium can, weighed and subsequently reheated in an oven before sealing the can closed and placing the can under vacuum in the neutron beam. A completely dehydrated sample of LT-$HfMo_2O_8$ would thus give rise to accurate cell parameters.

2.4 Thermal Decomposition Study of $ZrW_2O_7(OH)_2(H_2O)_2$

To further investigate the structure of LT-AM_2O_8 phases and their synthesis from $AM_2O_7(OH)_2(H_2O)_2$ precursors, the chemistry of precursors containing $M = W$ was investigated. A pure sample of $ZrW_2O_7(OH)_2(H_2O)_2$ was prepared in conjunction with Nick Warmingham *via* a modified literature preparation by Dadachov and Lambrecht.[28] Details are supplied in Section 7.4; the synthesis is notably different compared to Clearfield's Mo precursor preparation in that the product formed post-reflux is amorphous and requires hydrothermal treatment with HCl to form a crystalline product.

A VTXRD measurement was performed on crystalline $ZrW_2O_7(OH)_2(H_2O)_2$ (sample i.d. NRW017b, chalky white powder) *via* the usual methodologies using a Bruker d8 diffractometer equipped with an Anton Paar HTK1200 furnace so that the dehydrated products could be identified *in situ*. 30-minute powder patterns were recorded every 10 K from 308 K to 998 K between $10 - 70\,°$ 2θ; a close-up of these patterns is displayed in Figure 2.27.

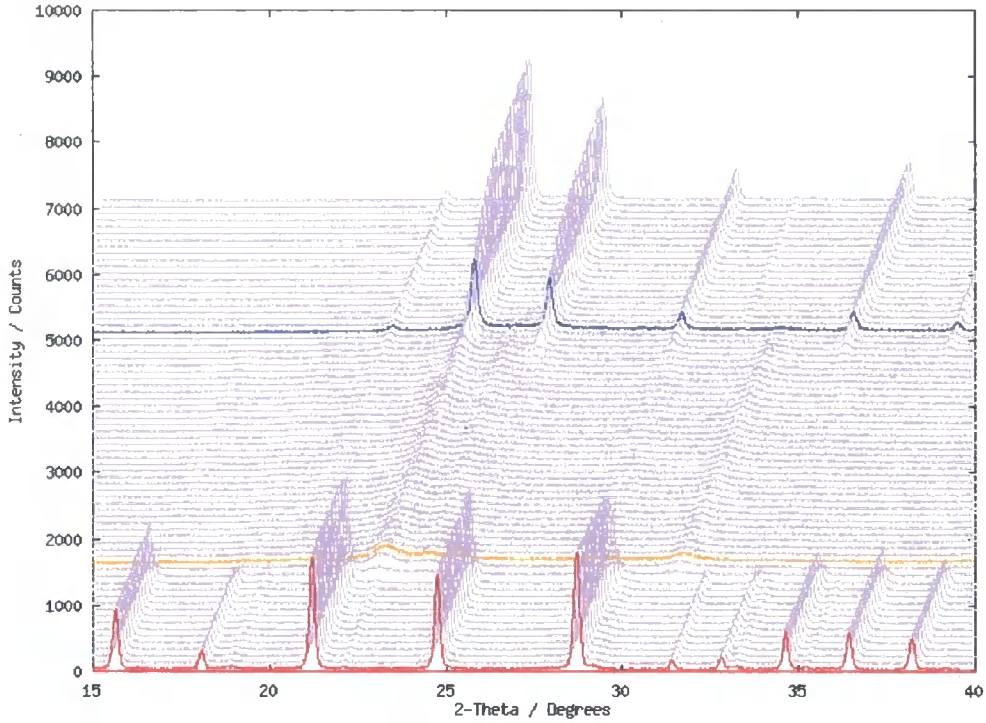

Figure 2.27. X-ray diffraction patterns (d8_01536) every 10 K between 308 – 998 K showing the *in situ* dehydration products of $ZrW_2O_7(OH)_2(H_2O)_2$ (NRW017b): LT-ZrW_2O_8 and cubic ZrW_2O_8.

The figure indicates the absence of a trigonal polymorph of ZrW_2O_8, in contrast to $ZrMo_2O_8$ and $HfMo_2O_8$. Indeed it has been mentioned in Chapters 1 and 5 that this phase is only observed *via* a sol-gel type synthesis. A large region in which the cubic phase is stable exists instead. Above 1000 K (not shown) decomposition to WO_3 and ZrO_2 occurs. An LT polymorph seems to exist here although visual comparison to the $ZrMo_2O_8$ and $HfMo_2O_8$ VT data (Figures 2.1 and 2.20) show that LT-ZrW_2O_8 seems to be even less crystalline - almost amorphous. Neutron data were not collected upon a sample of LT-ZrW_2O_8. It was found, however, that using the atomic coordinates and spherical harmonic obtained from the neutron diffraction of, *e.g.* LT-$HfMo_2O_8$, would give a reasonable fit to the X-ray data. These parameters were used in the Rietveld refinement of the above set of VTXRD patterns.

A simplified *TOPAS* seed refinement file consisting of 25 variables was used to model the temperature dependence of the phase evolution in d8_01536. The following were refined: 14 global parameters (12 background terms, a sample height correction and a single temperature factor), 4 variables for the precursor (a histogram scale factor, two

lattice parameters, one peak profile term), 4 for LT (a scale factor, three cell edges (the pseudo-Voigt peak shape was fixed)) and 3 for cubic ZrW_2O_8 (a scale factor, a cubic cell parameter and one peak profile term). See the e-Appendix for the complete file. The refinement was repeated at each temperature from 308 to 998 K and the phase fractions extracted to give the plot in Figure 2.28 (see the e-Appendix for the relevant *Excel* sheet).

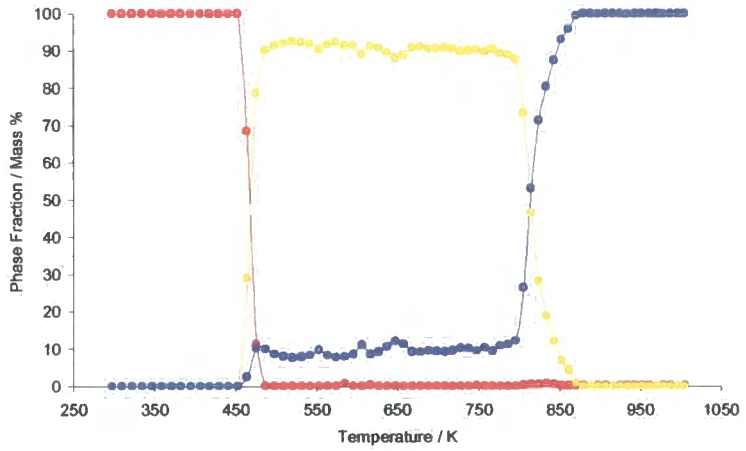

Figure 2.28. The phase fraction of $ZrW_2O_7(OH)_2(H_2O)_2$ and its dehydrated products, LT-ZrW_2O_8 and cubic ZrW_2O_8, every 20 K between 303 and 983 K (d8_01536, NRW017b).

It seems that $ZrW_2O_7(OH)_2(H_2O)_2$ possesses a slightly greater thermal stability than any of the other $AM_2O_7(OH)_2(H_2O)_2$ phases considered in this chapter. Figure 2.28 shows that the precursor is stable up to 453 K whereas the others decompose at ~ 400 K. LT-ZrW_2O_8 exists over the widest temperature range of any LT phase studied; it exists as a pure phase between 487 and 795 K. The refined ~ 10% phase fraction of cubic ZrW_2O_8 between these temperatures is misleading; it is difficult to accurately fit the extremely broad peaks LT phase in these rapid diffraction patterns, more so here than in the previously described cases. The LT to cubic transformation begins at ~ 795 K.

Figure 2.28 clearly shows a low temperature route to pure cubic ZrW_2O_8; annealing the precursor between 870 and 1000 K will give the pure cubic phase. Contrast this to the classically high temperature route where temperatures of around 1400 K are required. This was actually noted in an *ex situ* study by Closmann and co-workers in 1998 who calcined $ZrW_2O_7(OH)_2(H_2O)_2$ at various temperatures.[29] They reported that calcinations

below 873 K gave an amorphous product (actually the LT form) and that pure cubic ZrW_2O_8 could be prepared upon annealing at 973 K for 10 hours.

The rehydration properties of LT-ZrW_2O_8 were also investigated; hydrothermal treatment of LT-ZrW_2O_8 (a grey powder) with water at 373 K overnight did not result in rehydration back to the precursor phase. However, heating at 443 K for 40 hours gave a white powder and full rehydration was confirmed by X-ray diffraction. Of the three LT phases considered in this chapter, LT-ZrW_2O_8 was the most inert to rehydration. In contrast to LT-$ZrMo_2O_8$, there was no evidence to suggest that LT-ZrW_2O_8 would spontaneously rehydrate under ambient conditions at room temperature; even after one year there was no change in the identity of its powder pattern.

2.5 Conclusion

The main conclusion of this chapter is that the cubic phase of AM_2O_8 (A = Zr, Hf; M = Mo, W) can only be prepared from the $AM_2O_7(OH)_2(H_2O)_2$ precursor *via* LT-AM_2O_8, a "low-temperature" intermediate. Lind *et al.* noted this as an experimental observation,[10] whereas the *ex situ* preparation and a full structural characterisation of LT-AM_2O_8 as well as its mechanistic role in the precursor-cubic transformation have been described in this work.

The structure of this new family of orthorhombic LT-AM_2O_8 materials has been solved by combined neutron and X-ray powder diffraction. Extensive anisotropic strain exists within these materials and has been modelled with spherical harmonics. The directionality of the strain has been related to the relative magnitude of polyhedral rearrangements that occur during the low-temperature (~ 400 K) dehydration of the precursor.

Orthorhombic LT-AM_2O_8 phases are metastable and rehydrate back to $AM_2O_7(OH)_2(H_2O)_2$ hydrated precursors, enabling the re-conversion of LT-$ZrMo_2O_8$ to "$ZrMo_2O_7(OD)_2(D_2O)_2$". This allowed regular O, hydroxy O, and aquo O atoms of the precursor to be distinguished. A topotactic dehydration mechanism was subsequently suggested. Orthorhombic LT phases also display negative thermal expansion like their

cubic analogues and share some similarity in selected portions of their structures. Both the LT and cubic AM_2O_8 structures are comprised of corner-sharing distorted MO_4 tetrahedra and AO_6 octahedra. Portions of the structure of the cubic phase are basically preformed in the LT intermediate. This explains why the cubic phase forms directly from the LT phase in preference to the thermodynamic trigonal polymorph of $ZrMo_2O_8$, the formation of which requires more drastic structural rearrangements.

In situ variable temperature powder X-ray diffraction and quantitative Rietveld refinements have been used to follow the decomposition paths of $AM_2O_7(OH)_2(H_2O)_2$ precursors to various AM_2O_8 polymorphs up to ~ 1000 K. New preparative routes to cubic and trigonal AM_2O_8 phases *via* their hydrated precursors have been observed and are employed in Chapters 3 (cubic AMo_2O_8) and 5 (trigonal $HfMo_2O_8$).

2.6 References

1. T. A. Mary, J. S. O. Evans, T. Vogt, A. W. Sleight, *Science*, **272**, 1996, 90-92.
2. J. S. O. Evans, T. A. Mary, T. Vogt, M. A. Subramanian, A. W. Sleight, *Chem. Mater.*, **8**, 1996, 2809-2823.
3. J. Graham, A. D. Wadsley, J. H. Weymouth, L. S. Williams, *J. Am. Ceram. Soc.*, **42**, 1959, 570.
4. L. L. Y. Chang, M. G. Scroger, B. Phillips, *J. Am. Ceram. Soc.*, **50**, 1967, 211-215.
5. J. S. O. Evans, W. I. F. David, A. W. Sleight, *Acta Cryst.*, **B55**, 1999, 333-340.
6. J. D. Jorgensen, Z. Hu, S. Teslic, D. N. Argyriou, S. Short, J. S. O. Evans, A. W. Sleight, *Phys. Rev. B*, **59**, 1999, 215-225.
7. C. Lind, A. P. Wilkinson, Z. B. Hu, S. Short, J. D. Jorgensen, *Chem. Mater.*, **10**, 1998, 2335-2337.
8. A. Clearfield, R. H. Blessing, *J. Inorg. Nucl. Chem.*, **34**, 1972, 2643-2663.
9. J. S. O. Evans, P. A. Hanson, R. M. Ibberson, U. Kameswari, N. Duan, A. W. Sleight, *J. Am. Chem. Soc.*, **122**, 2000, 8694-8699.
10. C. Lind, A. P. Wilkinson, C. J. Rawn, E. A. Payzant, *J. Mater. Chem.*, **11**, 2001, 3354-3359.
11. N. R. Warmingham, M.Chem. Thesis, University of Durham, 2002.

12. J. W. Visser, *J. Appl. Cryst.*, **2**, 1969, 89-95.
13. A. A. Coelho, *TOPAS v2.0: General Profile and Structure Analysis Software for Powder Diffraction Data*, Bruker AXS, Karlsruhe, 2000.
14. Y. G. Andreev, P. G. Bruce, *J. Chem. Soc., Dalton Trans.*, 1998, 4071-4080.
15. A. A. Coelho, *J. Appl. Cryst.*, **33**, 2000, 899-908.
16. S. Kirkpatrick, C. D. Gelatt, M. P. Vecchi, *Science*, **220**, 1983, 671-680.
17. H. M. Rietveld, *J. Appl. Cryst.*, **2**, 1969, 65-71.
18. *Cerius^2 v3.8: Modelling and Simulation Environment for SG Systems*, Molecular Simulations Inc., San Diego, 1998.
19. M. Järvinen, *J. Appl. Cryst.*, **26**, 1993, 525-531.
20. *Maple v8.00: Mathematical Calculation Package for Unix Systems*, Waterloo Maple Inc., Waterloo, 2002.
21. X. Zhao, Q. Wang, H. Ma, *Chin. Res. Chin. Univ.*, **18**, 2002, 233-236.
22. V. N. Serezhkin, V. A. Efremov, V. K. Trunov, *Russ. J. Inorg. Chem*, **32**, 1987, 1568-1570.
23. I. D. Brown, D. Altermatt, *Acta. Cryst.*, **B41**, 1985, 244-247.
24. N. E. Brese, M. O'Keeffe, *Acta. Cryst.*, **B47**, 1991, 192-197.
25. G. S. Pawley, *J. Appl. Cryst.*, **14**, 1981, 357-361.
26. T. I. Loboda, V. I. Krivobok, M. V. Mokhosoev, *Russ. J. Inorg. Chem*, **23**, 1978, 1669-1671.
27. W. Freundlich, J. Thoret, *Compt. Rend. Acad. Sci. Paris*, **C265**, 1967, 96-98.
28. M. S. Dadachov, R. M. Lambrecht, *J. Mater. Chem.*, **7**, 1997, 1867-1870.
29. C. Closmann, A. W. Sleight, J. C. Haygarth, *J. Solid State Chem.*, **139**, 1998, 424-426.

Chapter Three: Study of the Order-disorder Phase Transition in Cubic AM_2O_8 Phases

3.1 Introduction

In 1996 the structure of cubic ZrW_2O_8 (Figure 1.3) and its property of negative thermal expansion (NTE; Figure 1.4) was reported by Evans and co-workers.[1,2] Considerable interest has arisen from their findings as a result of the fact that the material possesses the rare property of isotropic contraction over as large temperature range as 0.3 to 1050 K. Additionally, the material was reported to undergo a second-order phase transition at ~ 448 K.[3] Evans showed this was a continuous order-disorder transition in which the orientation of the WO_4 groups was randomised through an inversion-type motion (Figure 1.5). As a result, disordering of the terminal oxygen atoms occurred throughout the lattice, giving rise to substantial ionic mobility (Figure 1.7).[2] Further details are given in Chapter 1.

Other cubic materials in the $ZrW_{2-x}Mo_xO_8$ family have since been prepared to establish whether they show similar behaviour. For the three most-studied materials, $x = 0$,[1-3] 1,[4] and 2,[4,5] isotropic NTE is displayed throughout but interestingly, all seem to behave in a different manner with regard to the order-disorder phase transition. Such a transition in the material could limit its use as a component in composite materials. For example, failure of ZrW_2O_8-containing precision components could result if subject to temperatures above 448 K as the high-temperature β form possesses reduced expansion over the room-temperature α form (Figure 1.4). In this chapter, the phase transition is investigated in further detail for $ZrMo_2O_8$ and $ZrWMoO_8$, and is briefly revisited in ZrW_2O_8. A variety of variable temperature neutron and laboratory X-ray diffraction experiments have been devised to study the thermal expansion behaviour but also the kinetics of the order-disorder transition. In addition the thermal expansion of $HfMo_2O_8$ is studied for the first time for comparison to the behaviour shown by $ZrMo_2O_8$.

3.2 Cubic $ZrMo_2O_8$

3.2.1 Background

Cubic $ZrMo_2O_8$ was first prepared in 1998 by Lind and co-workers.[5] Chapter 1 provides more details of their findings but essentially, the material's thermal expansion was studied in 50 K intervals over an 11 – 573 K temperature range. An absence of any change of gradient in the lattice parameter versus temperature plot indicated isotropic negative thermal expansion and a lack of a second-order phase transition (Figure 1.8). It was thus concluded that only the centric, $Pa\bar{3}$ β-ZrW_2O_8 structure was adopted by $ZrMo_2O_8$ throughout the temperature range considered, in contrast to cubic ZrW_2O_8, which upon cooling converts to the acentric, $P2_13$ α polymorph at around 448 K. In 2000, Evans and co-workers subsequently investigated the thermal expansion of $ZrMo_2O_8$ in greater detail albeit on a sample that contained the trigonal polymorph as an impurity.[4] This impurity arose owing to the difficulty of preparing the pure cubic form before Lind's improved synthesis *via* the perchlorate-derived $ZrMo_2O_7(OH)_2(H_2O)_2$ precursor was reported in 2001.[6] Again the disordered $Pa\bar{3}$ β-ZrW_2O_8 structure appeared to be retained throughout. However, puzzling discrepancies between the values of the cell parameter on warming and cooling data were observed (Figure 1.9), *i.e.* thermal history of the sample seemed to play an important role in its thermal expansion properties. Further investigation on a pure sample is desirable and is reported in the following section.

3.2.2 Thermal Expansion Properties of $ZrMo_2O_8$

A large sample of pure cubic $ZrMo_2O_8$ was prepared by the dehydration of a $ZrMo_2O_7(OH)_2(H_2O)_2$ precursor. The precursor itself was prepared by Nick Warmingham from zirconyl perchlorate, ammonium *para*-molybdate and perchloric acid, as described in Section 7.2 (sample i.d. NRW036).[7] The optimal temperature to subsequently decompose the precursor and form pure cubic $ZrMo_2O_8$ without the co-crystallisation of the trigonal impurity was chosen following the quantitative *in situ* X-ray diffraction studies in Section 2.2.5, where the decomposition of the precursor and the evolution of dehydrated $ZrMo_2O_8$ phases were monitored from ~ 300 to 1000 K.

The sample was carefully dehydrated at 723 K as deemed suitable from Figure 2.11. The full conditions employed to prepare a ~ 13.8 g pure sample (i.d. SA97B) are outlined in Section 7.2.1.

Variable temperature (VT) neutron diffraction data were recorded on pure cubic $ZrMo_2O_8$ (SA97B) using the High Resolution Powder Diffractometer (HRPD) at the ISIS pulsed neutron source of the Rutherford Appleton Laboratory, UK. The aim was to obtain a detailed set of VT data to investigate any possible phase transition and also to ascertain any difference in thermal expansion trend between a quench-warmed and a slow-cooled sample as shown by cubic $ZrWMoO_8$ and $ZrMo_2O_8$ by Evans *et al.*.[4] 6.44 g of salmon pink/pale orange powder were packed into a rectangular (cadmium-shielded) aluminium slab can equipped with a heater cartridge, externally quenched from room temperature to 77 K in liquid nitrogen, placed in an AS Scientific Instruments cryofurnace and cooled to 2 K. VT data were obtained every 4 K from 2 K up to 502 K, for a count time of ~ 8.5 minutes (equivalent to 5 μA of beam current) plus a 2 minute equilibration interval, at each temperature. Data were then collected upon cooling the sample every 7 K from 502 to 12 K. The sample was held at 12 K for ~ 67 minutes, cooled to 3 K and data then collected every 1 K on re-warming up to 17 K. Diffraction data were recorded in three banks - 168 ° (back-scattering), 90 ° and 30 ° (low-angle). Back-scattering data were of higher precision and are discussed in detail. Results from other banks were consistent with this and are not presented. Back-scattering data were refined over the time-of-flight range of 39000 – 114000 μs. A Rietveld refinement was performed on the first rapid scan at 2 K (run # 24847) using the *TOPAS* suite of software (Section 6.1.11).[8,9] For all other temperatures, the above refinement was used as a seed and *MultiTOPAS* used to perform the remaining 213 refinements. 33 variables were refined for the back-scattering data set; nine background terms, a histogram scale factor, two peak shape parameters (FWHM and Lorentzian terms), a cubic cell parameter, two atomic fractional occupancy parameters (O(3) and O(4) modelled independently), eleven atomic fractional coordinates and seven isotropic temperature factors. The seed Rietveld refinement at 2 K is displayed in Figure 3.1. The full seed input file and the *Excel* spreadsheet displaying the temperature-dependence of the structural parameters are located in the Electronic Appendix (e-Appendix). Figure 3.2 displays the temperature dependence of the cubic cell parameter of $ZrMo_2O_8$ extracted from the spreadsheet.

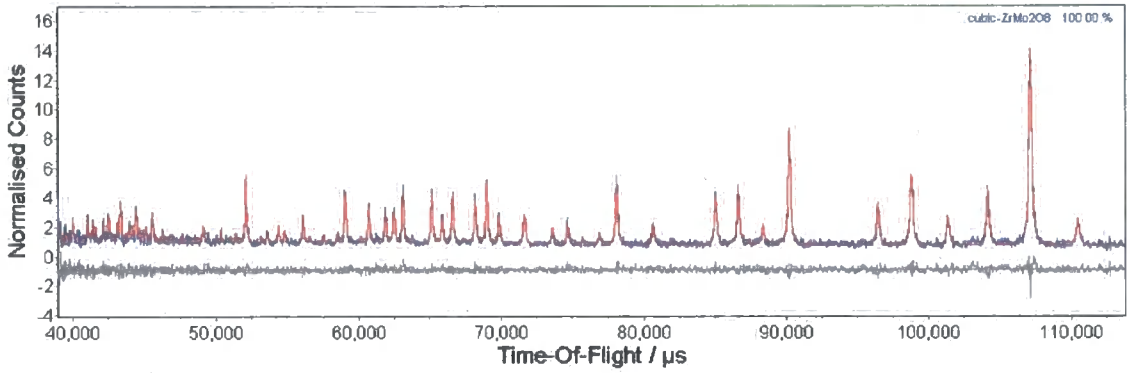

Figure 3.1. Seed back-scattering Rietveld refinement of the ~ 8.5 minute powder pattern of cubic $ZrMo_2O_8$ recorded on HRPD at 2 K (SA97B, run # 24847). Observed and calculated data are represented by the blue and red traces, respectively. The difference curve is shown in grey. The corresponding *d*-spacing range is 0.81 to 2.36 Å.

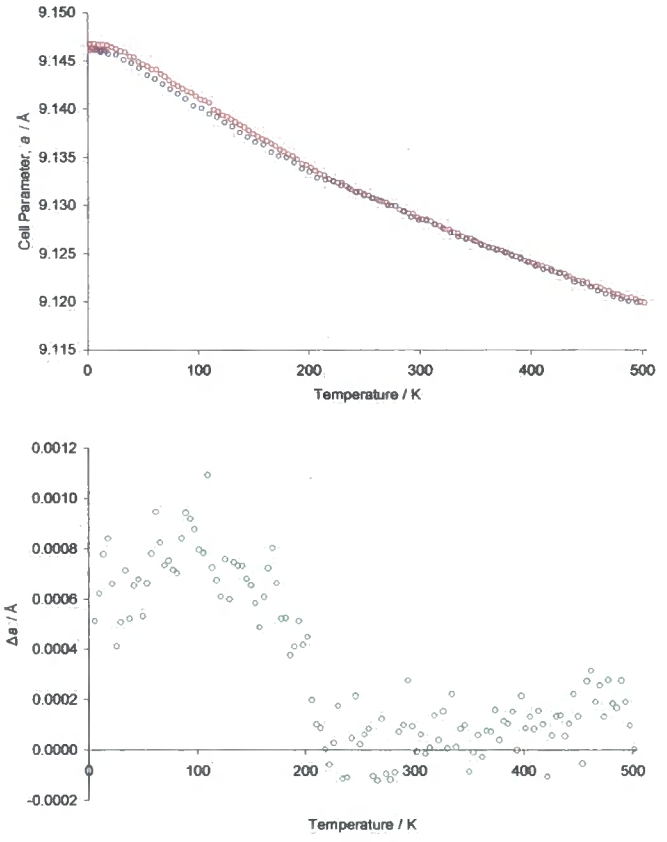

Figure 3.2. Refined lattice parameter of cubic $ZrMo_2O_8$ (SA97B) from back-scattering HRPD data (*top*); data were collected as the sample was initially quench-warmed from 2 to 502 K, cooled from 495 to 12 K and finally warmed from 3 to 17 K. Also shown is the excess cell parameter on warming over cooling as a function of temperature ($\Delta a(T)$, *below*).

No major discontinuity in the unit cell parameter of $ZrMo_2O_8$ over temperature is apparent in Figure 3.2. This is in contrast to ZrW_2O_8 and $ZrWMoO_8$, which exhibit

clear second-order phase transitions at 448 and 270 K (Figures 1.4 and 1.10), respectively. The data were refined using the disordered β-ZrW_2O_8-type model throughout; no evidence for the conversion to the ordered, α structure was present as shown by the oxygen fractional site occupancy plots in Figure 3.3, which remain close to ½ (disordered oxygen) throughout.

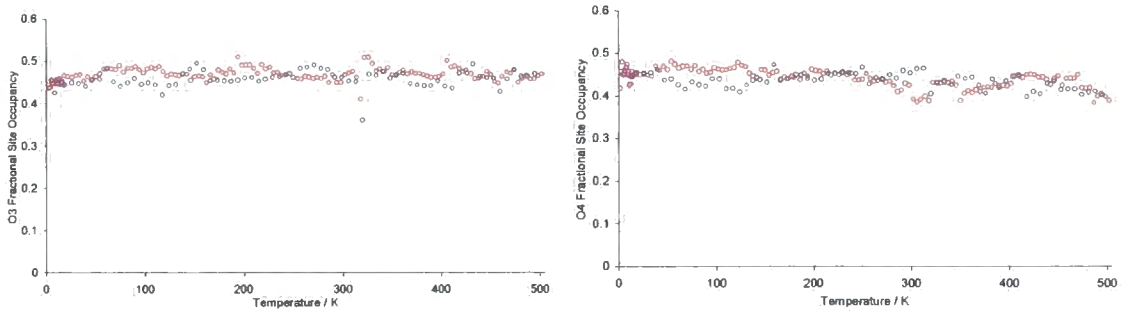

Figure 3.3. Site occupancy of O(3) and O(4) in $ZrMo_2O_8$: quench-warm, slow-cool and slow re-warm data.

If the ordered phase were to form, it would be envisaged that the fractional occupancy would rise from ~ ½ towards 1 (compare Figure 1.6). Instead the occupancies remain at ~ ½, implying the $Pa\bar{3}$ space group is correct throughout. Both Lind *et al.* and Evans *et al.* also concluded that the β structure was adopted, albeit with less comprehensive data. Close inspection of Figure 3.2 at $\leq$ 215 K, reveals a slight but significant discrepancy between the cell parameters of the quench-warmed and the slow-cooled sample. Rebinning of the warming and cooling data into 4 K steps and plotting the discrepancy, Δa in the lower part of Figure 3.2 confirms this. On average, the discrepancy is 0.00072 Å below 150 K compared to less than 0.00009 Å above 250 K. The quench-warmed sample has a slightly larger lattice parameter than a subsequently slow-cooled sample. It is worth noting that the final data collected shown in Figure 3.2 were between 3 and 17 K, and these lie on the lower curve. This reinforces the difference between the thermal expansion properties of a quenched sample and a slow-cooled/re-warmed sample. If an order-disorder phase transition was apparent at ~ 215 K, it might be expected that the slow-cooled sample would have a larger unit cell than when it is quenched, as found for $ZrWMoO_8$. However, the hysteresis is in the opposite direction for $ZrMo_2O_8$. Table 3.1 shows the calculated cell parameters at 0 K, a_0 and linear expansion coefficients, α_l for the quenched and slow-cooled samples versus literature values. The a_0 cell parameters were calculated by fitting the warming and cooling data

(in Figure 3.2) to the Einstein model of thermal expansion, as in Equation 3.1, which is a specific case of the general expression given in Equation 1.7.[10]

$$\ln a_{calc} = \ln a_0 + \frac{c_1\theta_1}{\exp(\theta_1/T)-1} + \frac{c_2\theta_2}{\exp(\theta_2/T)-1} \qquad (3.1)$$

The second term on the right hand side of Equation 3.1 describes the contribution to the negative thermal expansion by low-energy transverse vibrations; the third term models the positive thermal expansion that arises from "normal" lattice vibrations. The Einstein temperatures θ_i and c_i constants were refined and are displayed in Table 3.1; the corresponding fits are shown in Figure 3.4 (and in an *Excel* spreadsheet in the e-Appendix).

	$ZrMo_2O_8$, quench-warmed	$ZrMo_2O_8$, slow-cooled
a_0 / Å	9.14677 (5)	9.14623 (3)
c_1 / × 10^{-7} K^{-1}	–88.8 (14)	–91.8 (20)
θ_1 / K	67 (4)	62 (4)
c_2 / × 10^{-7} K^{-1}	53.4 (9)	49.2 (20)
θ_2 / K	709 (25)	518 (25)

Table 3.1. Coefficients used to model the thermal expansion of cubic $ZrMo_2O_8$ obtained from neutron diffraction data shown in Figure 3.2. The constants, c_i are a combination of the isothermal compressibility, Grüneisen parameters, density of states and volume of the material. The Einstein temperatures are defined as $\theta_i = h\upsilon_i/k_B$.

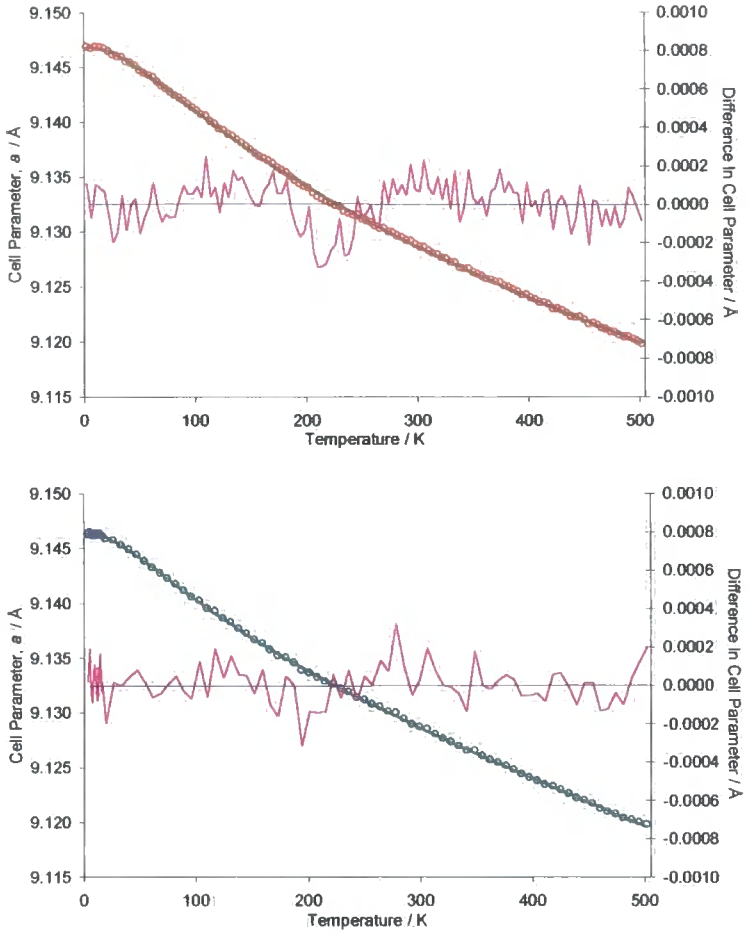

Figure 3.4. Fitting of the quench-warmed (*above*) and slow-cooled/re-warmed (*below*) $ZrMo_2O_8$ cell parameter data using the parameters in Table 3.1 and Equation 3.1. Calculated data for each are shown as the green bold line and the difference curve in pink.

	Cell parameter a_0 / Å	α_l / × 10^{-6} K^{-1}	α_l / × 10^{-6} K^{-1}
SA97B, quench-warm	9.14677	–7.9 (42 – 210 K)	–5.0 (214 – 494 K)
Evans, quench-warm	9.14820	–7.8 (0 – 450 K)	
SA97B, cool	9.14623	–7.6 (201 – 40 K)	–5.0 (488 – 208 K)
Evans, cool	9.14721	–7.6 (300 – 0 K)	

Table 3.2. Calculated cubic cell parameters at 0 K and mean linear expansion coefficients (over applicable temperature ranges) $\alpha_l = (a_T - a_0) / a_0(T - T_0)$, for samples of $ZrMo_2O_8$ in this neutron diffraction study and from the literature.

Linear expansion coefficients, α_l were calculated at each temperature using the warming and cooling HRPD cell parameters as shown in Figure 3.5, while mean values are

shown in Table 3.2. The full analysis is given in the cell fitting spreadsheet located in the e-Appendix.

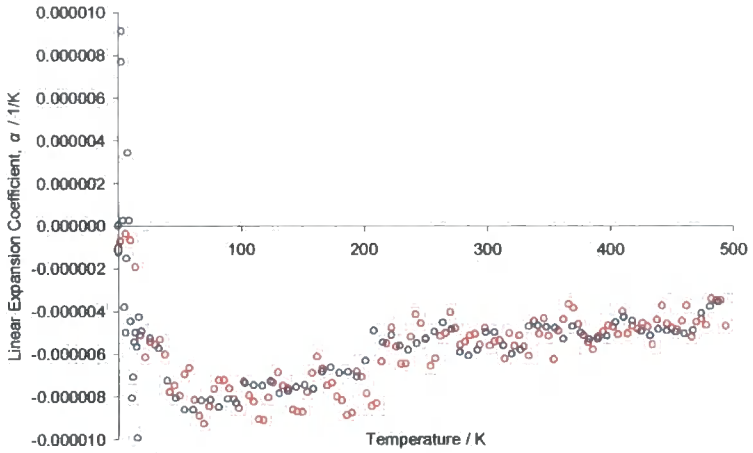

Figure 3.5. Linear expansion coefficients as a function of temperature upon quench-warming and slow-cooling/re-warming cubic $ZrMo_2O_8$. The values were determined from the gradient at each point in Figure 3.2 (*top*) using 5 values around each point.

Reduced expansion above ~ 215 K is apparent from Figure 3.5 shown by the smaller magnitude of the α_l values determined for this work. The discontinuity in α_l at ~ 215 K seems consistent with a second-order phase transition. The α_l values below ~ 215 K are similar to those quoted by Evans *et al.* although an average value over the whole temperature range was given in their case. The actual differences in the α_l values between the quench-warmed and slow-cooled cases are minimal.

It is inferred that the discrepancy in the cell parameters observed and the change in thermal expansion around 215 K is again related to oxygen disorder in the material. The lack of a more pronounced discontinuity in the cell parameter trend shared by other members of the $ZrW_{2-x}Mo_xO_8$ family, suggests that perhaps 215 K is too low a temperature for ordering to fully occur. Presumably the sample would "prefer" to convert to the ordered, α-ZrW_2O_8 structure type but there is insufficient thermal energy to order the oxygen atoms at this temperature. However, at higher temperatures *e.g.* 250 K where there is enough energy in the system, the disordered β–ZrW_2O_8 structure type is the stable form.

The low "phase transition" temperature observed in $ZrMo_2O_8$ of ~ 215 K is consistent with the empirical observation that in the cubic $ZrW_{2-x}Mo_xO_8$ family of materials, the introduction of Mo into the lattice lowers the α to β phase transition temperature; the trend being, ZrW_2O_8 (448 K), $ZrW_{1.6}Mo_{0.4}O_8$ (393 K), $ZrWMoO_8$ (270 K) and $ZrMo_2O_8$ (215 K). However, whilst no α to β transition is apparent in $ZrMo_2O_8$ from the data, the clear discrepancy in cell parameters at 215 K and the corresponding change in gradient of the thermal expansion provides strong evidence for some structural transition at this point. By analogy with other materials it is suggested that this is a change from statically to dynamically disordered oxygen ions upon warming. The two different cell parameter trends for the quenched and slow-cooled sample suggest two slightly different static disordering relationships for the oxygen atoms in the structure.

A possible explanation for the lowering of the ordering temperature with increasing Mo content can be made through simple electrostatic arguments. In an extreme view one could consider the Madelung potential of O···O electrostatic repulsions as being a significant driving force for oxygen ordering in these materials. Owing to the greater electronegativity of Mo relative to W,[11] Mo–O bonds will have lower ionic character than W–O. As a consequence, neighbouring apical O(4)···O(4) repulsions will be reduced with increasing Mo content, and Mo-rich cubic AM_2O_8 phases will tend to order at lower temperatures than their W-rich analogues. The actual phase transition temperature is presumably determined by competing electrostatic, and entropic (as well as other) contributions, which drive ordering and disordering, respectively.

Only the extremely high precision of cell parameters determined on HRPD (Rietveld ESD of 0.00001 Å) permits the above cell parameter discrepancy to be observed. A slow-cooling diffraction experiment was also carried out on $ZrMo_2O_8$ (SA97B) using laboratory X-ray equipment. A Bruker d8 diffractometer equipped with an Oxford Cryosystems PheniX cryostat (which cannot perform rapid quenches; only slow cooling experiments) was used to collect 30-minute diffraction patterns between 300 and 17 K at a rate of 5 Khr^{-1}, in the range of 10 – 100 ° 2θ (run # d8_01721; details of laboratory diffraction methods are outlined in Section 6.1). A *TOPAS* seed file was set up with the following 54 independent parameters for variable temperature Rietveld refinement: twelve terms to model the background profile, a sample height correction, histogram scale factor, cubic cell parameter, six pseudo-Voigt (PV) peak profile coefficients, a

fractional site occupancy parameter, eleven fractional atomic coordinates and seven isotropic temperature factors, for $ZrMo_2O_8$. For the aluminium sample holder, a Pawley fit was employed to model the data,[12] using a separate height correction, cubic cell parameter, six PV peak terms and six parameters to model the intensity under the six Bragg peaks due to Al. The seed input file and spreadsheet containing full *MultiTOPAS* results are presented in the e-Appendix; the laboratory-determined temperature variation of the cell parameter is given in Figure 3.6.

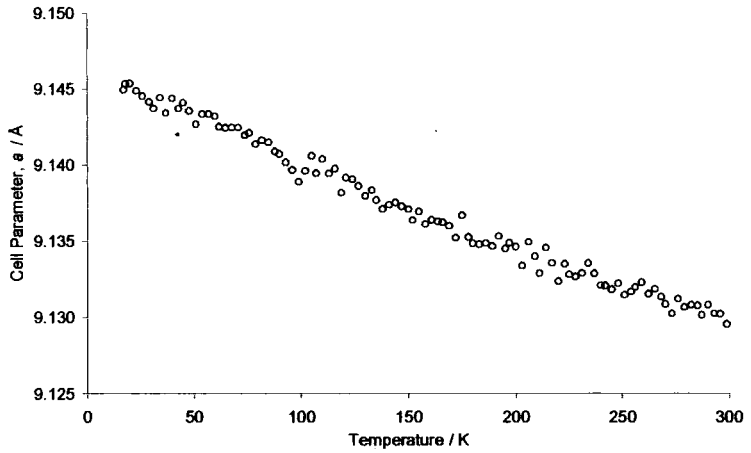

Figure 3.6. Variation of cubic lattice parameter with temperature for $ZrMo_2O_8$ (SA97B), refined from data collected on a laboratory based X-ray diffractometer and cryostat.

The main point to notice in Figure 3.6 is the relatively large amount of scatter in the data compared to Figures 3.2 or 3.4. Error bars (not shown in the plots) are artificially small; typical ESDs were smaller than the size of the actual data points as calculated from Rietveld refinement. The larger scatter in the X-ray data implies that even if a quench-warm experiment could be performed in the laboratory it is very doubtful the discrepancy between slow cooling and quench-warming determined using HRPD could be resolved.

3.3 Cubic $HfMo_2O_8$

Lind *et al.*, using an analogous preparation of $ZrMo_2O_8$, briefly mentioned the synthesis of cubic $HfMo_2O_8$ in 1998.[5] The thermal expansion of this material, however, has not been reported although its pressure-dependent behaviour was investigated in 2001.[13] Bearing in mind the similar nature of Hf and Zr compounds, it was interesting to see

whether or an order-disorder transition would be observed in $HfMo_2O_8$, compared to $ZrMo_2O_8$ in Section 3.2. *In situ* diffraction studies on the decomposition of $HfMo_2O_7(OH)_2(H_2O)_2$ showed pure cubic $HfMo_2O_8$ as the only phase observed between 718 and 757 K (Figure 2.23). *Ex situ* synthesis thus proved to be relatively straightforward at 723 K; full details of the synthesis of sample SA93A are provided in Section 7.3.2. A yellow powder was obtained, sprinkled on a silicon wafer and its purity checked at room temperature using a Siemens d5000 powder diffractometer. A 14-hour diffraction pattern between 10 and 120 ° 2θ was collected (machine details given in Section 6.1.9). Figure 3.7 shows the results of the Rietveld refinement performed. The *TOPAS* input file can be found in the e-Appendix. The following 41 variables were refined: an axial divergence parameter for the d5000, twelve background terms, a sample displacement correction, histogram scale factor, cubic lattice parameter, fractional occupancy parameter, six pseudo-Voigt peak shape coefficients, eleven independent atomic coordinates and seven isotropic temperature factors.

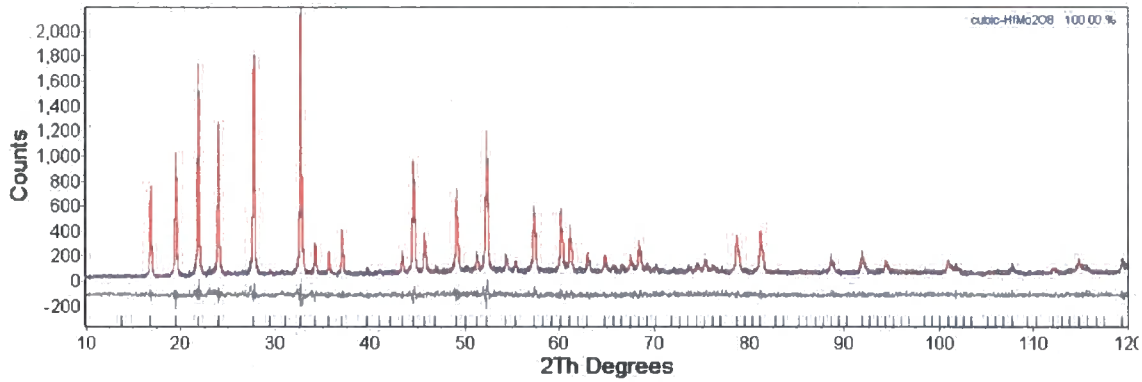

Figure 3.7. Room temperature Rietveld refinement of cubic $HfMo_2O_8$ (SA93A, d5_03043). A trace amount of trigonal $HfMo_2O_8$ is present as shown by the peak at ~ 23.0 ° 2θ.

The initial refinement model was based on the high-temperature, oxygen disordered, β form of $ZrMo_2O_8$ *i.e.* using the space group $P2_13$ and a fractional occupancy of ½ to mimic $Pa\bar{3}$. The final fit of $HfMo_2O_8$ required only a small adjustment in cell parameters and atomic positions from those of $ZrMo_2O_8$. The cell parameter refined to 9.10108 (13) Å. As was the case with the LT-AMo_2O_8 polymorphs (A = Zr, Hf) in Chapter 2, the cell parameter of (cubic) $HfMo_2O_8$ is slightly smaller than that of its Zr analogue *e.g.* by neutron diffraction in Section 3.2, $a(ZrMo_2O_8)$ = 9.12839 (1) Å at

299 K for a slow-cooled sample. The fractional occupancy parameter (*frac*) refined to 0.49 (4) confirming the β-ZrW_2O_8 structure was adopted at room temperature.

Initial variable temperature X-ray diffraction experiments were carried out on a Bruker d8 diffractometer with an Anton Paar TTK450 cryofurnace to look for possible oxygen ordering in this material. 30-minute diffraction patterns were recorded on a sample of cubic $HfMo_2O_8$ (SA93A) at 10 K intervals from 620 to 90 K, between 15 and 70 ° 2θ with a heat rate of 0.2 Ks^{-1} between each range. 50 variables were used in the *TOPAS* seed refinement at "620 K" (actual temperature corrected by the calibration polynomial given in Section 6.1.4 being 530 K), the input file of which is given in the e-Appendix. The same variables were used as for the d5000 refinement except that only five temperature factors were refined (three metals, terminal O and bridging O) and atoms were restrained to maintain a stable refinement since the data quality was not as high in these rapid scans. Also eleven variables were used to describe the diffraction due to the Al sample holder, giving a total of 50 independent variables. The temperature dependence of the most important parameters are given in a spreadsheet in the e-Appendix, while Figure 3.8 shows the trend in cell parameter as a function of temperature compared to that of $ZrMo_2O_8$.

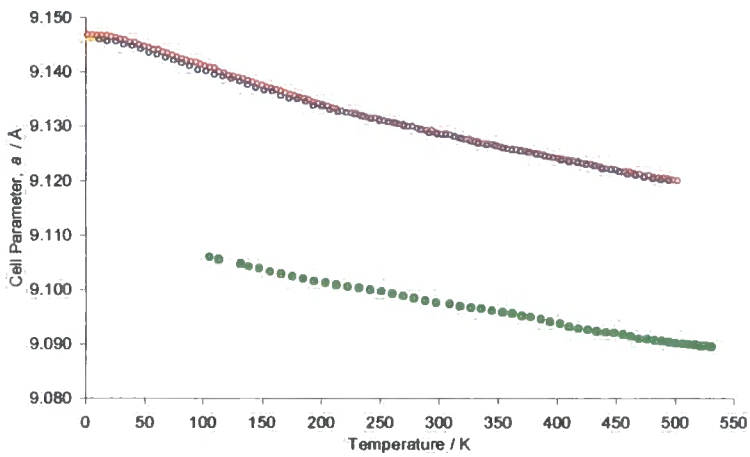

Figure 3.8. Negative thermal expansion in cubic $HfMo_2O_8$ (closed points; SA93A, lab X-ray, d8_01676) and $ZrMo_2O_8$ (open points; SA97B, HRPD neutron). Set temperatures for $HfMo_2O_8$ have been back-calibrated using the polynomial obtained using an α-Al_2O_3 standard, required since the sample temperature in the cryofurnace is low by ~ 90 K at ~ 620 K (Section 6.1.4).

The essentially linear contraction shown by $HfMo_2O_8$ in Figure 3.8 implies the lack of an order-disorder transition over this temperature range in this material. The mean expansion coefficient is -4.2×10^{-6} K^{-1}, slightly smaller in magnitude than that of the Zr analogue above 215 K (Table 3.2 and Figure 3.5). No change in gradient is apparent for $HfMo_2O_8$ but the precision of the data is probably an order of magnitude less than that of the HRPD $ZrMo_2O_8$ data.

3.4 Cubic $ZrWMoO_8$

3.4.1 Background

Cubic $ZrWMoO_8$ was prepared by Closmann *et al.* in 1998,[14] and its thermal expansion behaviour investigated *via* a neutron diffraction study by Evans *et al.* in 2000.[4] Their work is outlined in Chapter 1; the order-disorder transition was observed at 270 K and a value for the activation energy of the α to β phase transition derived. The kinetics of the α to β (oxygen ordering) phase transition are further investigated here by novel "quench-anneal" X-ray diffraction experiments as a function of temperature, and also by "quench-warm" experiments as a function of warming rate.

3.4.2 Quench-anneal Experiments on $ZrWMoO_8$

Multiple quench-anneal (*i.e.* quench-hold) experiments were performed upon cubic $ZrWMoO_8$ using a Bruker d8 powder X-ray diffractometer equipped with an Anton Paar TTK450 cryofurnace. The aim was to take a sample of disordered, high-temperature β-$ZrWMoO_8$ and rapidly quench the structure to low temperature and monitor the conversion back to the thermodynamically stable α phase using a continuous series of rapid diffraction data collections at that temperature. The β to α transition was then monitored as a function of time, at different anneal temperatures. In this way it was possible to gain further kinetic information of the phase transition. Table 3.3 gives details of the quench-anneal runs performed. The sample of $ZrWMoO_8$ employed was the same as that used by Evans in the HRPD neutron study in 2000.[4] To eliminate effects due to sample hydration the material was heated to 473 K for 2 hours prior to each experiment. The sample was sprinkled onto an Al plate coated with

Vaseline (for adhesion). The sample was held under vacuum for around 2 weeks in the TTK450 cryofurnace as multiple quench-anneal experiments were performed. The Al sample holder was sufficiently covered to not give rise to its own diffraction pattern and thus could be ignored in the analysis.

Anneal temp. / K	Run #	Number of scans
205	d8_01798	92
210	d8_01795	106
215	d8_01790	97
220	d8_01792	80
225	d8_01794	75
230	d8_01791	85
235	d8_01789	73
240	d8_01788	95
245	d8_01786	100
250	d8_01785	89

Table 3.3. Details of laboratory X-ray diffraction quench-anneal experiments on $ZrWMoO_8$.

An infinite number of 13-minute scans between 15 and 70 ° 2θ (step size of 0.0144 °) were programmed into the cryofurnace controller software. The actual number of scans shown in Table 3.3 was limited by the amount of liquid nitrogen consumed by the cryofurnace, which varied slightly from run to run. Figure 3.9 shows *e.g.* the 75 diffraction patterns obtained for the 225 K anneal.

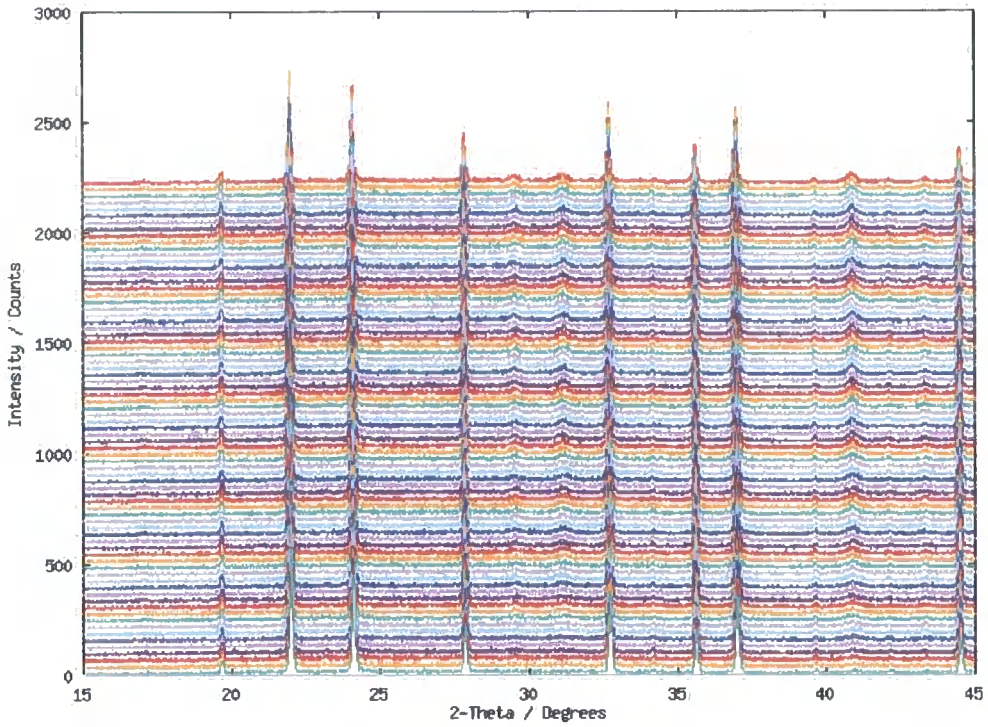

Figure 3.9. A plot of the 75 successive 13-minute diffraction patterns performed on quenched β-$ZrWMoO_8$ held at 225 K (d8_01794), with increasing time from the base to top of the figure. Peaks evolving at ~ 17.1, 29.5, 31.1 and 40.8 ° 2θ are due to the formation of the α phase.

Evolution of the lower symmetry $P2_13$ α-$ZrWMoO_8$ from the disordered, quenched β phase can be seen in Figure 3.9 by a new set of broad Bragg peaks: the (*111*) at ~ 17.1 ° (very weak), (*221*) at ~ 29.5 °, (*301*) at ~ 31.1 ° and (*401*) at ~ 40.8 ° 2θ. *TOPAS* was used in peak fitting mode to fit the intensity under these four peaks with respect to time. The ten seed *TOPAS* input files set up for peak-fitting are displayed in the e-Appendix (a sample input file is also given in Appendix A2.1). Two sets of pseudo-Voigt (PV) profile functions were required to describe both the sharp and the broad peaks. 13 sharp peaks, common to both the α and β phases, were fitted between the range 15 to 46.5 ° 2θ to check that they did not vary significantly during the course of the β to α conversion. 34 variables were refined in total: a sample height correction, twelve Chebyshev background terms, a cubic cell parameter (from which peak positions were calculated), one PV peak shape term to describe the FWHM for the broad peaks, two PV terms for the FWHM of the sharp peaks and seventeen parameters to describe the intensity under the Bragg reflections in the 2θ range considered. Figure 3.10 shows a fit of the final (75^{th}) range of the 225 K measurement.

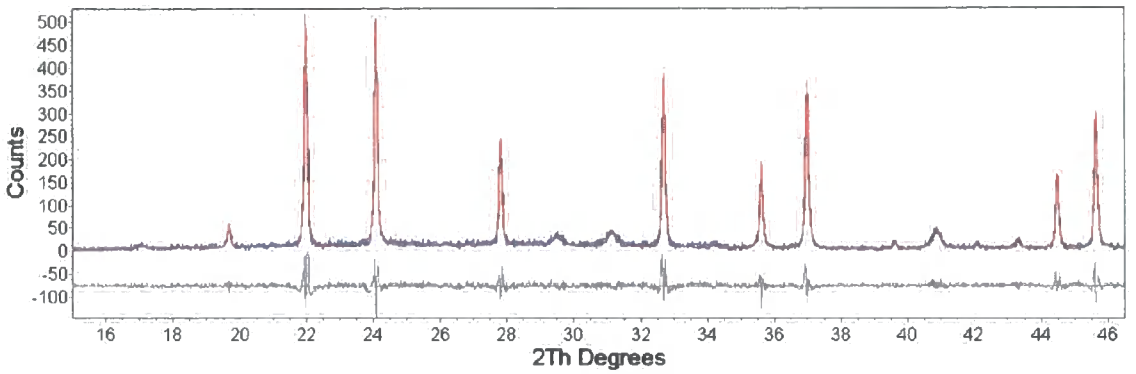

Figure 3.10. *TOPAS* peak fit of the final range of the 225 K anneal of $ZrWMoO_8$ (d8_01794:75). The broad α peaks at ~ 17.1, 29.5, 31.1 and 40.8 ° 2θ are modelled using a separate function to the remaining peaks. The observed trace is shown in blue, calculated trace in red and difference in grey.

Peak-fitting refinements were performed for each data set as a function of time and tabulated. Individual intensities of the four broad peaks followed similar trends with time and were thus summed, which reduced the scatter in individual data points. The summed intensity as a function of time was fitted using an exponential rise to a maximum function, $I = a(1-exp(-k_T t)) + c$, where a is a scale factor, c is an intensity offset parameter, k_T is the rate constant and t is time in seconds. The experimental time was extracted from the diffractometer *raw* file by conversion to *uxd* format using the *XCH* exchange program,[15] and processing with *Multirange*.[16] *Sigmaplot* was used for curve fitting to obtain standard errors of the curve fitting parameters. The e-Appendix gives the refined intensity versus time data in *Excel* format and the *Sigmaplot* curve fitting data are displayed in Figure 3.11 and Table 3.4.

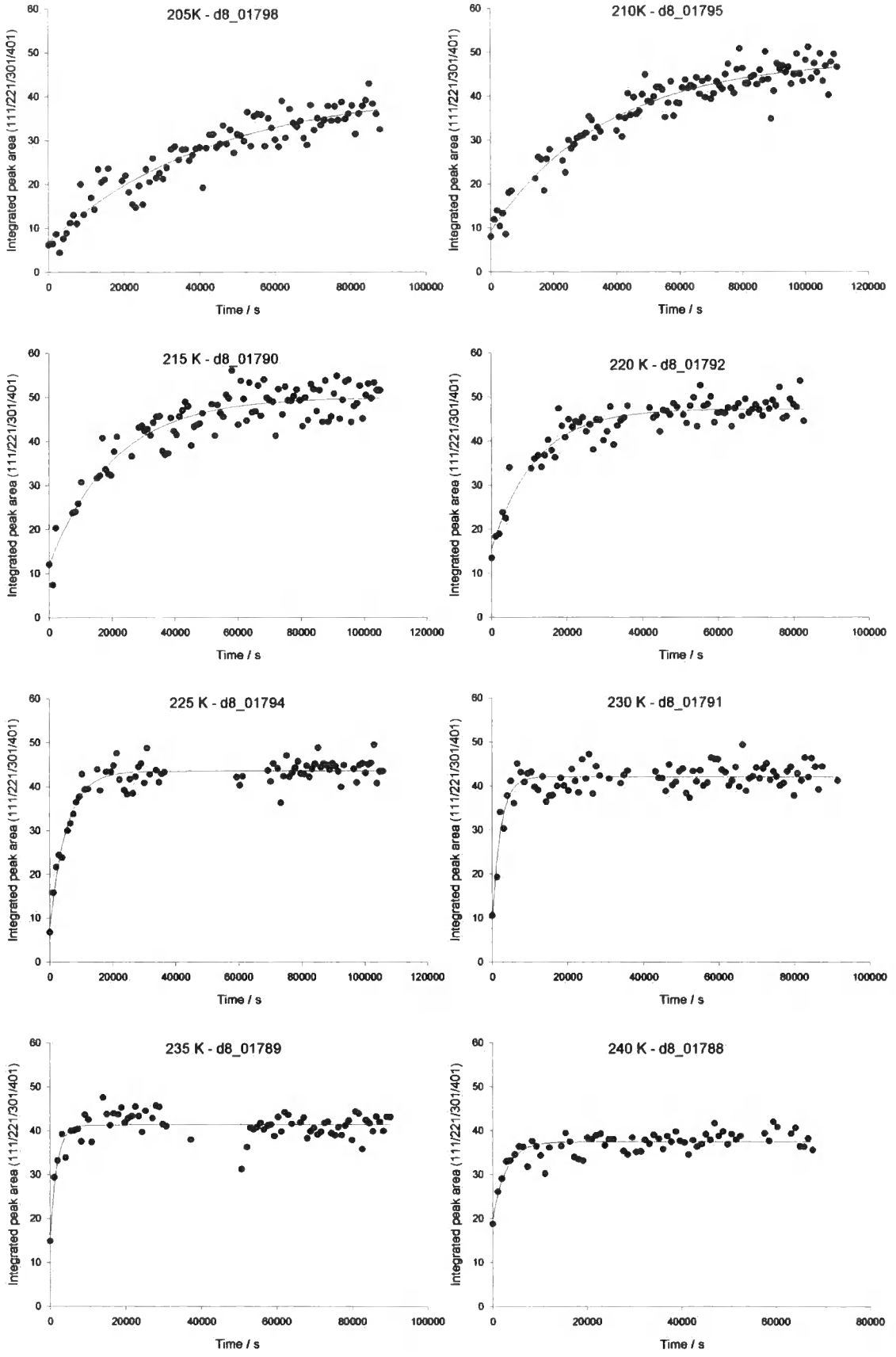

Figure 3.11. Evolution of the summed intensity of the (*111*), (*221*), (*301*) and (*401*) reflections due to the α cubic form of $ZrWMoO_8$ upon annealing at 205 – 240 K. Rate constants obtained from the curve fitting (solid lines) are located in Table 3.4.

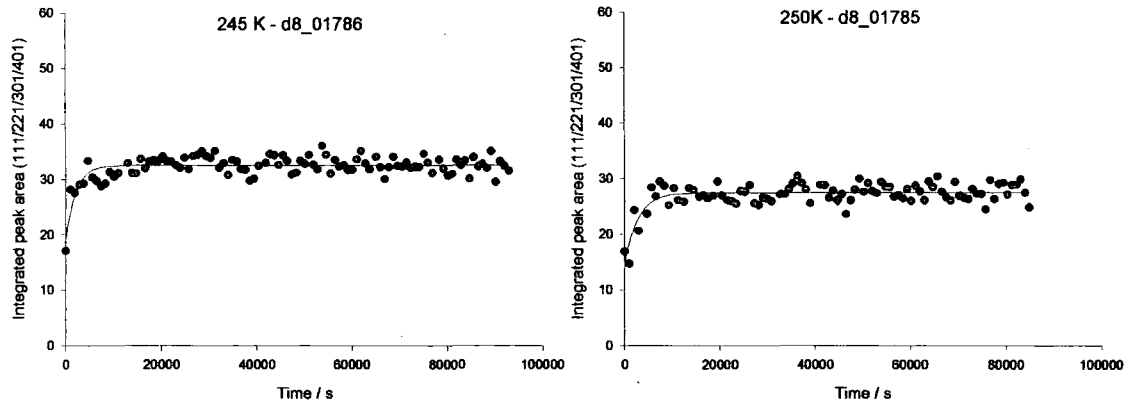

Figure 3.11 (cont). Evolution of the summed intensity of the (*111*), (*221*), (*301*) and (*401*) reflections due to the α cubic form of $ZrWMoO_8$ upon annealing at 245 and 250 K.

The kinetic data plots in Figure 3.11 show the increasing rate at which the α phase forms from the β phase, with increasing temperature. At the lowest temperature considered (205 K) the β to α conversion is slow; a plateau of intensity of the evolving peaks is never observed even after one day of holding at the sample at this temperature. At 230 K and above the reaction is sufficiently rapid to be essentially complete within the first few scans (*e.g.* the reaction is complete within an hour at 240 to 250 K). Figure 3.11 reveals large interruptions between some of the data points; this is an intermittent problem that unfortunately exists with the cryofurnace/diffractometer control software although none of the early, rate-determining data were affected.

Anneal temp. / K	k_T / × 10^{-4} s^{-1}
205	0.231 (37)
210	0.273 (27)
215	0.485 (44)
220	0.854 (71)
225	1.88 (16)
230	4.45 (58)
235	5.67 (107)
240	3.53 (63)
245	4.83 (84)
250	3.56 (71)

Table 3.4. Rate constants, k_T at each temperature determined using *Sigmaplot* to curve fit the data given in Figure 3.11 with the first-order expression, $I = a(1-\exp(-k_T t)) + c$. Errors are shown in parentheses.

The rapid reaction rate at 230 K and above mean there are few data points obtained that actually lie on the initial part of the curve hence the rate constants obtained are unreliable. For the Arrhenius plot shown in Figure 3.12 (*right*), only data between 205 and 225 K were used. Higher temperature data did not lie on the same straight line as the lower temperature data (sub-225 K; Figure 3.12, *left*). The approximate activation energy for the β to α transition can be found from the gradient of the line of best fit; the value calculated from Figure 3.12 (*right*) is ~ 41 (8) $kJmol^{-1}$. The associated error was calculated using a least squares method, shown in a spreadsheet in the e-Appendix. The associated error is large resulting from the significant scatter and relatively few data points.

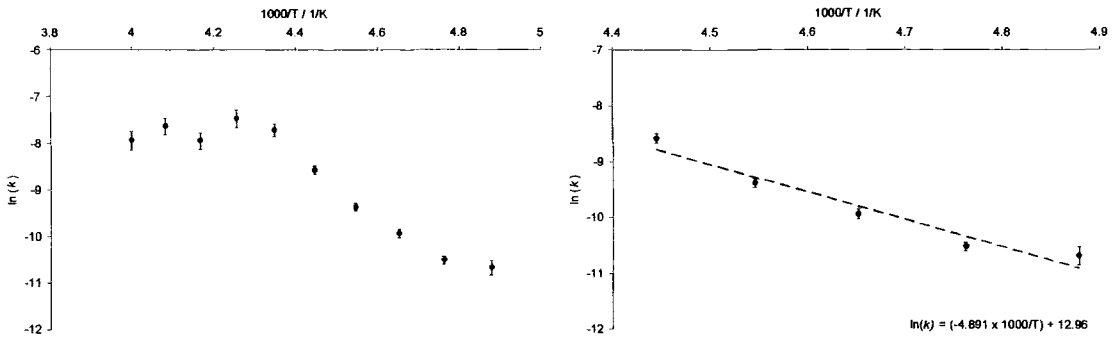

Figure 3.12. Arrhenius (logarithm of rate constant versus inverse temperature) plot for β- to α-$ZrWMoO_8$ between 205 – 250 K (*left*), and 205 – 225 K (*right*). The equation of the line of best fit is also shown and based on the Arrhenius law: $k_T = A\exp(-E_A/RT)$. The Arrhenius constant, $\ln(A)$ is given by the intercept of the plot (= 13 s^{-1}). The activation energy, E_A is equivalent to the gradient multiplied by $-R$ (Gas constant, 8.3145 $JK^{-1}mol^{-1}$), and is found to be 40.7 $kJmol^{-1}$.

The value of the activation energy obtained here is considerably greater than that obtained by Evans *et al.* in their neutron diffraction analysis (41 (8) versus 22 (5) $kJmol^{-1}$), although a different kinetic analysis is employed here. Evans' method extracted kinetic information from neutron diffraction of a quench-warmed sample by analysis of the hump in the cell parameter trend. An analogous method based on X-ray measurements is investigated in Section 3.4.3. It seems likely that the activation energy is not constant throughout the temperature range considered as emphasised by the non-linearity of the Arrhenius plot. It is not surprising that a different value has resulted in this analysis compared to that obtained by Evans and co-workers.

The above kinetic data were analysed using multiple Rietveld refinements between 205 and 250 K by Dr. John S. O. Evans. Complete details are not included here but key results are presented in Figure 3.13. A full Rietveld analysis allows further kinetic information to be obtained *via e.g.* the time dependence of the unit cell and fractional site occupancy parameters. Refinements were performed using *TOPAS* with a variable peak shape to account for the broad α phase reflections. 26 variables were refined at each temperature: a histogram scale factor, nine background coefficients, sample height correction, cubic lattice parameter, fractional site occupancy parameter, one peak shape broadening term (for broad reflections; the pseudo-Voigt peak width was fixed otherwise), eleven atomic position parameters and a single atomic thermal parameter (for all atoms).

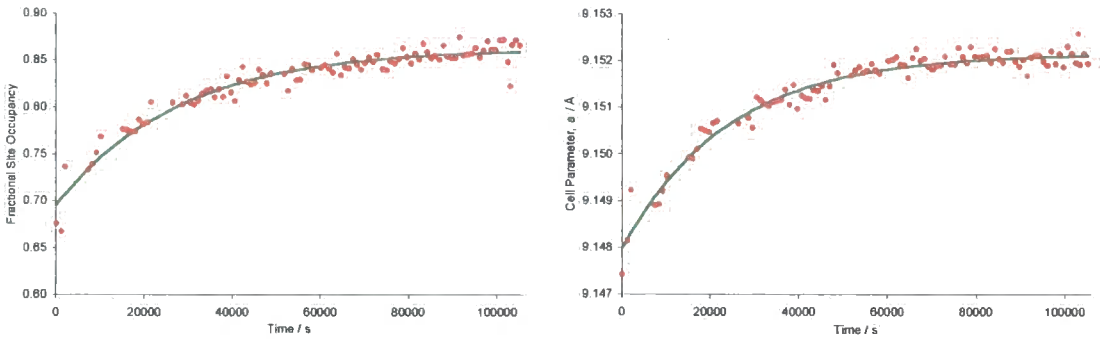

Figure 3.13. Observed and fitted O(4) fractional occupancy (*left*) and cell parameter of $ZrWMoO_8$ (*right*), as a function of time for the quench-anneal at 215 K (d8_01790) measurement. Observed data were fitted using $y_{calc} = A(1-\exp(-k_T y_{obs}) + B/A)$, where y is the occupancy parameter, *frac* or the cell parameter, a; A is a scale factor and B is a y offset parameter; k_T is the rate constant.

Figure 3.13 illustrates a smoother trend than that observed from the sum of the raw intensities of the four broad α reflections in Figure 3.11. Similar smooth curves for the other 9 data sets between 205 and 250 K were obtained and the fitted rate constants are displayed in Arrhenius plots given Figure 3.14. The increase in cell parameter with time is due to the smaller, quenched β phase converting to the larger thermodynamically stable α phase during the anneal process. The increase in the *frac* parameter is due to the quenched, partially disordered β material becoming more oxygen-ordered as it converts to the α form with increasing time. Ideally the *frac* parameter would be ½ at $t = 0$ but it is a difficult parameter to accurately model in rapid diffraction patterns where the large background contribution affects the modelling of the (*111*), (*221*), (*301*) and (*401*) peaks. Also at higher temperatures, the reaction rate is sufficient to mean the β form partially converts to α during the quench thus giving a *frac* value of greater than ½ at $t = 0$.

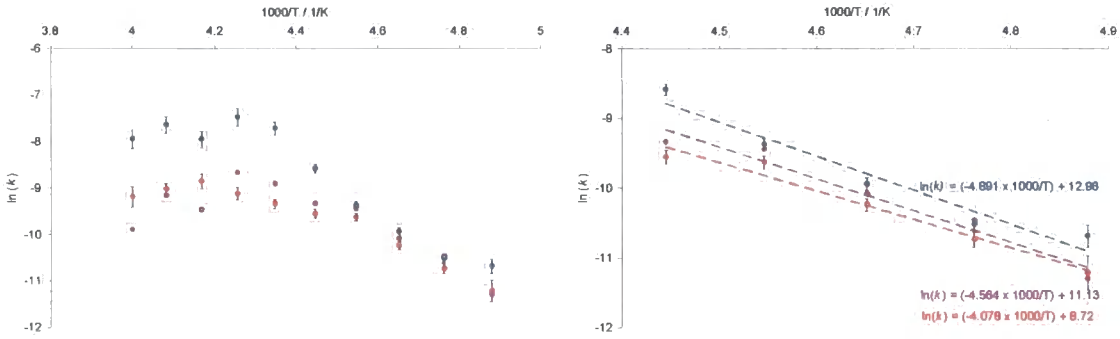

Figure 3.14. Arrhenius plots for quench-anneal experiments at 205 – 250 K (*left*) and 205 – 225 K (*right*) obtained from fitting the time-dependence of the cell parameter and O(4) occupancies of $ZrWMoO_8$. For comparison, rate constants determined from peak-fitting the same datasets are also displayed (from Figure 3.12).

As mentioned earlier in the analogous peak fitting analysis, the reaction rate at higher anneal temperatures was too rapid to give accurate rate constants. Only lower temperatures (205 – 225 K) were used to give an approximate value of the activation energy determined from Figure 3.14 (*right*). The activation energies for the Rietveld refined cell parameter and occupancy parameter are ~ 38 (5) and 34 (6) $kJmol^{-1}$ (compare 41 (8) $kJmol^{-1}$ from the peak-fitting method). The errors are large as previously discussed yet all three values of activation energies determined by different methods are similar.

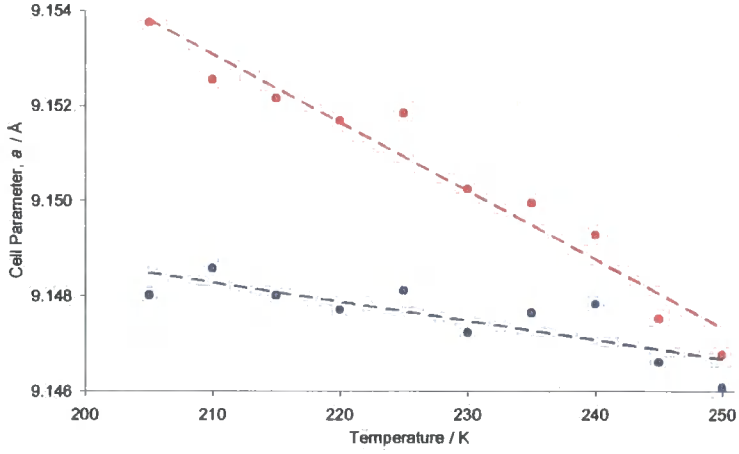

Figure 3.15. Initial versus final fitted cell parameters as a function of temperature for $ZrWMoO_8$ in quench-anneal experiments between 205 and 250 K.

Figure 3.15 shows the values of the fitted refined cell parameter at $t = 0$ (blue curve) and at t = "infinity" (red curve) for the ten sets of *MultiTOPAS* Rietveld refinements at each anneal temperature. Convergence of the two values is apparent above 250 K,

which is effectively that shown by the slow-cool and quench-warm cell parameter trend in the literature (Figure 1.10). That is, at ~ 260 K there is basically no change in cell parameter upon annealing a β quenched sample, whereas at 205 K appreciable conversion to α-$ZrWMoO_8$ occurs.

3.4.3 Quench-warm Experiments on $ZrWMoO_8$

Evans *et al.* reported a method to obtain the activation energy of the α to β phase transition by extracting kinetic information from the hump in the cell parameter trend on warming a quenched sample of $ZrWMoO_8$.[4] In this type of diffraction experiment, the material is rapidly quenched to low temperature and trapped in an unstable state (the β phase) and a "hump" is observed when it starts to equilibrate back to its stable α configuration upon warming (Figure 1.10). By varying the warming rate of a quenched sample of β-$ZrWMoO_8$ it is in principle possible to observe different sized humps and thus different proportions of the α phase using laboratory X-ray diffraction equipment.

The sample of $ZrWMoO_8$ used in these laboratory quench-warming experiments was identical to that used by Evans *et al.* in their HRPD neutron study;[4] the sample was loaded into an Anton Paar TTK450 cryofurnace and diffraction data collected using a Bruker d8 powder diffractometer. Three runs were performed in which the sample was rapidly quenched in the cryofurnace to 90 K and data collected upon warming at different rates as detailed in Table 3.5.

Warming rate / Khr^{-1}	Run #	Temperature range (interval) / K	Time per scan / min
~ 15	d8_00862	90 – 402 (4 K)	15
~ 36	d8_00861	90 – 402 (4 K)	6
~ 66	d8_00860	90 – 410 (20 K)	15

Table 3.5. Details of quench-warming experiments on $ZrWMoO_8$ in the TTK450 cryofurnace. Average warming rates are shown as a guide only (calculated from the total time over the temperature range used).

TOPAS was used to refine the variable temperature data with 33 variables at each temperature in each of the three TTK450 cryofurnace runs. The following variables

were used in the seed Rietveld refinements at 90 K: a histogram scale factor, seven background terms, a sample height correction, a cubic cell parameter, six PV peak parameters, a fractional occupancy (*frac*) parameter, two metal atomic coordinates and one temperature factor; the Al sample holder was modelled using a Pawley fit with its own sample height correction, cubic cell parameter, six PV terms and five parameters to model the intensity under the five Al peaks between 10 and 90 ° 2θ. The seed input files and the *MultiTOPAS* results spreadsheets can be found in the e-Appendix.

Figure 3.16 shows the temperature dependence of the cell parameter for the three runs along with slow-cooling data (d8_00888, also modelled with the same 33 parameters). The figure shows that the slower the rate of warming a quenched β sample, the greater the size of the hump at around 200 – 270 K. At slow heat rates, the material has a longer period in which it can convert to the thermodynamically stable α form, before re-converting back to the high-temperature β phase above 270 K. Conversely, the rapid warm at 66 Khr^{-1} (purple points) means the quenched β phase does not form an appreciable amount of α-$ZrWMoO_8$, as shown by the cell parameter trend which is almost linear.

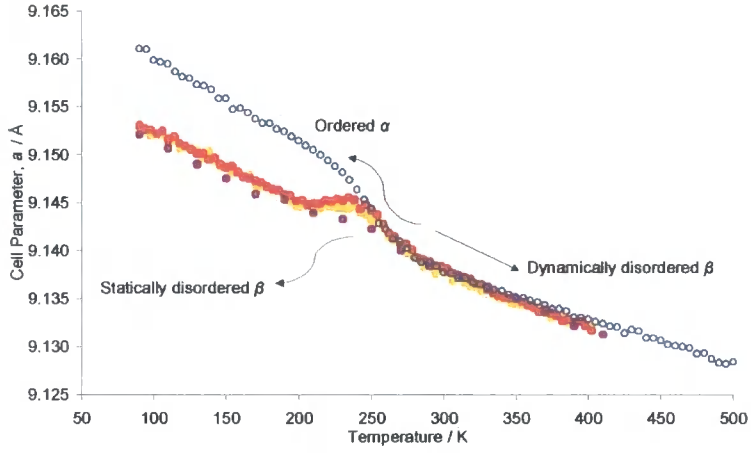

Figure 3.16. Refined lattice parameter of quench-warmed β-$ZrWMoO_8$ as a function of temperature and warming rate (66 Khr^{-1}, 36 Khr^{-1} and 15 Khr^{-1}). Also shown are slow-cooling refined data for β-$ZrWMoO_8$ which converts to α-$ZrWMoO_8$ under equilibrium conditions at 270 K.

Kinetic information can be extracted from these data *via* the temperature-time dependence of the refined fractional occupancy (*frac*) parameter of O(4) in $ZrWMoO_8$.

The trends in the *frac* parameter for the three (quench-) warming experiments and the slow-cooling experiment are shown in Figure 3.17.

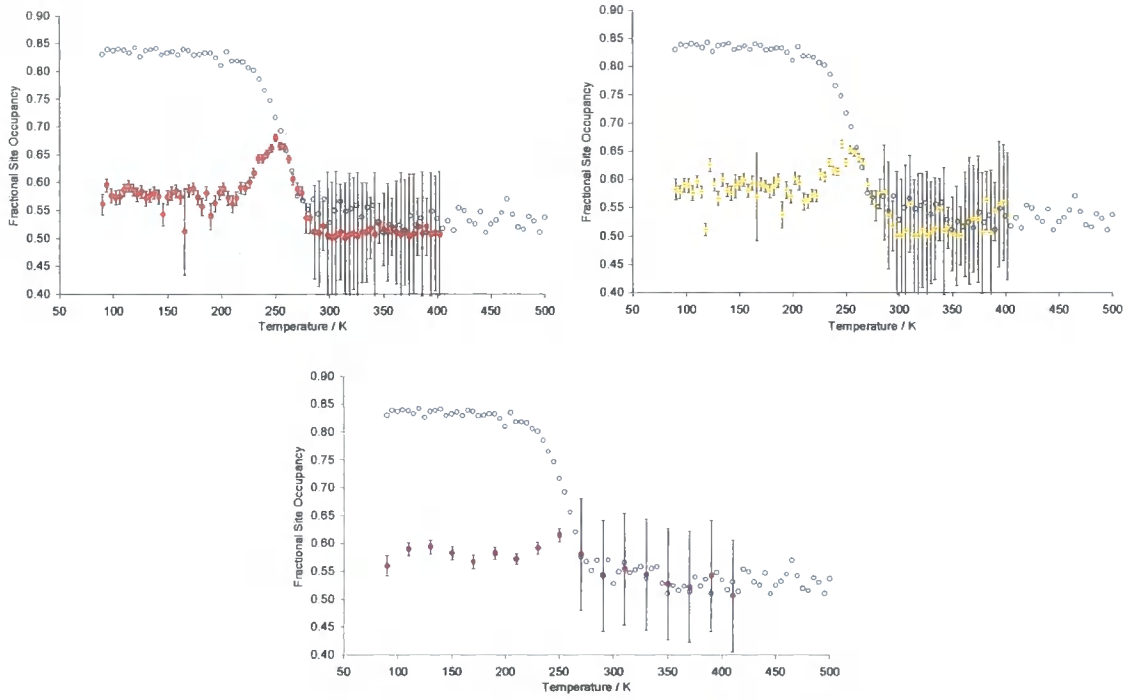

Figure 3.17. O(4) fractional site occupancy as a function of temperature for quench-warming experiments on $ZrWMoO_8$ at 15 Khr^{-1} (d8_00862), 36 Khr^{-1} (d8_00861) and 66 Khr^{-1} (d8_00860) versus "equilibrium" slow-cooled conditions (d8_00888). For clarity error bars for the slow-cool data are not shown.

The O(4) fractional occupancy plots in Figure 3.17 mirror the cell parameter trends described above. At low temperature the quenched sample is predominantly in its high-temperature oxygen-disordered state (*frac* ~ 0.57). Upon warming to ~ 210 K, the material gains sufficient thermal energy for the oxygens to begin to migrate back to their thermodynamically most stable configuration as shown by an increase in fractional occupancy to a maximum value of 0.68 at 250 K in the slowest warming (15 Khr^{-1}) experiment. Above this temperature the β form becomes stable and so *frac* begins to fall and converge back towards ~ ½. For the quicker warming experiments at 36 and 66 Khr^{-1}, the maximum value of *frac* achieved is reduced to lower values of ~ 0.65 and 0.62, respectively.

The *frac* value can be converted to more convenient "excess oxygen" parameter O_{excess}, which can be used to monitor the α-$ZrWMoO_8$ to β-$ZrWMoO_8$ conversion. Whereas *frac* can take values between ½ (fully disordered oxygens) and 1 (fully ordered), O_{excess}

can be defined to take values between 0 (fully disordered sites or zero excess oxygen at site O(4)) and 1 (fully ordered or 100% excess order). The definition used is given in Equation 3.2.

$$O_{excess} = \frac{frac_{O4} - frac_{O41}}{frac_{total}} = \frac{frac_{O4} - (1 - frac_{O4})}{frac_{total}} = 2(frac_{O4} - 0.5) \qquad (3.2)$$

Equation 3.2 relies on there only being one value of *frac* and that the total occupancy is 1, which is the case for the α to β model employed in the refinements. From the O_{excess} parameter, the "extent of reaction" parameter can be defined, $\alpha(t,T) = O_{excess,warm} / O_{excess,eqm}$. In this expression the equilibrium value of the excess oxygen parameter is determined by the slow-cooling experiment (d8_00888), assumed to proceed under equilibrium conditions. Thus one can calculate the rate constant, k_T at a variety of temperatures once a relationship to the extent of reaction has been determined. As the material is never held at a given temperature for long enough for full oxygen ordering to occur, the total extent of oxygen ordering at any temperature T, depends on the rate of oxygen migration at that temperature, k_T and on all the migration that has occurred at lower temperatures. Appendix A2.2 gives the mathematical derivation of the rate expression used which is re-displayed in Equation 3.3; at any given temperature during the warming of a quenched sample, the total extent of ordering in the "humped" region (as a function of time and temperature) is given by this expression.

$$\Delta\alpha_T = \left(1 - \sum_{0}^{T-1} \Delta\alpha_T\right)(1 - \exp(-k_T t)) \qquad (3.3)$$

Equation 3.3 is a cumulative kinetic expression; the total extent of reaction at any given time in the reaction is dependent on the sum of all the values for the previously elapsed ordering in the experiment, $\Sigma\Delta\alpha_T$. Using Equation 3.3 and the Arrhenius Law ($k_T = A\exp(-E_A/RT)$), the observed total extent of reaction trend can be calculated and the Arrhenius constant and activation energy determined by least-squares fitting (*i.e.* by minimising the difference between the observed and calculated total $\Delta\alpha_T$ values). Full analyses are given in three spreadsheets located in the e-Appendix. The fitting of the

excess oxygen parameter in the three warming experiments is also shown below in Figure 3.18.

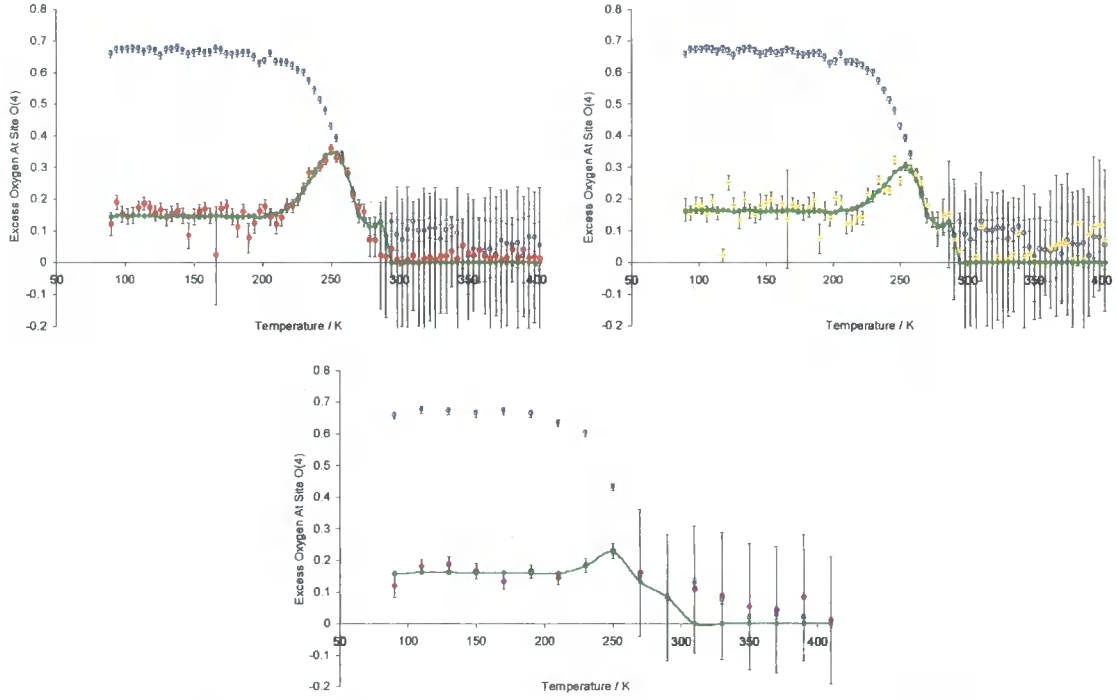

Figure 3.18. Calculated versus observed excess oxygen parameter as a function of temperature for three quench-warming experiments on $ZrWMoO_8$. Observed data are colour-coded as follows, d8_00862 – 15 Khr^{-1}, d8_00861 – 36 Khr^{-1} and d8_00860 – 66 Khr^{-1}. Interpolated slow-cooling (d8_00888) data are shown for comparison.

The resulting activation energy, E_A from the least-squares fitting of the 15 Khr^{-1} (red) data is 38.9 $kJmol^{-1}$ with an Arrhenius constant of 57500 s^{-1}; the corresponding value of $\ln(A) = 10.95$ s^{-1}, which is similar to those in Figure 3.14. This value of E_A was subsequently fixed for the fitting of the remaining analyses, which are based on more rapid warming experiments (36 and 66 Khr^{-1}). These possess fewer data points in their humped regions (Figure 3.18, *right* and *below*) so their refined E_A values would be less accurate. The individual Arrhenius constants refined to values of 94800 and 59100 s^{-1} for the 36 and 66 Khr^{-1} data, respectively. Figure 3.18 shows that the quality of the fit at 36 and 66 Khr^{-1} is sufficiently good to give confidence in this method of analysis, without the need to refine individual activation energies for these two datasets. An E_A value of ~ 39 $kJmol^{-1}$ is comparable to those obtained from the quench-anneal experiments in Section 3.4.2 (34 (6) to 41(8) $kJmol^{-1}$). An estimated error on E_A would be around 5 $kJmol^{-1}$ since similarly good fits to the 36 and 66 Khr^{-1} warming data can

be attained by varying the activation energy by ± 5 kJmol^{-1}, and re-refining the pre-exponential constant.

All four of the activation energies for the α - β phase transition in $ZrWMoO_8$ determined in this chapter are larger than the value obtained by Evans *et al.* in their HRPD quench-warm analysis (E_A = 22 (5) kJmol^{-1}). The quench-warm method is perhaps less reliable than the quench-anneal peak-fitting analysis since in the latter case there are fewer assumptions and no structural models employed. The analysis here based on fractional site occupancies also contains fewer assumptions than the HRPD analysis reported by Evans, based on unit cell parameter variations. However only an average value of the activation energy is obtained in all cases. Evans obtained an activation energy of 65 (1) kJmol^{-1} from impedance (conductivity) measurements on $ZrWMoO_8$ albeit at temperatures above ~ 575 K. The temperature dependence of the activation energy is likely the cause of the discrepancy in the above analyses versus the literature data as suggested by the curved Arrhenius plots in Figure 3.14.

In Section 3.4.4, a slightly different method is used to model the slow-cooling (d8_00888) X-ray data. This takes into account slightly different peak widths for the "ordering reflections" and influences the absolute value of the fractional occupancy, determined by the intensity of the four relatively weak reflections shown *e.g.* in Figure 3.9. It is noted that this has minimal effect on the value of the excess oxygen parameter at site O(4) used in the above kinetic analysis.

3.4.4 Slow-cool Experiments on $ZrWMoO_8$

It is intriguing that the experiments on $ZrWMoO_8$ described so far, and those previously performed by Evans *et al.* never led to a fully ordered α material. The maximum value of the O(4) fractional occupancy ('$frac_{max}$') refined in this work (d8_00888, Figure 3.17) is ~ 0.83 whereas that reported by Evans was 0.80.[4] This in sharp contrast to ZrW_2O_8, which is fully ordered at ≤ 300 K, *i.e.* $frac_{max}$ ~ 1.0 in Figures 1.6 or 3.26. To investigate this phenomenon a series of slow-cooling experiments at different rates were performed on a sample of $ZrWMoO_8$ to determine whether a higher state of ordering could be attained.

The sample of $ZrWMoO_8$ studied was the same as that used in Sections 3.4.2 and 3.4.3; $ZrWMoO_8$ was freshly heated in a furnace at 473 K before each experiment ensuring that the material was fully in its β state and fully dehydrated. Cooling experiments were performed using a laboratory Bruker d8 X-ray diffractometer equipped with an Oxford Cryosystems PheniX cryostat or an Anton Paar TTK450 cryofurnace (Section 6.1), as shown in Table 3.6.

Cooling rate / Khr^{-1}	Run #	Temperature range (interval) / K	Time per scan / min
~ 120 (cryofurnace)	d8_00705	500 – 90 (10 K)	5
~ 35 (cryofurnace)	d8_00642	500 – 120 (10 K)	15
~ 19 (cryofurnace)	d8_00888	500 – 90 (5 K)	15
8 (cryostat)	d8_01763	300 – 200 (~ 4 K), 200 – 159 (~ 8.5 K)	30
4 (cryostat)	d8_01765	299 – 200 (~ 2 K), 200 – 20 (~ 8.5 K)	30
2 (cryostat)	d8_01775/6	301 – 200 (~ 1.4 K), 200 – 17 (~ 12 K)	43

Table 3.6. Details of slow-cooling X-ray diffraction experiments on $ZrWMoO_8$. The cryostat provides continuous cooling with a set cooling rate and so average temperature intervals are given. The cryofurnace performs repeated ramp/holds with a set temperature interval and so effective mean cooling rates are given. To save time during the very slow cryostat runs, once 200 K was reached, and no further ordering apparent, the cooling rates were increased to 17 Khr^{-1}.

TOPAS was used to refine the VTXRD data and the input files for Rietveld refinement can be found in the e-Appendix. The seed refinements were performed at 500 K for the cryofurnace and at ~ 300 K for the cryostat runs. Since the (*111*), (*221*), (*301*) and (*401*) peaks due to the α phase were significantly broader than other reflections they were modelled using a normal pseudo-Voigt function plus an extra peak-broadening parameter. Otherwise the same set of parameters as employed in Section 3.4.3 were refined for the three TTK450 cryofurnace runs here except that nine background terms were refined as well as all eleven independent atomic positions, giving a total of 45 refined variables at each temperature. The same 45 parameters were also used to refine two of the three PheniX cryostat runs. For the slowest cooling (d8_01775/6) run however, an expanded 2θ range of 10 to 120 ° was employed, which gave rise to eight Al sample holder peaks and so eight parameters (to fit the area under these peaks) were required giving a total of 48 parameters used in this seed refinement. Figure 3.19 gives a

portion of a typical Rietveld fit to the PheniX data at low temperature to show the successful modelling of the broader (*111*), (*221*), (*301*) and (*401*) peaks.

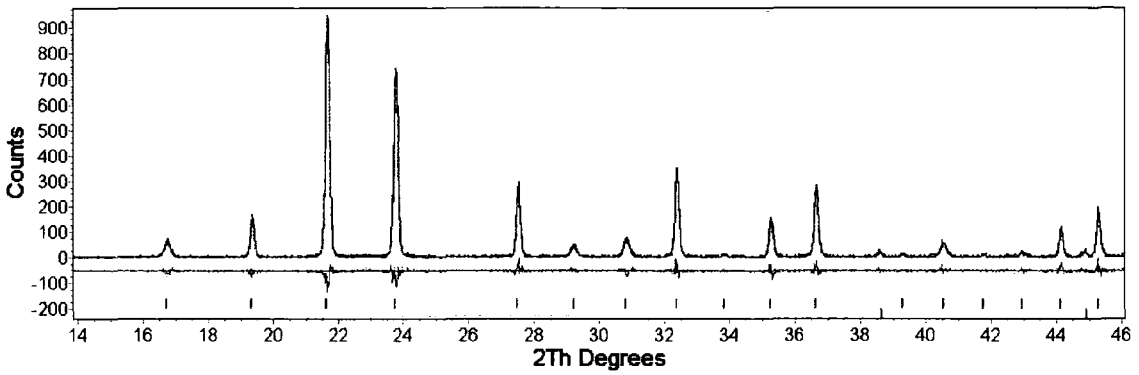

Figure 3.19. Partial Rietveld fit at 17 K of slow-cooled $ZrWMoO_8$ (d8_01776:61). Upper blue tick marks are calculated positions for $ZrWMoO_8$, lower marks for the Al sample holder. Without the use of an additional broadening term, reflections at ~ 16.8, 29.2, 30.8 and 40.6 ° are incorrectly modelled as too sharp.

The Rietveld fit in Figure 3.19 was for the slowest-cooled sample of $ZrWMoO_8$ *i.e.* 50 hours to cool between 300 and 200 K. The (*111*), (*221*), (*301*) and (*401*) peaks are significantly sharper than in the quench-annealed samples in Section 3.4.2 (Figure 3.10). Cooling rates of up to ~ 1200 Khr^{-1} were purposely employed in Section 3.4.2 during the quenching process, in order to trap the material in its high-temperature β state. The cause of the broadened evolved peaks is presumably a domain size effect. Slow cooling allows the formation of larger ordered α-$ZrWMoO_8$ domains. More rapid cooling is likely to disrupt the growth of ordered domains due to faults, which lead to a smaller domain size and therefore broader Bragg reflections.

The complete results of the variable temperature refinements are shown in a series of spreadsheets in the e-Appendix, from which the most important result is given in Figure 3.20. The order-disorder transition of the W/MoO_4 groups can be seen to occur between ~ 300 and 200 K. The extent of ordering (upon cooling) depends on the cooling rate as shown in the figure and in Table 3.7. The maximum fractional occupancy is 0.92 – 0.93 when cooled at 2 or 4 Khr^{-1}, *i.e.* there is considerable disorder present even at these slow rates. It seems unlikely that complete ordering will occur no matter how slowly $ZrWMoO_8$ is cooled. This is in contrast to ZrW_2O_8 where complete ordering occurs even with rapid cooling rates (Section 3.5.1 and Figure 1.6).

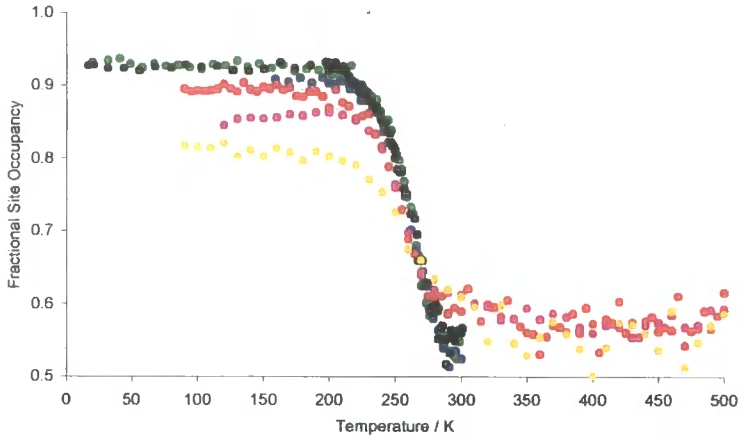

Figure 3.20. The O(4) site occupancy of $ZrWMoO_8$ as a function of temperature and cooling rate, coded as follows: 120, 35, 19, 8, 4 and 2 Khr^{-1}.

Cooling rate / Khr^{-1}	$frac_{max}$
120 (cryofurnace)	0.809 (8)
35 (cryofurnace)	0.856 (6)
19 (cryofurnace)	0.892 (7)
8 (cryostat)	0.906 (5)
4 (cryostat)	0.927 (5)
2 (cryostat)	0.924 (5)

Table 3.7. Maximum site occupancy values taken by averaging the values obtained (from Figure 3.20) at 200 K and below.

The $frac_{max}$ parameters and cooling rates do not agree very closely with those obtained by Evans *et al.*; all $frac_{max}$ values obtained here are greater than those obtained in their experiments. The experiments presented here were, however, carried out in a systematic fashion on a single sample of material, with a consistent pre-experiment heat treatment. Figure 3.20 also shows that for the cryofurnace data, the value of *frac* does not fall precisely to ½ at high temperature. This is related to the difficulty of fitting accurately the broad superstructure reflections, given the relatively complex background in the cryofurnace and poor signal to noise at these fast-cooling rates. In the cryostat measurements, the background is smoother, the data quality higher and *frac* therefore better determined. For the sake of consistency the same refinement model has been chosen for both data sets.

3.5 Cubic ZrW_2O_8

3.5.1 Quench-anneal Experiments on ZrW_2O_8

Evans *et al.* showed that oxygen ordering in cubic ZrW_2O_8 was a facile process *i.e.* below 300 K the maximum fractional occupancy of O(4) reaches 1.0 (Figure 1.6).[3] This is in contrast to $ZrWMoO_8$, as shown in Section 3.4.4, where complete ordering of $ZrWMoO_8$ does not occur even on very slow cooling. In fact, attempts to quench β-ZrW_2O_8 to low temperatures using the same *in situ* X-ray diffraction methodologies employed for $ZrWMoO_8$ were not possible. Conversion back to the thermodynamically stable α form was too rapid and so useful kinetic information on ZrW_2O_8 could not be achieved in the same manner. For example, a sample of ZrW_2O_8 was heated to 473 K in the TTK450 cryofurnace and a quench of its β phase to 273 K attempted. However, during the ~ 5 minute delay in reaching 273 K, the material had already converted back to the α form.

It was found that a more rapid quench could be performed by externally cooling a sample of β-ZrW_2O_8 from a hot furnace to room temperature. A 15 mm pellet of ZrW_2O_8 was heated to 623 K and quenched in ice-cold water. The reasons for using water were that liquid nitrogen did not give a suitably rapid quench and also ZrW_2O_8 has been reported to be inert to hydration at ambient temperature.[17] Details of hydration studies of cubic ZrM_2O_8 phases are discussed in Chapter 4. After quenching, the pellet was rapidly mounted in a Bruker d8 powder X-ray diffractometer in ambient flat-plate reflection mode and a series of very rapid diffraction patterns collected at room temperature. The elapsed time between removing the pellet from the furnace and beginning the diffraction measurement was ~ 55 seconds. Forty 30-second diffraction patterns were collected between 15 and 34 ° 2θ (Figure 3.21), enabling the time-dependent evolution of the following α phase Bragg reflections to be monitored: (*111*) at ~ 16.8 °, (*221*) at ~ 29.3 °, and (*301*) at ~ 31.0 °.

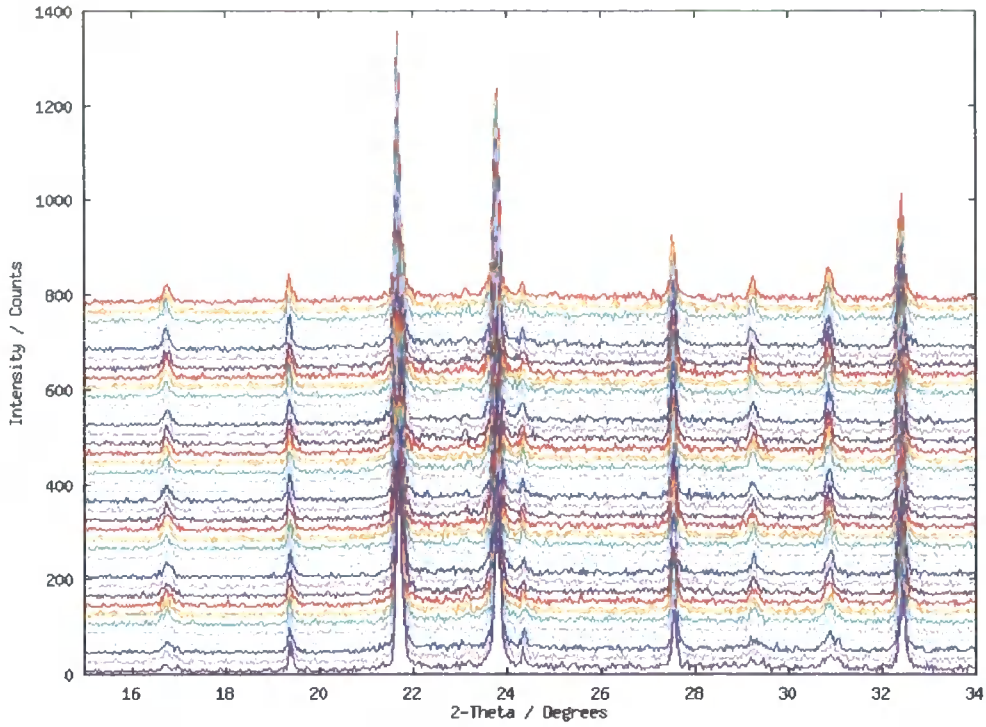

Figure 3.21. Spontaneous conversion of quenched β-ZrW_2O_8 to α-ZrW_2O_8 at room temperature (d8_00253). Diffraction patterns were taken every 30 seconds from the base of the figure at time zero. The β to α conversion is already partially complete at $t = 0$ as shown by the evolving α reflections at ~ 16.8, 29.3 and 31.0 ° 2θ.

TOPAS was used to peak-fit the data in Figure 3.21 by a similar method described for $ZrWMoO_8$ in Section 3.4.2, except that the summed intensity of the three evolving α peaks were normalised using that of the five remaining peaks. The following 14 variables were used in the *TOPAS* peak-fitting seed file (see the e-Appendix): three background terms, a sample height correction, a cubic cell parameter (so that 2θ values of the Bragg reflections could be calculated), three parameters to model the intensity under the evolving (*111*), (*221*) and (*301*) α reflections and five to model the remaining the peaks common to both the α and β phases in the 2θ range considered - (*002*), (*201*), (*211*), (*022*) and (*311*). A single parameter was employed to describe the FWHM for all eight peaks and Figure 3.22 gives an example peak-fit for the final range of the measurement. Figure 3.23 shows the increase in summed area of the three evolving α phase peaks (normalised to the remaining peaks) with respect to time.

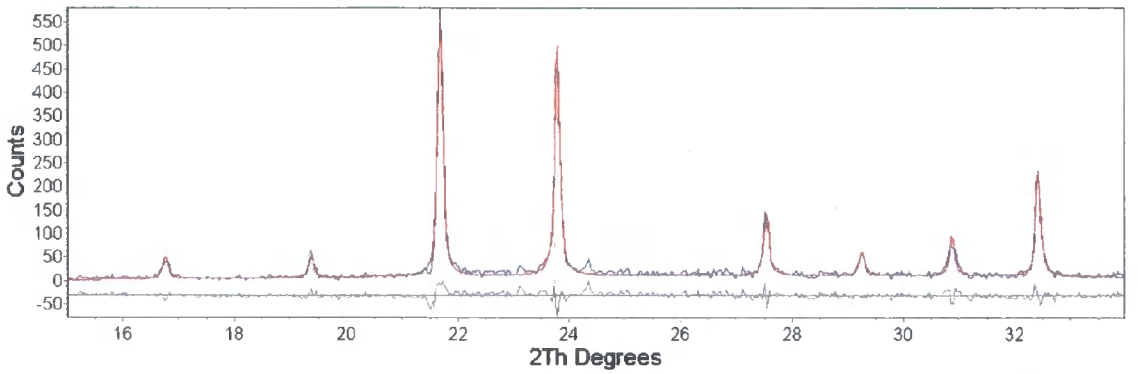

Figure 3.22. Peak fitting of quenched ZrW_2O_8 in final range of a "room-temperature anneal" experiment (d8_00253:40). Peaks at ~ 23.1 and 24.3 ° 2θ are due to a minor WO_3 impurity.

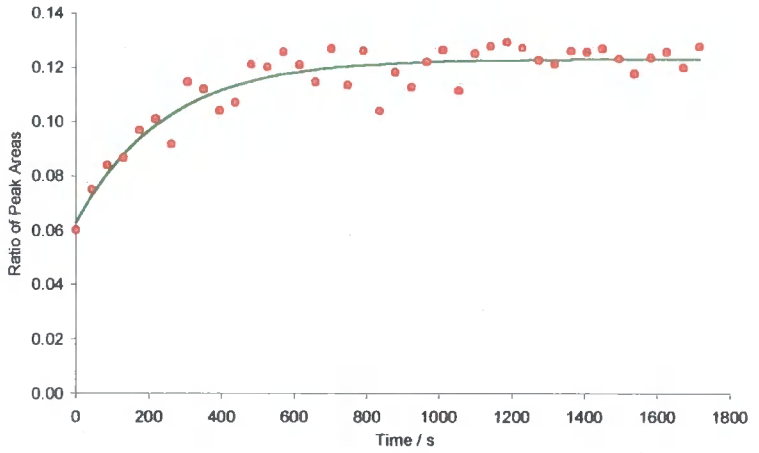

Figure 3.23. The ratio of the summed intensities of the evolving three α-ZrW_2O_8 peaks to the summed intensity of remaining five peaks shared by both α- and β-ZrW_2O_8 *i.e.* intensity ratio = $\{I(111)+I(221)+I(301)\}$ / $\{I(002)+I(201)+I(211)+I(022)+I(311)\}$. Observed data are shown with a subsequent exponential rise to a maximum fit using the same form of function for the Rietveld fitting of $ZrWMoO_8$ given in the caption of Figure 3.13.

The resulting value of the rate constant obtained from the kinetic fitting for β- to α-ZrW_2O_8 is 0.00416 s^{-1} (see e-Appendix spreadsheet). The above manual quenching experiment could not be repeated at different temperatures since a sample cannot be mounted straight into the cryofurnace at *e.g.* 250 K so only one rate constant is given. Extrapolating the Arrhenius plot for $ZrWMoO_8$ in Figure 3.12 (*right*) to a temperature of 300 K gives $k_{300} = 0.0353$ s^{-1}. The rate constant actually seems larger in $ZrWMoO_8$ than in ZrW_2O_8 at room temperature. The k_T value for ZrW_2O_8 is for qualitative comparison only; the temperature of the pellet will be constantly changing between 270 K and room temperature thus the rate constant is only an average value. Also, the process that is being modelled is not simply the rapid conversion of β- to α-ZrW_2O_8 but

also the partial sharpening of Bragg reflections as the system anneals. β-ZrW_2O_8 cannot be successfully quench-annealed in the cryofurnace in the same way that $ZrWMoO_8$ can because α-ZrW_2O_8 is thermodynamically stable at ~ 180 K higher than $ZrWMoO_8$. The rate of β to α conversion is determined by the reaction rate around T_c. For ZrW_2O_8, the rate is slower at room temperature because the actual β to α conversion occurs at 400 – 450 K. Hence there is sufficient thermal energy and time to order β-ZrW_2O_8 even with a rapid cool. With $ZrWMoO_8$, ordering occurs around 200 – 250 K, which is a much lower temperature - the thermal energy of the system is much reduced and so the process can be studied on a longer timescale.

3.5.2 Hysteresis in the Thermal Expansion of ZrW_2O_8.

Close inspection of the variable temperature neutron diffraction data collected on cubic ZrW_2O_8 by Evans *et al.* (Figure 1.4, expanded in Figure 3.24),[3] shows hysteresis in the cell parameter around the order-disorder phase transition region, *i.e.* discrepancies between warming and cooling cell parameter data.

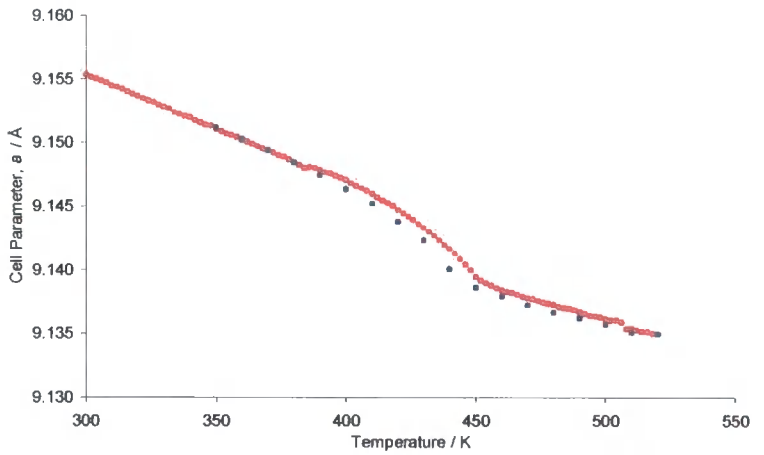

Figure 3.24. Refined cell parameter of cubic ZrW_2O_8 from variable temperature neutron diffraction data collected by Evans *et al.*.[3] Only a portion of the full data set (Figure 1.4) is shown to emphasise the hysteresis behaviour between warming and cooling around the second-order phase transition at 448 K.

Upon warming, Evans noted that a 4 hour beam-loss enforced anneal at 386 K gave a discrepancy in the unit cell which was larger than expected compared to cooling. The increase was prior to the onset of the phase transition and was suggested to be related to the small amount of disordered oxygen present at that temperature (~ 8%, according to

Figure 1.6); sample annealing apparently allowed any small amount of disorder to anneal over a long range throughout the material. Evans highlighted, *via* an argument similar to that shown by Equation 1.8, that the entropy of a material is inversely related to its volume. Hence, the anneal gave rise to a small increase in cell parameter over time at 386 K. A similar effect was observed in the cell parameter by Yamamura *et al.*,[18] where diffraction patterns ~ 105 minutes in length plus a 20 minute delay were recorded on warming and an anomaly observed at ~ 400 K.

It was decided to see if this effect could be repeated by performing a loop around the phase transition using a regime similar to that of Yamamura, with relatively long scans. 55-minute scans plus a 20 minute equilibration period at each temperature were recorded using a Bruker d8 diffractometer and Anton Paar HTK1200 furnace. A silicon internal standard was added to a sample of ZrW_2O_8 as described in Section 7.5.2 (resulting sample i.d. SA25A). Good quality powder patterns were collected every 10 K between 303 to 403 K and every 5 K from 413 to 523 K on warming, then every 10 K on cooling from 520 to 310 K (d8_00602). The data was refined using *MultiTOPAS*; the seed file at 303 K can be found in the e-Appendix and describes the 54 parameters used for the first of the multi-temperature refinements (57 in all). Twelve background terms and a global sample height correction were refined along with a histogram scale factor, cubic cell parameter, six PV peak terms, one *frac* parameter, eleven independent atomic coordinates and five temperature factors for ZrW_2O_8. For Si, a scale factor, cubic cell parameter, six PV terms and one temperature factor were employed. A small amount of monoclinic WO_3 impurity was modelled with a scale factor, three cell parameters, β cell angle, one peak shape term, and one temperature factor. A Rietveld fit for the seed 303 K data set is shown in Figure 3.25, while Figure 3.26 shows the resultant temperature dependent behaviour of the lattice parameter and O(4) fractional site occupancy of ZrW_2O_8. The e-Appendix gives a spreadsheet displaying complete results of the multiple refinements.

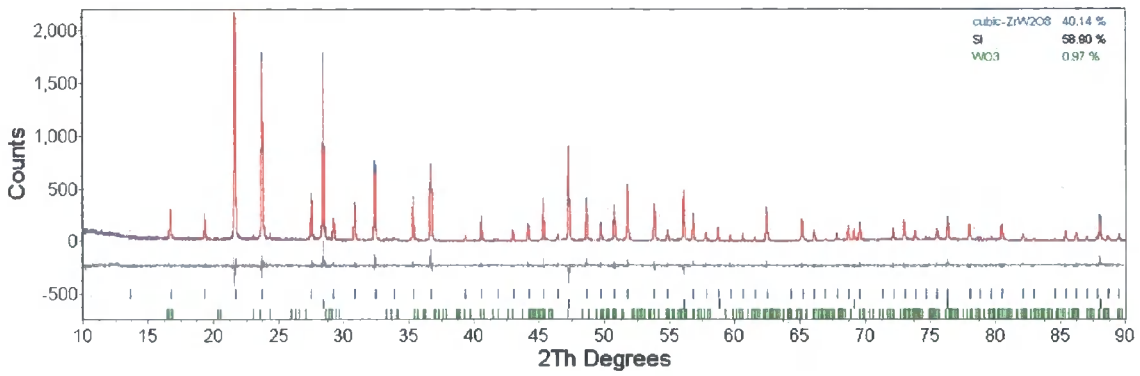

Figure 3.25. Rietveld refinement of cubic ZrW_2O_8 at room temperature (SA25A, d8_00602). Calculated tick marks are shown in blue for ZrW_2O_8, black for Si and green for WO_3.

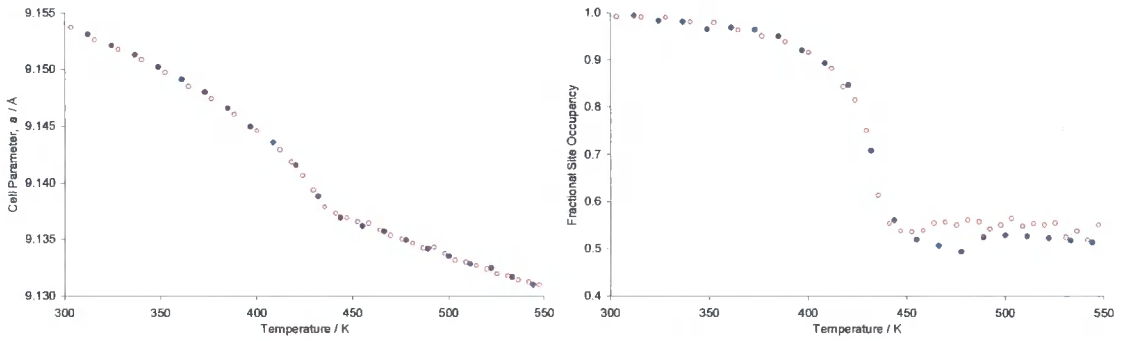

Figure 3.26. Cell parameter and O(4) fractional occupancy in a slow-warming and cooling loop experiment through the phase transition at ~ 435 K in cubic ZrW_2O_8 (d8_00602). Temperatures have been corrected according to calibration curve given for the HTK1200 furnace in Section 6.1.3. Note that upon cooling, complete ordering of WO_4 groups has occurred by ~ 300 K (*frac* = 1.0).

Figure 3.26 shows there is no warming/cooling discrepancy in the thermal expansion behaviour of ZrW_2O_8 unlike in the experiments performed by Evans *et al.* and Yamamura *et al.*. The phase transition temperature, T_c is observed at ~ 435 K comparable to 448 K by neutron diffraction,[3] 431 K by calorimetry,[19] 430 K by dilatometry.[2]

In a second experiment, the conditions of Evans' HRPD experiment were mimicked as closely as realistically possible in the laboratory to see if the cell parameter anomaly could be observed. Diffraction collections were performed every 2 K from 303 – 521 K on warming and 520 – 310 K on cooling, for ~ 6 minutes each plus 2 minutes equilibration time, with a ~ 4 hour hold at 385 K and 507 K (38 and 39 repeated 6 minute scans were performed at these anneal temperatures, respectively). In comparison to the previous (d8_00602) refinement, only one overall temperature factor for all atoms

in ZrW_2O_8 was used and atoms were restrained to within ~ 0.9 Å of their room temperature positions to maintain a stable refinement. Cell parameters of WO_3 were not refined as the phase was barely visible above background levels. Otherwise the same variables were employed, giving a total of 50 independent parameters (see e-Appendix for the seed input file and *MultiTOPAS* spreadsheet).

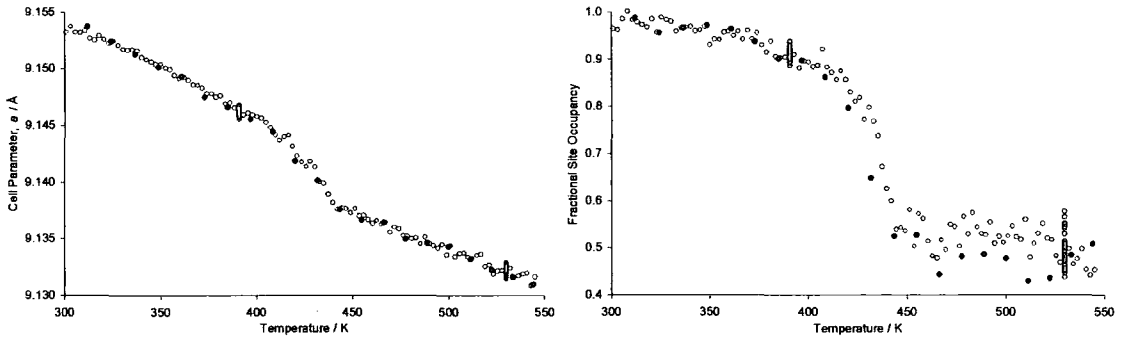

Figure 3.27. Refined cell parameter and O(4) site occupancy upon warming and cooling for a set of 208 rapid scans around the phase transition of ZrW_2O_8 (d8_00599). The order-disorder phase transition is seen to occur at ~ 440 K. Data were corrected using the usual HTK1200 temperature calibration (Si cell parameter too scattered to act as a reliable internal standard).

The data quality of the "mock HRPD" experiment was roughly an order of magnitude less than the X-ray experiment above (d8_00602) owing to very short collection times. This is manifested by the larger degree of observed scatter when Figure 3.27 is compared to Figure 3.26. A six-minute diffraction pattern on a modern laboratory X-ray machine is no match for a six-minute collection on HRPD (compare the precision of the refined cell parameter plots in Figures 3.27 and 3.24 respectively). One cannot draw too many conclusions from Figure 3.27; repeated scans at ~ 385 K (T_{corr} = 391 K) did not give a sequential rise in cell parameter but rather random scatter. Also at 507 K (T_{corr} = 530 K), roughly where Evans observed a decrease in cell parameter upon annealing, again only random scatter was observed. There is possible evidence to suggest hysteresis in the *frac* parameter; upon cooling, *frac* converges back to its maximum value at a temperature $\leq$ 10 K lower than upon warming. However, this observation cannot be viewed as concrete as *frac* is a difficult parameter to determine accurately with noisy data. In summary, it has not been possible to reproduce the ZrW_2O_8 cell parameter anomaly that has been reported in the literature.

With hindsight, lower anneal temperatures should have been employed to account for the temperature error inherent to the HTK1200 furnace so that a closer replica of Evans' experiment could have been performed. However, this was an early experiment using new equipment and calibration procedures not fully determined at that time.

3.6 Conclusion

A variety of new studies on the thermal expansion and phase transitions in cubic AM_2O_8 materials has been presented. Comprehensive variable temperature neutron diffraction data have been collected and refined for cubic $ZrMo_2O_8$ confirming the lack of an order-disorder phase transition, but revealing a change from statically to dynamically disordered (MoO_4 terminal) oxygen atoms at 215 K. The trend in α to β phase transition temperatures for the $ZrW_{2-x}Mo_xO_8$ materials are, ZrW_2O_8: 435 K (in this work; 448 K according to Evans' studies),[3] $ZrW_{1.6}Mo_{0.4}O_8$: 393 K,[14] $ZrWMoO_8$: 270 K,[4] and $ZrMo_2O_8$: 215 K (in this work). The introduction of Mo into the lattice seems to lower the phase transition temperature and stabilise the disordered (β) structure.

Preliminary studies on the thermal expansion of cubic $HfMo_2O_8$, synthesised using *in situ* diffraction studies performed in Chapter 2, are also reported for the first time. Laboratory variable temperature X-ray experiments show no evidence for an order-disorder transition. $HfMo_2O_8$ thus behaves in a similar fashion to $ZrMo_2O_8$. The temperature at which the transition would be thermodynamically favoured is presumably sufficiently low that the transformation is kinetically barred in this material.

Kinetic investigations of the order-disorder transition in $ZrWMoO_8$ *via* quench-hold and quench-warm laboratory diffraction experiments have suggested an activation energy of around 40 $kJmol^{-1}$ for the phase transition. Methods employed in these kinetic analyses have included simple peak fitting, as well as Rietveld refinement and subsequent fitting of the oxygen fractional site occupancy and unit cell parameter. Similar activation energies have been attained in each case. The simple peak-fitting method has one main advantage over the Rietveld method in that it is model-independent *i.e.* free from any assumptions inherent in a Rietveld refinement.

Variable rate slow-cooling experiments between 300 and 200 K on $ZrWMoO_8$ reveal that the amount of the ordered α form increases with slower cooling rates. However, pure α is never observed even with a cooling rate of 2 Khr^{-1}; a minimum 7% of disordered β-$ZrWMoO_8$ is always present. This is in sharp contrast to ZrW_2O_8, which converts fully to its α form even on very rapid cooling; ZrW_2O_8 could not be quenched in the same way. Despite being reported in the literature, hysteresis behaviour in the cell parameter between warming and cooling around the phase transition in ZrW_2O_8 could not be reproduced in the laboratory.

3.7 References

1. T. A. Mary, J. S. O. Evans, T. Vogt, A. W. Sleight, *Science*, **272**, 1996, 90-92.
2. J. S. O. Evans, T. A. Mary, T. Vogt, M. A. Subramanian, A. W. Sleight, *Chem. Mater.*, **8**, 1996, 2809-2823.
3. J. S. O. Evans, W. I. F. David, A. W. Sleight, *Acta Cryst.*, **B55**, 1999, 333-340.
4. J. S. O. Evans, P. A. Hanson, R. M. Ibberson, U. Kameswari, N. Duan, A. W. Sleight, *J. Am. Chem. Soc.*, **122**, 2000, 8694-8699.
5. C. Lind, A. P. Wilkinson, Z. B. Hu, S. Short, J. D. Jorgensen, *Chem. Mater.*, **10**, 1998, 2335-2337.
6. C. Lind, A. P. Wilkinson, C. J. Rawn, E. A. Payzant, *J. Mater. Chem.*, **11**, 2001, 3354-3359.
7. N. R. Warmingham, M.Chem. Thesis, University of Durham, 2002.
8. H. M. Rietveld, *J. Appl. Cryst.*, **2**, 1969, 65-71.
9. A. A. Coelho, *TOPAS v2.0: General Profile and Structure Analysis Software for Powder Diffraction Data*, Bruker AXS, Karlsruhe, 2000.
10. R. R. Reeber, *Phys. Status Solidi*, **A32**, 1975, 321-331.
11. P. M. Woodward, Personal Communication, 2003.
12. G. S. Pawley, *J. Appl. Cryst.*, **14**, 1981, 357-361.
13. C. Lind, D. G. VanDerveer, A. P. Wilkinson, J. Chen, M. T. Vaughan, D. J. Weidner, *Chem. Mater.*, **13**, 2001, 487-490.
14. C. Closmann, A. W. Sleight, J. C. Haygarth, *J. Solid State Chem.*, **139**, 1998, 424-426.

15. Bruker AXS, *XCH v3.02: Exchange Program for Converting Bruker RAW files to XY Format*, Karlsruhe, 1998.
16. J. S. O. Evans, *Multirange - Fortran 77 routine*, University of Durham, 1999.
17. N. Duan, U. Kameswari, A. W. Sleight, *J. Am. Chem. Soc*, **121**, 1999, 10432-10433.
18. Y. Yamamura, N. Nakajima, T. Tsuji, *Phys. Rev. B*, **64**, 2001, 184109.
19. Y. Yamamura, N. Nakajima, T. Tsuji, *Solid State Commun.*, **114**, 2000, 453-455.

Chapter Four: Labelling, NMR and Hydration Studies of Cubic ZrM_2O_8 Materials

4.1 ^{17}O Labelling of Cubic ZrW_2O_8

4.1.1 Introduction

Chapter 3 describes the results of a series of investigations on the order-disorder phase transition in cubic AM_2O_8 materials (A = Zr, Hf; M = W, Mo) by novel diffraction techniques. Kinetic analyses of the phase transition in both $ZrWMoO_8$ and ZrW_2O_8 have been performed. It has been confirmed that the greater the Mo content in the $ZrW_{2-x}Mo_xO_8$ family the lower the phase transition temperature. Chapter 3 suggests that for $ZrMo_2O_8$, T_c is sufficiently low that oxygen ordering does not occur on a realistic experimental timescale. A subtle dynamic to static transition is however observed in this material. Evans *et al.* have showed that the phase transition gives rise to considerable oxygen ion mobility in these materials as shown by impedance measurements.[1,2]

To date, little is known about the actual low-temperature oxygen migration process in these materials, apart from the fact that diffraction data can be modelled by pairs of MO_4 tetrahedra which undergo S_N2 type inversions, their orientations becoming averaged leading to an increase in unit cell symmetry ($P2_13$ to $Pa\bar{3}$) at T_c.[1] Whether this proceeds *via* $2MO_4^{2-} \leftrightarrow M_2O_7^{2-} + O^{2-}$, *via* local $4MO_4^{2-} \leftrightarrow M_2O_7^{2-} + M_2O_9^{6-}$ disordering equilibria or *via* a more complex mechanism has not been established. This section describes preliminary ^{17}O solid-state MAS NMR studies to try and probe the local environment of oxygen atoms in the structure above and below T_c. ^{17}O is the only NMR active isotope of oxygen, with a nuclear spin magnetic moment of $I = {}^5/_2$. With a very low natural abundance of 0.037%, it is a difficult nucleus to probe using NMR and ^{17}O enrichment of materials under investigation is essential. Labelled ^{17}O samples of ZrW_2O_8 have therefore been prepared *via* an air sensitive route in which the only source of oxygen used was from 28% enriched ^{17}O labelled water.

4.1.2 Preparation of $Zr^{17}O_2$ and $W^{17}O_3$

ZrW_2O_8 is normally prepared in air by prolonged heating of WO_3 and ZrO_2 at 1423 – 1473 K, followed by a rapid quench in air.[3] An isotopically labelled sample of ZrW_2O_8 cannot realistically be made in the same manner using labelled ^{17}O binary oxides due to rapid exchange with atmospheric oxygen at high temperature and therefore reactions had to be performed in the absence of air.

ZrO_2 is a known oxide ion conductor at ~ 900 K, emphasising the need for air-sensitive synthetic techniques in order to avoid loss of ^{17}O, especially since this isotope of oxygen is rare and expensive. The synthetic route chosen was to separately make ^{17}O-containing samples of ZrO_2 and WO_3 by small-scale solution based routes, and subsequently to combine these anaerobically to prepare a ^{17}O-enriched sample of ZrW_2O_8 for use in MAS NMR studies.

$Zr^{17}O_2$ was prepared by the controlled hydrolysis of $ZrCl_4$ using Schlenk line techniques and subsequent heating under vacuum as in the reaction scheme given below;

$$ZrCl_{4(s)} + 2H_2{}^{17}O_{(l)} \xrightarrow[\text{ii. 473 K, 1 hr, vacuum}]{\text{i. } Et_2O\text{, dry, stir, RT}} Zr^{17}O_{2(s)} + 4HCl_{(g)}$$
$$\text{iii. 1123 K, 3 hrs, vacuum}$$

Further synthetic details are given in Section 7.5.1. A grey powdered material was recovered in 67% yield (0.243 g; SA82B). An initial heat to 473 K was necessary to remove any HCl; crystallisation of the amorphous material was achieved at 1073 K under dynamic vacuum. A room temperature X-ray diffraction pattern was recorded using a Bruker d8 diffractometer (see Section 6.1), suggesting the presence of monoclinic ZrO_2 as a major phase,[4] and the high temperature tetragonal form as a minor phase.[5,6] Tetragonal ZrO_2 is normally only stable above 1373 – 1493 K and cannot be quenched to room temperature,[7] even so this phase has been observed in low-temperature sol-gel crystallisations as an intermediate to the monoclinic phase.[8] Garvie has attributed the metastability of the tetragonal phase at room temperature to its small crystallite size.[9,10] Figure 4.1 shows the results of Rietveld refinement of the product obtained using the *TOPAS* suite of software (Section 6.1.11).[11,12] 29 parameters were used to describe monoclinic ZrO_2: twelve background coefficients, a sample

displacement correction, a histogram scale factor, three cell parameters, a β cell angle, a single peak shape term, nine atomic coordinates and one temperature factor. The tetragonal ZrO_2 impurity was modelled with a further six parameters; histogram scale factor, two cell parameters, one peak shape term, one atomic coordinate and one single temperature factor. The *TOPAS* input file is hyper-linked in the Electronic Appendix (e-Appendix).

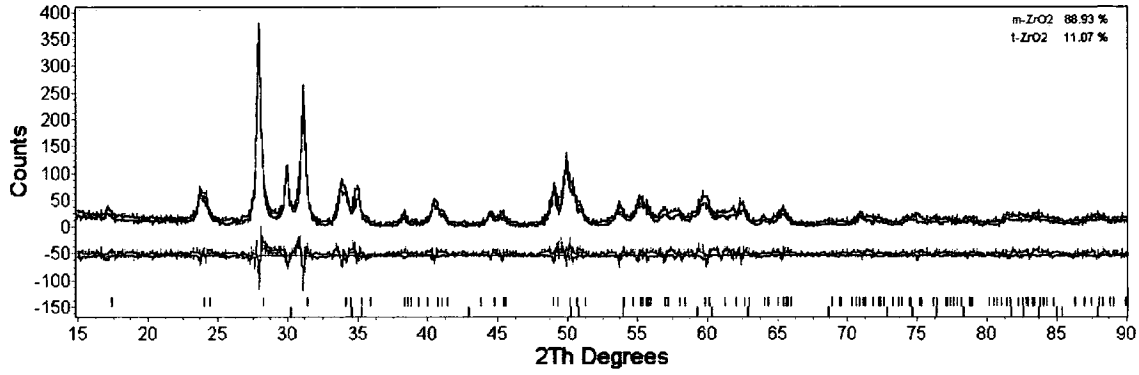

Figure 4.1. Rietveld refinement of a 30-minute diffraction pattern of monoclinic ZrO_2 prepared by the ^{17}O hydration of $ZrCl_4$ (SA82B; d8_01375). Calculated Bragg reflections for the desired monoclinic phase are represented by blue tick marks. Black tick marks at the base of the plot, for example at ~ 30.0 ° 2θ represent the tetragonal ZrO_2 impurity.

The sample was not subsequently heated in air to obtain pure monoclinic $Zr^{17}O_2$ as the potential to exchange ^{17}O with ambient O was too great. It was envisaged further annealing of the sample under vacuum in subsequent stages would remove the tetragonal phase and not affect the preparation of ZrW_2O_8. The broad reflections observed are probably due to poor crystallinity in the material, as it has not been sufficiently annealed. A room temperature ^{17}O MAS NMR was recorded by Dr. David Apperley using a Varian Unity Plus 300 spectrometer (see Experimental Section 6.5). Figure 4.2 gives the 1-D ^{17}O spectrum of $Zr^{17}O_2$.

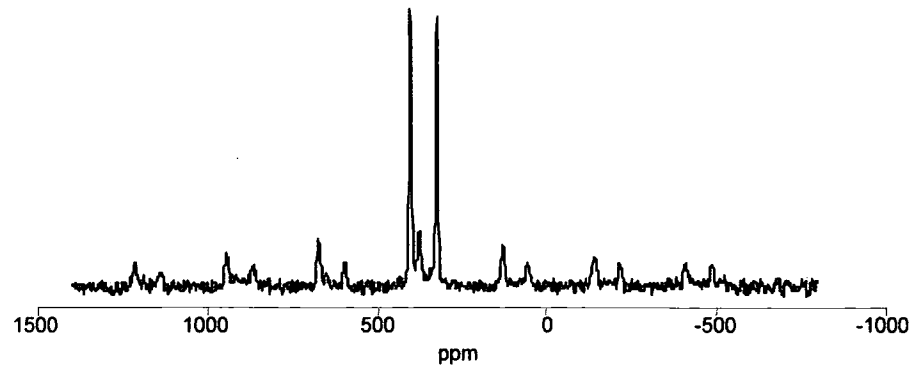

Figure 4.2. ^{17}O MAS NMR spectrum of monoclinic $Zr^{17}O_2$ showing strong resonances at 401 and 323 ppm. The tetragonal $Zr^{17}O_2$ impurity gives rise to the small peak at 376 ppm. Remaining peaks are due to spinning side-bands.

The two intense, sharp peaks at 401 and 323 ppm in a 1 : 1 ratio are assigned to the two trigonal and tetrahedral O environments of the monoclinic structure as reported in the literature.[13,14] The small peak at ~ 376 ppm is due to presence of a single O site in tetragonal ZrO_2.[13]

$W^{17}O_3$ was prepared by an analogous method detailed in Section 7.5.1; WCl_6 was hydrated under a nitrogen atmosphere using ^{17}O water as outlined below.

$$WCl_{6(s)} + 3H_2{}^{17}O_{(l)} \xrightarrow[\text{ii. 473 K, 1 hr, vacuum}\\ \text{iii. 1173 K, 3 hrs, vacuum}]{\text{i. } Et_2O\text{, dry, stir, RT}} W^{17}O_{2.72(s)} + 6HCl_{(g)}$$

A deep blue crystalline solid was obtained after heating under vacuum. X-ray diffraction revealed the identity of this intermediate as $WO_{2.72}$; a phase described by Magneli as $W_{18}O_{49}$. This phase is related to WO_3 in terms of its structure but with a regular array of extended defects; every sixth row consists of edge-sharing WO_6 polyhedra instead of purely corner-sharing. This reduced form of WO_3 is presumably due to heating under dynamic vacuum. Preliminary test experiments revealed that ZrW_2O_8 cannot be prepared successfully from this oxygen deficient phase. It was therefore decided to briefly fire the sample in air in order to oxidise it to WO_3. The chosen conditions were 1223 K for 1 hour; $WO_{2.72}$ was still evident if lower temperatures were used. An 88% yield (1.183 g; SA82A) of bright yellow monoclinic $W^{17}O_3$ was obtained. Phase purity was confirmed by X-ray diffraction. Figure 4.3 shows the Rietveld refinement of SA82A performed using *TOPAS*.

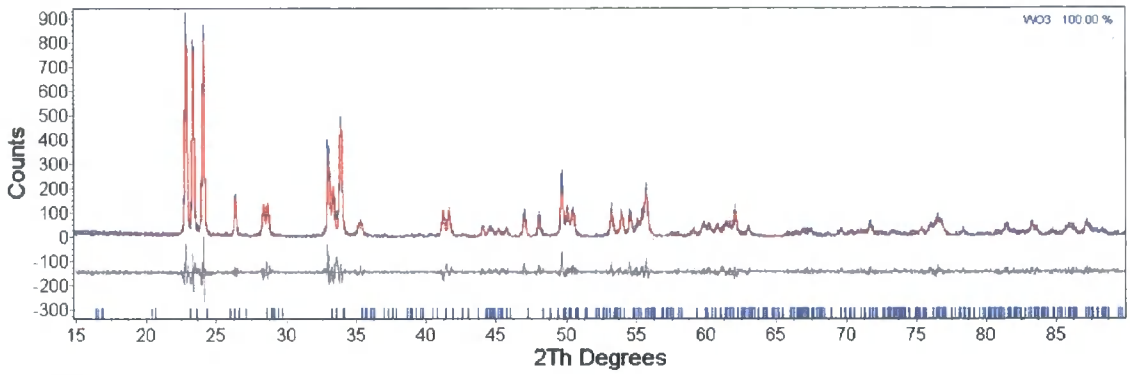

Figure 4.3. Rietveld refinement of a 30-minute X-ray diffraction pattern of $W^{17}O_3$ (SA82A; d8_01376).

A monoclinic starting model for WO_3 was used as reported by Woodward *et al.*;[15] the input file in the e-Appendix shows only minor deviations between the refined and literature lattice parameters. The *TOPAS* refinement shown in Figure 4.3 included 49 variables in its input file: twelve background terms, a sample height correction, a histogram scale factor, six pseudo-Voigt peak terms, three cell parameters and one β cell angle, twenty-four atomic positional parameters (all atoms on general positions) and one overall temperature factor.

^{17}O MAS NMR was performed by Dr. Ian J. King with the assistance of Prof. Dominique Massiot and Dr. Franck Fayon at CNRS-CRMHT, Orléans, France, to verify the presence of ^{17}O in the sample. Figure 4.4 shows the room temperature NMR spectrum of $W^{17}O_3$ (SA82A) obtained using a Bruker DSX 300 spectrometer. Six oxygen sites are assigned from the three observed resonances as discussed by King,[16] confirming the X-ray structure given by Woodward.

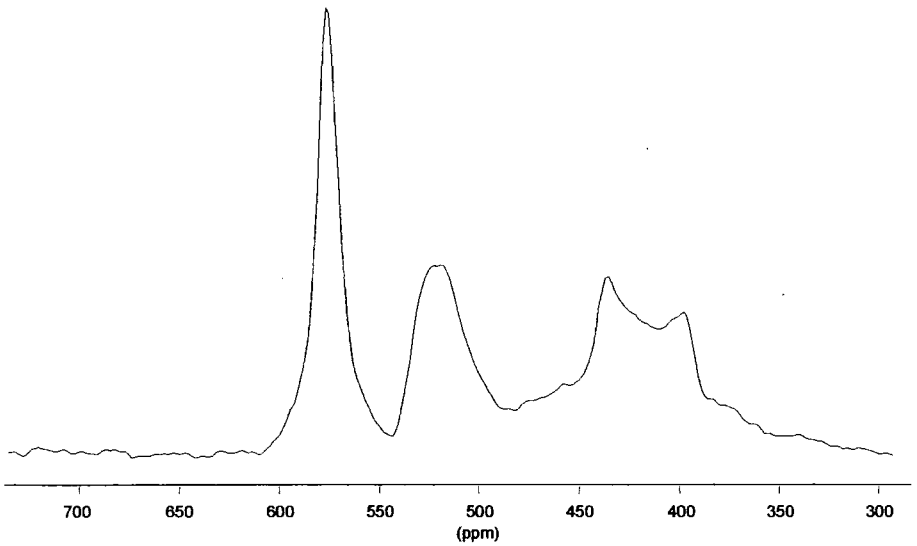

Figure 4.4. $W^{17}O_3$ 1-D ^{17}O NMR pattern (SA82A). The three resonances can be assigned to the six crystallographically distinct oxygens.[16]

4.1.3 Preparation and Characterisation of $ZrW_2{}^{17}O_8$

0.25 g $ZrW_2{}^{17}O_8$ (SA83A) was prepared from a 1 : 2 mole ratio of $Zr^{17}O_2$ (SA82B) and $W^{17}O_3$ (SA82A), in order to obtain variable temperature (VT) ^{17}O NMR data. To prevent exchange of ^{17}O, the sample was prepared in an evacuated quartz tube at 1473 K (see Section 7.5.1 for further details). The purest sample of $ZrW_2{}^{17}O_8$ could be obtained by quenching the ampoule from 1473 K into liquid nitrogen. Rietveld refinement using the *TOPAS* software showed that the best sample (SA83A) contained ~ 72% ZrW_2O_8 and a ~ 28% mixture of monoclinic ZrO_2 and WO_3 (Figure 4.5). Tetragonal ZrO_2 was absent as an impurity. 49 parameters were included in the refinement as shown by the input file displayed in the e-Appendix. A global set of 12 background terms and a sample displacement correction were applied. For ZrW_2O_8, a histogram scale factor, a cubic cell parameter, fractional occupancy parameter, six pseudo-Voigt parameters, eleven (restrained) atomic coordinates and two temperature factors (one for Zr/W, one for O) were refined. ZrO_2 and WO_3 were each described with a scale factor, a single peak shape parameter, three cell parameters, a monoclinic β cell angle and a single temperature factor.

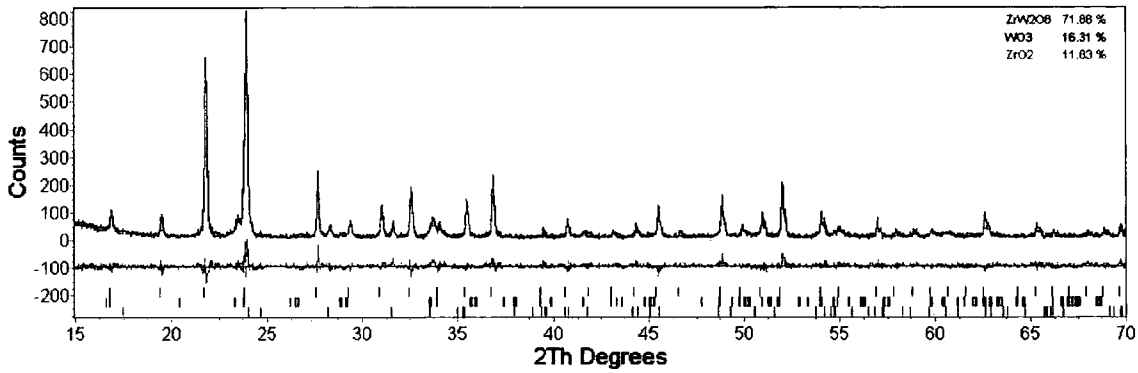

Figure 4.5. Rietveld refinement of $ZrW_2{}^{17}O_8$ (SA83A; d5_02746). The observed 1-hour diffraction pattern recorded on Siemens d5000 X-ray powder diffractometer (detailed in Section 6.1.9) is given in blue; the calculated pattern in red and the difference in grey. Calculated Bragg peak tick marks for ZrW_2O_8 are in blue, WO_3 are in black and ZrO_2 are in green.

It is intriguing to consider why pure ZrW_2O_8 is significantly harder to prepare in sealed tubes than in a normal synthesis using a Pt crucible (as in Section 7.5.2). The Pt crucible presumably allows rapid cooling of the sample when removed from a hot furnace thus promoting the kinetic stabilisation of the ZrW_2O_8 phase. When a sealed tube is used, the quartz tube apparently stays hot for a longer period of time even when quenched in water or liquid nitrogen compared to a Pt crucible in air; this is a sufficiently long period to prevent the rapid cool required to give a pure sample. The pellets of quenched ZrW_2O_8 from an evacuated tube were normally cream/pale grey colour on their surface (*i.e.* ZrW_2O_8) and dark grey within the bulk (ZrO_2/WO_3 impurities), where the quenching was least effective. Pellets were coated in Pt foil to try and dissipate heat more efficiently but this proved unsuccessful. Pure test samples of non-labelled ZrW_2O_8 could occasionally be made in sealed tubes but this seemed chance rather than skill. Repeatability, even after around 50 attempts trying various conditions, proved arduous with sample purities ranging from *e.g.* 2 – 96% with similar heat/quench treatments!

VT solid-state ^{17}O MAS NMR was performed using a Bruker DSX 400 by Dr. Ian J. King with the assistance of Prof. Dominique Massiot and Dr. Franck Fayon at CNRS-CRMHT, Orléans, France. The 1-D MAS NMR spectra at various temperatures are shown in Figure 4.6.

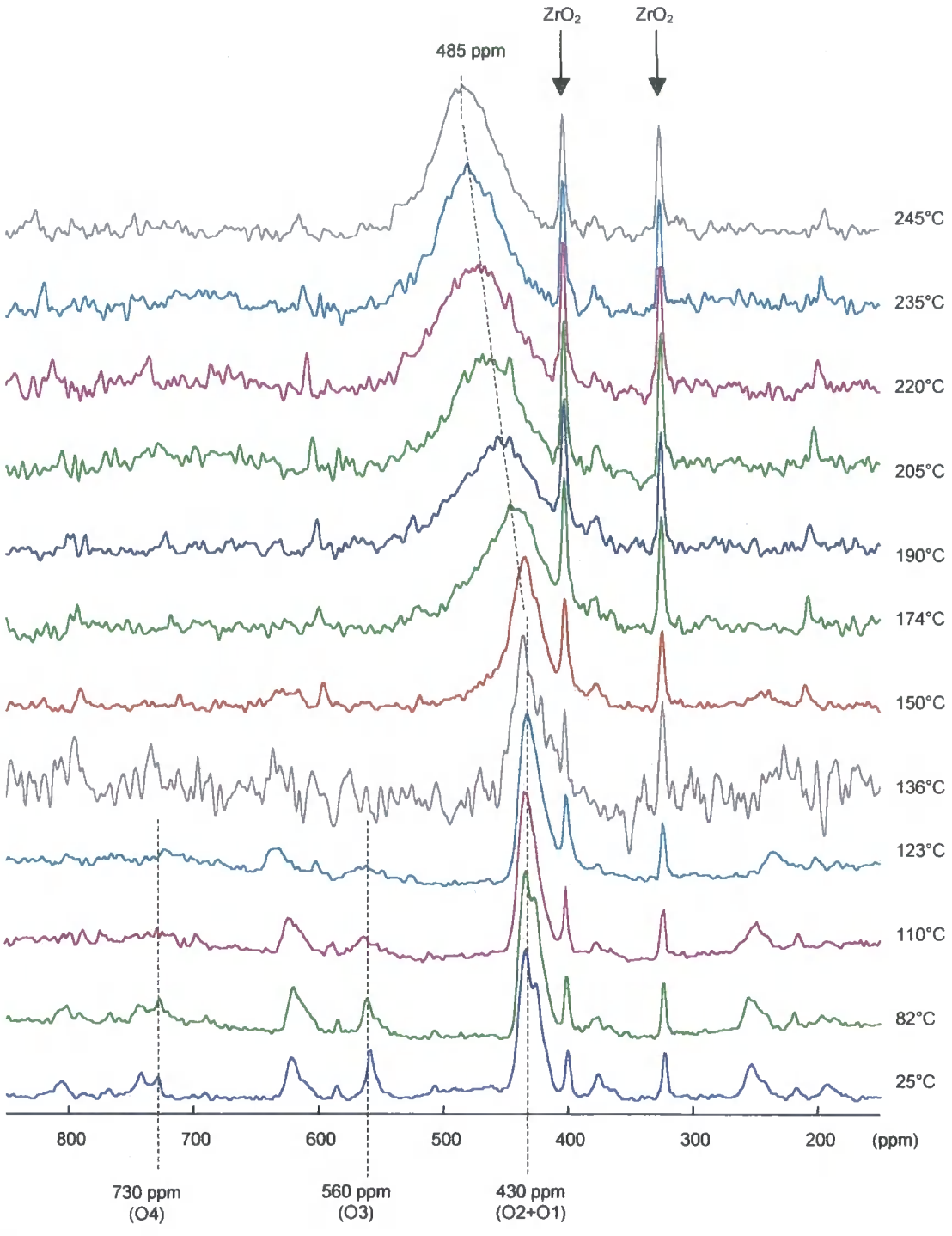

Figure 4.6. Variable temperature ^{17}O MAS NMR of $ZrW_2{}^{17}O_8$ (SA83A). Resonances due to the four unique oxygen atoms of α-ZrW_2O_8 at room temperature are marked, as is the apparent coalescence of these to a single broad resonance at high temperature in β-ZrW_2O_8.

The room temperature spectrum shows four O sites attributable to ZrW_2O_8 consistent with the asymmetric unit of the room temperature $P2_13$ structure reported by Evans.[17] King assigned the peaks at 426 and 434 ppm to the bridging O(1) and O(2) atoms,[16]

while the lower intensity resonances at higher ppm were attributed to the non-bridging O(3) and O(4). The 730 ppm peak was assigned to the strictly one coordinate O(4) atom, consistent with observations in other oxide systems such as $Li_2TiOSiO_4$.[18] Two sharp peaks due to the ZrO_2 impurity are apparent at ~ 400 and 325 ppm. However the WO_3 impurity observed by X-ray diffraction is strangely absent from the spectrum. A possible explanation is the ^{17}O exchange rate between WO_3 could be much greater than that for ZrO_2, such that the resonances due to WO_3 are absent.

As the temperature is increased, the peaks due to "non-bridging" O(3) and O(4) broaden and disappear followed by the broadening of the resonances assigned to bridging O(1) and O(2). Coalescence to form a single broad peak centred at higher chemical shift compared to O(1) and O(2) is finally observed. Above 400 K, the single peak continues to broaden, re-sharpening slightly above 460 K and converging to a chemical shift of ~ 485 ppm. This value is actually approximately equal to the weighted mean chemical shift of the four ZrW_2O_8 resonances at room temperature (483.7 ppm), as presented by King. The implication of this is that complete oxygen exchange occurs in β-ZrW_2O_8; the process is fully reversible as four resonances were observed upon cooling back to room temperature.

The observations by NMR are in contrast to models suggested in the literature for this process. The complete scrambling of O(1) to O(4), which requires the breaking of strong W–O–Zr bonds at such low temperatures is remarkable. Further studies are required to understand this phenomenon; the preparation of $ZrWMo^{17}O_8$ or $ZrMo_2{}^{17}O_8$ and their characterisation by NMR would be interesting. $ZrWMoO_8$ displays an analogous phase transition but at a reduced temperature of 270 K, a room temperature 1-D spectrum would be enough to ascertain if the O equivalence is also apparent in its β phase.

4.2 Hydration of ZrM_2O_8 Phases

4.2.1 Background

To try and develop more effective routes to $ZrW_2{}^{17}O_8$ and other members of this family, investigations of the hydration chemistry of these materials were performed.

Cubic ZrW_2O_8 is inert to hydration at room temperature, however Duan *et al.* have shown that under the autogenous pressure created by hydrothermal conditions at 453 K, water can be inserted in the structure (Figure 1.3) adopting the vacant site at, *e.g.* ~ (¾, ¾, ¾) to give the structure shown in centre of Figure 4.10.[19] Two adjacent WO_4 thus transform to give a vertex bridged pair of pentagonal bipyramids, *i.e.* a $W_2O_8(H_2O)^{4-}$ group, with a concurrent reduction of the unit cell parameter. The hydrated material, $ZrW_2O_8.xH_2O$ does not show negative thermal expansion (NTE) presumably since the flexibility of the Zr–O–W links in the framework is reduced by the included water. Duan also noted that α-ZrW_2O_8 could be reformed by annealing $ZrW_2O_8.xH_2O$ at 423 K in air.

Hydration properties of other cubic $ZrW_{2-x}Mo_xO_8$ phases have not been reported. Of particular interest would be those of $ZrMo_2O_8$ since ^{17}O enrichment of this material cannot be achieved using the methods described in Section 4.1; direct combination of $Zr^{17}O_2$ and $Mo^{17}O_3$ would simply lead to the formation of the thermodynamic trigonal $ZrMo_2{}^{17}O_8$ polymorph. A possible alternative method of enriching cubic $ZrMo_2O_8$ could be direct hydration using $H_2{}^{17}O$, followed by dehydration in air, bearing in mind the similar structures of ZrW_2O_8 and $ZrMo_2O_8$, and the apparent rapid oxygen exchange between all the oxygen sites in ZrW_2O_8. Hydration of cubic $ZrMo_2O_8$ is discussed in the remainder of this chapter.

4.2.2 *In situ* X-ray Diffraction Using Synchrotron Radiation

In situ diffraction experiments were performed on Station 16.4 of the Synchrotron Radiation Source (SRS), Daresbury Laboratory, UK to investigate the reaction of $ZrMo_2O_8$ with H_2O under hydrothermal conditions.

The experimental rig on Station 16.4 takes advantage of the high intensity of synchrotron X-ray radiation, the beam of which passes through a customised steel-walled Parr autoclave,[20] which contains the reactant mixture. Rapid *in situ* diffraction data can be collected as the reaction proceeds. Information such as the extent of reaction as a function of time or the existence of any reaction intermediates can thus be attained. This is in contrast to laboratory hydrothermal reactions where the "black box" nature of the autoclave means *in situ* information cannot be obtained.

In order to penetrate the 0.4 mm steel autoclave, Station 16.4 utilises a high-energy white X-ray beam. In a conventional diffraction experiment one varies 2θ to meet the Bragg condition, $n\lambda = 2d_{hkl}\sin\theta$, for different d_{hkl} values. In energy dispersive diffraction one can use a fixed detector angle, θ allowing simpler cell design. The corresponding Bragg equation becomes $E = K / d_{hkl}\sin\theta$, where E is the detected energy of the diffracted X-rays, θ is the fixed Bragg angle of 2.42 °, and K is a constant equal to 6.19926 keVÅ. One then essentially measures different d_{hkl} values *via* the varying energy of the incident X-rays. Section 6.4 gives further background on *in situ* synchrotron X-ray diffraction.

4.2.3 Hydrothermal Hydration of Cubic $ZrMo_2O_8$

Prior to the synchrotron experiments, several test reactions were performed in the laboratory to ascertain the best conditions to prepare "$ZrMo_2O_8.xH_2O$". Cubic $ZrMo_2O_8$ was prepared as described in Section 7.2.1. Table 4.1 shows the results of initial hydration reactions. Samples of $ZrMo_2O_8$ were weighed out into a 23 ml Teflon lined Parr bomb and various quantities of distilled water added. Different heating regimes were used and these are also outlined in the table, while full experimental details are provided in Section 7.6.1. Laboratory diffraction patterns were recorded using a Siemens d5000 diffractometer and phase fractions derived from Rietveld refinements using *TOPAS*.

Sample i.d.	RAW file	m / g	m_{water} /g	T / K	t / hr	% hydrate	% cubic	% precursor
SA105C	d5_03973	0.1	15	403	1	0	> 99	< 1
SA106C	d5_03990	0.1	15	453	1	0	99	1
SA106A	d5_03981	0.1	15	413	54	0	0	100
SA106B	d5_03987	0.1	15	473	1.25	0	96	4
SA105B	d5_03949	0.5	15	473	2	0	7	93
SA105A	d5_03941	0.5	15	473	16	0	< 2	> 98

Table 4.1. Experimental conditions and product phase percentages for laboratory hydrothermal hydrations of cubic $ZrMo_2O_8$.

The surprising result from the hydration attempts in Table 4.1 is the fact that cubic $ZrMo_2O_8.xH_2O$ is actually never observed. Instead, cubic $ZrMo_2O_8$ apparently rehydrates back to the $ZrMo_2O_7(OH)_2(H_2O)_2$ precursor from which it was originally prepared (Sections 1.3.2.1, 2.2.6 and 7.2). Conversion to $ZrMo_2O_7(OH)_2(H_2O)_2$ is almost complete when heating for 2 hours at 473 K. This alternative hydration process has been observed for the first time. It is noteworthy in the laboratory tests performed above that the LT-$ZrMo_2O_8$ intermediate phase was absent, when a mixture of cubic and precursor was present. Figure 4.7 gives a portion of a Rietveld fit of cubic $ZrMo_2O_8$ after hydrothermal treatment at 473 K for 75 minutes (SA106B). Additional small peaks at ~ 15.6, 24.7 and 28.6 ° 2θ are due to the evolution of the precursor phase. Typical refinement input files are included in the e-Appendix and contained 26 independent parameters: a sample height correction, twelve background terms, a histogram scale factor for each of the three phases, four cell parameters in total (for the tetragonal precursor and two cubic phases), one peak shape term for each phase and one temperature factor for each phase.

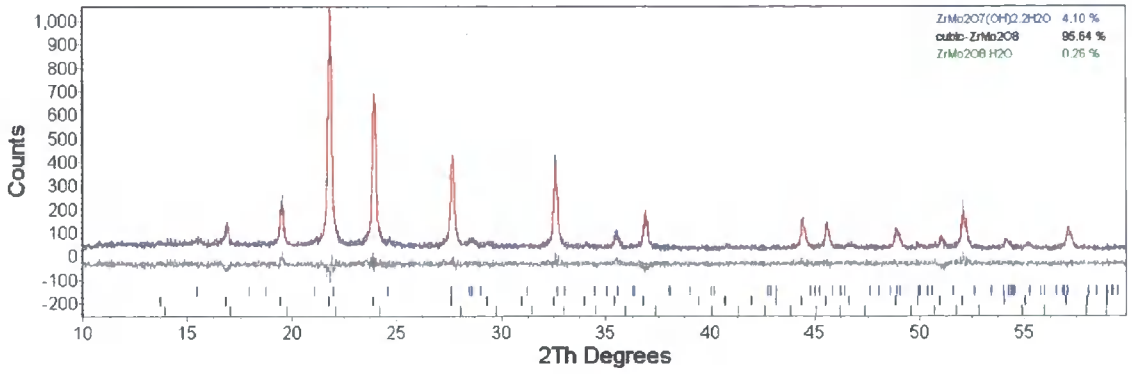

Figure 4.7. Rietveld refinement of partially hydrated cubic $ZrMo_2O_8$ (SA106B; d5_03987, 3.5 hour data collection). Blue tick marks show the appearance of the hydrated $ZrMo_2O_7(OH)_2(H_2O)_2$ phase.

Figure 4.8 displays successive *in situ* diffraction patterns obtained from the hydration of cubic $ZrMo_2O_8$ at 473 K using the hydrothermal rig at Station 16.4, Daresbury Laboratory. Experimental details are located in Section 7.6.1 for run #103205.

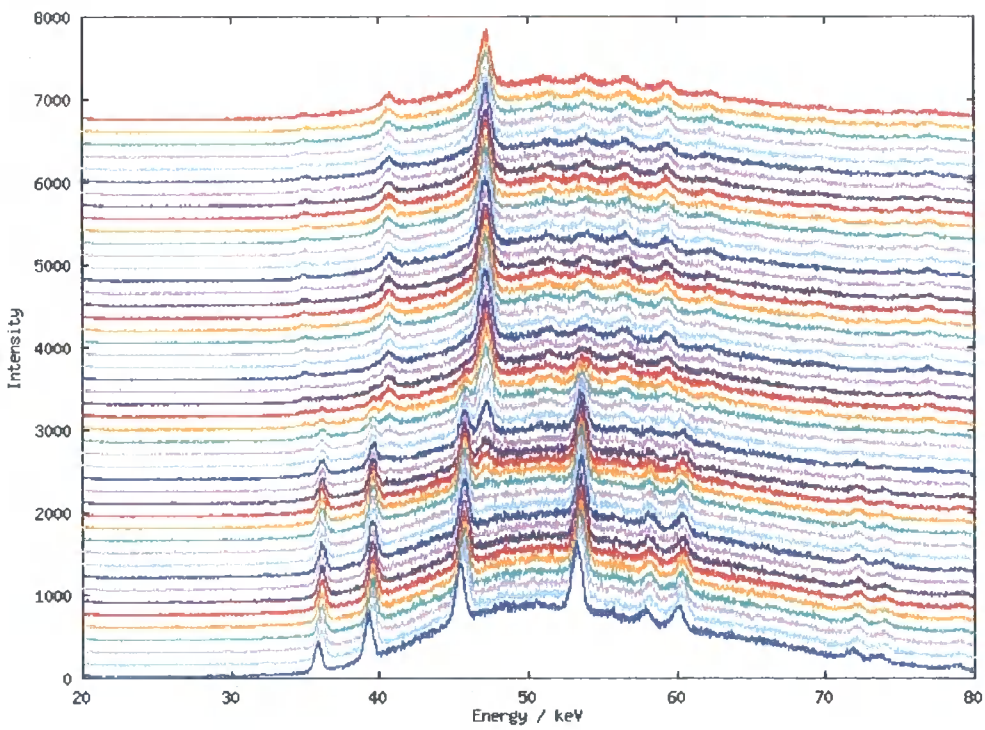

Figure 4.8. 6-minute *in situ* X-ray synchrotron patterns as a function of time for the hydration of cubic $ZrMo_2O_8$ (base of figure) to $ZrMo_2O_7(OH)_2(H_2O)_2$ (top of figure). The corresponding *d*-spacing range shown is 7.34 to 1.84 Å.

TOPAS was configured to model the energy dispersive diffraction data in Figure 4.8 and Pawley fits performed on the cubic starting phase (range #1) and final product hydrated phase (range #45).[21] Relative intensities of peaks were fixed at values from these

individual fits and a two-phase Pawley refinement performed on each experimental range (see the e-Appendix for the seed input file). Scale factors from these fits were normalised for beam decay and scaled to vary from 0 to 1 to represent the extent of reaction. Figure 4.9 gives the extent of reaction as a function of time and clearly shows the complete conversion of the cubic phase to the precursor after 2 hours. A cross-over point at precisely one-half is observed, implying there are no intermediates involved in the reaction nor is there any significant build up of amorphous material. The lack of a LT intermediate is apparent from the *in situ* data given in Figure 4.8 and the intensity plot of Figure 4.9, which confirms the above laboratory observations.

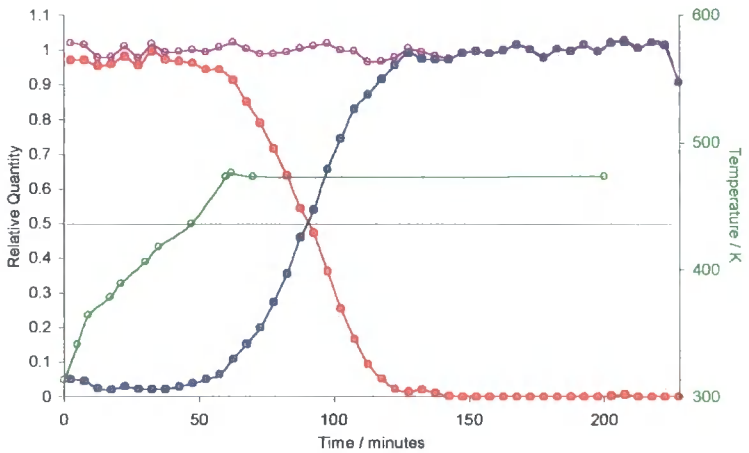

Figure 4.9. Refined and normalised extent of reaction versus time for the *in situ* hydration of cubic $ZrMo_2O_8$ to $ZrMo_2O_7(OH)_2(H_2O)_2$ upon warming to 473 K (run #103205). The temperature profile through the course of the reaction, and scaled sum of normalised scale factors are also shown. This plot is taken from a spreadsheet given in the e-Appendix.

Since cubic $ZrMo_2O_8$ hydrates to $ZrMo_2O_7(OH)_2(H_2O)_2$, the $ZrMo_2O_8$ phase relationship cycle can be revised from that given in Figure 1.12. Information described in Chapter 2 on LT phases that relate the precursor to cubic $ZrMo_2O_8$ upon dehydration can also be added. The reverse relationship has been described here albeit minus the occurrence of the LT intermediate. The updated $ZrMo_2O_8$ phase chart at ambient pressure is displayed in Figure 4.10.

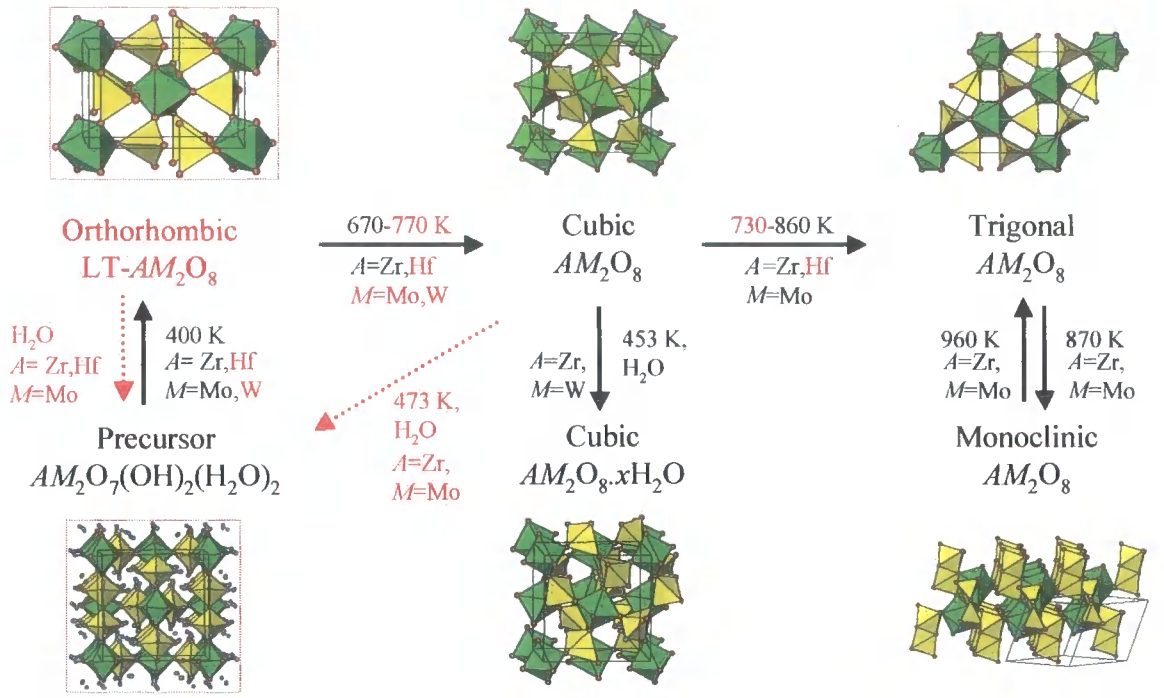

Figure 4.10. Summary of the temperature-dependence of AM_2O_8 and related phases taken from the literature, and from studies presented in this thesis so far (highlighted in red). One final phase will be appended from studies found in Chapter 5.

The hydration of cubic $ZrMo_2O_8$ under ambient conditions was investigated although the material seemed to be inert like ZrW_2O_8. In contrast to LT-$ZrMo_2O_8$, the diffraction pattern of cubic $ZrMo_2O_8$ remained unchanged after a sample had been left in a vial for 4 months. Exposing a sample to warm, moist conditions for 1 month also had no affect on its diffraction pattern; conversion back to the precursor is clearly not as facile as in the case of rehydration of the LT intermediate (Section 2.2.6). Hydrothermal treatment of cubic $ZrMo_2O_8$ seems necessary in order for the material to rehydrate back to the precursor.

4.2.4 Hydration of Trigonal $ZrMo_2O_8$

The existence of a possible "hydrated trigonal" phase was briefly investigated, however an attempt to hydrate in a Parr autoclave at 473 K overnight was unsuccessful (details in Section 7.6.2). The powder pattern of the resulting material (SA109A) was identical to the starting material (SA6A, Section 7.7), emphasising the high stability of the condensed trigonal phase relative to the cubic polymorph.

4.3 Conclusion

A novel air-sensitive route to the ^{17}O enrichment of ZrW_2O_8 has been devised and the results of variable temperature (VT) ^{17}O MAS NMR presented, with the goal of achieving further information on the change in local structure during the α to β phase transition described *via* VT X-ray and neutron diffraction studies by Evans *et al.*.[17] VT NMR studies have shown that the four oxygen environments of α-ZrW_2O_8 which exist at room temperature become equivalent above the phase transition temperature of 448 K. Complete exchange between all oxygen sites at this temperature is surprising. Perhaps the best way to further this work would be the ^{17}O preparation and NMR study of purer, more highly enriched samples of this and other members of the cubic $ZrW_{2-x}Mo_xO_8$ family. The hydration chemistry of ZrM_2O_8 phases developed in this chapter may enable such samples to be prepared.

With regards to hydration of ZrM_2O_8 phases, the literature reports that cubic ZrW_2O_8 hydrates to $ZrW_2O_8.xH_2O$ by hydrothermal insertion of H_2O.[19] In contrast, it has been shown in this chapter when cubic $ZrMo_2O_8$ is subject to the same conditions it hydrates directly to $ZrMo_2O_7(OH)_2(H_2O)_2$. This is the reverse reaction to that described in Chapter 2, although *in situ* studies have shown that no LT intermediate is observed during the course of the hydration reaction. It suggests that ^{17}O could be introduced into cubic $ZrMo_2O_8$ by successive hydration/dehydration for use in future ^{17}O MAS NMR studies. Cubic $ZrMo_2O_8$ seems to be relatively stable towards hydration at ambient temperature and pressure unlike *e.g.* $ZrWMoO_8$, which is noted to hydrate in air giving a broadened diffraction pattern. The ease of hydration of ZrM_2O_8 materials qualitatively follows the trend: LT-$ZrMo_2O_8$ > cubic $ZrWMoO_8$ >> cubic $ZrMo_2O_8$ > cubic ZrW_2O_8 > trigonal $ZrMo_2O_8$. Note, however that the hydration process referred to in LT and cubic $ZrMo_2O_8$ is distinct to that in cubic ZrW_2O_8.

4.4 References

1. J. S. O. Evans, T. A. Mary, T. Vogt, M. A. Subramanian, A. W. Sleight, *Chem. Mater.*, **8**, 1996, 2809-2823.

2. J. S. O. Evans, P. A. Hanson, R. M. Ibberson, U. Kameswari, N. Duan, A. W. Sleight, *J. Am. Chem. Soc.*, **122**, 2000, 8694-8699.
3. L. L. Y. Chang, M. G. Scroger, B. Phillips, *J. Am. Ceram. Soc.*, **50**, 1967, 211-215.
4. D. K. Smith, W. Newkirk, *Acta Cryst.*, **18**, 1965, 983-991.
5. O. Ruff, F. Ebert, *Z. Anorg. Chem.*, **180**, 1929, 19-41.
6. G. Teufer, *Acta Cryst.*, **15**, 1962, 1187.
7. R. N. Patil, E. C. Subbarao, *Acta Cryst.*, **A26**, 1970, 535-542.
8. A. V. Chadwick, G. Mountjoy, V. M. Nield, I. J. F. Poplett, M. E. Smith, J. H. Strange, M. G. Tucker, *Chem. Mater.*, **13**, 2001, 1219-1229.
9. R. C. Garvie, *J. Phys. Chem.*, **69**, 1965, 1238-1243.
10. R. C. Garvie, *J. Phys. Chem.*, **82**, 1978, 218-223.
11. H. M. Rietveld, *J. Appl. Cryst.*, **2**, 1969, 65-71.
12. A. A. Coelho, *TOPAS v2.0: General Profile and Structure Analysis Software for Powder Diffraction Data*, Bruker AXS, Karlsruhe, 2000.
13. T. J. Bastow, S. N. Stuart, *Chem. Phys.*, **143**, 1990, 459-467.
14. T. J. Bastow, M. E. Smith, H. J. Whitfield, *J. Mater. Chem.*, **2**, 1992, 989-990.
15. P. M. Woodward, A. W. Sleight, T. Vogt, *J. Phys. Chem. Sol.*, **56**, 1995, 1305-1315.
16. I. J. King, Ph.D. Thesis, University of Durham, 2003.
17. J. S. O. Evans, W. I. F. David, A. W. Sleight, *Acta Cryst.*, **B55**, 1999, 333-340.
18. T. J. Bastow, G. A. Botton, J. Etheridge, M. E. Smith, H. J. Whitfield, *Acta Cryst.*, **A55**, 1999, 127-132.
19. N. Duan, U. Kameswari, A. W. Sleight, *J. Am. Chem. Soc*, **121**, 1999, 10432-10433.
20. J. S. O. Evans, R. J. Francis, D. O'Hare, S. J. Price, S. M. Clark, J. Flaherty, J. Gordon, A. Nield, C. C. Tang, *Rev. Sci. Instr.*, **66**, 1995, 2442-2445.
21. G. S. Pawley, *J. Appl. Cryst.*, **14**, 1981, 357-361.

Chapter Five: Variable Temperature Structural Studies and Phase Transitions in Trigonal AMo_2O_8 Materials

5.1 Trigonal $ZrMo_2O_8$

5.1.1 Background

Several different polymorphs of $ZrMo_2O_8$ have been reported in the literature and also in Chapters 2 (LT-$ZrMo_2O_8$) and 3 (cubic γ-$ZrMo_2O_8$) of this thesis. Trigonal α-$ZrMo_2O_8$,[1] and monoclinic β-$ZrMo_2O_8$,[2] are the thermodynamically stable ambient pressure polymorphs at high and low temperatures, respectively. The β to α transition occurs at around 960 K;[2] the reverse reaction requires prolonged heating at 873 K.[3] Cubic γ-$ZrMo_2O_8$ is metastable and converts to trigonal α-$ZrMo_2O_8$ at 663 K.[4] Under the influence of pressure, trigonal α-$ZrMo_2O_8$ reversibly converts to a different monoclinic phase termed δ-$ZrMo_2O_8$ at around 1.1 GPa which subsequently becomes triclinic ε-$ZrMo_2O_8$ above 2.0 GPa.[5] Cubic γ-$ZrMo_2O_8$ also undergoes a reversible pressure-induced first order phase transition at 0.7 GPa although to date, details of this distorted cubic phase are not known.[6] Figure 1.12 outlines the relationships between the various members of the known $ZrMo_2O_8$ polymorphs mentioned above.

As mentioned above, trigonal α-$ZrMo_2O_8$ is the most thermodynamically stable polymorph at high temperature (at 1 bar), being a more condensed phase than the cubic γ form (density = 3.93 gcm^{-3} versus 3.59 gcm^{-3} for cubic). It can be prepared relatively easily by direct combination of the binary oxides ZrO_2 and MoO_3 and has been known since the 1960s.[7,8] This basic preparation is in stark contrast to ZrW_2O_8, where only the cubic phase (and not trigonal) is observed using traditional high temperature solid-state synthesis. Another route as stated above is *via* monoclinic β-$ZrMo_2O_8$ which converts to the trigonal form at 963 K and, when rapidly quenched in air, is recoverable at room temperature.[2]

The room temperature (RT) structure of trigonal $ZrMo_2O_8$ was convincingly reported in a single crystal study in 1986 by Auray *et al.*.[1] Single crystals were prepared from a 1:2 ZrO_2/MoO_3 mix with an excess of MoO_3 at 1123 K. Thoret *et al.* had previously reported powdered trigonal $(Zr/Hf)Mo_2O_8$ in the 1960s and gave the correct space group of $P\bar{3}1c$ and approximately correct cell parameters.[7] However the atomic coordinates reported seem incorrect and do not make chemical sense (see Section 5.2.1).[9] The re-determined structure presented by Auray is shown in Figure 5.1 and consists of non-bonded layers of two types of regular $Zr^{IV}O_6$ octahedra vertex linked to six distorted $Mo^{VI}O_4$ tetrahedra. They have three vertices each shared to ZrO_6 and one vertex that is not linked; the O(4) atom remains mono-coordinate and has a shorter bond to Mo compared to the other three oxygens (bond length of 1.69 Å versus 1.76 Å). It is generally a rare feature that a condensed solid possesses a mono-coordinate oxygen but it is quite common in the various polymorphs of AM_2O_8 (see LT phases in Chapter 2 and cubic phases in Chapter 3).

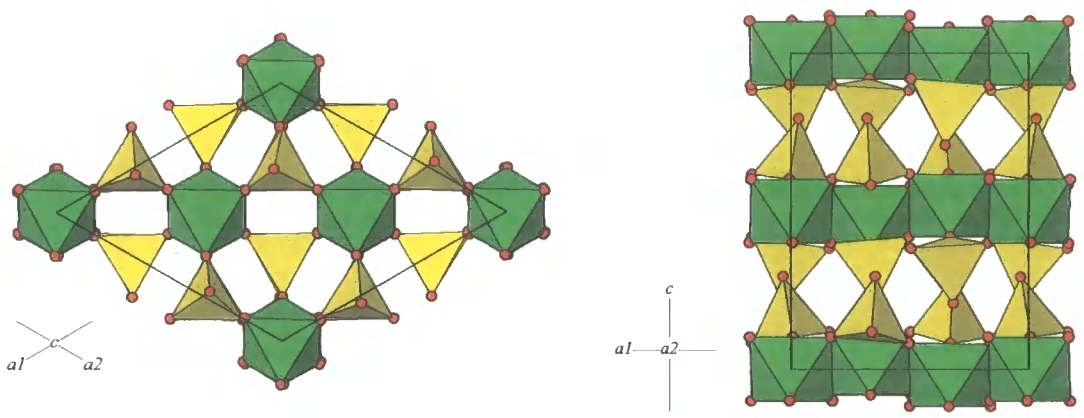

Figure 5.1. Projections of Auray's structure of trigonal $ZrMo_2O_8$ viewed down the *c* (*left*) and *b* axes (*right*), showing two crystallographically distinct ZrO_6 and one MoO_4 polyhedra. One vertex of each MoO_4 group remains uncoordinated (the O(4) atom).

It is worth noting that the Mo–O(4) bond is not parallel to the *c* direction and the base of the tetrahedra lie slightly out of the *ab* plane. The non-bonded layers are stacked along [001] with two layers per unit cell and are held together by inter-layer Mo···O(4) van der Waals interactions.[10]

Mittal *et al.* briefly reported the thermal expansion behaviour of trigonal $ZrMo_2O_8$ in 1999,[11] through a series of Rietveld refinements of a powder sample at ten different temperatures from 80 – 925 K.[12] A $P\bar{3}1c$ structure was assumed throughout; the *a* axis

was shown to undergo low negative thermal expansion with a mean linear expansion coefficient of $\alpha_a = -3.9 \times 10^{-6}\ K^{-1}$ ($\alpha_a = (a_T - a_0)/a_0(T - T_0)$). The c axis showed large positive thermal expansion, presumably as a result of the weak bonding of the layers in this direction. The mean expansion coefficient was $\alpha_c = +52 \times 10^{-6}\ K^{-1}$ but, as shown in Figure 5.2, the expansion is very anisotropic in nature.

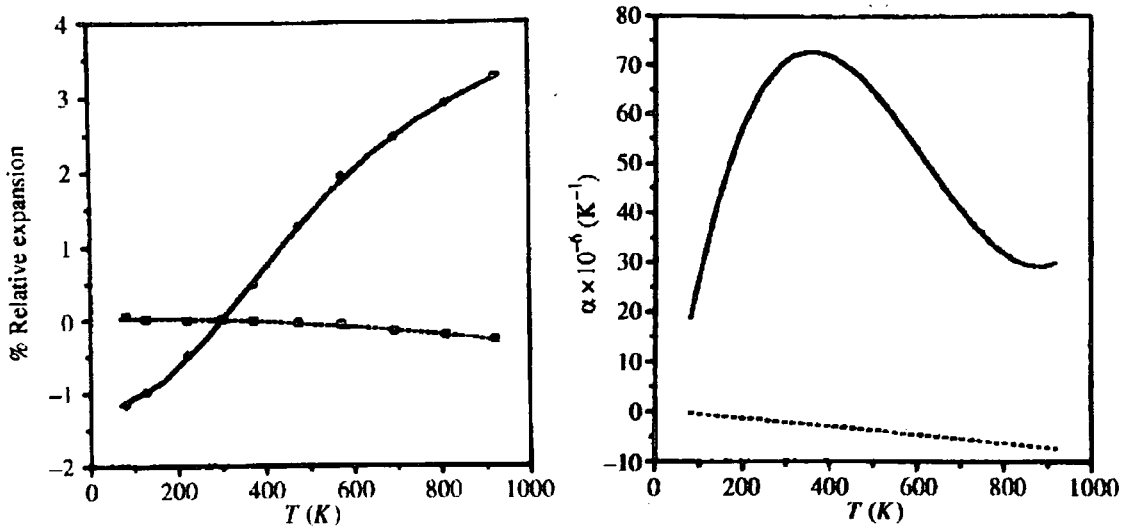

Figure 5.2. The expansion of the a axis (dotted line) and c axis (bold line) relative to 300 K (*left*) of trigonal $ZrMo_2O_8$ obtained by Mittal. Also shown is the corresponding temperature dependence of the linear expansion coefficients, α_a (dotted) and α_c (bold) (*right*).

The thermal expansion shown in Figure 5.2 is puzzling. The material shows a continuous expansion over the whole temperature range studied, though the rate of expansion seems to decrease significantly at higher temperatures. Such behaviour is contrary to that seen in most materials, where a simple phonon-driven expansion generally leads to essentially linear expansion at high temperatures. Thus, more detailed variable temperature work was deemed necessary and is described in this chapter.

In 1999, Wilkinson *et al.* reported the existence of trigonal ZrW_2O_8 for the first time, which was prepared *via* a sol-gel route.[13] Unlike the molybdate, the trigonal tungstate is not observed by direct combination of ZrO_2 and WO_3 at high temperature. The reported synthesis was of a more complex nature; $Zr(O^iPr)_4 \cdot {}^iPrOH$ in THF/$^iPr_2O$ was added to WCl_6 in $CHCl_3$, sealed in a tube and heated at 383 K for one week, after which the solid was centrifuged and dried. Trigonal ZrW_2O_8 was obtained from this amorphous gel by heating to 773 K for 2 hours, 873 K for 1 hour, and placing the resultant material in a

preheated furnace at 1013 K for 30 minutes. The powder pattern obtained was very similar to that of trigonal $ZrMo_2O_8$ and the refined cell parameters obtained were comparable to those given by Auray for $ZrMo_2O_8$ as in Table 5.1. Wilkinson also put forth an alternative structural model: the $P\bar{3}$ model observed in the perrhenate, MRe_2O_8 (M = Mn, Co, Ni and Zn) series of materials which seemed to give just as good Rietveld refinements, although no residual factors were quoted.

The perrhenate $P\bar{3}$ structure and its similarity to trigonal $ZrMo_2O_8$, was published by Butz *et al.*.[14] The structure is given in Figure 5.3. It shares features with trigonal $ZrMo_2O_8$ in that it consists of non-connected layers of vertex linked $Mn^{II}O_6$ and $Re^{VII}O_4$ where one apex of the tetrahedra is mono-coordinated.

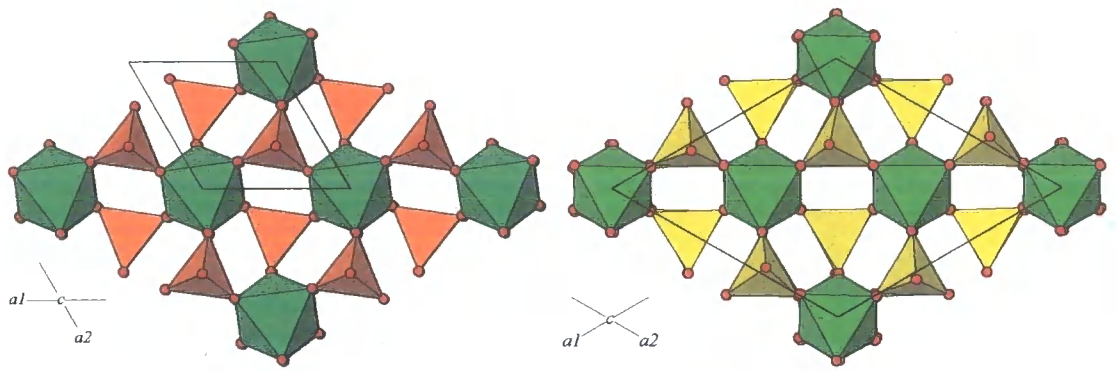

Figure 5.3. Projections of $MnRe_2O_8$ (*left*) and trigonal $ZrMo_2O_8$ (*right*) along [001].

The principal difference between the two structure types is that there is only one type of octahedron and tetrahedron in the $MnRe_2O_8$ structure. There are three-fold axes down the centre of the tetrahedra and octahedra, and the volume of the $P\bar{3}$ unit cell is one-sixth of that in $P\bar{3}1c$. The key to the different structures is apparent from the contrasting the polyhedral distortions present. In the perrhenate, the tetrahedra are only free to rotate about the three-fold axis and their basal plane is therefore forced to lie parallel to the *ab* plane of the unit cell; in the $ZrMo_2O_8$ structure this is not the case (Figure 5.1, *right*).

5.1.2 Synthesis and Room Temperature Structural Refinement of $ZrMo_2O_8$

A 2 g sample of trigonal $ZrMo_2O_8$ (SA6A) was prepared by a slight modification of published methods and its identity and purity confirmed by powder XRD.[11,15] The actual conditions used are given in Section 7.7.

A high-resolution 8 hour room temperature powder pattern was collected on the d8 X-ray diffractometer (HTK1200 furnace stage, sprinkled sample on SiO_2 disk, 1 ° divergence slit, 10 – 120 ° 2θ and a step size of 0.0144 ° 2θ) and was refined using *TOPAS* (Section 6.1.11);[16] the resulting Rietveld plot is shown below in Figure 5.4. A trace amount of ZrO_2 impurity is present. Refinement results compared to the single-crystal values given by Auray,[1] are shown in Table 5.1. A rigid-tetrahedral approach with bond length constraints was employed because the O(4) atom could not be easily refined in presence of the heavy metal atoms. Detailed refined parameters are available as the sample *TOPAS* input file in Appendix A3.1 or in the Electronic Appendix (e-Appendix). In total 43 variables were refined including 12 background terms, a global sample height correction, 23 variables for $ZrMo_2O_8$ (histogram scale, two trigonal cell parameters, six Pseudo-Voigt (hereafter, PV) peak profile terms, one Zr(2) and three Mo atomic coordinates, three rigid-body tetrahedral rotational angles and seven atomic displacement parameters) and 7 parameters for the trace ZrO_2 impurity (histogram scale, three cell parameters, one cell angle and one peak shape term and one isotropic temperature factor).

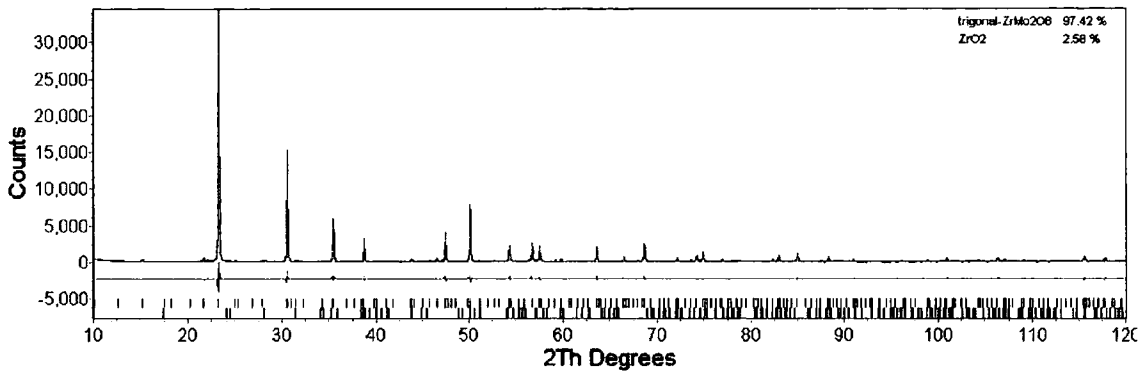

Figure 5.4. Rietveld refined pattern for trigonal $ZrMo_2O_8$ (SA6A, d8_01945:1). Red trace = calculated pattern, blue trace = observed pattern, grey trace = difference, blue tick marks are calculated positions for $ZrMo_2O_8$ Bragg reflections and black tick marks are calculated for ZrO_2.

The rigid-body model in the above refinement is employed throughout this chapter and consists of a rigid MoO_4 tetrahedron with bond lengths fixed at distances given by Auray.[1] The tetrahedron is defined such that the Mo atom is at the origin with the oxygens placed at the corners of a distorted tetrahedron in which the two-coordinate O(1), O(2), O(3) are 1.76 Å away from Mo while the terminal O(4) atom is fixed at 1.69 Å from Mo. The oxygen atoms now lose their individual translational degrees of freedom and only the three molybdenum coordinates and three tetrahedral rotational angles, *rotx*, *roty*, *rotz* are introduced, and refined. These rotational angles give information on how much rotation there is about the *a*, *b* and *c* axes, respectively and will be the most important refined parameters in this chapter. The values are defined such that when the base of the tetrahedron exactly lies in the *ab* plane, *rotx* and *roty* are zero. *Rotz*, which describes the rotation of the basal plane of the tetrahedron, is defined such that a value of –30 ° corresponds to a Zr–O–Mo bond angle whose projection down the *ab* plane is 180 ° (compare Figure 5.1 and Table 5.1). The refined rotational angles at room temperature show that the tetrahedra are tilted away from the *ab* plane (magnitude of *rotx* = 6.4 °, *roty* = 10.8 °).

	302 K, d8_01945:1	Auray single crystal
Cell parameter *a* / Å	10.14097 (6)	10.1391 (6)
Cell parameter *c* / Å	11.71111 (13)	11.7084 (8)
Cell volume *V* / Å^3	1043.01 (2)	1042.4 (2)
Rotational angle *rotx* / °	–6.4 (8)	N/A
Rotational angle *roty* / °	–10.8 (4)	N/A
Rotational angle *rotz* / °	–29.2 (2.9)	N/A
Zr(1) *x*, *y*, *z*	0, 0, 0	0, 0, 0
Zr(2) *x*, *y*, *z*	⅓, ⅔, 0.98256 (34)	⅓, ⅔, 0.98132 (8)
Mo *x*, *y*, *z*	0.32929, 0.33757, 0.14917	0.32871 (7), 0.33891 (7), 0.14900 (3)
O(1) *x*, *y*, *z*	0.33405, 0.49347, 0.07843	0.3323 (9), 0.4959 (6), 0.0814 (3)
O(2) *x*, *y*, *z*	0.49731, 0.33310, 0.11847	0.4979 (5), 0.3364 (9), 0.1178 (3)
O(3) *x*, *y*, *z*	0.17006, 0.16698, 0.10638	0.1731 (6), 0.1664 (6), 0.1008 (4)
O(4) *x*, *y*, *z*	0.31631, 0.35593, 0.29153	0.3189 (6), 0.3522 (6), 0.2923 (3)
Zr(1) B_{iso} / Å^2	2.37 (35)	1.06 (3)
Zr(2) B_{iso} / Å^2	1.56 (13)	0.93 (2)
Mo B_{iso} / Å^2	1.70 (3)	0.80 (2)
O(1) B_{iso} / Å^2	2.40 (48)	1.9 (2)
O(2) B_{iso} / Å^2	3.21 (62)	1.9 (2)
O(3) B_{iso} / Å^2	3.65 (99)	1.7 (1)
O(4) B_{iso} / Å^2	2.53 (30)	2.3 (2)
R_{Bragg} ($\equiv R_{F^2}$)	0.0261 (trigonal)	0.031
${}_wR_p$	0.106	N/A
χ^2	1.68	N/A

Table 5.1. Refined parameters in $P\bar{3}1c$ for trigonal $ZrMo_2O_8$ at room temperature versus literature values by Auray *et al.*. Note the figures in brackets denote the standard error (ESD). No such ESD values exist for Mo and O coordinates in the rigid-body refinement as *rotxyz* are refined instead.

5.1.3 Variable Temperature XRD and Rietveld Refinement of $ZrMo_2O_8$

The aim of this work was to carry out a more detailed variable temperature X-ray diffraction (VTXRD) study on powdered trigonal $ZrMo_2O_8$, to that reported by Mittal *et al.*. It was envisaged that carrying out a full Rietveld refinement every 10 K (instead of every 90 K or so in Mittal's data collection) would help reveal the origin of the unusual expansion of this material.

A > 97% pure sample of trigonal $ZrMo_2O_8$ (SA6A) was ground and an α-Al_2O_3 internal standard was added (see Section 7.7), so that the actual sample temperature in the Anton Paar HTK1200 furnace could be calibrated. The combined trigonal $ZrMo_2O_8/Al_2O_3$ sample (SA6B) was sieved onto an amorphous SiO_2 disc coated with a thin layer of vacuum grease and mounted in the HTK1200 furnace of a Bruker d8 diffractometer (further instrument details are given in Section 6.1). 30-minute X-ray powder patterns were recorded in air from 302 to 922 K in 10 K increments (giving a total of 63 ranges in the run d8_01861). A heat rate of 0.2 Ks^{-1} was used and the 2θ range collected at each temperature was $10 - 115\,°$. A maximum temperature of 922 K was chosen, similar to that employed by Mittal (925 K), since Figure 2.8 illustrates that trigonal $ZrMo_2O_8$ is only stable up to ~ 990 K, decomposing to ZrO_2 and MoO_3 above this temperature.

Low temperature X-ray data on trigonal $ZrMo_2O_8$ were acquired using an Oxford Cryosystems PheniX cryostat from 300 – 17 K, at a constant cooling rate of 13 Khr^{-1} and in the range $12 - 120\,° 2\theta$. Trigonal $ZrMo_2O_8$ (SA6A) was sprinkled onto a Vaseline-smeared flat aluminium sample holder and 30 minute scans were recorded (thus on average one scan every ~ 6.5 K was obtained).

For the HTK1200 data, d8_01861, a *TOPAS* file was set up for a two-phase atomic refinement at room temperature and is reported with all the refined values in the e-Appendix. 44 variables were refined - the global variables were twelve Chebyshev background coefficients and one sample displacement. For $ZrMo_2O_8$, a scale factor, two cell parameters, six PV profile parameters, four atomic coordinates, three tetrahedral angles of rotation and seven isotropic temperature factors were also refined. In addition,

a scale factor, two cell parameters, one peak shape parameter, two atomic coordinates and two temperature factors were refined for Al_2O_3. The ZrO_2 impurity was not modelled since it is not detectable in these rapid scans. A typical Rietveld plot (that at 302 K) is shown in Figure 5.5. This refinement was used as a seed for all other temperatures.

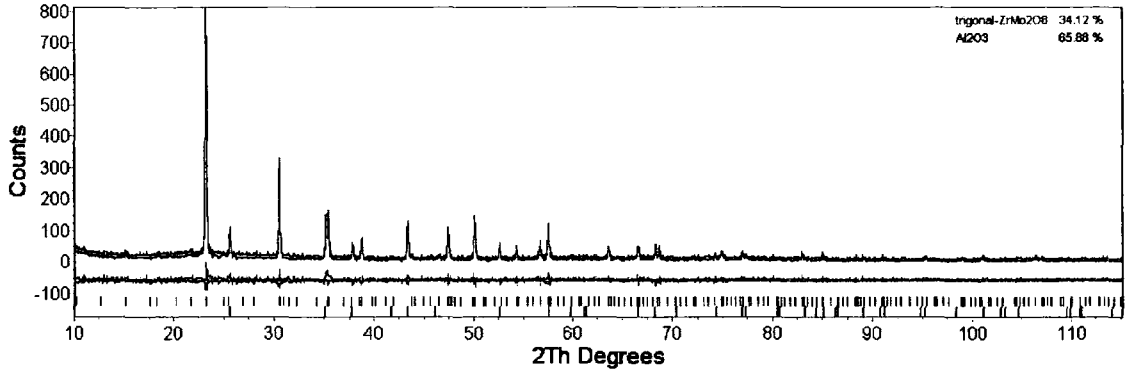

Figure 5.5. 302 K two-phase Rietveld plot of trigonal $ZrMo_2O_8$ (blue calculated tick marks) and Al_2O_3 (black calculated tick marks); sample SA6B, run number d8_01861.

An α-Al_2O_3 internal standard was employed so the actual sample temperatures throughout the VT data collection could be determined. The temperature dependence of the cell volume of α-Al_2O_3 has been accurately collated and parameterised by Taylor.[17] A simple scaled second-order polynomial expression is sufficient to describe the trend and further details are given in Section 6.1.3. Figure 5.6 illustrates the refined versus Taylor cell volume of α-Al_2O_3 from 302 – 922 K. The discrepancy in temperature inherent to the HTK1200 (the sample is hotter than the thermocouple reading) is thus extracted from the cell volumes and fitted with a cubic function; this is also shown in the figure. The full analysis is given in the *Excel* sheet in the e-Appendix.

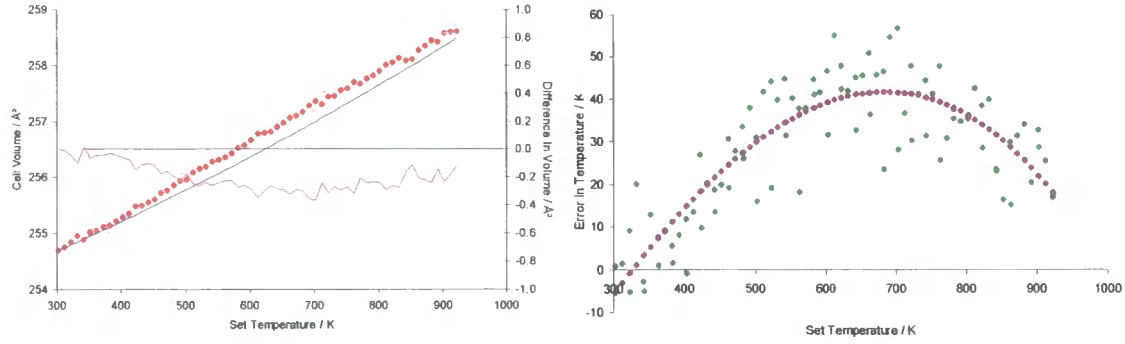

Figure 5.6. Observed versus Taylor literature cell volume data for α-Al_2O_3 including difference curve (d8_01861; *left*). The resultant temperature error and its parameterisation are shown on the right.

The PheniX data were refined using the *TOPAS* input file presented in the e-Appendix and a typical Rietveld plot is given in Figure 5.7.

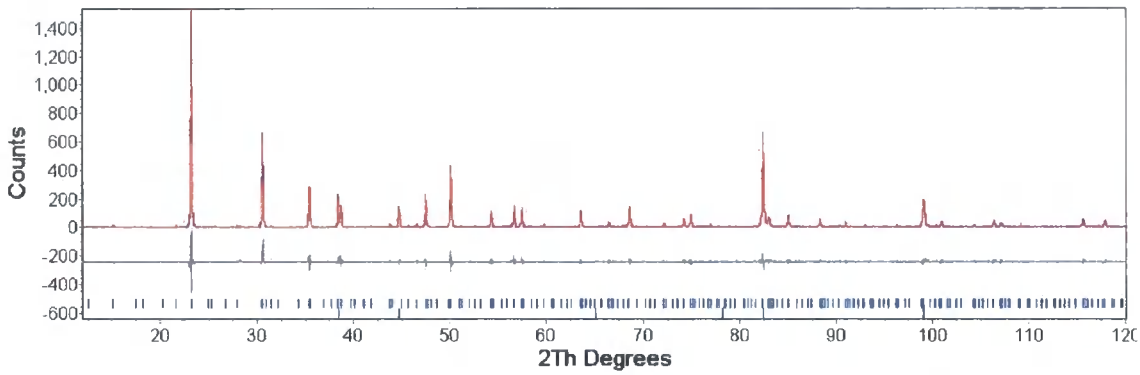

Figure 5.7. Room temperature Rietveld plot for the VT PheniX run, d8_01771. Upper blue tick marks calculated for trigonal $ZrMo_2O_8$ (SA6A); lower blue marks are for the Al sample holder Pawley fit.

An internal standard was unnecessary since the sample temperature in the PheniX has been shown to be essentially identical to the set temperature; this is discussed in Section 6.1.5. 50 variables were refined in the PheniX RT Rietveld including 12 background terms and 24 variables for trigonal $ZrMo_2O_8$ (scale factor, two cell parameters, individual sample height correction, six PV coefficients, four atomic positions, three *rot* angles and seven atomic displacement parameters). The remaining 14 variables were used to describe the aluminium sample holder, which is crystalline and gives rise to its own powder pattern. It was modelled in a structure-less fit *via* the Pawley method,[18] using a sample displacement parameter, six PV terms, one cubic cell parameter and six parameters to fit the intensity under the six peaks due to Al. A separate sample height was required for Al since the sample holder sits slightly below the sample surface. An

atomic fit was not suitable since the aluminium is machined and thus textured meaning a full structure analysis is complex. Nevertheless the cell parameter of the Al is extractable and is a useful independent measure of the cryostat temperature. It is shown in Figure 5.8 and compared to literature data by Wang and Reeber therein (see also d8_01771.xls in the e-Appendix).[19] An excellent agreement is observed between the two data sets and thus no temperature correction is required in the PheniX.

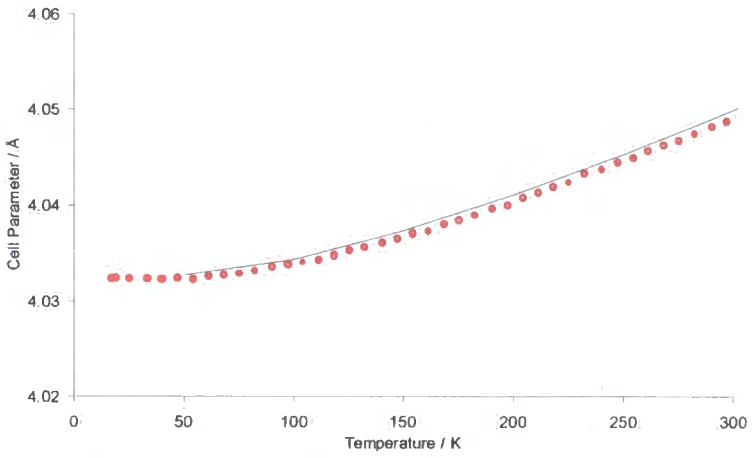

Figure 5.8. The observed and literature trend of the cubic cell parameter of Al in the PheniX cryostat.

The most important room temperature refined values for trigonal $ZrMo_2O_8$ are compared below in Table 5.2; excellent agreement between cryostat and furnace X-ray data is observed.

	HTK1200 d8_01861:1	PheniX d8_01771:1	Auray single crystal
Cell parameter *a* / Å	10.14006 (48)	10.14013 (19)	10.1391 (6)
Cell parameter *c* / Å	11.71004 (95)	11.70625 (36)	11.7084 (8)
Cell volume *V* / Å^3	1043.73 (13)	1042.40 (5)	1042.4 (2)
Rotational angle *rotx* / °	2.6 (4.4)	4.9 (1.5)	N/A
Rotational angle *roty* / °	11.2 (2.3)	10.3 (9)	N/A
Rotational angle *rotz* / °	–31.7 (3.2)	–33.7 (9)	N/A
R_{Bragg} ($\cong R_{F^2}$)	0.0518 (trigonal)	0.0812 (trigonal)	0.031
${}_wR_p$	0.270	0.331	N/A
χ^2	1.10	1.21	N/A

Table 5.2. Refined room temperature values used as seed refinements in the VT HTK1200 and PheniX data collections on trigonal $ZrMo_2O_8$.

The RT refinements above were used as a seed for all the other temperatures. The temperature dependence of the trigonal $ZrMo_2O_8$ cell volume and individual cell parameters are shown in Figure 5.9. The furnace temperatures were corrected from the α-Al_2O_3 cell. The two sets of VTXRD data are consistent with each other, in terms of the near equality of the cell parameters at the 300 K intersection point.

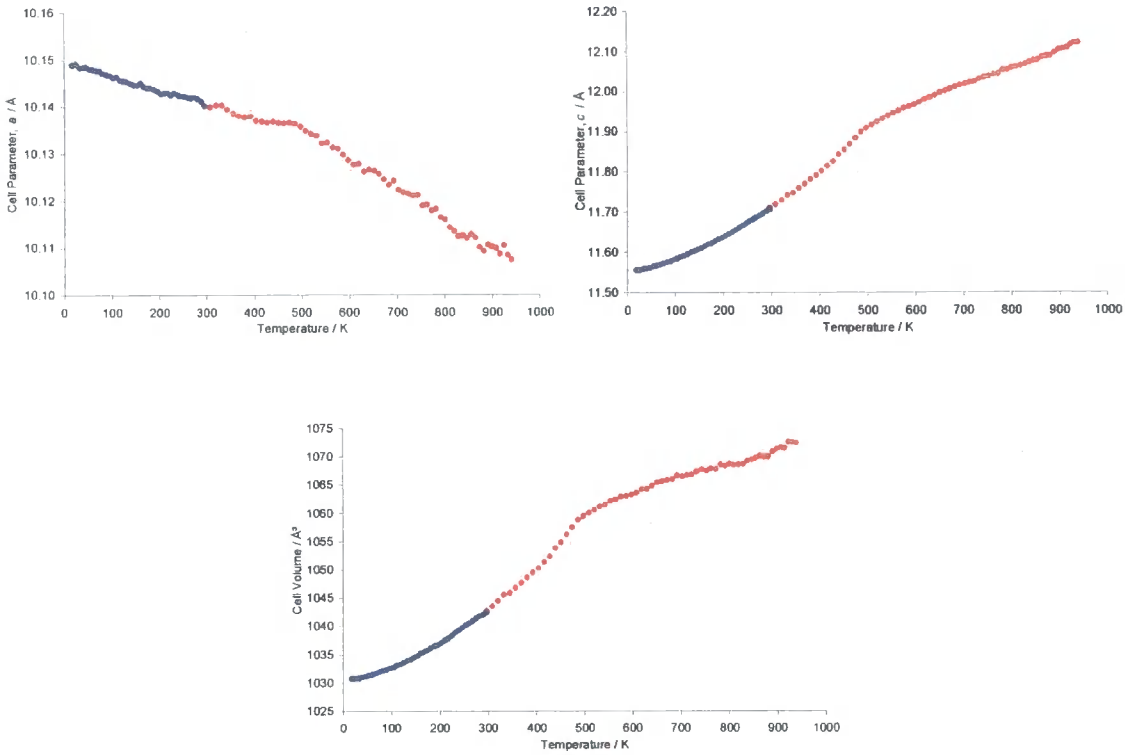

Figure 5.9. Collated PheniX (d8_01771) and HTK1200 (d8_01861) VTXRD data for trigonal $ZrMo_2O_8$: refined unit cell dimensions are shown as a function of temperature. HTK1200 data are temperature-corrected with an α-Al_2O_3 reference.

Figure 5.10 shows what the HTK1200 data would look like had an internal standard not been used. The calibrated phase transition temperature, T_c is ~ 487 K which is slightly higher than the un-calibrated value of ~ 463 K due to the under-reading HTK1200 furnace.

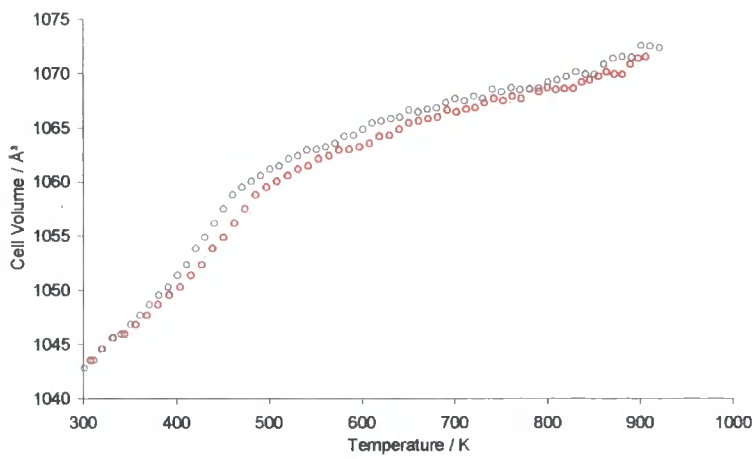

Figure 5.10. The corrected/uncorrected temperature dependence of cell volume of trigonal $ZrMo_2O_8$ in the HTK1200.

The form of the curves in Figure 5.9 can be compared to Mittal's data in Figure 5.2; the current data are more comprehensive and clearly show a point of inflection in all the cell parameters at ~ 487 K. The behaviour is characteristic of a second-order phase transition, which has never been reported for any of the AM_2O_8 trigonal phases. The mean linear expansion coefficients derived from the VT data are given in Table 5.3.

	α_a / × 10^{-6} K^{-1}	α_c / × 10^{-6} K^{-1}	α_V / × 10^{-6} K^{-1}
17 – 297 K	–2.9	+47	+41
297 – 475 K	–2.4	+82	+77
487 – 940 K	–6.4	+38	+25

Table 5.3. Approximate mean expansion coefficients of trigonal $ZrMo_2O_8$ over different temperature ranges.

The *a* cell parameter shows a small relative negative thermal expansion (NTE) of -0.41% from 17 – 940 K, similar to Mittal's findings in Figure 5.2 (*left*). However this NTE is not monotonous due to the kink at around 487 K. Above 487 K the expansion coefficient along the *a* direction, α_a approximately doubles (Table 5.3). The NTE along the *a* axis is presumably due to intra-layer polyhedral twisting motions. The magnitude of these librations presumably increase in the high temperature structure. The MoO_4 groups find themselves in a less constricted environment as a result of continual expansion of the *c* axis, which results in a greater coefficient of NTE along *a*. The structure is made up from the same rigid polyhedral units as in cubic ZrM_2O_8 with flexible bridging oxygen links. It is envisaged that quasi-rigid unit modes (qRUMs) are thus also present in the trigonal form. Hence transverse vibrations dominate the thermal expansion properties within the layer. The *c* axis undergoes significant positive expansion of around +4.6% in total over the 923 K range studied (similar to Figure 5.2, *left*). The magnitude of the expansion in *c* is much greater than *a* due to the absence of any strong bonding between separate layers. Only weak interlayer van der Waals type forces hold the layers together. The expansion along the *c* axis is greater below T_c. This is presumably due to the tetrahedra which tilt towards the *c* axis as the phase transition is approached and force the layers apart. Above T_c the expansion in this direction is only due to thermal motion and so the overall expansion coefficient is somewhat reduced.

Cell parameter data above 882 K show increased scatter due to a trace amount of decomposition of trigonal $ZrMo_2O_8$ to ZrO_2 and amorphous MoO_3. Re-refinement of HTK1200 data suggested that > 2% mass of ZrO_2 was present at the top temperatures. Partial decomposition occurred despite the fact that in Figure 2.8, trigonal $ZrMo_2O_8$ was shown to be stable up to ~ 980 K. It is possible that a partial reaction with alumina is the cause for this decomposition.

5.1.4 Second-order Phase Transition in $ZrMo_2O_8$

The nature of the phase transition observed from the cell parameter trends in the previous section is discussed through detailed analysis of the rigid-body VTXRD refinements. In addition to the reported 8 hour scan at 302 K (Rietveld details shown in Table 5.1), a Rietveld quality scan above T_c of trigonal $ZrMo_2O_8$ (SA6A) was also acquired in the HTK1200 to ascertain any difference in the structure at low and high temperature. An 8 hour powder pattern was recorded at 600 K in the HTK1200 furnace from 10 – 120 ° 2θ (d8_01945:2). Table 5.4 shows the main results of the subsequent refinements of trigonal $ZrMo_2O_8$ at the two temperatures. The same 43 variables were refined as for the 302 K refinement in Section 5.1.2. The full input file is given in the e-Appendix.

	302 K, d8_01945:1	600 K, d8_01945:2
Cell parameter *a* / Å	10.14097 (6)	10.12687 (7)
Cell parameter *c* / Å	11.71111 (13)	11.99014 (12)
Cell volume *V* / Å^3	1043.01 (2)	1064.89 (2)
Rotational angle *rotx* / °	–6.4 (8)	0.5 (1.1)
Rotational angle *roty* / °	–10.8 (4)	5.1 (7)
Rotational angle *rotz* / °	–29.2 (2.9)	–26.9 (4)
Zr(1) *x*, *y*, *z*	0, 0, 0	0, 0, 0
Zr(2) *x*, *y*, *z*	⅓, ⅔, 0.98256 (34)	⅓, ⅔, 1.00435 (8)
Mo *x*, *y*, *z*	0.32929, 0.33757, 0.14917	0.33214, 0.33205, 0.14596
O(1) *x*, *y*, *z*	0.33405, 0.49347, 0.07843	0.31748, 0.49114, 0.10385
O(2) *x*, *y*, *z*	0.49731, 0.33310, 0.11847	0.49585, 0.34247, 0.08542
O(3) *x*, *y*, *z*	0.17006, 0.16698, 0.10638	0.16868, 0.16316, 0.10202
O(4) *x*, *y*, *z*	0.31631, 0.35593, 0.29153	0.34594, 0.33146, 0.28640
Zr(1) B_{iso} / Å^2	2.37 (35)	2.63 (68)
Zr(2) B_{iso} / Å^2	1.56 (13)	2.89 (36)
Mo B_{iso} / Å^2	1.70 (3)	2.26 (4)
O(1) B_{iso} / Å^2	2.40 (48)	3.55 (1.27)
O(2) B_{iso} / Å^2	3.21 (62)	7.38 (1.09)
O(3) B_{iso} / Å^2	3.65 (99)	2.40 (1.00)
O(4) B_{iso} / Å^2	2.53 (30)	3.95 (27)
R_{Bragg} ($\equiv R_{F^2}$)	0.0261 (trigonal)	0.0382 (trigonal)
${}_wR_p$	0.106	0.121
χ^2	1.68	1.97

Table 5.4. Comparison of 302 K and 600 K $P\bar{3}1c$ Rietveld refinement details for trigonal $ZrMo_2O_8$.

Examination of the results in Table 5.4 and the structures in Figure 5.11 provides some clue to the nature of the phase transition that occurs. Two major differences are observed. Firstly both *rotx* and *roty* approach 0 °; this has the effect of aligning the

(terminal) Mo–O(4) bond with the *c* axis of the crystal. Secondly there is a slight apparent change in *rotz*, which rotates the tetrahedron in the *ab* plane.

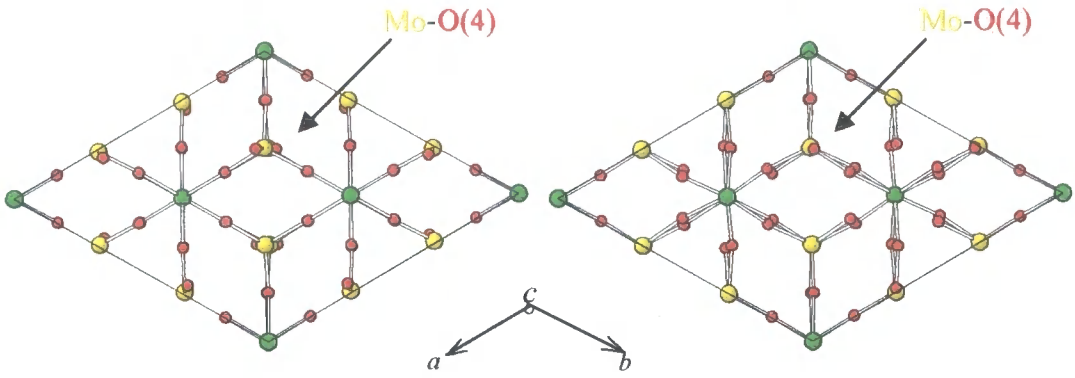

Figure 5.11. Ball and stick representation of the refined unit cells of trigonal $ZrMo_2O_8$ (d8_01945) viewed down the *c* axis at 302 K (*left*) and 600 K (*right*).

The apparent alignment of the three-fold axis of the MoO_4 tetrahedron with the *c* axis suggests that the high temperature structure of $ZrMo_2O_8$ could be equally well modelled using the $MnRe_2O_8$ structure type. Whilst this structure is formally in a lower symmetry space group ($P\bar{3}$ as opposed to $P\bar{3}1c$) the smaller cell volume means that the structure is of higher symmetry and contains a single Zr and Mo site in the asymmetric unit.

The 600 K refinement (d8_01945:2) was therefore repeated in space group $P\bar{3}$ so comparisons to the $P\bar{3}1c$ refinement could be made. The relevant *TOPAS* file is shown in the e-Appendix. As for $P\bar{3}1c$, a rigid-tetrahedral model was used and the same Zr–O and Mo–O bond constraints were applied. 35 variables were refined in total including 15 for $ZrMo_2O_8$ (a scale factor, two cell parameters, six PV peak shape terms, a *rotz* term, the *z*(Mo) coordinate and four isotropic temperature factors) and 7 for the trace ZrO_2 impurity (as for other refinements). A mutual sample height correction and twelve Chebyshev background terms were also refined. Only two crystallographically unique O atoms exist in the perrhenate structure so in order to apply the rigid-tetrahedral model (with four O atoms), three identical O(1) atoms were defined, each with an occupancy of ⅓ (Table 5.6). Figure 5.12, and Tables 5.5 and 5.6 provide the Rietveld fit and key results, respectively.

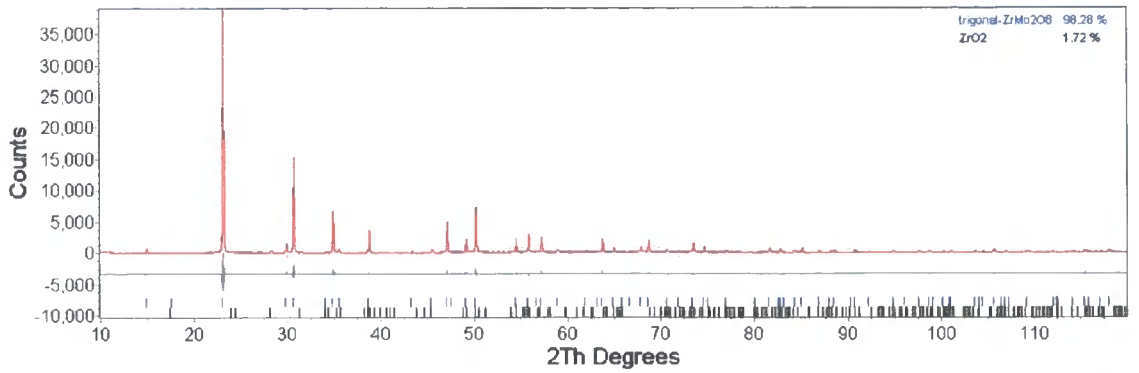

Figure 5.12. Two-phase Rietveld difference plot for trigonal $ZrMo_2O_8$ modelled in $P\bar{3}$, (with ZrO_2 impurity) at 600 K (d8_01945:2, SA6A). Blue tick marks = calculated for trigonal, black tick marks = ZrO_2.

	$P\bar{3}1c$	$P\bar{3}$	$P\bar{3}m1$
Cell parameter a / Å	10.12687 (7)	5.84673 (4)	5.84673 (4)
Cell parameter c / Å	11.99014 (12)	5.99517 (6)	5.99517 (6)
Cell volume V / Å^3	1064.89 (2)	177.484 (3)	177.484 (3)
Rotational angle *rotx* / °	0.5 (1.1)	0	0
Rotational angle *roty* / °	5.1 (7)	0	0
Rotational angle *rotz* / °	–26.9 (4)	–34.7 (3)	–30
R_{Bragg} ($\equiv R_{F^2}$)	0.0382 (trigonal)	0.0398 (trigonal)	0.0406 (trigonal)
$_wR_p$	0.121	0.122	0.122
χ^2	1.97	1.98	1.98

Table 5.5. Main refined parameters for trigonal $ZrMo_2O_8$ at 600 K (d8_01945:2) in the $P\bar{3}1c$, $P\bar{3}$ and $P\bar{3}m1$ space groups. The $P\bar{3}/P\bar{3}m1$ and $P\bar{3}1c$ unit cells are rotated by 30 ° with respect to each other and so 30 has been subtracted from refined $P\bar{3}/P\bar{3}m1$ *rotz* values to aid comparison with $P\bar{3}1c$. Note, *rotx* and *roty* must be 0 by definition of the symmetry inherent in $P\bar{3}$; additionally *rotz* must be 0 (shown as –30 ° above) in $P\bar{3}m1$.

The R-factors given in Table 5.5 are very similar which tells us that the simple $P\bar{3}$ model provides as good a fit to the high temperature data as the more complex $P\bar{3}1c$ model. By convention the space group with the highest symmetry and smallest unit cell is the one that should be quoted ($P\bar{3}$). The magnitudes of *rotz* in $P\bar{3}$ and $P\bar{3}1c$ are roughly equivalent, *i.e.* they deviate from the "zero position" of –30 ° by a similar amount. The two models describe approximately equivalent polyhedral rotations overall.

Since the literature refers to trigonal $ZrMo_2O_8$ as the α polymorph, it is proposed that the high temperature form be denoted as α'-$ZrMo_2O_8$ hereafter.

Despite the attraction of describing the α to α' phase transition occurring between the $P\bar{3}1c$ $ZrMo_2O_8$ structure and the $P\bar{3}$ $MnRe_2O_8$ structure, there are problems with such a conclusion. In particular the $P\bar{3}$ to $P\bar{3}1c$ descent in symmetry is not actually permitted for a second-order phase transition as $P\bar{3}1c$ is not a sub-group of $P\bar{3}$. Examination of the $P\bar{3}$ model of α'-$ZrMo_2O_8$ revealed, however, that there were only minor deviations in atomic coordinates from the higher symmetry space group $P\bar{3}m1$ (see refined coordinates in Table 5.6). Also, $P\bar{3}m1$ to $P\bar{3}1c$ is an allowed symmetry descent for a second-order transition. It was therefore decided to repeat refinements of the α' structure in $P\bar{3}m1$: 34 variables were used in the *TOPAS* rigid-body refinement for the 600 K dataset (see the e-Appendix). The same variables used for $P\bar{3}$ were refined again in $P\bar{3}m1$ with the exception that by symmetry, *rotz* cannot be refined and must be fixed at zero. The Rietveld plot is displayed in Figure 5.13 and is almost identical to that in Figure 5.12. Table 5.5 compares all three α'-$ZrMo_2O_8$ refinements; in terms of the *R*-factors $P\bar{3}m1$ gives as good fit as the other two lower symmetry structures, and being of higher symmetry seems the best choice of space group. The corresponding transformation matrix for $P\bar{3}m1$ to $P\bar{3}1c$ is (2,1,0; $\bar{1}$,1,0; 0,0,2). Further strong support for this choice of space group comes from the studies on trigonal $HfMo_2O_8$ described in Section 5.2.

	$P\bar{3}$				$P\bar{3}m1$			
	x	y	z	B_{iso} / Å²	x	y	z	B_{iso} / Å²
Zr	0	0	0	2.87 (6)	0	0	0	2.90 (6)
Mo	⅓	⅔	0.29233	2.27 (3)	⅓	⅔	0.29312	2.25 (3)
O(1)	0.19310	0.85378	0.19425	4.17 (14)	0.16910	0.83090	0.19504	4.59 (13)
O(2)	0.66067	0.80690	0.19425	4.17 (14)	0.66179	0.83090	0.19504	4.59 (13)
O(3)	0.14622	0.33933	0.19425	4.17 (14)	0.16910	0.33821	0.19504	4.59 (13)
O(4)	⅓	⅔	0.57422	4.14 (25)	⅓	⅔	0.57501	4.23(25)

Table 5.6. Comparison of refined rigid-body atomic coordinates of α'-$ZrMo_2O_8$ at 600 K in $P\bar{3}$ and $P\bar{3}m1$ space groups (d8_01945:2). For rigid-body purposes, O(1) – (3) are defined to describe the base of MoO_4 (hence the same z-coordinate and temperature factor B_{iso}). Note, the models differ by the fact that a symmetry-enforced relationship exists between x(O(1)) and y(O(1)) in $P\bar{3}m1$.

The slight differences in the x and y O(1) positions between $P\bar{3}$ and $P\bar{3}m1$ shown in Table 5.6 could mean that final choice of space group given by Butz *et al.* for $MnRe_2O_8$ could in fact be questionable.[14] Their $P\bar{3}$ model relies only on the values of relatively poorly determined oxygen coordinates derived from laboratory powder X-ray data and cannot be viewed as definitive.

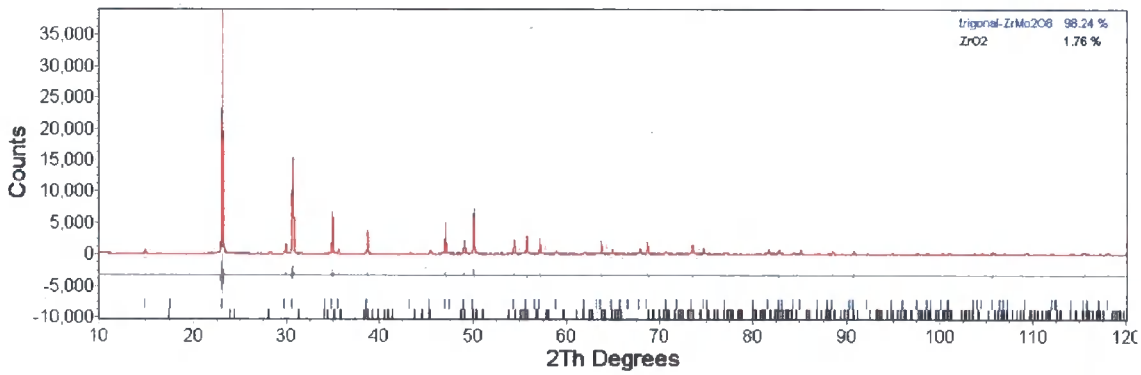

Figure 5.13. Two-phase Rietveld difference plot for α'-$ZrMo_2O_8$ modelled in $P\bar{3}m1$, (with ZrO_2 impurity) at 600 K (d8_01945:2, SA6A). Blue tick marks = calculated for trigonal, black tick marks = ZrO_2.

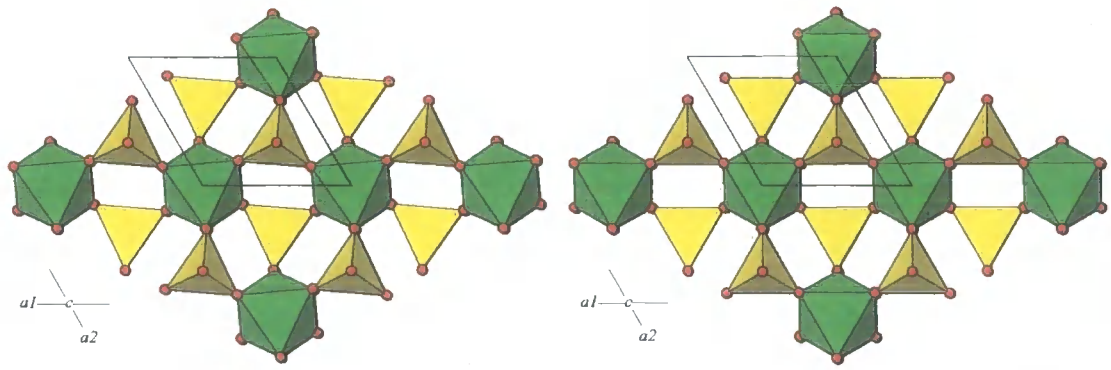

Figure 5.14. The refined $P\bar{3}$ (*left*) and $P\bar{3}m1$ (*right*) model structures of α'-$ZrMo_2O_8$ viewed down the *c* axis.

The above figure illustrates the subtle difference between the $P\bar{3}$ and $P\bar{3}m1$ structures. Since *rotz* refines to a non-zero value in $P\bar{3}$, a coupled polyhedral tilt about the *c* axis is present (Figure 5.14, *left*). In $P\bar{3}m1$ (Figure 5.14, *right*), *rotz* is zero by definition, hence the presence of an extra mirror plane perpendicular to the diagonal of the *ab* face. The results of the Rietveld refinements of the two models have been shown to be essentially identical (Table 5.5). The $P\bar{3}m1$ model also contains a polyhedral tilt pattern closer to that observed in $P\bar{3}1c$ at room temperature. This is apparent when Figures 5.14 (*right*) and 5.3 (*right*) are compared; both structures have *rotz* values of approximately zero. It seems likely that the apparent tilt in $P\bar{3}$ (*i.e.* the non-zero *rotz* value) is merely caused by the incorrect choice of space group.

Overall the $P\bar{3}m1$ space group is preferred for α'-$ZrMo_2O_8$ since it (a) has a higher symmetry yet gives as good a fit to the data as more complex models, (b) can undergo a symmetry allowed transition to the well defined α structure, (c) shows a polyhedral tilting pattern similar to the α phase and (d) is consistent with findings based on work on trigonal $HfMo_2O_8$.

The phase transition manifests itself by loss of small supercell peaks apparent by close inspection of the diffraction patterns that have been refined in this section. Figure 5.15 shows that the (*021*), (*013*) and (*211*) reflections at ~ 21.7 °, ~ 25.0 ° and ~ 28.0 ° respectively, are absent at high temperature. Their disappearance is related to the contraction of the supercell to one-sixth of its volume at 487 K. The peak at ~ 28.3 ° is due to a trace ZrO_2 impurity. The large peak that has evolved in the 600 K pattern at

~ 29.9 ° is the (*002*), which was coincident with the strong (*030*) peak at ~ 30.6 ° at room temperature. The relatively large 2θ shift in (*00l*) reflections is due the substantial expansion of the *c* axis versus that of the *a* axis (4.6% compared to 0.4%). The supercell peaks are only just visible above the level of the background noise in the VT run (Figure 5.5) hence it is difficult to refine meaningful *rotxyz* values at all different temperatures.

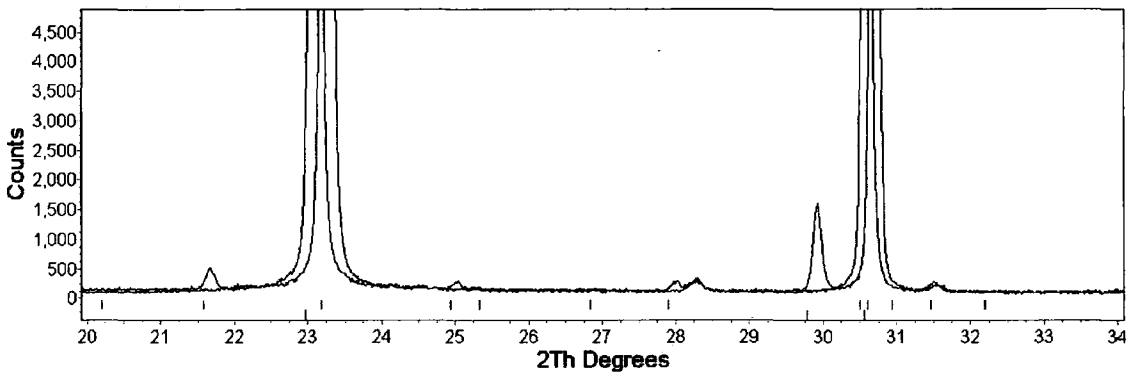

Figure 5.15. Close-up of trigonal $ZrMo_2O_8$ diffraction patterns modelled with a Pawley (structure-less) fit of d8_01945 at 302 K and 600 K. Calculated patterns for each are absent for clarity. Bragg reflections at ~ 21.7 °, 25.0 ° and 28.0 ° disappear in the high temperature pattern. Calculated, upper tick marks are for $P\bar{3}m1$ (600 K model), lower marks are for $P\bar{3}1c$ (302 K model).

It seems likely that the phase transition in trigonal $ZrMo_2O_8$ is displacive in nature. As the material is warmed the librations of the constituent polyhedra gradually increase until the Mo–O(4) vector is at least on average parallel to the crystallographic *c* axis. The variable temperature X-ray diffraction data are consistent with a phase transition from $P\bar{3}1c$ to $P\bar{3}m1$, which occurs at approximately 487 K.

5.2 Trigonal $HfMo_2O_8$

5.2.1 Introduction

The first reported synthesis of trigonal $HfMo_2O_8$ was in 1967,[7,8] and its structure from powder diffraction published in 1968 by Rimsky, Thoret and Freundlich, albeit with misleading atomic coordinates.[9] This prompted Auray's single crystal work on trigonal $ZrMo_2O_8$ in 1986,[1] and re-investigation of trigonal $HfMo_2O_8$ a year later.[3] The variable temperature behaviour of trigonal $HfMo_2O_8$ is studied in this section, in a similar manner to the Zr analogue set out in Section 5.1. The aim is to ascertain whether or not it could confirm the $P\bar{3}1c$ – $P\bar{3}m1$ phase transition observed in $ZrMo_2O_8$ at ~ 487 K, bearing in mind the similar nature of Zr^{IV} and Hf^{IV} compounds.

A review of AM_2O_8 structures in 1974 by Thoret re-iterates the trigonal $P\bar{3}1c$ structure for $HfMo_2O_8$ and $ZrMo_2O_8$ given in the 1960s.[20] Most of the reported atomic positions for $HfMo_2O_8$ remain incorrect when compared to Auray's later work on $ZrMo_2O_8$. The coordinates are compared in Table 5.7.

	$x(HfMo_2O_8)$	$x(ZrMo_2O_8)$	$y(HfMo_2O_8)$	$y(ZrMo_2O_8)$	$z(HfMo_2O_8)$	$z(ZrMo_2O_8)$
A(1)	0	0	0	0	0.250	0
A(2)	0.333	⅓	0.666	⅔	0	0.98132
Mo	0.321	0.32871	0	0.33891	0.229	0.14900
O(1)	0.213	0.1731	0.256	0.1664	0.361	0.1008
O(2)	0.261	0.3323	0.193	0.4959	0.128	0.0814
O(3)	0.467	0.4979	0.306	0.3364	0.362	0.1178
O(4)	0.298	0.3189	0.441	0.3522	0.110	0.2923

Table 5.7. A comparison of the literature atomic positions for trigonal $HfMo_2O_8$ (Thoret) and $ZrMo_2O_8$ (Auray).

Thoret's published coordinates of $HfMo_2O_8$ make little sense. The reported coordination number of Hf(1) is 12 (hexagonal anti-prismatic) with bond lengths 2.59 – 2.62 Å. Hf(2) was determined to be 6 coordinate but in a triangular prismatic coordination, with

bond lengths of 2.47 – 2.49 Å. These bond lengths are at least 0.4 Å longer than expected from Shannon's ionic radii.[21] However the paper contains powder diffraction data that are over thirty years old and at least the correct $P\bar{3}1c$ space group at room temperature was given. Thoret's unit cell of a = 10.01 Å and c = 11.60 Å, is reasonably close to that published by Auray (a = 10.005 (3) Å and c = 11.7230 (5) Å),[3] and that found in this work.

5.2.2 Preparation of $HfMo_2O_8$

The simplest way to synthesise trigonal $HfMo_2O_8$ would be a direct combination of HfO_2 and MoO_3 at high temperature similar to the method described for $ZrMo_2O_8$. This was performed, albeit with an excess of MoO_3, by Auray in order to prepare single crystals of trigonal $HfMo_2O_8$. However in this study a new preparative route was used, as a result of the VTXRD results in Chapter 2. Figure 2.23 shows trigonal $HfMo_2O_8$ as the sole phase formed in the *in situ* decomposition of $HfMo_2O_7(OH)_2(H_2O)_2$ between ~ 840 – 1070 K. Thus for this work pure (> 99.6%) trigonal $HfMo_2O_8$ was prepared by decomposing $HfMo_2O_7(OH)_2(H_2O)_2$ at 1000 K (SA100A). Further details of the synthesis are given in Section 7.8. The VTXRD studies in Chapter 2 permitted the preparation of a pure sample on a first attempt, which proves the *in situ* studies to be a useful synthetic tool even if trigonal $HfMo_2O_8$ can be made by other means.

An 8 hour d8 powder pattern (HTK1200, SiO_2 holder, 1 ° divergence slit, 10 – 120 ° 2θ) of sample SA100A was recorded and analysed by Rietveld refinement using Auray's $ZrMo_2O_8$ structure as a starting model. The refinement is plotted in Figure 5.16, with basic rigid-body refinement details in Table 5.8 and full details in the *TOPAS* input file set out in the e-Appendix.

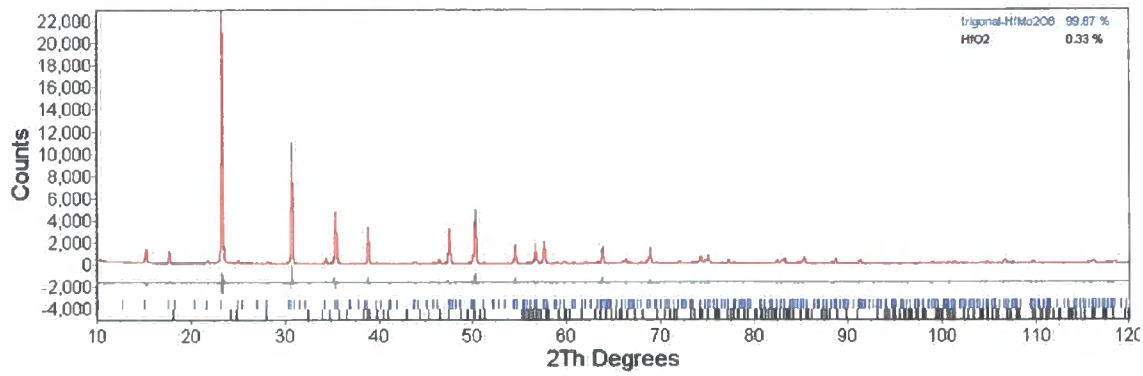

Figure 5.16. Rietveld refinement plot for trigonal $HfMo_2O_8$ (d8_1947:1, SA100A). Only a trace amount of HfO_2 is present (whose calculated Bragg reflections shown by black tick marks).

As for the Zr analogue in Section 5.1.2, a rigid-body refinement was employed and 36 variables were used. The refined parameters included twelve background terms, and 24 variables for $HfMo_2O_8$ (a sample height correction, histogram scale factor, two cell parameters, six PV peak shape coefficients, four atomic coordinates, three tetrahedral rotational angles and seven isotropic temperature factors). HfO_2 was included as a second phase although all its structural parameters were fixed at literature values since it was only present as a very small impurity.

	$HfMo_2O_8$, d8_01947:1	$ZrMo_2O_8$, d8_01945:1
Cell parameter *a* / Å	10.10575 (9)	10.14097 (6)
Cell parameter *c* / Å	11.74309 (16)	11.71111 (13)
Cell volume *V* / Å^3	1038.60 (2)	1043.01 (2)
Rotational angle *rotx* / °	6.1 (8)	–6.4 (8)
Rotational angle *roty* / °	13.3 (4)	–10.8 (4)
Rotational angle *rotz* / °	–30.1 (1.6)	–29.2 (2.9)
A(1) *x*, *y*, *z*	0, 0, 0	0, 0, 0
A(1) *x*, *y*, *z*	⅓, ⅔, 1.01902 (20)	⅓, ⅔, 0.98256 (34)
Mo *x*, *y*, *z*	0.33766, 0.33023, 0.14918	0.32929, 0.33757, 0.14917
O(1) *x*, *y*, *z*	0.33459, 0.50071, 0.12375	0.33405, 0.49347, 0.07843
O(2) *x*, *y*, *z*	0.49196, 0.33557, 0.07488	0.49731, 0.33310, 0.11847
O(3) *x*, *y*, *z*	0.16480, 0.17297, 0.10172	0.17006, 0.16698, 0.10638
O(4) *x*, *y*, *z*	0.35838, 0.31245, 0.29020	0.31631, 0.35593, 0.29153
A(1) B_{iso} / Å^2	0.99 (14)	2.37 (35)
A(2) B_{iso} / Å^2	1.26 (7)	1.56 (13)
Mo B_{iso} / Å^2	1.21 (6)	1.70 (3)
O(1) B_{iso} / Å^2	4.75 (77)	2.40 (48)
O(2) B_{iso} / Å^2	1.93 (52)	3.21 (62)
O(3) B_{iso} / Å^2	1.56 (74)	3.65 (99)
O(4) B_{iso} / Å^2	0.92 (36)	2.53 (30)
R_{Bragg} ($\equiv R_{F^2}$)	0.0418 (trigonal)	0.0261 (trigonal)
$_wR_p$	0.115	0.106
χ^2	1.78	1.68

Table 5.8. Essentials of the 302 K refinements of trigonal $HfMo_2O_8$ (d8_01947:1, SA100A) compared to $ZrMo_2O_8$ (d8_01945:1, SA6A).

When comparing the d8 Rietveld plots of the two trigonal materials (Figures 5.4 and 5.16) one can immediately see the presence of extra low angle peaks in the $HfMo_2O_8$ pattern. For example, an extra trigonal peak at 17.6 ° 2θ (the (*110*) reflection) was

observed for $HfMo_2O_8$. Due to the relative scattering powers of Zr versus Mo (as opposed to Hf versus Mo in $HfMo_2O_8$), this peak accidentally has very low intensity in the $ZrMo_2O_8$ pattern but is much stronger in that of $HfMo_2O_8$. This can be checked by merely swapping Hf for Zr in the $ZrMo_2O_8$ structure and calculating its powder pattern.

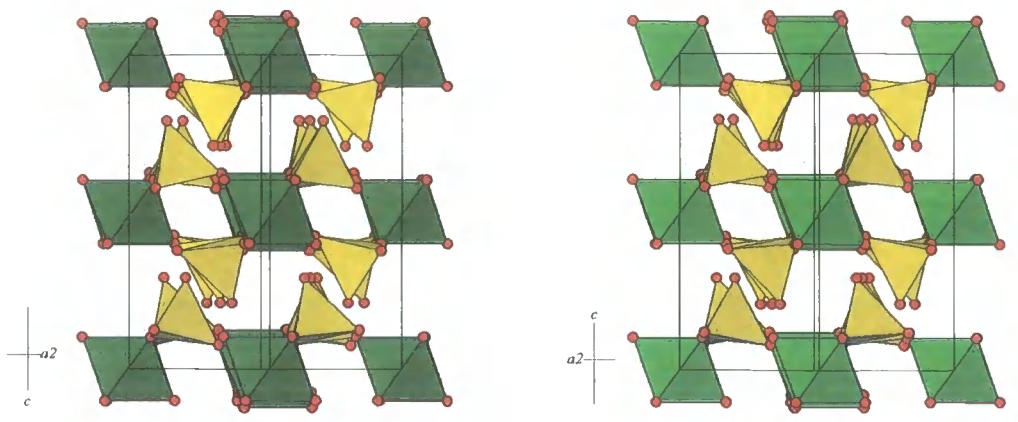

Figure 5.17. Polyhedral representations of the room temperature refined trigonal $HfMo_2O_8$ (SA100A, *left*) and $ZrMo_2O_8$ structures (SA6A, *right*) along the [110] direction.

Table 5.8 shows the *roty* value shows a greater deviation from zero at room temperature (*i.e.* the tetrahedra are further tilted away from the *ab* plane) in trigonal $HfMo_2O_8$ than in $ZrMo_2O_8$. Close inspection of Figure 5.17 illustrates the larger tetrahedral tilt apparent in $HfMo_2O_8$. A smaller cell volume is calculated for $HfMo_2O_8$ despite a larger refined *c* lattice parameter. This is because in trigonal symmetry the volume is given by $(\sqrt{3}/2)a^2c$. Despite the fact that Hf is a third row transition metal, it has a similar ionic radius in the +IV state with 6-coordination (0.71 Å versus 0.72 Å for Zr^{IV}),[21] yet it gives rise to a smaller unit cell volume in its trigonal molybdate. Good agreement is observed between the $HfMo_2O_8$ cell volume of 1035.8 (1) Å given by Auray,[3] and that obtained with the Rietveld analysis of sample SA100A (V = 1038.60 (2)Å).

5.2.3 Existence of a Second-order Phase Transition in $HfMo_2O_8$

VTXRD measurements were performed on trigonal $HfMo_2O_8$ similar to those performed for $ZrMo_2O_8$. An α-Al_2O_3 reference was ground in with a sample of trigonal $HfMo_2O_8$ (SA100A) to give sample SA112A (Section 7.8) which enabled a full temperature calibration analysis. The combined trigonal $HfMo_2O_8/Al_2O_3$ sample

(SA112A) was sieved onto an amorphous SiO_2 disc coated with a thin layer of vacuum grease and mounted in the HTK1200. X-ray powder patterns were recorded in air from 302 to 922 K in 10 K increments and for 25 minutes at each temperature; a total of 63 ranges were collected in the run d8_01863. A one-degree divergence slit and a heat rate of 0.2 Ks^{-1} were used and data collected between 13 – 100 ° 2θ.

The PheniX cryostat was used to obtain X-ray data on slightly impure trigonal $HfMo_2O_8$ (SA98A, ~ 5% HfO_2 present; see Section 7.8) from 300 – 17 K, at a constant cooling rate of 7 Khr^{-1} and in the range 10 – 120 ° 2θ. SA98A was sprinkled onto a Vaseline-smeared flat aluminium sample holder and 30 minute scans were recorded (thus on average one scan every ~ 3.5 K was obtained); a total of 73 ranges were recorded in the d8_01778 measurement. An internal temperature standard was not required.

For the d8_01863 VT HTK1200 run, a similar *TOPAS* file was used as for the Zr case. The two-phase atomic refinement at room temperature is displayed with all the refined values in the e-Appendix. The same 44 variables that are described in Section 5.1.3 were refined. The room temperature Rietveld results are shown in Figure 5.18 and Table 5.9.

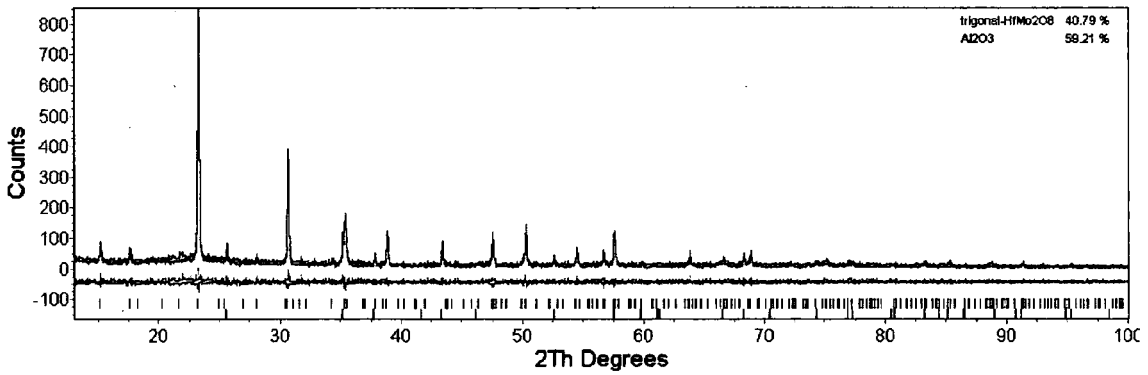

Figure 5.18. Rietveld plot of the 302 K scan of trigonal $HfMo_2O_8/Al_2O_3$ (SA112A; d8_01863:1) Blue calculated tick marks are for the trigonal phase. Black calculated tick marks are for α-Al_2O_3.

	HTK1200 d8_01863:1 SA112A	PheniX d8_01778:1 SA98A
Cell parameter *a* / Å	10.10487 (44)	10.10460 (22)
Cell parameter *c* / Å	11.73438 (78)	11.73369 (40)
Cell volume *V* / Å^3	1037.65 (11)	1037.54 (6)
Rotational angle *rotx* / °	5.2 (3.4)	3.6 (1.5)
Rotational angle *roty* / °	14.7 (2.5)	12.3 (9)
Rotational angle *rotz* / °	–29.2 (6.0)	–27.6 (2.4)
R_{Bragg} ($\equiv R_{F^2}$)	0.0389 (trigonal)	0.0682 (trigonal)
${}_wR_p$	0.229	0.239
χ^2	1.05	1.15

Table 5.9. Room temperature refined data for two different samples of trigonal $HfMo_2O_8$ (SA112A, pure, with added Al_2O_3; and SA98A, with 5% HfO_2 impurity), used as a seed for variable temperature refinements.

The room temperature PheniX trigonal $HfMo_2O_8$ data (SA98A) were used for a seed refinement and consisted of 57 variables. An analogous set of the 50 parameters used in the $ZrMo_2O_8$/Al PheniX refinements (Section 5.1.3) was refined although Zr atoms were replaced with Hf. A further 7 parameters were used to model the additional HfO_2 impurity phase (scale factor, three cell parameters, monoclinic cell angle, one peak profile function and one temperature factor). The results are given in Figure 5.19, Table 5.9 and in the e-Appendix.

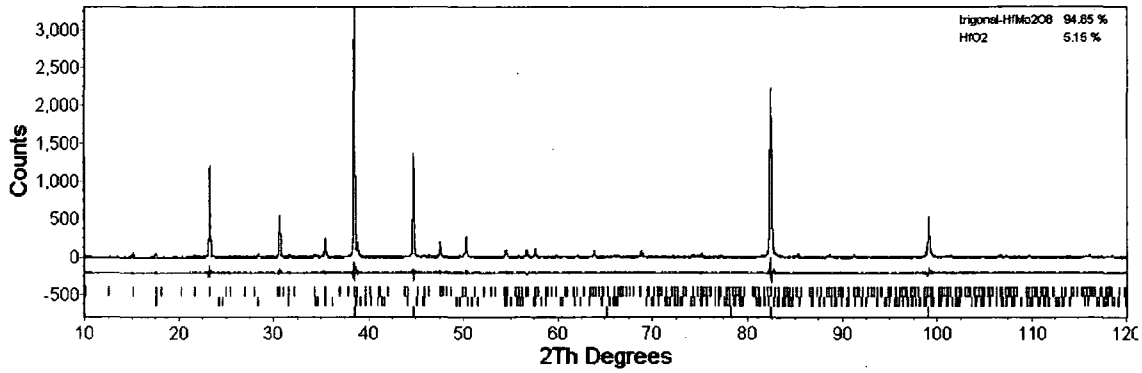

Figure 5.19. Seed refinement plot of room temperature PheniX data collected on slightly impure trigonal $HfMo_2O_8$ (SA98A; d8_01778:1). The upper blue tick marks show calculated reflections for $HfMo_2O_8$, the black tick marks for HfO_2 and the lower blue tick marks for the Al sample holder.

The VT refinements were performed using the room temperature models described above as a seed. The main results of these are presented below in Figure 5.20, with complete results displayed in files d8_01863.xls (furnace) and d8_01778.xls (cryostat) in the e-Appendix. The furnace temperatures for the trigonal data were back-calibrated from the α-Al_2O_3 in a similar manner to that explained in Section 5.1.3. The calibration curve is very similar and is given in the e-Appendix.

Figure 5.20 shows that trigonal $HfMo_2O_8$ and $ZrMo_2O_8$ respond to temperature in a very similar way. The form of the expansion in the *a* and *c* directions is virtually identical. Both *a* axes show NTE whereas the *c* axes show an order of magnitude larger, positive expansion. A change in gradient is present in all the unit cell dimensions in both compounds. Comparing Tables 5.3 and 5.10 shows how similar the expansion coefficients for the materials are. The chief differences are that the phase transition occurs at a slightly lower temperature of around 463 K in $HfMo_2O_8$ (compared to 487 K in $ZrMo_2O_8$) and the unit cell volume of $HfMo_2O_8$ is smaller throughout (although its *c* axis is larger).

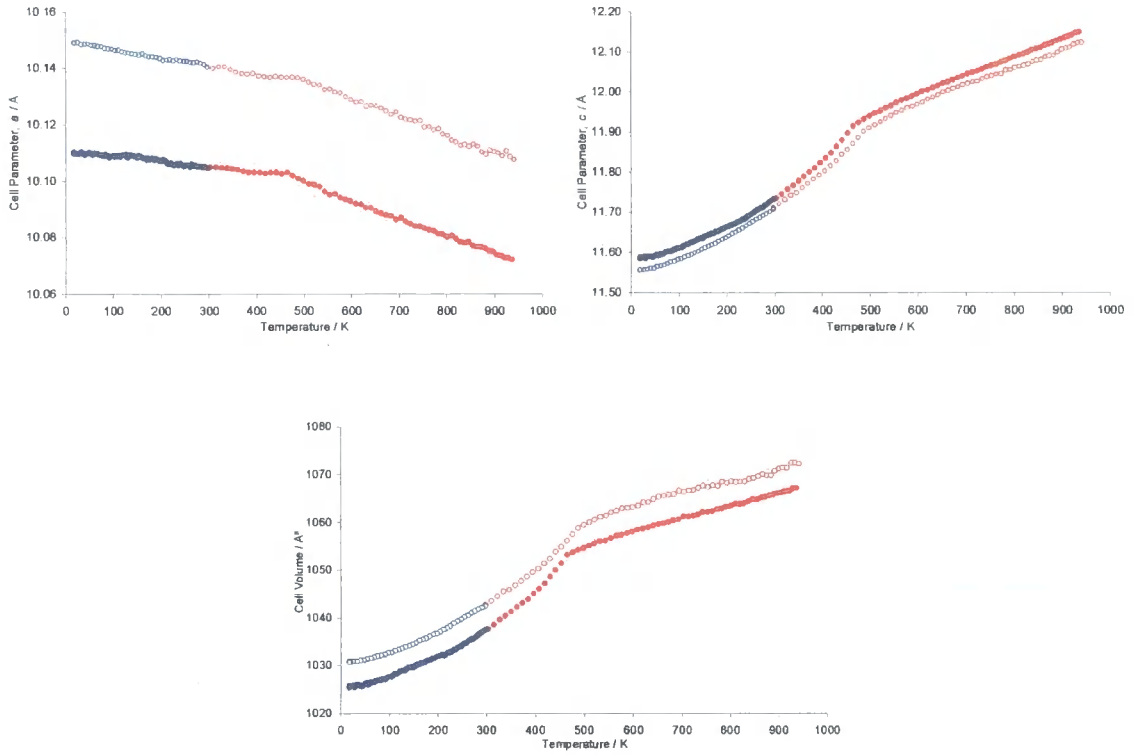

Figure 5.20. The temperature dependence of the unit cell dimensions obtained for trigonal $HfMo_2O_8$ (full circles) compared to $ZrMo_2O_8$ (open circles). Cryostat data given in blue; temperature corrected furnace data given in red.

	α_a / × 10^{-6} K^{-1}	α_c / × 10^{-6} K^{-1}	α_V / × 10^{-6} K^{-1}
17 – 297 K	–1.9	+43	+40
303 – 452 K	–1.7	+89	+86
463 – 940 K	–6.2	+39	+27

Table 5.10. Mean linear expansion coefficients of the *a* and *c* cell parameters and of the cell volume for trigonal $HfMo_2O_8$.

The $P\bar{3}1c$ to $P\bar{3}m1$ transition observed for trigonal $ZrMo_2O_8$ is also seen to occur in the Hf analogue. Evidence for this comes from consideration of the temperature dependent behaviour of the refined metal atom coordinates shown in Figure 5.21. The Hf(2) *z* coordinate tends towards the special position ($z = 1$) that is inherent to the high symmetry $P\bar{3}m1$ space group such that Hf(1) and Hf(2) become equivalent. This is also confirmed by the Mo *x*/*y* coordinates, which converge towards the special position value of ⅓ (see Table 5.6), above the phase transition temperature.

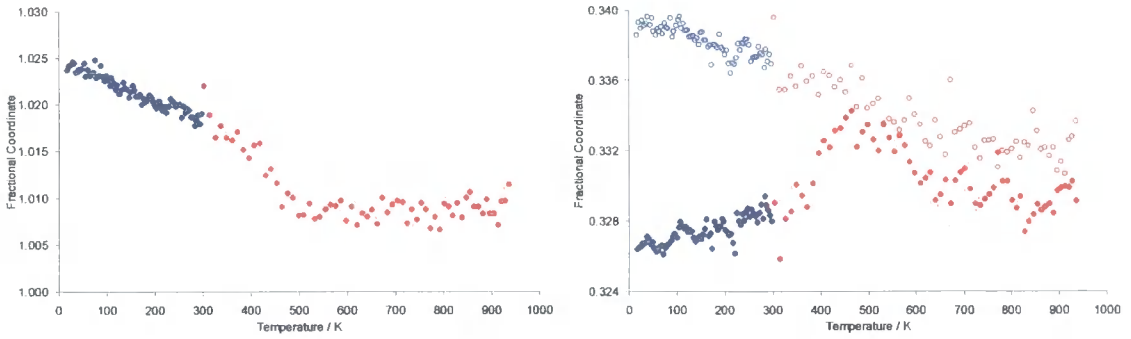

Figure 5.21. The refined temperature dependence of the z(Hf(2)) (*left*) and x(Mo)/y(Mo) coordinates (*right*); PheniX data are in blue and HTK1200 in red whereas x(Mo) shown by open points and y(Mo) are represented by closed points.

A temperature dependent trend shown by the *rotxyz* rotational angles used in the rigid-tetrahedral model would ideally confirm the phase transition, as observed in the long 302 K and 600 K refinements of trigonal $ZrMo_2O_8$. However the quality of the short HTK1200 VT runs is not sufficient to obtain such information accurately; reflections such as (*021*), (*013*) and (*211*) at ~ 21.8 °, ~ 25.2 ° and ~ 28.1 ° (which disappear at high temperature) are unfortunately barely distinguishable from the background noise (Figure 5.18). These reflections are due to the supercell that exists in the large $P\bar{3}1c$ cell below 463 K. Better data could, however be obtained from another sample of trigonal $HfMo_2O_8$ (SA98A, ~ 5% HfO_2 impurity) run in an Anton Paar TTK450 cryofurnace. The sample was mounted as described in Section 6.1.4. High quality VT data were obtained in a cooling experiment from 620 – 120 K in the 2θ range 12 – 70 ° and with a heat rate of 0.2 Ks^{-1} (d8_01682). For each 30-minute VT run the intensity of detected X-rays was over a factor of three higher than the HTK1200 data for roughly the same length of scan (although a shorter 2θ range was used). Figure 5.22 shows a portion of the Rietveld refinement of the 120 K measurement - the last range in the VT experiment (d8_01682:51). The (*021*), (*013*) and (*211*) supercell peaks are small but can be distinguished more clearly than in Figure 5.18.

For the TTK450 VT refinement, a rigid-tetrahedra seed file at 620 K was initially refined using 54 variables for two atomic phases (trigonal $HfMo_2O_8$ and HfO_2) and a Pawley fit of the Al sample holder inset. The same parameters were used as for the $HfMo_2O_8$ PheniX seed file except that due to the smaller 2θ range used, only 3 Al peaks were present and so only 3 variables to describe the intensity of these peaks were

required. The *TOPAS* seed input file is given in the e-Appendix. *MultiTOPAS* was used to refine parameters at the 51 different temperatures from 620 – 120 K.

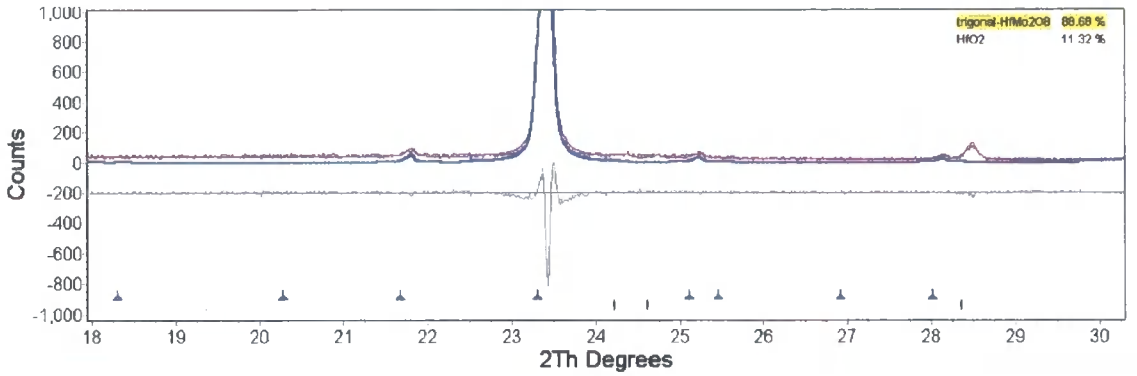

Figure 5.22. Partial Rietveld refinement plot of trigonal $HfMo_2O_8$ at 120 K in the TTK450 (SA98A, d8_01682:51). Supercell reflections are observed at *e.g.* 21.8 °, 25.2 ° and 28.1 °. The observed pattern is shown as the black trace, the calculated pattern the red trace. The calculated trigonal pattern is highlighted in bold blue. The peak at ~ 28.5 ° is the $(1\bar{1}\bar{1})$ reflection of HfO_2.

The data in Figure 5.22 are of comparable quality to the long scans of $ZrMo_2O_8$ shown in Figure 5.15. More detailed information on the loss of the supercell during the VT run could thus be obtained. In fact Figure 5.23 illustrates such information: the temperature dependence of the rotational angles of the rigid-tetrahedra.

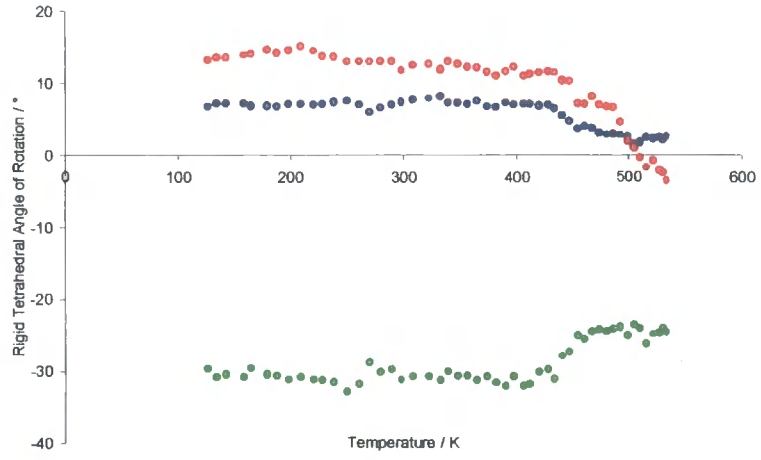

Figure 5.23. The variation of the refined rigid-body rotational angles, *rotx*, *roty* and *rotz* with temperature for trigonal $HfMo_2O_8$ (SA98A, TTK450, d8_01682). Temperatures have been back-calibrated with α-Al_2O_3; a general calibration curve for the TTK450 cryofurnace is given in Section 6.1.4.

Figure 5.23 clearly shows how the MoO_4 group begins to rotate in the crystal as the phase transition temperature of ~ 463 K is approached. The trend is what is expected

from the work done on trigonal $ZrMo_2O_8$ in Section 5.1.4. It seems that *rotx* and *roty* tend to zero as the tetrahedral basal planes become aligned parallel to the crystallographic *ab* plane. This in turn allows the terminal Mo–O(4) bond to align itself with the *c* axis and lie along a new 3-fold axis. Again this suggests the simple $P\bar{3}m1$ type structure would describe high temperature structure equally well. Meanwhile *rotz* moves away from the "zero position" of –30 ° around and above 463 K causing a rotation of MoO_4 in the *ab* plane.

Following on from the discussions given on $ZrMo_2O_8$ in Section 5.1.4, the variable temperature (TTK 450) refinements in the higher symmetry $P\bar{3}$ and $P\bar{3}m1$ space groups were repeated for $HfMo_2O_8$ and compared to $P\bar{3}1c$. For the $P\bar{3}$ seed refinement, 46 variables were refined in total including 16 for trigonal $HfMo_2O_8$ (sample height, scale factor, two cell parameters, six PV peak terms, *z*(Mo) coordinate, *rotz* angle and four temperature factors). Also refined were the usual 7 variables for monoclinic HfO_2 (histogram scale factor, three cell parameters, β cell angle, one peak shape parameter and one temperature factor) and 11 parameters to describe a structure-less model of the Al sample holder inset (sample displacement, cell parameter, six PV peak shape terms, three peak area parameters for the three Al peaks present). The background was fitted with a twelfth-order Chebyshev polynomial. See the e-Appendix for the seed *TOPAS* input file. The spreadsheet showing all the refinement results is also given in the e-Appendix.

Forty-five variables were refined in the equivalent $P\bar{3}m1$ VT refinement; the parameters were identical to the $P\bar{3}$ refinement except that *rotz* was fixed at zero. Translation along the *c* axis was the only degree of freedom available to the MoO_4 group due to imposed constraints and symmetry restrictions. The *TOPAS* seed file and full results of the VT refinement are included in the e-Appendix.

The most important result of the above trigonal $HfMo_2O_8$ TTK450 refinements in the three space groups is given in Figure 5.24.

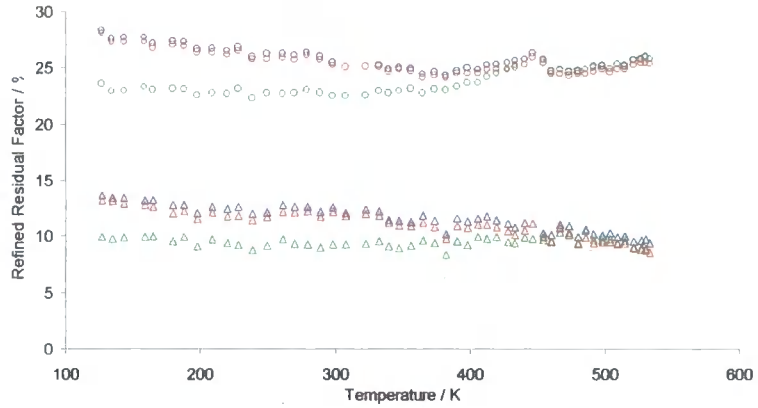

Figure 5.24. Weighted profile *R*-factors (circles) and Bragg *R*-factors (triangles) for trigonal $HfMo_2O_8$ from 120 – 620 K when refined in the $P\bar{3}1c$, $P\bar{3}$ and $P\bar{3}m1$ space groups. *R*-factors are quoted as percentages. Sample: SA98A, TTK450 cryofurnace, d8_01682 dataset. Temperatures have been corrected (so *e.g.* sample temperature is only ~ 533 K when preset/thermocouple temperature is 620 K).

The *R*-factor plot in Figure 5.24 shows that above the transition temperature (~ 460 K in the TTK450) all three space groups essentially provide as good a model of the trigonal structure as each other. Upon cooling below 460 K, and as the MoO_4 groups tilt away from the *c* axis, one can see that the $P\bar{3}$ and $P\bar{3}m1$ models are no longer as valid, shown by the gradual increase in both *R*-factors and one has to choose the $P\bar{3}1c$ space group and the large unit cell. Since $P\bar{3}$ - $P\bar{3}1c$ is not a symmetry-allowed change for a second-order phase transition, it was argued in Section 5.1.4 that a $P\bar{3}m1$ model is preferable. Figures 5.21, 5.23 and 5.24 add to the case put forward with trigonal $ZrMo_2O_8$ in Section 5.1; the basal movement of MoO_4 into the *ab* plane causes the large $P\bar{3}1c$ supercell to collapse to a cell one-sixth its volume with $P\bar{3}m1$ symmetry. It is emphasised that above T_c the *R*-factors for $HfMo_2O_8$ are identical in $P\bar{3}1c$ and $P\bar{3}m1$ giving strong support that the latter provides as good a fit to the data as the former.

5.3 Conclusion

A second-order phase transition has been observed in trigonal α-AMo_2O_8 materials (A = Zr, Hf) *via* variable temperature powder X-ray diffraction. The α to α' phase transition occurs at 487 K in trigonal $ZrMo_2O_8$ and at 463 K in trigonal $HfMo_2O_8$. The transition is most likely displacive in nature and has not been previously reported in the literature for any trigonal AM_2O_8 materials. The phase transition manifests itself as a change of gradient in the cell parameter trend as shown in Figure 5.20. Upon warming

the material, the $P\bar{3}1c$ supercell contracts to one sixth of its original volume. Through rigid-body refinements it has been shown that that the phase transition is due to movement of the basal plane of the rigid MoO_4 groups into the *ab* plane and consequent alignment of the Mo—O(4) bond with the *c* axis. This lowers the symmetry upon warming the material from the larger $P\bar{3}1c$ unit cell to a smaller $P\bar{3}m1$ unit cell. The trigonal α' phase is new addition to the family of known $ZrMo_2O_8$ materials that exist at ambient pressure. It is represented with other $ZrMo_2O_8$ phases in the Quick Reference Figure displayed in the inner cover of this thesis.

5.4 References

1. M. Auray, M. Quarton, P. Tarte, *Acta Cryst.*, **C42**, 1986, 257-259.
2. R. F. Klevtsova, L. A. Glinskaya, E. S. Zolotova, P. V. Klevtsov, *Sov. Phys. Dokl.*, **34**, 1989, 185-187.
3. M. Auray, M. Quarton, P. Tarte, *Powder Diffr.*, **2**, 1987, 36-38.
4. C. Lind, A. P. Wilkinson, C. J. Rawn, E. A. Payzant, *J. Mater. Chem.*, **12**, 2002, 990-994.
5. S. Carlson, A. M. Krogh Andersen, *Phys. Rev. B*, **61**, 2000, 11209-11212.
6. C. Lind, D. G. VanDerveer, A. P. Wilkinson, J. Chen, M. T. Vaughan, D. J. Weidner, *Chem. Mater.*, **13**, 2001, 487-490.
7. W. Freundlich, J. Thoret, *Compt. Rend. Acad. Sci. Paris*, **C265**, 1967, 96-98.
8. V. K. Trunov, L. M. Kovba, *Russ. J. Inorg. Chem*, **12**, 1967, 1703-1704.
9. A. Rimsky, J. Thoret, W. Freundlich, *Compt. Rend. Acad. Sci. Paris*, **C267**, 1968, 1468-1470.
10. V. N. Serezhkin, V. A. Efremov, V. K. Trunov, *Russ. J. Inorg. Chem*, **32**, 1987, 1568-1570.
11. R. Mittal, S. L. Chaplot, N. P. Lalla, R. K. Mishra, *J. Appl. Cryst.*, **32**, 1999, 1010-1011.
12. H. M. Rietveld, *J. Appl. Cryst.*, **2**, 1969, 65-71.
13. A. P. Wilkinson, C. Lind, S. Pattanaik, *Chem. Mater.*, **11**, 1999, 101-108.
14. A. Butz, G. Miehe, H. Paulus, P. Strauss, H. Fuess, *J. Solid State Chem.*, **138**, 1998, 232-237.

15. M. S. Samant, S. R. Dharwadkar, A. B. Phadnis, P. N. Namboodiri, *Mater. Chem. Phys.*, **35**, 1993, 120-125.
16. A. A. Coelho, *TOPAS v2.0: General Profile and Structure Analysis Software for Powder Diffraction Data*, Bruker AXS, Karlsruhe, 2000.
17. D. Taylor, *Br. Ceram. Trans. J.*, **83**, 1984, 92-98.
18. G. S. Pawley, *J. Appl. Cryst.*, **14**, 1981, 357-361.
19. K. Wang, R. R. Reeber, *Phil. Mag. A*, **80**, 2000, 1629-1643.
20. J. Thoret, *Rev. Chim. Miner.*, **11**, 1974, 237-261.
21. R. D. Shannon, *Acta. Cryst.*, **A32**, 1976, 751-767.

Chapter Six: Diffraction and Other Analytical Methods

6.1 Laboratory Powder X-ray Diffraction

6.1.1 Introduction

The bulk of the structural data collected, analysed and presented in this thesis were acquired using a new state-of-the-art Bruker AXS d8 Advance X-ray powder diffractometer (only the second of its type built). Before any definitive structural information could be obtained on the samples presented in this thesis, a series of in-house calibration procedures were necessary to ensure that accurate structural information of standard materials could be obtained. Considerable effort was made to collect and analyse data on standard compounds and to calibrate the operation of new variable temperature stages in addition to the diffractometer itself. The bulk of this chapter describes these methodologies as well as details of the corresponding data analyses. A new and very versatile software package called *TOPAS* was predominantly used for Rietveld refinement of both variable temperature (VT) X-ray and time-of-flight neutron diffraction data,[1,2] as well as peak fitting of X-ray data, structure-less (Pawley) fitting of laboratory and synchrotron X-ray data,[3] and even structure solution from powders *via* the technique of "simulated annealing".[4-6]

Throughout this thesis, diffraction data collected using the d8 (using any of the three variable temperature attachments) are referred to with a "d8_0*xxxx*" code, where *xxxx* is a sequentially ordered reference number. Data collections from the d8 frequently consisted of a series of diffraction patterns recorded at different temperatures. These separate diffraction patterns are referred to as "ranges" and denoted as, *e.g.* d8_01687:8, which refers to the eighth diffraction pattern of the d8_01687 data set, recorded at the eighth programmed temperature or time. Typically a Rietveld refinement was performed on the first range (*e.g.* d8_0*xxxx*:1) and this used as a seed for all other temperatures using multiple *TOPAS* refinements (see Section 6.1.11).

Several room temperature diffraction patterns reported in this thesis were collected using a Siemens d5000 diffractometer and brief details are given later. Such diffraction patterns are referred to using an analogous "d5_0*xxxx*" code. They only ever consisted of a single range collected at room temperature.

Brief details on the technique of time-of-flight neutron diffraction (results presented in Chapter 2), and energy-dispersive synchrotron X-ray diffraction (Chapter 4) are also discussed. Finally the experimental details of solid-state magic-angle spinning (MAS) NMR experiments on cubic ZrW_2O_8 (Chapter 3) are provided.

6.1.2 Bruker d8 Powder Diffractometer

The laboratory in Durham is equipped with a Bruker d8 powder X-ray diffractometer, which can be used for temperature-dependent investigations using the various attachments shown in Table 6.1 and Figure 6.1.

	Temperature range / K	Atmosphere (with temps)	Modes available
HTK1200 furnace	298 – 1473	air / vacuum / inert gas / 5% H_2 + N_2	flat plate
TTK450 cryofurnace	77 – 723	vacuum < 298 K, > 573 K. 298 < vac / air < 573 K	flat plate
PheniX cryostat	15 – 300	vacuum only	flat plate, capillary

Table 6.1. Brief operational details of the three variable temperature stages available to the Durham d8 diffractometer. Temperature ranges given are manufacturers' values.

Figure 6.1. The d8 powder diffractometer and the three compatible variable temperature stages available in Durham. The diffractometer is shown with the PheniX attached to the goniometer. Full alignment procedures were performed whenever the HTK1200 furnace, TTK450 cryofurnace or PheniX cryostat stages were interchanged.

The X-ray generator of the diffractometer operates at 40 kV and 40 mA and the d8 uses Ge (*111*)-monochromated Cu $K\alpha_1$ radiation ($\lambda = 1.540598$ Å). In normal flat-plate reflection mode (also when any of the stages in Table 6.1 are attached), the monochromatic X-rays pass through a 6 mm aperture slit, an anti-scatter tube, a fixed soller slit and an automated divergence slit in fixed or variable slit mode before reaching the sample. The role of the soller slit is to decrease axial divergence to minimise peak shifts and asymmetric broadening. A radial soller precedes a Braun PSD-50M linear Position Sensitive Detector (PSD), which collects the diffracted X-rays. A fixed step size of 0.0144 ° was used in all data collections and the collection time per step was adjusted as necessary. A PC using Bruker's *Diffrac*^{Plus} software controls the diffractometer, the HTK1200 furnace and the TTK450 cryofurnace.[7] The PheniX cryostat was delivered in April 2002 and runs independently using its own Oxford Cryosystems *CryoPad* software.[8]

6.1.3 Usage and Calibration of an HTK1200 Furnace

Powdered samples were mounted on a 17 mm alumina crucible inside the Anton Paar HTK1200 furnace (Figure 6.2, *left*, ref #4). Sample spillage at high temperatures and high 2θ angles was a problem in early test variable temperature experiments. The possibility of preparing samples as 15 mm pellets using a press and holding them in place using a 1 mm thick section of quartz tubing was investigated. Although this prevented sample spillage, potential problems associated with pressure-induced phase transitions and preferred orientation were likely. For example, pressing a 15 mm pellet of cubic α-ZrW_2O_8 to 10 tonnes would give the reported orthorhombic γ polymorph.[9] This method was therefore used infrequently and only for well-established materials.

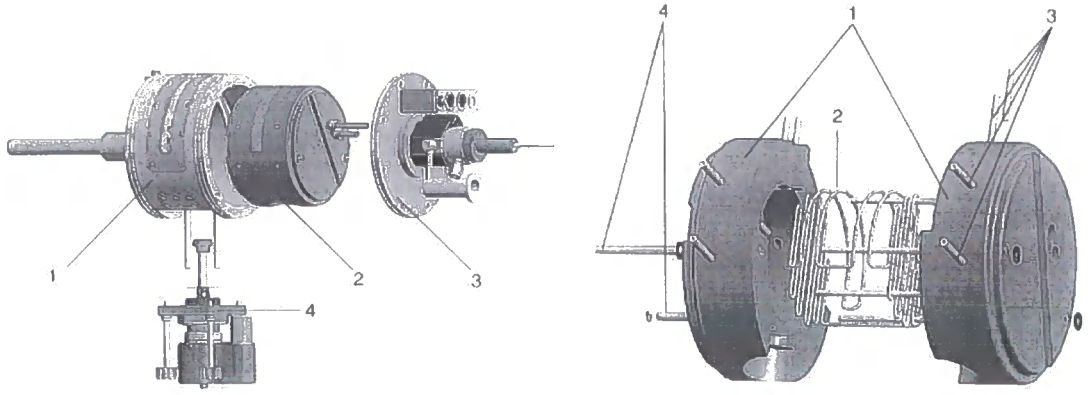

Figure 6.2. The Anton Paar HTK1200 high temperature furnace (*left*) and an expanded view of the oven (*right*). Left-hand key: (1) housing, (2) oven, (3) vacuum bleed/thermocouple/spinner connector plate, and (4) sample stage with alumina crucible sample holder. Right-hand key: (1) oven body, (2) 22% Cr, 5.8% Al/Fe radial heater, (3) sample stage mounting pins, and (4) centering pins. Figure taken from the HTK1200 handbook.[10]

For most VT data collections performed in the HTK1200 furnace, samples were sieved onto Vaseline or vacuum grease-coated amorphous quartz discs, around 15 mm in diameter, with the excess powder shaken off to leave a thin layer of sample. Discs were then placed in the alumina sample holder and raised into the body of the furnace. The height of the furnace was adjusted using a stepper motor such that the observed and calculated 2θ value of a strong Bragg peak were in agreement. The use of quartz discs avoided the pressure-induced problem above (also the fact that some powders cannot be pressed into pellets without breaking very easily) although it meant that the

signal : noise ratio was poorer simply because there was much less sample in the beam compared to a bulk powder/pellet. Another slight disadvantage was the difficulty in consistently achieving a uniformly flat surface with a sprinkled sample. Sample effects such as absorption and surface roughness could be different each time and would affect temperature factors slightly. Discs had to be discarded if used at high temperature owing to the inevitable crystallisation of quartz. Data for all samples studied in this thesis using the HTK1200 were collected under a normal ambient atmosphere.

Prior to the investigation of new materials in the HTK1200 furnace, an assessment of its true temperature profile was required. The radial heating elements in the HTK1200 are designed to give uniform temperature throughout the furnace. These are illustrated in Figure 6.2 (*right*). For the structural studies in this thesis it is imperative that the sample temperatures are accurately known if subtle changes in lattice parameter as a function of temperature are to be determined. Unfortunately the thermocouple is not located in exactly the same region of the furnace as the sample, as it would interfere with the X-ray beam. The thermocouple is a minimum of 5 mm from the sample holder and is fixed axially into the camera. The sample-thermocouple displacement implies that the temperature felt by thermocouple is not equivalent to the sample temperature. One must therefore calibrate the furnace such that the true sample temperature is known. There are several ways to achieve the calibration. One is by using standard materials whose cell parameters are well established.

To help eliminate other sources of error, a mixture of two standards, α-Al_2O_3 (0.701 g, 99%, Aldrich) and Si (0.279 g, 99.5%, Alfa) were ground together (sample i.d. SA13A), and a ~ 0.5 g 15 mm pellet pressed with PVA binder and mounted in the HTK1200 furnace. The pellet was then subjected to the following successive diffraction data collections: a scan at 303 K for 2 hours, 17-minute scans between 313 – 1123 K (every 10 K), a 2 hour scan at 1124 K followed by further rapid scans from 1118 – 308 K, and finally a two hour scan at 304 K. A Rietveld refinement on the 303 K scan was initially performed, as a two phase mixture using the *GSAS* refinement program.[11] A total of 25 variables were employed: two histogram scale factors, nine Chebyshev background terms, three cell parameters, two sets of peak shape parameters (three Lorentzian coefficients), a sample height correction, two atomic coordinates on Al and O, and two thermal parameters (one for Si; those of Al and O were equated). The refinement was

used as a seed for the remaining 166 diffraction patterns in the d8_00361 measurement, which were split into individual ranges using *Multirange*,[12] and refined using *GSASparameterise*.[13] The cell volumes were subsequently extracted and plotted as a function of temperature. These were compared to the values determined by Taylor (alumina),[14] and Okada (silicon).[15]

Taylor has collated how cell parameters vary as a function of temperature for many oxide materials using a combination of dilatometer and diffraction data from the literature, expressing results using Equation 6.1.[14]

$$a_{calc} = a_0(1 + x_1T + x_2T^2) \tag{6.1}$$

Since α-Al_2O_3 has two cell parameters a and c, it is convenient to use cell volumes so that alumina and silicon may be directly compared. For alumina, the parameters x_1 and x_2 according to Taylor are 1.96×10^{-5} K^{-1} and 6.54×10^{-9} K^{-2}. Also V_0 replaces a_0 (the former refines to 254.512 $Å^3$), leading to Equation 6.2.

$$V_{calc} = V_0(1 + x_1T + x_2T^2) \tag{6.2}$$

Silicon data from Okada were fitted using Equation 6.3, where $a_0 = 5.42805$ Å, $c_1 = 0.0192$ Å and $\theta_1 = 799$ K.

$$a_{calc} = a_0 + \frac{c_1}{e^{\theta_1/T} - 1} \tag{6.3}$$

One method used to obtain a calibration curve for the furnace is derived from the difference in unit cell volumes of the two materials. The observed cell volume of a sample, V can be considered as the sum of the actual (true) volume, V_{true} and the associated volume error, V_{err} which contains both systematic and random contributions. This applies to both Si and α-Al_2O_3 and so evaluating $V_{Si} - V_{alumina}$ would eliminate from V_{err}, the systematic terms due to factors such as sample height and absorption. Figure 6.3 shows a plot of $(V_{alumina} - V_{Si})_{calc}$ and $(V_{alumina} - V_{Si})_{obs}$ versus the set temperature.

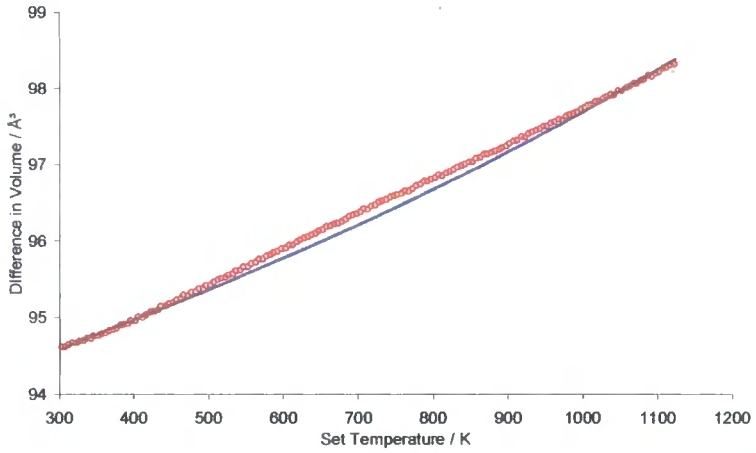

Figure 6.3. Observed and calculated differences in volumes of Al_2O_3 and Si as a function of temperature. It is apparent that the observed volume difference is larger than expected at intermediate temperatures, *i.e.* the sample is hotter than expected.

The corrected temperature was found by plotting the inverse of Figure 6.3, after fitting the calculated ΔV curve with a third-order polynomial. Then the error in temperature, ΔT was plotted by finding the difference between the calculated and observed temperatures as a function of set temperature and is shown in Figure 6.4.

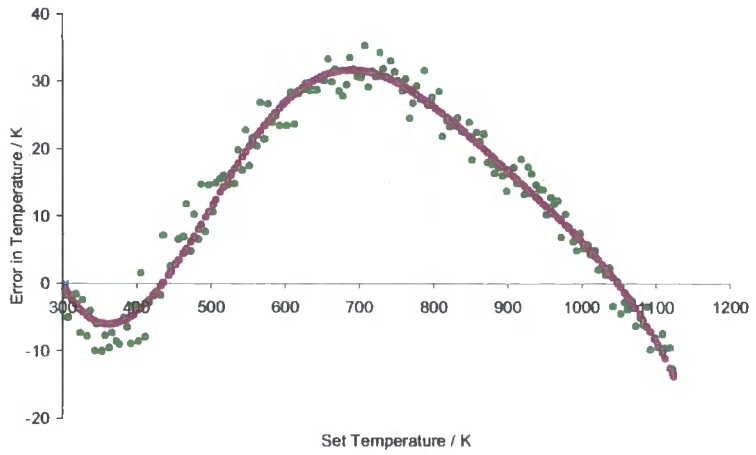

Figure 6.4. Calibration curve for the HTK1200 furnace using the difference in cell volumes of Si and Al_2O_3, shown in green (d8_00361). The violet curve is a fitted sine function scaled by two polynomials.

Two polynomials were used to scale a sine curve to give the fitted curve shown in violet in Figure 6.4. The true temperature of the sample, T_{corr} is expressed in the form,

$$T_{corr} = -\left(h_1 + h_2 T_{set} + h_3 T_{set}^2\right)\sin\left(x_1 + x_2 T_{set}^2 + x_3 T_{set}^3\right) \quad (6.4)$$

The *h* coefficients scale the height of the sine curve whereas the *x* values determine the width. Using Equation 6.4, it is possible to obtain interpolated values of the true furnace temperature when given a set of thermocouple recorded temperatures, such that corrected temperatures can be obtained for VT experiments.

Figure 6.4 shows that the maximum error in the furnace is ~ 32 K, at ~ 700 K. The sample seems to be significantly hotter than the thermocouple over a large temperature range (450 – 1050 K). More complete details of the above calibration procedure are given in a series of plots located in a dedicated spreadsheet in the Electronic Appendix (e-Appendix).

The above calibration analysis was repeated to check its validity using a sprinkled Si/Al_2O_3 sample on a quartz disc (SA13A, d8_01652). 24-minute powder patterns were recorded in the HTK1200 in 10 K intervals between 303 and 1073 K. A simpler calibration procedure was performed using only the alumina phase. The volume of the unit cell of Al_2O_3 was refined as a function of temperature with *TOPAS*. The following 25 variables were refined for the two-phase mixture at each temperature: twelve background terms, a sample height correction, and a total of two histogram scale factors, three cell parameters, two peak shape parameters, two atomic coordinates (for Al_2O_3), and three temperature factors. The *TOPAS* input file for the seed refinement can be viewed in the e-Appendix. It worth noting that an instrument axial divergence correction was applied to the data although not refined. This gives a Si cell parameter close to the literature value at room temperature.[15,16] Such a correction was employed in all HTK1200 refinements in this thesis. The effect of axial divergence on the cell parameter of Si is discussed later in this section.

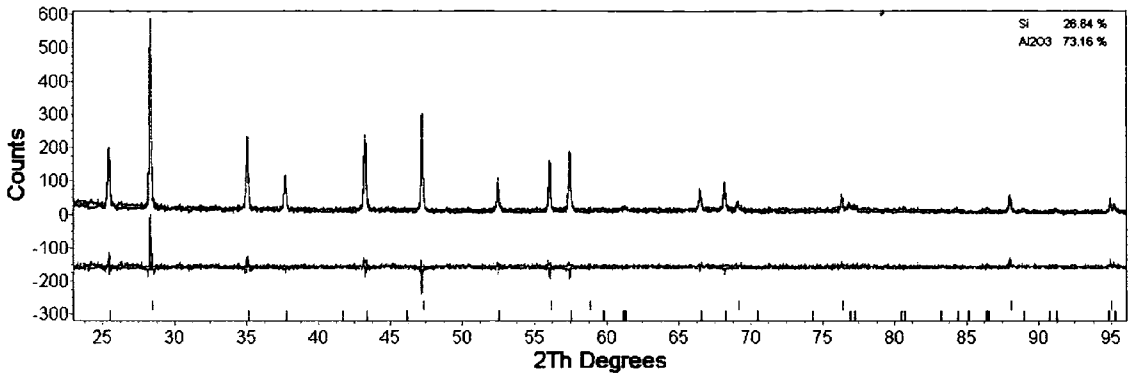

Figure 6.5. A two-phase Rietveld refinement of Si and Al_2O_3 at room temperature in the HTK1200 furnace (SA13A, d8_01652:1). Observed data are shown by the blue trace whereas, calculated data are in red; blue and black tick marks represent calculated peak positions for Si and Al_2O_3, respectively. Refined masses are also displayed and are within 2% of the actual masses used. The above refinement was used as a seed for those at all other temperatures. Data were collected on a sieved powder on a quartz disc.

Taylor's equation (6.2) was again used to calculate the temperature dependence of the unit cell volume of Al_2O_3. Temperatures were calculated from the observed volumes by rearranging Taylor's equation and the error in temperature plotted as a function of temperature. A third-order polynomial was fitted to this curve to give a calibration curve. Full details of this analysis are illustrated in the spreadsheet located in the e-Appendix. The calibration curve is re-shown in Figure 6.6 suggesting a maximum error of ~ 30 K at ~ 670 K. This is similar to that obtained in Figure 6.4 for a sample in pellet form using the more complex "difference in volumes" approach, and gives confidence in both calibration methods.

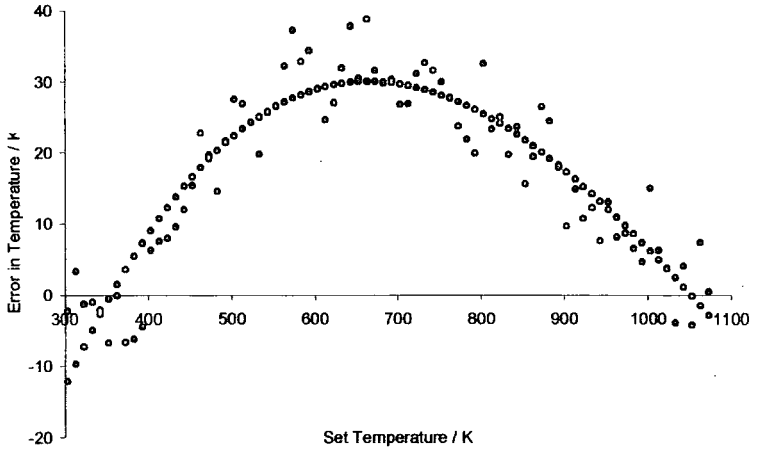

Figure 6.6. Calibration curve for the HTK1200 furnace derived from the refined and literature cell volume of Al_2O_3 (d8_01652). A fitted third-order polynomial is also shown: The sample studied was sieved onto a quartz disc; compare to Figure 6.4, where the sample was prepared as a pressed pellet.

From Figure 6.6, the set temperatures in the HTK1200 can be corrected as shown in Equation 6.5,

$$T_{corr} = T_{set} + \left(aT_{set}^{\ 3} + bT_{set}^{\ 2} + cT_{set} + d\right) \qquad (6.5)$$

with, $a = 1.61 \times 10^{-7}$ K^{-2}, $b = -5.86 \times 10^{-4}$ K^{-1}, $c = 0.565$, $d = -134$ K. This calibration curve was applied to most of the *in situ* $AM_2O_7(OH)_2(H_2O)_2$ precursor dehydrations presented in Chapter 2. Where appropriate, samples were ground with their own internal standard so an individual calibration curve for each specific run could be verified. For example, trigonal phases (Chapter 5) were mixed with Al_2O_3 to determine an accurate temperature for the phase transition observed for the first time. Although the HTK1200 calibration curve was similar each time, it is good practice to make regular use of internal standards wherever possible. The accuracy of the HTK1200-determined temperatures reported in this thesis is estimated at 5 – 10 K, as illustrated by the scatter in the data of Figures 6.4 and 6.6. It is noted that these calibration procedures have yielded phase transition temperatures for several systems in excellent agreement with those determined by other methods.

In a typical variable temperature data collection using the HTK1200 furnace, the sample moves upwards as a result of the expansion of the alumina sample holder. When heating

to around 1173 K (temperatures this high actually unnecessary to studies in this thesis), the change in sample height relative to that at 298 K can be up to around +0.5 mm. It was necessary ensure that cell parameters could be accurately determined despite such large sample height errors. Such high temperatures were mimicked using Si at room temperature and manually adjusting the height of the furnace. For the d8_00737 data set, the Si sample height was adjusted such that the (*111*) peak was observed at the calculated value of 28.44 ° 2θ, and the height re-zeroed. 30-minute powder patterns were recorded at 9 different heights relative to the initial run and refined with *TOPAS* to give the silicon lattice parameters shown in Table 6.2.

h_{set} / mm	$-h_{refined}$ / mm	*a* / Å	Area (*111*)	FWHM (*111*)	Scan #
–1.000	–0.994	5.43030 (3)	952.9	0.126	d8_00745
–0.500	–0.482	5.43039 (3)	1155.2	0.119	d8_00744
–0.250	–0.220	5.43053 (3)	1242.3	0.117	d8_00743
–0.100	–0.069	5.43049 (3)	1284.3	0.116	d8_00742
0	0.0372	5.43048 (3)	1347.9	0.114	d8_00737
0.100	0.135	5.43041 (3)	1341.6	0.112	d8_00738
0.250	0.288	5.43055 (3)	1377.8	0.112	d8_00739
0.500	0.546	5.43056 (3)	1379.9	0.110	d8_00740
1.000	1.056	5.43059 (3)	1307.3	0.108	d8_00741

Table 6.2. HTK1200-refined cell parameters of Si at room temperature as a function of preset sample height (to mimic sample height variation during a VT run). Also shown are peak-fitted intensities and full-width at half maximum values for the (*111*) Si peak. Note the *TOPAS* sign convention is to report a positive height as a negative sample displacement value.

Silicon data were refined using 17 independent variables: twelve background terms, a sample height correction, a histogram scale factor, cubic cell parameter, single peak shape parameter and a single isotropic temperature factor. A simple axial model to account for peak asymmetry at low angle was employed, albeit fixed at the default value of 12 mm for the diffractometer. Exclusion of this parameter from the refinements would give a slightly poorer fit to the data and smaller cell parameters (~ 5.4297 Å)

than those given in Table 6.2. Such values are slightly further removed from the room temperature cell parameter of Si reported by Okada of 5.431073 (6) Å (298.2 K) or for the standard reference material, SRM640c, with a = 5.4311946 (92) Å (at 295.6 K).[16] It was decided that for all HTK1200 refinements in this thesis that the axial divergence model should be employed.

Table 6.2 illustrates that the refined heights agree well with the manually adjusted values; the fact that *TOPAS* refines a positive set height to a negative physical sample displacement is worth noting to avoid confusion. Overall, consistent Si cell parameters are refined between displacements of ±1.0 mm, with a mean value of 5.43048 (9) Å. However close inspection of the nature of the lowest angle (*111*) peak (Table 6.2 and in the raw data) reveals decreased intensity, increased peak broadening and asymmetry for the –0.5 and –1.0 mm data. This is presumably due to movement of the sample from the ideal focussing condition. For variable temperature refinements in this thesis, the height remains between ~ 0 and < 0.3 mm so one can be confident of accurate cell parameters at high temperatures and no significant peak shape problems to be concerned with.

6.1.4 Usage and Calibration of a TTK450 Cryofurnace

An Anton Parr TTK450 cryofurnace was attached to the Bruker d8 diffractometer for diffraction studies of materials at low and intermediate temperatures. Basic specifications of the cryofurnace are described in Table 6.1. Realistic operating temperatures were found to be 90 to 700 K. The cryofurnace uses a liquid nitrogen pump to cool the base of the sample holder and a base-mounted cartridge heater to warm the sample. Low temperatures were sometimes difficult to achieve due to insufficient liquid nitrogen flow, which proved frustrating especially in the kinetic experiments of Section 3.4, where many attempts at collecting the data were necessary.

Sample mounting in the TTK450 is *via* a steel holder to contain bulk, powdered samples. The sample holder contains a hole to accommodate a thermocouple coated in heat-conducting paste. The thermocouple is sandwiched between the heater and sample, with a displacement of several millimetres. Unfortunately it was discovered that the study of non-conducting bulk powders (*i.e.* all systems in this thesis) at low or high

temperatures using the as-supplied TTK450 was far from ideal. A very large temperature error was apparent owing to the large temperature gradient from the thermocouple through the steel sample holder and non-conducting powder to the sample surface. Figure 6.7 shows the variation of cubic cell parameter of Y_2O_3 obtained *via* variable temperature cryofurnace data collections. Literature data given by Taylor are shown for comparison.[14]

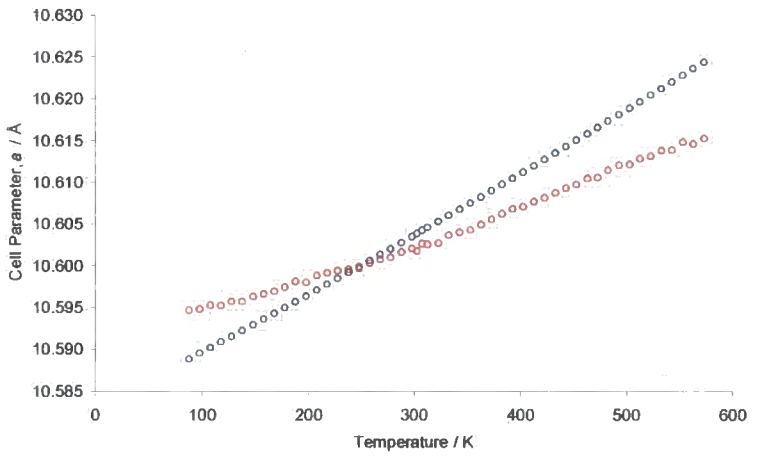

Figure 6.7. Refined versus literature-reported cubic cell parameter of Y_2O_3 collected using the TTK450 cryofurnace. A substantial temperature error is inherent to the "as supplied" cryofurnace, which under-reads by 120 K at "573 K", or by 90 K at "88 K".

10-minute data collections were acquired on bulk Y_2O_3 at 10 K intervals between set temperatures of 88 and 308 K (d8_00519), and between 303 and 573 K in a separate measurement (d8_00520). Data shown in Figure 6.7 were obtained using *GSAS* to refine the room temperature runs; *GSASparameterise* was used to duplicate the seed refinement at all other temperatures. 26 variables were refined at each temperature: a histogram scale factor, twelve background terms, a diffractometer zero point correction, a cubic cell parameter, four peak shape parameters, four atomic positions and three thermal parameters.

Even without fitting the Y_2O_3 data in Figure 6.7 to obtain a temperature error curve (as for the HTK1200 furnace), it was obvious the TTK450 cryofurnace required modification in order to be useful for accurate variable temperature experiments. The fact that the cryofurnace chamber must be evacuated when used at sub-ambient temperatures adds to problem of a large thermal gradient between thermocouple and the

sample surface exposed to the X-ray beam. It was presumed that bulk powders could not be used. A solution to the problem came in the form of a machined, flat aluminium insert onto which samples could be sieved thus achieving better thermal contact. This gave a much improved temperature profile at the expense of signal : noise. Samples were sieved onto the Al plate which was lightly coated with Vaseline on one side. The sample-coated Al plate would then reside in the steel sample holder recess with a small amount of heat conducting paste to aid thermal contact. All variable temperature cryofurnace data collections presented in this thesis were based on samples mounted in this way. It was noted that vacuum grease should be avoided as the sample-aluminium adherent as it crystallises below 220 K, whereas Vaseline remains amorphous. The Al plate gave rise to its own diffraction pattern on occasions, depending on how adherent each sample was to the Vaseline and therefore how exposed the Al was. The Al was normally modelled using a structure-less Pawley fit, and its cell parameter used as a quantitative internal thermometer.

The revised temperature profile of the cryofurnace with its Al plate was studied using an α-Al_2O_3 reference. Diffraction patterns of Al_2O_3 were recorded and refined between 620 and 90 K (a second phase LT-$ZrMo_2O_8$ was also present, as discussed in Chapter 2). The seed *TOPAS* input file for the Al_2O_3 refinements (d8_01687) is located in the e-Appendix and apart from twelve background terms, a further nine parameters were used to describe the Al_2O_3 phase (other parameters due to $ZrMo_2O_8$ and Al phases detailed in Section 2.2.8). The necessary Al_2O_3-specific variables employed were a histogram scale factor, a sample height correction, two rhombohedral cell parameters, a single peak shape parameter, two atomic coordinates and two thermal parameters. The first refinement (that at 620 K) was used as a seed for those at all lower temperatures, and the unit cell volumes extracted and plotted in a spreadsheet contained in the e-Appendix. The data were fitted and compared to the literature values obtained using Taylor's equation (Figure 6.8, *left*). The same fitting procedure was applied to the observed cell volume data as in the latter part of Section 6.1.3, *i.e.* calculated temperatures were obtained using the observed cell volumes and a rearrangement of Taylor's equation, followed by evaluation of the difference in set (or logged) temperature and the calculated values. A third-order polynomial was fitted to this ΔT versus T plot as derived in the e-Appendix and re-plotted in Figure 6.8 (*right*).

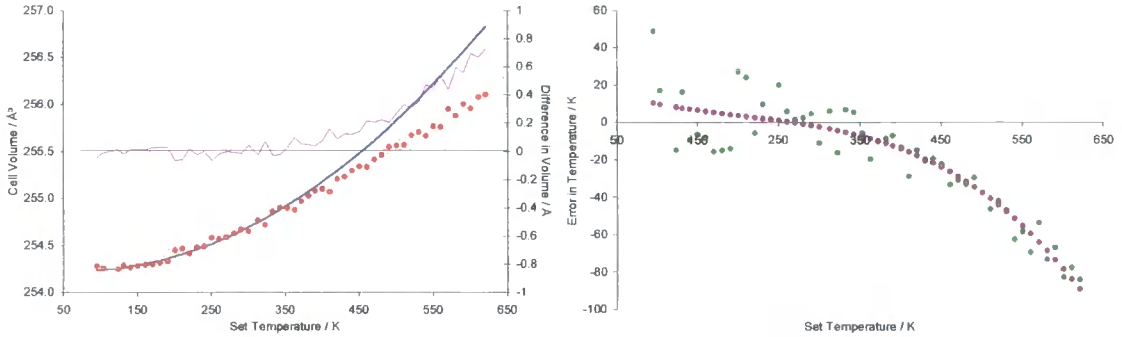

Figure 6.8. Refined TTK450 and Taylor literature cell volume data for α-Al_2O_3 including difference curve (*left*). The resultant temperature error and a fitted third-order polynomial are shown on the right (d8_01687).

With the improved sample holder the temperature experienced by the sample at low temperatures is much closer to that recorded by the thermocouple. Comparing Figure 6.8 (*left*) to Figure 6.7, the discrepancy at 100 K has reduced from ~ 90 K to ~ 10 K. At high temperature a large error is still apparent although it is an improvement to that observed with a bulk powder, *e.g.* a ~ 64 K error exists at a set temperature of 570 K compared to a ~ 120 K error as previously described.

In most instances where the TTK450 was used for structural studies in this thesis, an Al_2O_3 internal standard was included and the above analysis repeated for each individual sample. If an internal standard was not used the above TTK450 calibration curve was applied, the relevant polynomial being,

$$T_{corr} = T_{set} + \left(aT_{set}^{\ 3} + bT_{set}^{\ 2} + cT_{set} + d\right) \qquad (6.6)$$

with $a = -9.92 \times 10^{-7}$ K^{-2}, $b = 6.10 \times 10^{-4}$ K^{-1}, $c = -0.177$, $d = 22.4$ K.

The polynomial coefficients in Equation 6.6 varied slightly from sample to sample. The temperature profile of the modified TTK450 is dependent on both the thickness of the Vaseline layer and of the sample itself, since the sample is heated and cooled from beneath, with a dynamic vacuum above. However, the forms of the calibration curves were always similar and can be viewed in the appropriate spreadsheets given in the e-Appendix. In contrast, HTK1200 calibration curves were virtually identical from sample to sample owing to the superior convection-type heating rather than conduction-dependent heating in the TTK450.

6.1.5 Usage of a PheniX Cryostat

Oxford Cryosystems designed and built the first ever "PheniX" Closed Circuit Refrigerator (CCR) cryostat to be used in conjunction with the Durham Bruker d8 diffractometer in 2002 (Figure 6.1). The cryostat is engineered to the highest levels and extremely simple to use. Commissioning the PheniX was straightforward; there were no modifications necessary as in the case of the furnace or cryofurnace as discussed previously. The PheniX was designed to reach temperatures of 15 K. A turbo pump assembly provides the required operating atmosphere of around 10^{-4} mbar while gaseous He is pumped around the system from the circulator to the cold head *via* a compressor. Helium is repeatedly compressed and re-expanded adiabatically to provide the necessary cooling each time it completes a loop in the "closed-circuit" system. The actual minimum temperature obtainable with the PheniX was found to be ~ 16.5 K. Due to the closed-circuit nature of the PheniX, it requires only infrequent top-ups of gaseous He. It can be used for very slow cooling or warming experiments between 17 and 300 K. Contrast this to the TTK450 cryofurnace, where one is restricted to a single 25 litre dewar of liquid nitrogen, which gives around 12 – 15 hours to collect data below room temperature. Rapid cools ("quenches"), however, are not possible with the PheniX and so the cryofurnace had to be used *e.g.* in the quench kinetic experiments of Section 3.4.2 and 3.4.3.

Powdered samples can be sieved onto a supplied flat anodised Al plate, which screws into the coldhead of the PheniX. A thin layer of Vaseline was used to adhere samples to the Al holder. The PheniX can also be configured to accept samples packed into glass capillaries although all data collections described throughout this thesis were recorded in regular flat-plate mode. The cooling system in the PheniX is similar to the TTK450 cryostat in that it relies on conduction from the base of the sample holder. However it is a much more sophisticated design with the sample holder surrounded by an inner shield assembly that is cooled to 50 K, while the sample holder itself can then be cooled to 17 K. The dual cooling set-up of the PheniX means that the sample and thermocouple experience the same temperatures. Tests below using standard materials illustrate the accuracy of the PheniX throughout the whole temperature range.

The PheniX runs independently from the diffractometer and so the normal operating procedure involves the simultaneous execution of both a diffractometer job using *Diffrac*^{Plus} (in which infinite runs were programmed) and a temperature ramp in the PheniX *CryoPad* software. A default ramp setting of 17 Khr^{-1} was chosen, and typically 30 minute scans were performed implying diffraction patterns every ~ 8.5 K were recorded. Temperatures were logged and the average extracted for each diffraction pattern using *PheniXlogfile*.[17]

Commissioning of the PheniX was achieved using powdered Si powder, sieved onto an anodised Al holder and cooled at 17 Khr^{-1} from 295 to 17 K. 32 30-minute powder patterns were recorded between 25 and 140 ° 2θ (d8_01726). The material was subsequently warmed at 10 Khr^{-1} back from 20 to 300 K and a total of 54 diffraction patterns acquired (d8_01727). Seed *TOPAS* input files were set up for Rietveld refinement of the first range in each of the two measurements. 36 parameters in total were employed to describe the two-phase mixture. The Al sample holder gave rise to a very strong diffraction pattern (Figure 6.9) and was modelled with a Pawley fit. The variables used in the refinements were twelve background terms, two sample height corrections (one for Si, one for the Al holder), a histogram scale factor for Si, two cell parameters for Si and Al, twelve pseudo-Voigt peak shape terms (six for each phase), six parameters to model the intensity under the six observed Al peaks, and one temperature factor for the Si atom.

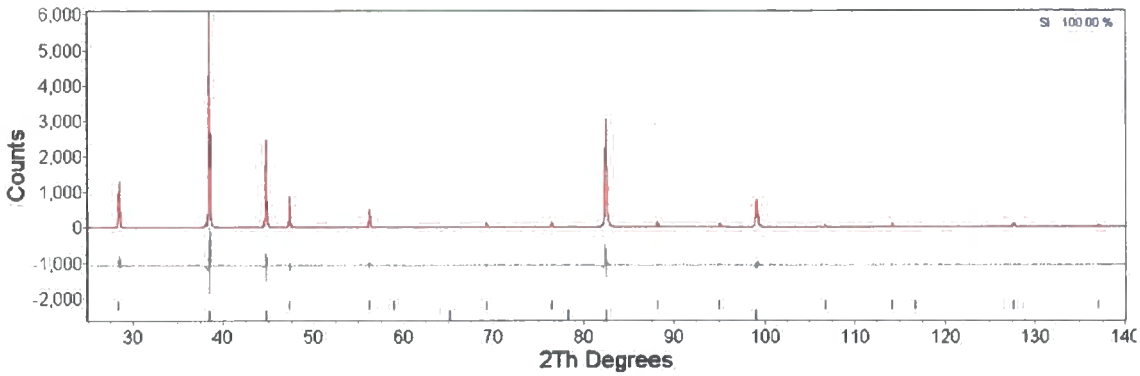

Figure 6.9. 295 K Rietveld refinement for the variable temperature data collection on Si in the PheniX cryostat (d8_01726:1). 30-minute diffraction pattern is shown in red, the calculated model in blue and the difference between the two, shown in grey. The upper and lower row of tick marks at the base of the figure show the calculated peak positions for Si and the Al sample holder, respectively.

The input file, which gives rise to the room temperature refinement illustrated in Figure 6.9, can be viewed in the e-Appendix. The instrument axial divergence parameter was fixed at the default value of 12 mm (as for the HTK1200 data). This parameter remained fixed in all other PheniX experiments described in this thesis.

Refined Si cell parameters as a function of temperature were extracted from the two sets of variable temperature refinements and compared to a set of dilatometry data reported by Lyon *et al.*.[18] The relevant spreadsheet located in the e-Appendix shows the data; the cell parameter plot is reproduced below in Figure 6.10. Lyon reported that between 4 and 18 K, and above 125 K positive expansion is exhibited by Si, whereas negative thermal expansion is displayed between these temperatures. The cell parameter for the Al sample holder versus that reported by Wang and Reeber is also shown.[19]

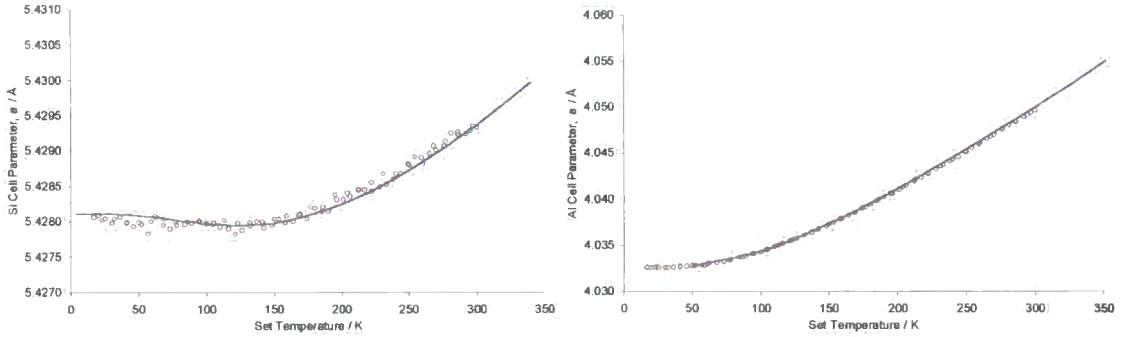

Figure 6.10. Refined cell parameters of Si (*left*), and the Al PheniX sample holder (*right*) upon cooling and warming (d8_01726 and d8_01727) versus literature data. Note that owing to the much larger expansion of Al, the scatter seems less compared to that of Si.

The refined temperature profile of the PheniX seems to be quite accurate judging from the results displayed in Figure 6.10. Si data are quite scattered owing to relatively short data collection times so at low temperatures one cannot resolve the subtle change between weakly positive then negative expansion as presented in the literature. The agreement between the Al data seems superior although it is worth noting that a relatively large cell parameter scale exists.

The thermal expansion of one of the materials studied in Chapter 3 and 4, cubic ZrW_2O_8, has been well documented in the literature.[20-22] As a final temperature profile assessment of the PheniX, a sample of cubic ZrW_2O_8 (provided by Evans) was studied in a similar manner to Si and Al described above; a 12 Khr^{-1} warm from 16.5 K to 299 K was programmed, over which time a total of 42 30-minute diffraction patterns recorded (d8_01569). The seed 16.5 K refinement for all other temperatures was performed using 49 variables in *TOPAS* including seven parameters to describe the background. To model the ZrW_2O_8 phase, a sample height correction, histogram scale factor, cubic cell parameter, six pseudo-Voigt peak shape terms and one temperature factor were refined. A first generation bulk Al sample holder was used although ZrW_2O_8 was only sprinkled inside to avoid spillage of a bulk powder. Consequently, a diffraction pattern from both the rim and base were observed. These "two Al phases" were modelled with Pawley fits each with their own sample displacement correction, six PV peak parameters, cubic cell parameter, and eight parameters to model the observed intensity under the eight Bragg peaks between 10 and 120 ° 2θ. The seed input file and VT Rietveld parameters are contained in a spreadsheet within the e-Appendix. The refined lattice parameter versus literature data for ZrW_2O_8 is shown in Figure 6.11.

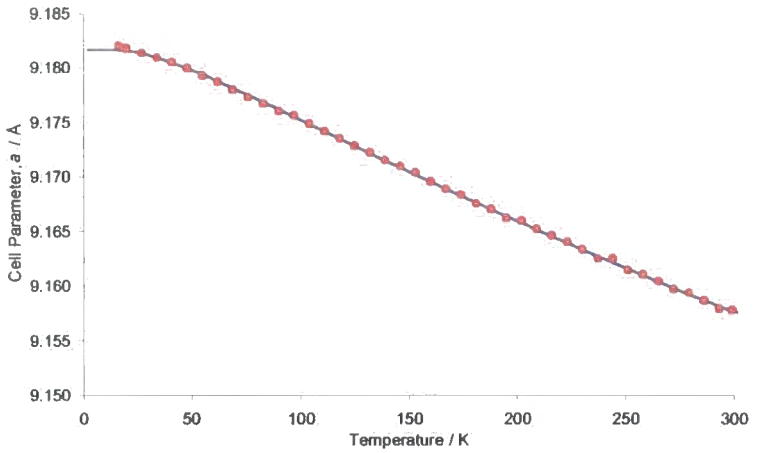

Figure 6.11. Refined cell parameter of cubic ZrW_2O_8 using data collected on the PheniX cryostat (d8_01569) versus the literature study by Evans *et al.*, using neutron diffraction.[22]

Figure 6.11 shows excellent agreement between the cell parameter trend obtained with the PheniX cryostat and that modelled on a simple Einstein model, fitted to neutron diffraction data collected by Evans *et al.*; the coefficient of expansion derived from the PheniX data is -9.5×10^{-6} K^{-1} (between 20 to 294 K) which is identical to that obtained from the literature neutron diffraction data.[22] Figures 6.11 and 6.10 clearly show that, unlike the TTK450 cryofurnace, the temperature profile obtained from the PheniX is very satisfactory and in-house modifications are not necessary.

6.1.6 Lorentz-polarisation-absorption Corrections of Lab Diffractometers

Since the characteristic radiation from an X-ray tube is unpolarised, *i.e.* the electric vector vibrates in all directions, and partial polarisation occurs upon diffraction, the intensities of detected X-rays are reduced. The amount of polarisation depends on the angle through which the radiation has been diffracted. An unpolarised beam can be considered as two vectors perpendicular to the propagation direction with amplitude $\sqrt{2}/2$. Diffracting electrons in the powder are compelled to vibrate parallel to these vectors, at right angles to the X-ray beam. As the angle of diffraction increases, the horizontal component remains undiminished but the vertical component of the diffracted beam decreases as the electrons radiate no energy parallel to their vibrational directions. The vertical electric vector scales with $(\sqrt{2}/2)\cos 2\theta$ and when $2\theta = 90°$ the

X-rays are only horizontally polarised. The reduction in intensity is calculated from the fact that the intensity is proportional to the square of the amplitude of the wave (Equation 6.7).

$$I \propto \left(\frac{\sqrt{2}}{2}\right)^2 + \left(\frac{\sqrt{2}}{2}\right)^2 \cos^2 2\theta = \frac{1}{2}\left(1 + \cos^2 2\theta\right) \tag{6.7}$$

The d8 diffractometer has a Ge (*111*) primary monochromator, which polarises the beam prior to diffraction by the sample. The beam is thus diffracted twice before reaching the detector so a more complex expression describes the extent of polarisation,

$$I \propto \frac{\left(1 + \cos^2 2\theta_{mono} \cos^2 2\theta\right)}{\left(1 + \cos^2 2\theta_{mono}\right)} \tag{6.8}$$

where, $2\theta_{mono}$ is the angle of the crystal monochromator.

The Lorentz factor is another instrument-related quantity, which affects the intensity of diffracted X-rays. It relates to the variation of time for which each diffraction plane in a crystalline sample is in the correct position to cause diffraction. As 2θ rises, the angular velocity effectively increases and the reflection spends less time in the diffracting condition. The intensity of high angle reflections are thus artificially reduced. This can be corrected as follows,

$$I \propto \frac{1}{\left(2\sin^2\theta\cos\theta\right)} \tag{6.9}$$

A further geometry-dependent effect which influences the intensity of diffraction peaks is sample absorption. This primarily affects the magnitude of refined temperature factors. For the X-ray Rietveld refinements performed using *TOPAS* in this thesis these three effects were combined into a single Lorentz-polarisation-absorption (LPA) correction of the form given in Equation 6.10.

$$LPA = \exp\left(-2fixb\sin^2\theta/\lambda^2\right)\frac{\left(1+\cos^2(2\theta_{mono})\cos^2 2\theta\right)}{\sin^2\theta\cos\theta} \qquad (6.10)$$

The first term in Equation 6.10 represents the absorption correction whereas the second part describes the Lorentz-polarisation (LP) factor. The parameters *fixb* and $2\theta_{mono}$ are discussed below.

The values of *fixb* in the LPA factor are dependent on the geometry of the diffractometer and method of sample mounting although, ideally, are independent of the chosen divergence slit setup. The various geometries of the Bruker d8 diffractometer are room temperature flat-plate reflection; flat-plate reflection in the furnace, cryofurnace and cryostat; flat-plate transmission and capillary transmission modes. By running room-temperature measurements of a standard material, the values of the LPA factors in each of the possible machine geometries can be determined empirically. Y_2O_3 was chosen as it is very crystalline, its structure is well known and diffracts strongly over a wide range of 2θ.

In order to be sure of obtaining reliable LPA corrections, a sensible set of temperature factors must be used when refining data. Literature values determined by X-ray synchrotron single crystal work are shown in Table 6.3 and were used as a benchmark.[23]

Y(1) B_{equiv} / Å^2	0.2131
Y(2) B_{equiv} / Å^2	0.2527
O(1) B_{equiv} / Å^2	0.3790
R_{F^2}	0.0590
Cell parameter, a / Å	10.5981(7)
Y1 x	0.96764(3)
O1 x, y, z	0.3907(2), 0.1518(2), 0.3801(2)

Table 6.3. Results of the synchrotron single crystal X-ray study of Y_2O_3.[23]

In each of the d8 geometries, a good quality data set was obtained on Y_2O_3 (99.99%, Aldrich), after the material had been dried at 800°C for half an hour and then ground

with a pestle and mortar. Y_2O_3 samples were mounted in the characteristic way for the different configurations of the d8, as in Table 6.4.

Refinements were performed with *TOPAS*; $2\theta_{mono}$ was fixed at the ideal value for each diffractometer and the *fixb* parameter refined. An earlier, more primitive approach was to simply let the LP factor refine on its own, and such refinements have been described elsewhere.[24]

Machine geometry; divergence slit configuration	Scan #	2θ range / degrees	Sample format	*fixb*
d8 ambient stage; V20 slit	**d8_00254:70**	**18 – 140**	**Bulk powder**	**0.036**
d8 with HTK1200; fixed 1° slit	**d8_00328**	**15 – 135**	**Bulk powder**	**-0.070**
d8 with HTK1200; V20 slit	d8_00335	15 – 135	Bulk powder	-0.326
d8 with TTK450; fixed 1° slit	d8_0518:1	15 – 135	Bulk powder	-0.094
d8 with TTK450; fixed 0.5° slit	d8_01706:6	15 – 130	Sprinkle (Al plate)	1.176
d8 with TTK450; V20 slit	d8_00518:2	15 – 135	Bulk powder	-0.031
d8 with TTK450; V6 slit	**d8_00518:3**	**15 – 135**	**Bulk powder**	**-0.283**
	d8_01706:2	15 – 130	Sprinkle (Al plate)	0.461
d8 with TTK450; V3 slit	d8_01706:3	15 – 130	Sprinkle (Al plate)	1.350
d8 with PheniX; fixed 1° slit	**d8_01720**	**15 – 135**	**Sprinkle**	**1.170**
d8 flat plate transmission	d8_00428	15 – 120	Sprinkle (polyimide)	0.493
d8 capillary	d8_00008	15 – 128	0.3mm glass cap.	-1.430
d5000; fixed 1° slit	**d5_00451**	**15 – 150**	**Bulk powder**	**0.182**
d5000; V6 slit	d5_00450	15 – 150	Bulk powder	0.233

Table 6.4. Room temperature Y_2O_3 scans run using various geometries of the d8 and d5000 diffractometers. Note, *e.g.* d8_00254:70 refers to a multiple room-temperature measurement and only the 70th range was refined here. $2\theta_{mono}$ values for the d8 and d5000 machines were fixed at 27.26 and 26.6 °, respectively. Refined *fixb* values contain information regarding the LPA correction in the respective machine geometry/slit setting shown. Note also a V20 slit refers to a variable 20 mm slit *etc.* Recommended slit settings for each given geometry (*i.e.* those that result in the most accurate refined intensities) are highlighted in bold.

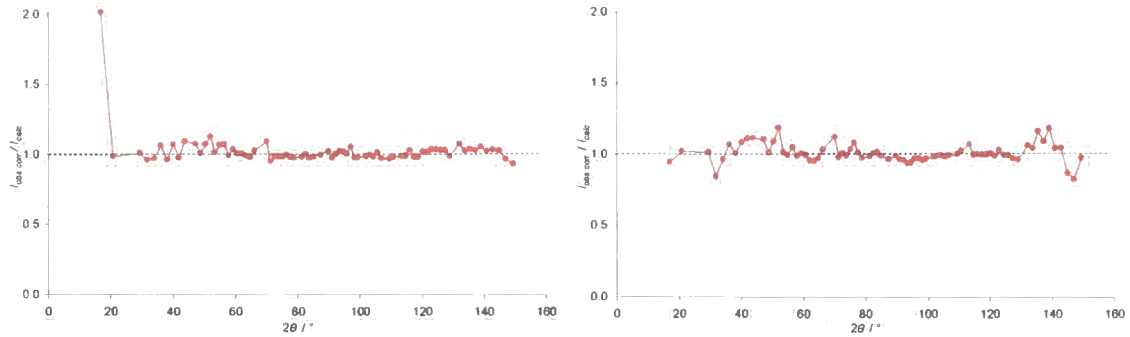

Figure 6.12. $I_{obs,corr}$ / I_{calc} versus 2θ plots for the Siemens d5000 with V6 (*left*) and 1 ° slits (*right*).

The effectiveness of the LPA corrections can be readily assessed from the plots of Figure 6.12 and 6.13 for the d8 and d5000 diffractometers. These plots compare the ratio of $I_{obs,corr}$ / I_{calc} for the best instrument configurations where $I_{obs,corr}$ is the observed intensity of individual *hkl* reflections obtained by Pawley fitting data with the LPA corrections of Table 6.4, and I_{calc} are intensities calculated from the X-ray synchrotron-determined coordinates of Table 6.3. For a perfect correction $I_{obs,corr}$ / I_{calc} would be 1.0 for all 2θ angles. The plots of Figure 6.13 contain significant experimental scatter, particularly for cases where $I_{obs,corr}$ and I_{calc} are small numbers. Their trends as a function of 2θ are, however, smooth giving confidence that the LPA correction used is appropriate.

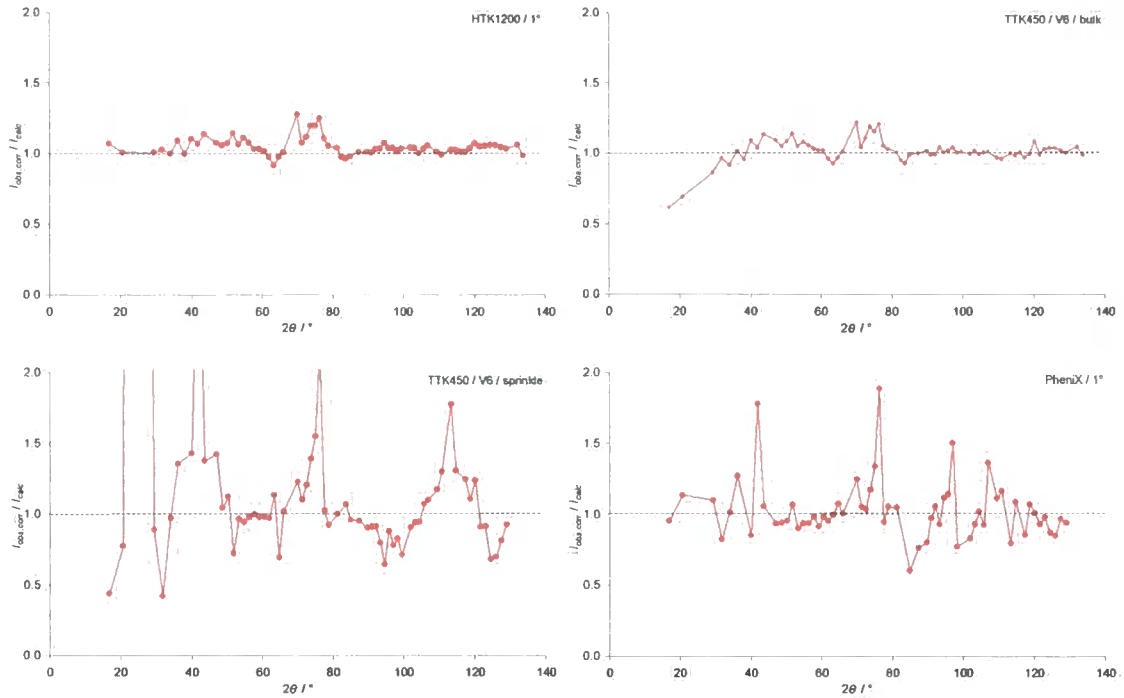

Figure 6.13. Selected $I_{obs,corr}$ / I_{calc} versus 2θ plots for the Bruker d8 diffractometer and the variable temperature stages and slit configurations.

Table 6.4 shows that different values of *fixb* are obtained using either a flat-packed bulk powder or a sprinkled sample in the TTK450 cryofurnace using a V6 (variable 6 mm) slit. Temperature factors are strongly affected by sample absorption and surface roughness and so in reality the *fixb* parameter will vary from sample to sample. However, the plot in Figure 6.14 shows completely different values of *fixb* and $2\theta_{mono}$ and how they compare. It can be seen just how correlated the temperature factor, scale factors and LPA factors are and at the end of the day, it does not matter greatly which values of *fixb* are used. It should be noted that the values derived are based on Y_2O_3 and may not be valid for materials with Bragg reflections at significantly lower 2θ values.

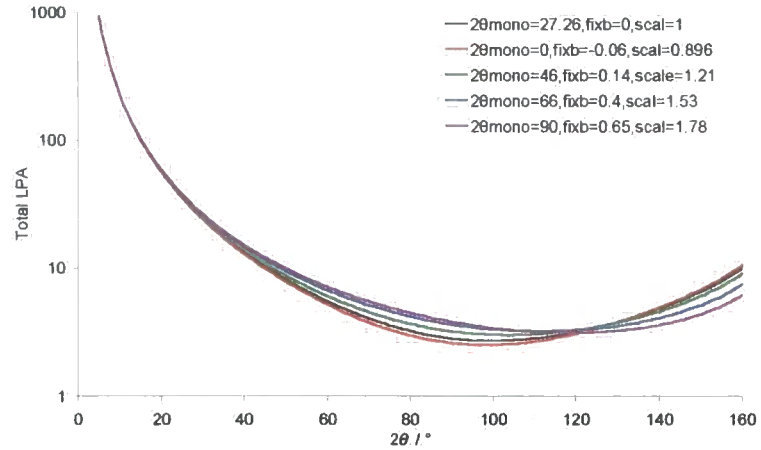

Figure 6.14. Lorentz-polarisation-absorption (LPA) corrections as a function of 2θ with various monochromator angles, scale factors and *fixb* values.

6.1.7 Bench-marking a d8 Diffractometer Using a Standard Reference Material

A good performance check of a diffraction instrument is to measure the full-width at half-maximum, FWHM variation as a function of 2θ, using a standard reference material (SRM) endorsed by the National Institute of Standards and Technology (NIST). The laboratory possesses a sample of SRM1976, a 45 mm sintered plate of high quality α-Al_2O_3 (corundum). The plate comes with an authenticity certificate describing the precise hexagonal a and c cell parameters of 4.758846 (109) Å and 12.99306 (238) Å, determined using a copper X-ray source of $\lambda = 1.540629$ Å.[25] The 45 mm specimen consists of a platelet-like microstructure of around $3 - 7\,\mu$m in diameter, $1 - 2\,\mu$m thick; these platelets are highly oriented with the basal plane parallel to the surface of the plate.

A second instrument test is to measure the difference in 2θ ($\Delta 2\theta$) as a function of 2θ, by comparing the observed peak positions with those predicted by NIST. The NIST1976 data set obtained on the d8 can also be refined and the accuracy of the unit cell parameters determined on the d8 can then be evaluated. Both detectors (a scintillation counter and a linear position sensitive detector, or PSD) available to the d8 were separately used in these two tests.

The d8 diffractometer was first set up in regular flat-plate reflection mode with V4 slits and a scintillation counter detector. A 14-hour room temperature scan of NIST Al_2O_3 (scan number d8_00300; 24 – 99 ° and 127 – 137 ° 2θ) was performed. The two ranges were dealt with separately but both were converted to single line intensity *dat* files using *XCH*.[26] A second scan (d8_00497, 10 – 130 ° 2θ, 2.5 hours) with a 1 ° divergence slit and a PSD was measured. The *XFIT* line-fitting program was used to fit pseudo-Voigt peaks to each of the reflections in the diffraction patterns.[27] Figure 6.15 shows the results of the analysis for FWHM versus 2θ.

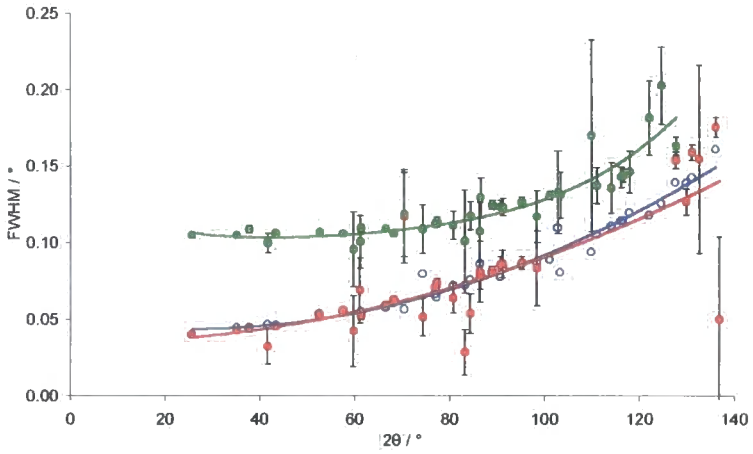

Figure 6.15. Variation of peak width at half maximum for NIST alumina, versus Bragg angle as obtained for the Durham d8 with scintillation counter, d8 with PSD and test data obtained by Bruker.

The figure above shows that the d8/scintillator performs well on average since the trend line in black lies almost on top of the test data set run by Bruker.[28] The PSD inherently gives rise to greater line-widths than the scintillation counter due to axial divergence since the PSD simultaneously collects 6 ° 2θ whereas the latter is a point detector. The maximum designed resolution of the PSD is such that FWHM ≤ 0.08 °. In contrast the intensity obtained by the PSD is far superior (around 15 times greater when comparing the two NIST scans discussed here). For this reason, the PSD is generally used as the routine flat-plate reflection detector on the d8, with the scintillation counter being used for studies where high resolution rather than large peak intensity is required. All the d8 data collections presented in this thesis were acquired using the PSD.

The accuracy of peak positions as a function of 2θ is shown for the PSD and scintillation detector in Figure 6.16. Both data sets show similar systematic changes in

$\Delta 2\theta$ with 2θ. The absolute $\Delta 2\theta$ offset of the PSD data relative to the scintillation data is irrelevant; it is most probably due to errors induced when the scintillation counter is mechanically removed and replaced by the PSD at the end of an alignment procedure. $\Delta 2\theta$ shows a more marked 2θ dependence than the Bruker test data, though this value depends on the precise slit and sample absorption set up for a particular data collection (and more than likely these were highly optimised on the Bruker machine in order to assist their diffractometer sales!).

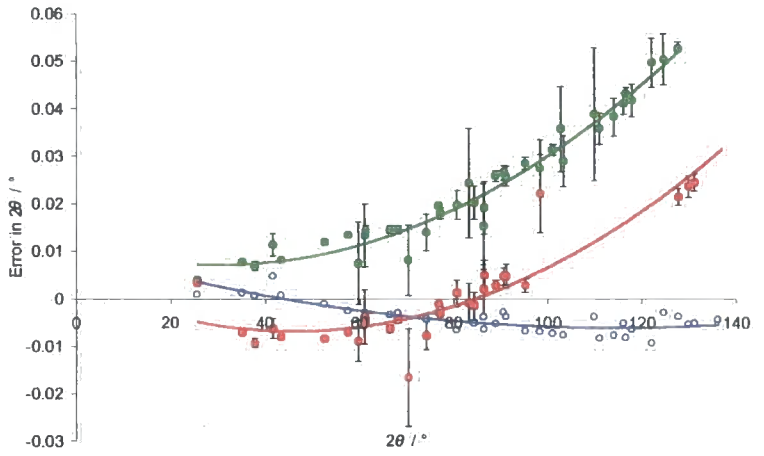

Figure 6.16. $\Delta 2\theta$ as a function of 2θ for the Durham d8 diffractometer with scintillation counter and PSD in comparison to d8 test data (taken from a spreadsheet in the e-Appendix).

To determine a typical cell parameter accuracy from d8 data, structural refinement of the above diffraction patterns of SRM1976 were performed. Fifteen variables were used in the *GSAS* refinement of Al_2O_3 data collected using the scintillator: one histogram scale factor, six background terms, six profile parameters (five for the peak shape, one to account for sample height) and two cell parameters. A structure-free Le Bail fit was performed where peak positions are constrained to lie at values predicted by cell parameters and space group. Intensities, cell parameters, peak shape parameters and instrument corrections (sample height) are then adjusted to give the best overall fit to the observed pattern.[29] Analogous structure-free Pawley fits were also carried out using *TOPAS* for comparison using six background terms, a sample displacement correction, two cell parameters, six PV peak parameters and thirty-one parameters to model the intensity under the thirty-one reflections between 24 and 99 ° 2θ.[3] The refined cell parameters obtained from the Al_2O_3/scintillator refinements are given in Table 6.5. Also

given are values for *a* and *c* refined from the d8 data using two independent programs *REFCEL*,[30] and *CELREF2*.[31]

	NIST standard	*GSAS*	*TOPAS*	*REFCEL*	*CELREF2*
Cell parameter, *a* / Å	4.75885 (11)	4.75874 (4)	4.75861 (4)	4.75839 (2)	4.7589 (1)
Cell parameter, *c* / Å	12.99306 (238)	12.9925 (1)	12.99213 (8)	12.9914 (2)	12.9916 (1)
Wavelength, λ / Å	1.540629	1.540598	1.540598	1.540598	1.540598

Table 6.5. NIST Standard and laboratory refined cell parameters of SRM1976 alumina. Laboratory data acquired using a Bruker d8 diffractometer with scintillation counter (d8_00300).

Comparing the standard and refined *a* (and *c*) lattice parameters of alumina reveal that all the values lie within 0.0005 Å (0.0015 Å) of each other. More importantly, the NIST and *GSAS* values only differ by 0.0001 Å (0.0006 Å) *i.e.* both within one ESD of the standard parameters. This corresponds to an accuracy of 99.9977% for *a*, and 99.9956% for *c*. One can conclude that the overall the d8 (with scintillation counter) performs well.

For the PSD-collected alumina data, twelve *GSAS* parameters (one scale factor, six background terms, two cell parameters, sample shift and two peak shape parameters) were used. 67 variables were used in a Pawley fit using *TOPAS* (six background terms, two cell parameters, a sample height correction, six PV peak shape terms, one crystallite size peak width term and fifty parameters to describe the intensity under the fifty peaks of the observed powder pattern). The refined cell parameters are shown in Table 6.6.

	NIST standard	*GSAS*	*TOPAS*	*REFCEL*	*CELREF2*
Cell parameter, *a* / Å	4.75885 (11)	4.75782 (2)	4.75842 (2)	4.75778 (1)	4.7579 (1)
Cell parameter, *c* / Å	12.9931 (24)	12.99001 (4)	12.99180 (4)	12.99003 (7)	12.9893 (2)
Wavelength, λ / Å	1.540629	1.540598	1.540598	1.540598	1.540598

Table 6.6. Standard versus refined cell parameters for NIST Al_2O_3 measurement of SRM1976, obtained using the d8 and a position sensitive detector (d8_00497).

Table 6.6 shows the *TOPAS* refined cell parameters of SRM1976 lie within 0.0004 Å and 0.001 Å of the NIST-determined *a* and *c* lattice parameters, respectively. Such discrepancies are of similar magnitude to the values obtained with the scintillation counter data. In conclusion, accurate cell parameters can be obtained with the Bruker d8 diffractometer at room temperature.

6.1.8 Determination of a Real ESD From the Cell Parameter of Silicon

There is substantial debate in the literature on the validity of the estimated standard deviations (ESDs) determined by Rietveld refinement. For example, the refined unit cell parameter of silicon in the HTK1200 furnace at a pre-set height of zero is 5.43048 (3) Å (Table 6.2). The question is whether or not the ESD of 0.00003 Å is a true indication of the precision of this value. It was decided to determine a real cell parameter standard deviation from a series of repeated measurements of Si diffraction patterns.

27 successive room temperature diffraction patterns ~30 minutes in length were collected on a bulk powder of Si. Each of the 27 ranges were refined using the same 23 independent parameters in *TOPAS* (an axial divergence parameter for the d8 instrument, twelve background terms, a sample height correction, Si histogram scale factor, six PV peak shape parameters, a cubic cell parameter and a single temperature factor). The seed Rietveld input file is attached in the e-Appendix. A typical Rietveld plot is shown in Figure 6.17.

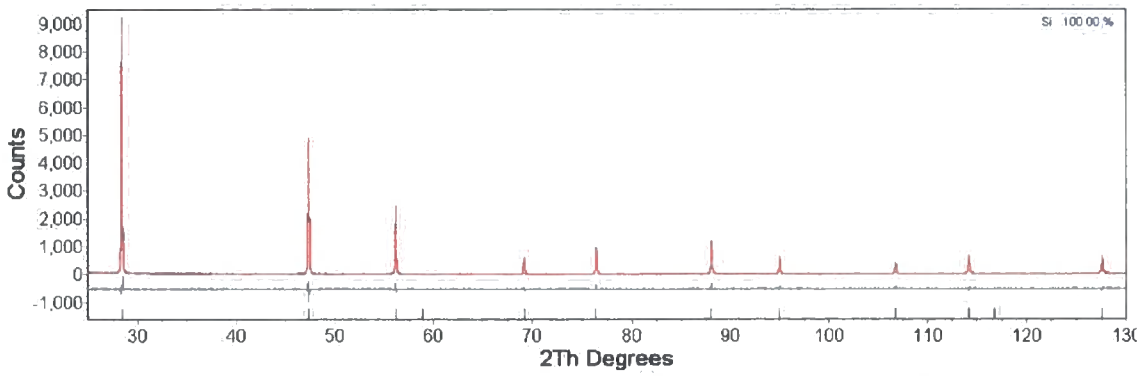

Figure 6.17. A typical Rietveld difference plot for Si at room temperature (d8 diffractometer, HTK1200 furnace, d8_00746:1).

A spreadsheet located in the e-Appendix shows the refined Si cell parameter for each of the 27 runs. The mean cell parameter and its standard deviation were calculated from these 27 values giving a value of 5.430594 Å and 0.000019 Å, respectively. The ESD compares very well to an individual Rietveld value of 0.00002 Å for these refinements. On this basis it seems that the Rietveld ESD is reliable.

6.1.9 Siemens d5000 Powder Diffractometer

The d5000 diffractometer is equipped with an automated sample changer used for room temperature diffraction patterns to check phase purities of powdered samples, *e.g.* cubic $ZrW_2{}^{17}O_8$ or hydration products of cubic $ZrMo_2O_8$, in Chapter 4. Rietveld quality data can also be acquired with this machine; data on the $ZrMo_2O_7(OD)_2(D_2O)_2$ precursor in Chapter 2 and cubic $HfMo_2O_8$ in Chapter 3 being the main examples.

The d5000 operates at 40 kV and 40 mA and uses a secondary beam graphite (*001*) monochromator to provide Cu *Kα* radiation (λ_{mean} = 1.54195 Å). Unlike the d8 with its incident beam monochromator, both $K\alpha_1$ and $K\alpha_2$ (λ = 1.540598 Å and 1.544493°Å, in a ~ 65 : 35 ratio) wavelengths are diffracted and collected by a scintillation counter detector.

Prior to diffraction by the sample, the X-rays pass through a set of soller slits and a variable (*e.g.* 6 mm) or fixed (*e.g.* 1 °) divergence slit. A variable slit is automated such that it opens as a function of Bragg angle and thus illuminates a constant area of sample throughout the entire 2θ range (thus giving higher intensities than a fixed slit at high 2θ). One possible disadvantage of such variable slits is that there can be a loss of resolution at high angles as a result of progressive de-focussing of the X-rays at the detector. This is only a minor problem with fixed slits since the illuminated area actually decreases with 2θ. Variable 20 mm (V20) slits were generally avoided since they actually illuminate an area greater than that of the sample at low angles. Diffracted X-rays were also collimated by a second set of soller slits to minimise axial divergence, prior to the monochromator and detector.

Samples were either mounted as bulk powders in a 25 mm holder, sieved onto an amorphous glass slide or silica wafer, adhered with a thin layer of Vaseline. Like the d8, the d5000 machine is controlled by the *Diffrac*^{Plus} software suite.[7]

6.1.10 Least-squares Refinement Via the Rietveld Method

A Rietveld refinement is used to obtain the best fit between an observed and a calculated powder diffraction pattern,[2] based on a mathematical model of the crystal structure. The calculated pattern is dependent on a number of parameters, which account for specimen characteristics such as atomic positions and unit cell parameters, and instrument factors such as the Lorentz-polarisation factor and the zero point error. Whereas the intensity of the Bragg reflections is dependent on the atomic parameters, their 2θ positions are dependent on the cell dimensions, sample absorption, sample height and instrument zero point error. A pseudo-Voigt function is most commonly used to describe the symmetric part of a Bragg peak;[32] it is simply a linear combination of Gaussian and Lorentzian components. An additional function, which describes peak asymmetry due to axial divergence of the diffracted beam at low-angle is also sometimes required.[33] Peak shape varies with 2θ and is governed by both the sample (domain size, microstrain, defects) and by the instrument (X-ray source, machine geometry and slit sizes).

All of the above parameters have to be considered for refinement if the best agreement between the observed and calculated models is to be achieved. The quality of the model can be shown graphically in terms of a difference profile plot or numerically in terms of residual factors or R indices.[34] The weighted-profile R-factor is defined in Equation 6.11, where, $y_i(obs)$ is the observed intensity at step i, $y_i(calc)$ the calculated intensity and w_i, the weight.

$$ {}_{w}R_{p} = \left\{ \frac{\sum_{i} w_i \left[y_i(obs) - y_i(calc) \right]^2}{\sum_{i} w_i \left[y_i(obs) \right]^2} \right\}^{1/2} \qquad (6.11) $$

The numeric value of ${}_wR_p$ can be misleading when high backgrounds are observed, as a large proportion of the intensity is accounted for by the background function, so the denominator will be large and ${}_wR_p$ turns out to be small despite a poor structural model.

A good refinement is one where ${}_wR_p$ approaches the statistically expected R value, R_{exp}, defined in Equation 6.12; N is the number of observations and P the number of parameters. R_{exp} reflects the quality of the data.

$$R_{\exp} = \left[(N-P) \Big/ \sum_i^N w_i y_i (obs)^2 \right]^{1/2} \tag{6.12}$$

From the ratio of the Equations 6.11 and 6.12, χ^2 is a more concise way of describing the quality of a refinement (Equation 6.13).

$$\chi^2 = {}_w R_p / R_{\exp} \tag{6.13}$$

However, χ^2 strongly depends on the length of time spent collecting data; rapid scans imply errors will be dominated by counting statistics and R_{exp} will be large so χ^2 could be less than 1. For "over-collected" data, R_{exp} will be very small and χ^2 correspondingly large. χ^2 is thus not a very accurate way of assessing the quality of a refinement.

The most reliable R value is the Bragg R-factor (Equation 6.14) where, $I_{hkl} = mF_{hkl}^2$ (m = multiplicity). R_{Bragg} is equivalent to R_{F^2}, the R value commonly reported in single crystal refinements.

$$R_{Bragg} = \frac{\sum_{hkl} |I_{hkl}(obs) - I_{hkl}(calc)|}{\sum_{hkl} |I_{hkl}(obs)|} \tag{6.14}$$

6.1.11 Rietveld Refinements Using *TOPAS*, the Total Pattern Analysis System

TOPAS is a modern *Windows* based peak fitting program which can be used to perform Rietveld refinements on powder X-ray and powder neutron diffraction patterns.[1] It consists of two modes of operation, *Interface* and *Launch (Input)* modes. The former mode allows pattern fitting *via* a graphical user interface. *Launch (Input)* mode was used exclusively throughout as it permits rapid, multiple least-squares refinements and contains more functionality. An input file is set up which contains the space group and cell information, and starting values for all the peak positions, background, instrument and atomic parameters. The real bonus of using *TOPAS* for Rietveld work is that all parameters can be simultaneously refined without causing divergence in the model and a lot of data at many different temperatures can be refined relatively quickly. The more-traditional program *GSAS*,[11] which is more laborious and less powerful, was employed for some early refinements however the bulk of the refinements were performed using *TOPAS*. Two sample input files can be seen in Appendices A2.1 (peak-fitting only) and A3.1 (full Rietveld).

In a typical variable temperature refinement, the first range was refined using *TOPAS* in *Launch* mode using an input file as mentioned above. This first refinement was then used as a seed for those to be performed at all remaining temperatures. The output file for the first refinement was copied to the input file for the subsequent refinement and a round of least-squares cycles performed until convergence was observed. Relevant refined parameters were written out in a text file and the whole process repeated again. The process was automated using a routine called *MultiTOPAS*, which operates from the *DOS* command line.

At the end of the multiple refinements, the results file showing the temperature dependence of the refined parameters was analysed in *Excel*, and the most important plots discussed in the main chapters of this thesis. The seed input file and final spreadsheet for every variable temperature (or time) refinement were copied to a CD-R, which is included at the back of the thesis.

TOPAS was also used for structure solution from powders using the technique of "simulated annealing" (Chapter 2).[6] *TOPAS* first produces a random arrangement of atoms within the unit cell and calculates a weighted profile *R*-factor. Then, instead of moving all atoms to completely new random positions (like Monte Carlo methods), it initially performs cycles of Rietveld refinement to improve the agreement between observed and calculated diffraction patterns. This solution will, in all probability, be merely a local minimum in *R*-factor space. Atoms are therefore perturbed in a (user-controlled) random fashion and the process repeated. These cycles are repeated many (~ 100000) times until a global minimum is obtained.

6.2 Powder Neutron Diffraction

6.2.1 Time-of-flight at ISIS and HRPD

The High-Resolution Powder Diffractometer (HRPD) based at the ISIS spallation source of the Rutherford Appleton Laboratory, UK is the highest resolution powder neutron diffractometer in the world. The resolution in *d*-spacing for the back-scattering detector bank is quoted as $\Delta d/d = 4 \times 10^{-4}$.[35] This resolution is obtained by the long (~ 100 m) primary flight path between the moderator and the instrument.

At ISIS, pulses of protons are accelerated to 800 MeV in a synchrotron (~ 10000 revolutions required), before being deflected along a proton beam line and colliding with a tantalum target. This process occurs with a frequency of 50 Hz and a beam of white neutrons is produced, so-called because many neutron wavelengths are present. The diffraction technique used is known as time-of-flight diffraction since the detectors are at fixed angle and the time taken for the neutrons to reach the detector from the target is recorded, converted to the corresponding velocity (and wavelength using the de Broglie relationship, $\lambda = h / mv$). Since all wavelengths (and therefore energies) are detected simultaneously, the whole diffraction pattern is collected concurrently in contrast to a laboratory fixed wavelength X-ray machine where the whole 2θ range must be scanned by a detector.

Neutrons emitted from the tantalum target nuclei have very high energies and must be moderated in order to be useable in diffraction experiments. HRPD uses a liquid methane moderator at 100 K; collisions with H atoms slowing the neutrons to more suitable energies. The resulting maximum neutron wavelength is ~ 10 – 12 Å.

Variable temperature studies on cubic $ZrMo_2O_8$ were carried out on HRPD using an AS Scientific Instruments cryofurnace (Chapter 3). The sample was packed into a 5.9 cm^3 rectangular aluminium slab can masked by cadmium shielding. The windows of the can were made from vanadium. Room temperature scans were obtained for LT-AMo_2O_8 phases in Chapter 2; samples were mounted in cylindrical vanadium cans, mounted on a "candlestick" and subjected to dynamic vacuum. Data collected from the array of ZnS scintillator, or ^{3}He gas detectors, that comprise the back-scattering and 90 °, or low-angle, detector banks were normalised and re-binned using *Ariel* software.[36]

6.2.2 Vega and Sirius Diffractometers at KEK

Vega and Sirius are time-of-flight powder diffractometers based at the KEK Neutron Scattering Facility (KENS) of the National Laboratory for High Energy Physics, Tsukuba, Japan. The neutron source is similar to that at ISIS. Protons are accelerated in a synchrotron to 500 MeV and collide with a tungsten target. Neutrons are produced in pulses with a frequency of 20 Hz. A solid methane moderator at 27 K is employed for these two diffractometers. Of the two instruments employed here, Sirius is the higher resolution, higher intensity instrument, with a total flight path of 40 m giving a $\Delta d/d = 1 \times 10^{-3}$ for the back-scattering bank;[37] this resolution is an order of magnitude worse than HRPD. The *d*-spacing range for the back-scattering bank is 0.2 to 2.5 Å. The detector bank consists of 320 linear ^{3}He position sensitive detectors (PSDs). Sirius also possesses a wide-angle 90 ° bank (*d*-spacing range of 0.3 to 3.5 Å; $\Delta d/d = 4 \times 10^{-3}$) although this was not utilised in the studies of $ZrMo_2O_7(OD)_2(D_2O)_2$ in Chapter 2.

Data at larger *d*-spacings were collected using the back-scattering bank of the Vega instrument. With a path length of 20 m, instrumental resolution is lower at $\Delta d/d = 2.5 \times 10^{-3}$ although data from 0.5 to 5 Å can be recorded again *via* a bank of PSDs. 90 ° and low-angle banks also exist on Vega, extending the available *d*-spacing

to 7 and 20 Å, although the data are less well resolved and were not used in the refinements in Section 2.2.6.

Room temperature data collections on $ZrMo_2O_7(OD)_2(D_2O)_2$ were acquired using Vega and Sirius and a combined neutron/laboratory X-ray refinement performed as discussed in Chapter 2.

6.3 Electron Diffraction

Transmission electron microscopy was used to confirm the lattice parameters of LT-$ZrMo_2O_8$ in Chapter 2. A series of high-resolution images consisting of an array of diffraction spots were obtained as shown in Figure 2.5. Dr. Wuzong Zhou and Prof. Russell Morris at the University of St. Andrews collected the electron diffraction data, which confirmed the unit cell derived from diffraction data.

6.4 Synchrotron X-ray Diffraction

The Synchrotron Radiation Source (SRS) at the Daresbury Laboratory, UK consists of a 12 MeV linear accelerator which injects a beam of electrons into an 600 MeV synchrotron providing a ~ 225 mA beam current. The electrons are further accelerated to energies of 2 GeV in the main storage ring. At these relativistic speeds high flux and high intensity white X-ray radiation is emitted at a tangent to the storage ring. Beam lifetimes can last for up to 19 hours with a beam re-injection twice a day, although three refills per day were in operation during the time allocated for experiments described in this thesis. To prevent rapid beam decay a radio frequency device boosts the energy of the electron beam each time it completes a loop of the storage ring. An ultra-low vacuum must be maintained to avoid the loss of beam through inelastic collisions with other electrons and gas molecules (~ 10^{-10} Torr).

By analogy to time-of-flight neutron diffraction mentioned in Section 6.2, the provision of white radiation provides X-rays of all energies for Bragg diffraction. Owing to the high flux, relatively rapid data collections can be obtained (as rapid as 30 s in some cases). Another advantage of a white beam of radiation is that a fixed geometry can be

employed, *i.e.* the detector can be fixed at a Bragg angle, θ relative to the sample. This simplifies the reaction cell design, which consists of a powdered sample in water contained in a Teflon-lined, steel-walled Parr-type autoclave. For the experimental cell used, the energy dispersive detectors on Station 16.4 receive useful X-ray flux over an energy range of ~ 20 to 80 keV which for a detector angle of 4.4 ° 2θ corresponds to a *d*-spacing range of 7.34 to 1.84 Å

6.5 Solid-state ^{17}O Magic-angle Spinning Nuclear Magnetic Resonance Spectroscopy

Room temperature 1-D ^{17}O MAS NMR was performed on a Varian Unity Plus 300 or a Bruker DSX 300 spectrometer. Variable temperature ^{17}O MAS NMR spectra meanwhile were recorded on a Bruker DSX 400 machine. Tap water was used as reference for ^{17}O throughout (0 ppm). All samples were packed into 4 mm zirconia rotors and spun at speeds of up to 15 kHz at the magic angle of 54.74 ° to average chemical shift anisotropy inherent to the study of nuclei in the solid state. A single 90 ° pulse, acquisition and recycle delay sequence was used for all 1-D spectra.

Dr. David Apperley, of the Industrial Research Laboratories, University of Durham, manages the Varian Unity 300 Plus spectrometer. The $Zr^{17}O_2$ spectrum presented in Chapter 4 was recorded on this instrument.

The Bruker DSX 300 spectrometer referred to in this thesis is based at CNRS-CRMHT, Orléans, France. The $W^{17}O_3$ spectrum was recorded by Dr. Ian J. King, Prof. Dominique Massiot and Dr. Franck Fayon.

Variable temperature NMR spectra of $ZrW_2{}^{17}O_8$ were recorded on a Bruker DSX 400 again at CNRS-CRMHT, France. Temperatures were calibrated using the reported temperature dependence of the ^{207}Pb chemical shift in $Pb(NO_3)_2$ - the so-called ^{207}Pb thermometer technique.[38] Heating was achieved by pressurised air (below 373 K) and nitrogen (above 373 K); the thermocouple is displaced from the sample rotor giving rise to thermal gradients which must be accounted for. The correction curve for the Bruker DSX 400 has been reported by King.[39] A simple linear dependence of error in

temperature (in degrees Celsius) is empirically found to be, $T_{corr} = 0.76T_{set} + 4.8$, which implies *e.g.* a discrepancy of –55 ° at 250 °C. Temperatures displayed in Figure 4.6 have been corrected appropriately. 20 minutes of equilibration time was also allowed prior to collection of spectra at each temperature.

6.6 References

1. A. A. Coelho, *TOPAS v2.0: General Profile and Structure Analysis Software for Powder Diffraction Data*, Bruker AXS, Karlsruhe, 2000.
2. H. M. Rietveld, *J. Appl. Cryst.*, **2**, 1969, 65-71.
3. G. S. Pawley, *J. Appl. Cryst.*, **14**, 1981, 357-361.
4. S. Kirkpatrick, C. D. Gelatt, M. P. Vecchi, *Science*, **220**, 1983, 671-680.
5. Y. G. Andreev, P. G. Bruce, *J. Chem. Soc., Dalton Trans.*, 1998, 4071-4080.
6. A. A. Coelho, *J. Appl. Cryst.*, **33**, 2000, 899-908.
7. Bruker AXS, *Diffrac^{Plus} v4.0: Software for Controlling Bruker Diffractometers*, Karlsruhe, 1998.
8. *CryoPad v1.1: PheniX Controller Software*, Oxford Cryosystems, Oxford, 2002.
9. J. S. O. Evans, Z. Hu, J. D. Jorgensen, D. N. Argyriou, S. Short, A. W. Sleight, *Science*, **275**, 1997, 61-65.
10. A. Löckner, *HTK1200 High Temperature Oven Camera Instruction Handbook*, Anton Paar GmbH, Graz, 1998.
11. A. C. Larson, R. B. Von Dreele, *GSAS: Powder Data Refinement Program for Unix Systems*, Los Alamos National Laboratory, Los Alamos, 1992.
12. J. S. O. Evans, *Multirange - Fortran 77 routine*, University of Durham, 1999.
13. J. S. O. Evans, *GSASparameterise - Fortran 77 routine*, University of Durham, 1999.
14. D. Taylor, *Br. Ceram. Trans. J.*, **83**, 1984, 92-98.
15. Y. Okada, Y. Tokumaru, *J. Appl. Phys.*, **56**, 1984, 314-320.
16. NIST Specification Certificate for Silicon (SRM640c), *http://patapsco.nist.gov/srmcatalog/common/view_cert.cfm?srm=640c.*
17. J. S. O. Evans, *PheniXlogfile: a Fortran 77 Routine for Extracting Mean Temperatures from Logfiles*, University of Durham, 2002.

18. K. G. Lyon, G. L. Salinger, C. A. Swenson, G. K. White, *J. Appl. Phys.*, **48**, 1977, 865-869.
19. K. Wang, R. R. Reeber, *Phil. Mag. A*, **80**, 2000, 1629-1643.
20. C. Martinek, F. A. Hummel, *J. Am. Ceram. Soc.*, **51**, 1968, 227-228.
21. J. S. O. Evans, T. A. Mary, T. Vogt, M. A. Subramanian, A. W. Sleight, *Chem. Mater.*, **8**, 1996, 2809-2823.
22. J. S. O. Evans, W. I. F. David, A. W. Sleight, *Acta Cryst.*, **B55**, 1999, 333-340.
23. E. N. Maslen, V. A. Streltsov, N. Ishizawa, *Acta Cryst.*, **B52**, 1996, 414-422.
24. S. Allen, First Year Report, University of Durham, 2000.
25. NIST Specification Certificate for Alumina (SRM1976), *http://ois.nist.gov/srmcatalog/certificates/view_cert2.cfm?certificate=1976.*
26. Bruker AXS, *XCH v3.02: Exchange Program for Converting Bruker RAW files to XY Format*, Karlsruhe, 1998.
27. A. A. Coelho, R. W. Cheary, *XFIT: X-ray Line Profile Fitting Program*, University of Technology, Sydney, 1997.
28. Bruker Test Data Supplied to Le Bail Group d8 Advance Powder Diffractometer, *http://sdpd.univ-lemans.fr/powdif/low_fwhm_and_rp.html.*
29. A. Le Bail, H. Duroy, J. L. Fourquet, *Mater. Res. Bull.*, **23**, 1988, 447-452.
30. J. K. Cockcroft, *REFCEL v3.03: a Unix Program for Refining Cell Parameters from XFIT Data*, Birbeck College, London, 1995.
31. J. Laugier, B. Bochu, *CELREF2: Least-squares Refinement Program for Obtaining Cell Parameters from Bruker RAW files*, INPG, Grenoble, 2000.
32. R. A. Young, D. B. Wiles, *J. Appl. Cryst.*, **15**, 1982, 430-438.
33. L. W. Finger, D. E. Cox, A. P. Jephcoat, *J. Appl. Cryst.*, **27**, 1994, 892-900.
34. L. B. McCusker, R. B. Von Dreele, D. E. Cox, D. Louër, P. Scardi, *J. Appl. Cryst.*, **32**, 1999, 36-50.
35. R. M. Ibberson, W. I. F. David, K. S. Knight, *The High Resolution Neutron Powder Diffractometer (HRPD) at ISIS - A User Guide*, CLRC, Chilton, 1992.
36. P. G. Radaelli, *Ariel V3.3: A Data Reduction and Visualisation Package*, 2002, http://www.isis.rl.ac.uk/disordered/GEM/ariel/index_ariel.htm.
37. T. Kamiyama, T. Ino, *KENS Report XIII 1999-2000*, KEK, Tsukuba, Japan, 2001.
38. A. Bielecki, D. P. Burum, *J. Magn. Reson.*, **A116**, 1995, 215-220.
39. I. J. King, Ph.D. Thesis, University of Durham, 2003.

Chapter Seven: Synthetic Experimental Details

The various AM_2O_8 phases prepared and characterised in this thesis were attributed a "SA*XXXY*" sample code, where *XXX* refers to a laboratory notebook page number and *Y* is a letter (A, B, C, etc.) to distinguish samples on the same page. Exceptions are in Chapter 2 where $AM_2O_7(OH)_2(H_2O)_2$ phases were prepared by, or in conjunction with Nick Warmingham (see below) and such samples were denoted as "NRW*XXX*".

7.1 Synthesis of Chloride-derived $ZrMo_2O_7(OH)_2(H_2O)_2$

6.686 g of $ZrMo_2O_7(OH)_2(H_2O)_2$ (sample i.d. NRW001) were prepared by Nick Warmingham (fourth year project student, University of Durham),[1] using a literature preparation given by Lind *et al.*.[2] 20 ml water was placed in a round bottomed flask and separate 30 ml solutions containing 7.871 g $ZrO_2Cl_2.xH_2O$ (98%, Avocado) and 5.296 g $(NH_4)_6Mo_7O_{24}.yH_2O$ (98%, Avocado) were added drop-wise. After subsequent addition of 80 ml 6 M $HCl_{(aq)}$ (Fisher), the solution was refluxed for 3 days. The water content of the Zr and Mo starting materials was analysed gravimetrically to yield x and y values of 7.25 and 3.88, respectively (*c.f.* supplier's values of 8 and 4). The actual Zr excess over the 1 : 2 Zr : Mo ratio is therefore 70%. Excess Zr was reported by Lind to minimise co-precipitation of amorphous MoO_3. The resulting precipitate was washed with water and centrifuged until the supernatant pH was ~ 4 – 5 and a negative test for chloride obtained using aqueous $Ag(NO)_3$. The precipitate was dried at 323 K and a lavender-coloured powder recovered. The yield of this "chloride-derived precursor" was 96% based on Mo. The decomposition of this material *via* various $ZrMo_2O_8$ phases was studied in this thesis by *in situ* variable temperature X-ray diffraction as outlined in Section 2.2.5. The study was also repeated using an internal standard in the form of 0.065 g crystalline α-Al_2O_3 (99%, Aldrich), which were added to 0.050 g $ZrMo_2O_7(OH)_2(H_2O)_2$ (NRW001) and the mixture ground.

7.1.1 Synthesis of LT-$ZrMo_2O_8$

A bulk sample of LT-$ZrMo_2O_8$ was obtained by heating ground $ZrMo_2O_7(OH)_2(H_2O)_2$ (NRW001) in an alumina crucible at 573 K for 8 hours. A 3.00 g powdered sample was used in the neutron diffraction experiment described in Section 2.2.2. The sample was peach in colour when freshly dehydrated however it rapidly darkens in air and turns grey due to spontaneous rehydration. On extended exposure to moist air it eventually turns lavender (Section 2.2.6). Whenever a sample of LT-$ZrMo_2O_8$ was used in any analysis it was pre-heated in an oven at 473 K. For the Rietveld X-ray dataset,[3] d8_01665, a sample of LT-$ZrMo_2O_8$ was reheated in a furnace to 473 K for 2 hours to re-attain the peach colour, mounted in the HTK1200 furnace of the diffractometer and heated to 423 K under dynamic vacuum for a further hour. After this the sample was presumed to be fully dehydrated; it was left to cool to room back temperature while still under vacuum and a 13-hour diffraction pattern recorded as described in Section 2.2.2.

For laboratory variable temperature diffraction experiments of LT-$ZrMo_2O_8$, an internal standard was used. 0.162 g freshly dehydrated LT-$ZrMo_2O_8$ (*via* NRW001 precursor, 473 K, 90 minutes) was ground with 0.052 g α-Al_2O_3. The LT/α-Al_2O_3 mixture is referred to as SA99A in Section 2.2.8 of the main text.

7.1.2 Deuteration of LT-$ZrMo_2O_8$

$ZrMo_2O_7(OD)_2(D_2O)_2$ (NRW026) was prepared in two consecutive stages. $ZrMo_2O_7(OH)_2(H_2O)_2$ was initially dehydrated (NRW001, 2.03 g) at 573 K for 18 hours, followed by rehydration of the resulting LT-$ZrMo_2O_8$ phase using 15 ml D_2O (99%, Aldrich), sealed in a 23ml Teflon-lined Parr steel autoclave. The Parr bomb was heated at a ramp rate of 1 $Kmin^{-1}$ to 373 K and held at this temperature for 3 days. An 86% yield of the grey deuterated precursor was recovered after suction filtration and brief drying in air. 1.43 g of the material was used in two powder neutron data collections (Section 2.2.6).

7.2 Synthesis of Perchlorate-derived $ZrMo_2O_7(OH)_2(H_2O)_2$

This precursor was prepared by Nick Warmingham in the same manner as the chloride-derived precursor described above, except that the reaction was scaled up. The Zr source was $ZrO(ClO_4)_2.8H_2O$ (unspecified purity, Aldrich; 27.521 g) and was dissolved in 75 ml water. 13.243 g $(NH_4)_6Mo_7O_{24}.zH_2O$ (99.999%, Alfa, z = 1.98 by gravimetry) were also dissolved in 75 ml H_2O. Aqueous HCl was replaced by $HClO_4$ (200 ml, 6 M) for the 3-day reflux. 15.665 g very pale green powdered $ZrMo_2O_7(OH)_2(H_2O)_2$ (NRW036) was prepared in 87% yield based on Mo. The approximate Zr : Mo excess was 58%. Experiments on this "perchlorate-derived precursor" and the $ZrMo_2O_8$ phases derived from it are described in Section 2.2.5.

7.2.1 Synthesis of Cubic $ZrMo_2O_8$

The optimal temperature to prepare cubic $ZrMo_2O_8$ from the perchlorate-derived precursor (NRW036) was investigated using *in situ* diffraction studies in Section 2.2.5: 15.190 g of $ZrMo_2O_7(OH)_2(H_2O)_2$ was placed in a large Pt crucible and heated in a muffle furnace at 2 $Kmin^{-1}$ to 723 K for 30 minutes, and then rapidly quenched in air. The purity of the resulting cream solid was checked by X-ray diffraction revealing a mixture of 80% cubic and 20% LT-$ZrMo_2O_8$. The sample was re-ground and placed back in the hot furnace for a further 15 minutes, quenched and another powder pattern recorded. This time complete conversion to peach/pink cubic $ZrMo_2O_8$ was observed (sample ref SA97B; mass = 13.373 g). 6.438 g of SA97B was used for variable temperature powder neutron diffraction. Portions of the same sample were also used in the hydration studies described in Section 4.2.3.

7.3 Synthesis of $HfMo_2O_7(OH)_2(H_2O)_2$

This $HfMo_2O_7(OH)_2(H_2O)_2$ precursor was prepared by Nick Warmingham by an analogous method to that described in Section 7.1; solutions of 9.818 g $HfOCl_2.uH_2O$ (98%, Alfa) and 5.234 g $(NH_4)_6Mo_7O_{24}.yH_2O$ (98%, Avocado) were refluxed in 6 M HCl. Gravimetry showed u and y were 6.11 and 3.88, respectively (*c.f.* supplier's values of 8 and 4). An excess of 76% over the 1 : 2 Hf : Mo reagent ratio was therefore used.

6.989 g of cream-yellow $HfMo_2O_7(OH)_2(H_2O)_2$ (NRW027) was obtained with a yield of 85% based on Mo.

7.3.1 Synthesis of LT-$HfMo_2O_8$

2.623 g $HfMo_2O_7(OH)_2(H_2O)_2$ (NRW027) were heated in a Pt crucible at 10 $Kmin^{-1}$ to 573 K for 22 hours. A 2.366 g sample of bright peach/orange LT-$HfMo_2O_8$ resulted (SA100B). 2.27 g of this was used for neutron diffraction. Rigorous dehydration procedures were essential (see discussion below). The sample was packed in a 5 mm diameter vanadium cylindrical can with its lid loosely screwed on and the sample reheated in a vacuum oven at 453 K for 2 hours. The can was removed from the warm oven, the lid tightened and immediately placed under vacuum in the neutron beam. Laboratory X-ray data were also collected under a dynamic vacuum at room temperature.

The thermal expansion behaviour of LT-$HfMo_2O_8$ is shown in Section 2.3.6 and the effect of a partially hydrated material outlined. The first, partially hydrated sample studied, NRW032 was made by Nick Warmingham by dehydrating $HfMo_2O_7(OH)_2(H_2O)_2$ at 573 K for 29 hours then storing the material in a vial at room temperature for 10 days before the first VT diffraction study. In a subsequent experiment, NRW032 was re-heated for 4 hours at 473 K and 0.0214 g α-Al_2O_3 internal standard added to 0.0723 g of LT-$HfMo_2O_8$; the resulting sample was referred to as SA99B. The sample was briefly reheated to 343 K for 15 minutes inside the cryofurnace. For the third variable temperature diffraction experiment, SA99B was heated in the cryostat for 2.5 hours at 473 K to obtain a fully dehydrated sample.

7.3.2 Synthesis of Cubic $HfMo_2O_8$

Cubic $HfMo_2O_8$ (SA93A) was quantitatively prepared by decomposing $HfMo_2O_7(OH)_2(H_2O)_2$; 0.1 g of the precursor (NRW027) were heated in a Pt crucible at 5 $Kmin^{-1}$ to 723 K for 4 hours and the furnace switched off. The ensuing yellow powder was confirmed pure (> 99%) by X-ray diffraction.

7.4 Synthesis of $ZrW_2O_7(OH)_2(H_2O)_2$

$ZrW_2O_7(OH)_2(H_2O)_2$ was prepared in conjunction with Nick Warmingham based on a method reported by Dadachov.[4] 10.016 g $Na_2WO_4.vH_2O$ (Alfa, 95%, $v = 2.00$ by thermal gravimetry) were dissolved in 30 ml water and added to a beaker containing 25 ml water. 4.883 g $ZrOCl_2.xH_2O$ (reagent as described in Section 7.1) was dissolved in a similar way. The two colourless solutions were then mixed; the Zr : W molar ratio was 1 : 1.92. A white gelatinous precipitate formed and this was repeatedly washed with water in a Buchner funnel, and left to dry overnight. The tacky precipitate was refluxed with 125 ml 12.2 M concentrated HCl (Fisher) for 4 hours, during which time the initial precipitate dissolved and reformed. The resulting white solid was washed and filtered with suction. A 16% yield of NRW017a was prepared which was amorphous by X-ray diffraction. 1 g NRW017a was weighed into a 23 ml Teflon-lined Parr autoclave and 15 ml 4 M aqueous HCl added. The bomb was heated in an oven to 443 K (heating at a rate of 10 $Kmin^{-1}$) and held for 3 days. A white solid (NRW017b) was recovered after washing and in 76% yield. Its identity was confirmed by powder X-ray diffraction and it was used for *in situ* variable temperature studies.

7.5 Synthesis of Cubic ZrW_2O_8

7.5.1 ^{17}O Labelling of ZrO_2, WO_3 and ZrW_2O_8

$Zr^{17}O_2$ (sample i.d. SA82B) was prepared as follows. 0.671 g $ZrCl_4$ (99.5%, Aldrich) was weighed out into a large glass Schlenk in a nitrogen-filled glovebox. The Schlenk was removed from the glovebox and connected to a nitrogen line. 30 ml of column-dried diethyl ether was added with continuous stirring. The white solid only partially dissolved at this stage. 0.327 g $H_2{}^{17}O$ (containing 28.0% ^{17}O, 29.8% ^{18}O, 42.2% ^{16}O, implying the calculated RMM = 18.892 $gmol^{-1}$; supplied by Eurisotop) was added to the Schlenk using a 100 μl Gilson pipette (a 6 : 1 $H_2O : ZrCl_4$ molar ratio). Slight effervescence was observed and the resulting white precipitate fell to the bottom of the Schlenk with clear, colourless ether above it. Stirring was continued under nitrogen for 2 hours. The ether was then removed under vacuum. 0.662 g of tacky, matt white powder was obtained and found to be completely amorphous to X-rays. The sample was

ground, placed in a quartz crucible and heated in a tube furnace (connected to a vacuum line) at 5 $Kmin^{-1}$ to 473 K for 1 hour to completely remove HCl or H_2O. The furnace was subsequently ramped to 1123 K at 10 $Kmin^{-1}$ for 3 hours to crystallise the material and then allowed to cool. The vacuum was released and a 0.243 g sample of grey powder recovered implying a yield of 67%. Diffraction showed that this material, SA82B was predominantly the desired monoclinic ZrO_2 product with metastabilised tetragonal ZrO_2 as a minor impurity (Section 4.1.2). ^{17}O MAS NMR revealed the presence of two peaks consistent with the two oxygen atoms in the asymmetric unit of monoclinic ZrO_2.

$W^{17}O_3$ (sample i.d. SA82A) was prepared in a similar manner to $Zr^{17}O_2$. 2.266 g WCl_6 (99%, Alfa) was weighed out in a glovebox. Upon addition of 30 ml ether the solution turned very dark green. When 0.972 g $H_2{}^{17}O$ was added (a 9 : 1 H_2O to WCl_6 molar ratio), a deep navy blue coloured precipitate and solution formed. After stirring, and removal of ether using a pre-trap, 1.610 g of shiny dark blue powder was recovered. The material was ground and heated at 10 $Kmin^{-1}$ under vacuum to 1173 K for 3 hours. 1.176 g of shiny dark blue/purple solid was obtained and shown by X-ray diffraction to be $WO_{2.72}$ (*i.e.* the Magneli phase $W_{18}O_{49}$). The material was re-ground and briefly oxidised in air by heating in a tube furnace at 10 $Kmin^{-1}$ at 1223 K for 1 hour and then cooled. 1.183 g of bright yellow WO_3 was obtained (SA82A) corresponding to an overall yield of 88%. Its identity was confirmed by X-ray diffraction and MAS NMR revealed the presence of three resonances attributable to three pairs of ^{17}O atoms in similar environments (Section 4.1.2), consistent with the monoclinic unit cell reported in the literature.

Cubic $ZrW_2{}^{17}O_8$ (SA83A) was synthesised from $Zr^{17}O_2$ and $W^{17}O_3$ in a 1 : 2 mole ratio. 0.105 g ZrO_2 and 0.395 g $W^{17}O_3$ were ground together and three 5 mm pale green pellets pressed and sealed in a quartz tube under vacuum. The tube was placed in a muffle furnace at 1173 K and ramped at 10 $Kmin^{-1}$ to 1473 K. After 14 hours the sample was removed from the furnace and quenched into a dewar full of liquid nitrogen to trap the kinetically stable $ZrW_2{}^{17}O_8$ phase. Upon exposing the tube to air, pale cream and dark grey coloured pellets were recovered. It was known from previous tests that the darkest grey/black portions of pellets were rich in ZrO_2 and WO_3 impurities so these fragments were discarded and 0.250 g of product retained (sample i.d. SA83A). X-ray

diffraction revealed that the material was ~ 72% pure, with ~ 28% ZrO_2 and WO_3 impurities. The discarded fragments were also analysed by diffraction and shown to contain only ~ 45% $ZrW_2{}^{17}O_8$. The 72% pure sample was analysed using variable temperature ^{17}O MAS NMR and is discussed in Section 4.1.3.

7.5.2 Preparation of ZrW_2O_8 by a High Temperature Route

Small samples (~ 0.5 g) of pure white ZrW_2O_8 could be prepared by heating powdered ZrO_2/WO_3 in a 1 : 2 mole ratio, from 1173 to 1448 K (ramping at 10 $Kmin^{-1}$) and annealing for 14 hours in a Pt crucible, followed by a quench in air. Reactions in an alumina crucible were notably unsuccessful - even at 1423 K (~ 107 K below its reported melting temperature) the material seemed to melt and fuse to the crucible. Larger scale reactions (~ 5 g) required annealing for ~ 20 hours with one re-grind.

The hysteresis behaviour of the order-disorder phase transition in cubic ZrW_2O_8 was investigated in Section 3.5.2. 0.357 g Si (99.5%, Alfa) internal standard were added to 0.741 g ZrW_2O_8 (supplied by Teledyne Wah Chang) and the mixture ground in a mortar and pestle. A 15 mm pellet was pressed and mounted in the HTK1200 furnace of the d8 diffractometer (more details in Section 6.1.3) and variable temperature diffraction performed.

7.6 Hydration of ZrM_2O_8 Materials

7.6.1 Hydration of Cubic $ZrMo_2O_8$

Laboratory hydration studies of cubic $ZrMo_2O_8$ (SA97B) were performed prior to the *in situ* experiment at Station 16.4 of the Daresbury Laboratory (Section 4.2.3). The peach/pink cubic phase (synthesised in Section 7.2.1) was weighed out in a 23 ml Teflon liner and a quantity of distilled water added, according to the amounts specified in Table 7.1 (a repeat of Table 4.1). The resulting suspension was sealed in a steel Parr autoclave and heated in an oven at 10 $Kmin^{-1}$ to a temperature (and anneal time) given in Table 7.1. After the allotted time, the Parr bomb was removed from the warm oven and allowed to cool. Upon opening the bomb, a violet/grey solid in a cloudy white

solution was noted for samples SA105A, SA105B and SA106A. Dull purple powders were recovered after suction filtration and dried in air. X-ray diffraction confirmed their identity as $ZrMo_2O_7(OH)_2(H_2O)_2$ - the so-called precursor to cubic $ZrMo_2O_8$. In the remaining three reactions in Table 7.1, the solid products remained unchanged in colour.

Sample i.d.	RAW file	m / g	m_{water} /g	T / K	t / hr	% hydrate	% cubic	% precursor
SA105C	d5_03973	0.1	15	403	1	0	> 99	< 1
SA106C	d5_03990	0.1	15	453	1	0	99	1
SA106A	d5_03981	0.1	15	413	54	0	0	100
SA106B	d5_03987	0.1	15	473	1.25	0	96	4
SA105B	d5_03949	0.5	15	473	2	0	7	93
SA105A	d5_03941	0.5	15	473	16	0	< 2	> 98

Table 7.1. Experimental conditions and product phase percentages for laboratory hydrothermal hydrations of cubic $ZrMo_2O_8$ presented in Section 4.2.3.

An *in situ* hydrothermal experiment was performed on Station 16.4 of the SRS at the Daresbury Laboratory (run #103205). 0.8 g $ZrMo_2O_8$ (SA97B) was added to a tall 29 ml Teflon liner containing 10 ml distilled water and a magnetic stirrer flea. The liner was enclosed in a 0.4 mm thick steel autoclave and heated at 30% power to 473 K, corresponding to an average heat rate of ~ 2.8 $Kmin^{-1}$. 46 6-minute runs were performed to follow the complete conversion of cubic $ZrMo_2O_8$ to $ZrMo_2O_7(OH)_2(H_2O)_2$ (Figure 4.8).

7.6.2 Hydration of Trigonal $ZrMo_2O_8$

Hydration of trigonal $ZrMo_2O_8$ was attempted in the laboratory using a Parr autoclave. 0.1 g trigonal $ZrMo_2O_8$ (SA6A; preparation given in Section 7.7) was weighed into a 23 ml Teflon liner and 15 ml H_2O added. The liner was sealed in an autoclave and heated at 10 $Kmin^{-1}$, to 473 K for 18 hours, then removed from the furnace and allowed to cool. A white powder was recovered upon filtering the solution. X-ray diffraction revealed that no reaction had occurred.

7.7 Synthesis of Trigonal $ZrMo_2O_8$

The synthesis was based on that described by Samant *et al.* except an extended anneal and slower ramp rate were used.[5] 3.531 g pure ZrO_2 (SA5A) was prepared by decomposing 10 g $ZrOCl_2.xH_2O$ (99.9985%, Alfa) at 1173 K for 4 days.

2 g trigonal $ZrMo_2O_8$ (SA6A) was synthesised by grinding a 1 : 2 molar ratio of 0.6 g of the above ZrO_2 and 1.4 g MoO_3 (99.95%, Alfa); 13 mm pellets were pressed and heated at 0.85 $Kmin^{-1}$ to 975 K for 71 hours with three intermittent re-grindings and re-pressings. A pure white powder resulted and the Rietveld refinement of the X-ray powder pattern is given in Section 5.1.2.

For variable temperature X-ray diffraction purposes, an internal standard in the form of crystalline α-Al_2O_3 (corundum) was added to trigonal $ZrMo_2O_8$; 0.060 g trigonal $ZrMo_2O_8$ (SA6A) were ground with 0.040 g powdered α-Al_2O_3 (99%, Aldrich) to give sample SA6B.

7.8 Synthesis of Trigonal $HfMo_2O_8$

0.34 g $HfMo_2O_7(OH)_2(H_2O)_2$ (sample i.d. NRW027) was ground and heated at 10 $Kmin^{-1}$ in a platinum crucible to 1000 K and held for a total of 21 hours, with re-grinding after the first 4 hours. Extended annealing was required to give a sharp diffraction pattern. The mass of the dark cream coloured trigonal $HfMo_2O_8$ (sample i.d. SA100A) obtained was 0.2830 g. The Rietveld refinement is discussed in Section 5.2.2.

A second trigonal $HfMo_2O_8$ sample (SA98A) was studied in Section 5.2.3, containing ~ 5% refined mass of monoclinic HfO_2 as an impurity. The sample was prepared from NRW027 at 1073 K resulting in its partial decomposition. Good quality PheniX and TTK450 cryostat data were obtained on this sample.

For VT diffraction in the furnace, a reference material in the form of crystalline α-Al_2O_3 was added to trigonal $HfMo_2O_8$ (SA100A) so an accurate temperature calibration could

be achieved. 0.065 g trigonal $HfMo_2O_8$ were ground with 0.070 g powdered α-Al_2O_3 (99%, Aldrich) and the resulting mixture referred to as SA112A.

7.9 References

1. N. R. Warmingham, M.Chem. Thesis, University of Durham, 2002.
2. C. Lind, A. P. Wilkinson, C. J. Rawn, E. A. Payzant, *J. Mater. Chem.*, **11**, 2001, 3354-3359.
3. H. M. Rietveld, *J. Appl. Cryst.*, **2**, 1969, 65-71.
4. M. S. Dadachov, R. M. Lambrecht, *J. Mater. Chem.*, **7**, 1997, 1867-1870.
5. M. S. Samant, S. R. Dharwadkar, A. B. Phadnis, P. N. Namboodiri, *Mater. Chem. Phys.*, **35**, 1993, 120-125.

Appendix One

A1.1 Determination of H_2O Versus D_2O Content in "$ZrMo_2O_7(OD)_2(D_2O)_2$" by EI Mass Spectrometry

Section 2.2.6 provides the results of the synthesis, neutron diffraction and Rietveld refinement of a sample of rehydrated "$ZrMo_2O_7(OD)_2(D_2O)_2$" (NRW026). It was suspected from initial refinements that partial exchange of D_2O with ambient H_2O had occurred during transit of the material implying the scattering power of both D and H had to be accounted for.

EI Mass Spectrometry was used to determine the mass ratio of D_2O to H_2O. The experiment itself involved heating a small sealed capillary of the material and simultaneously recording a series of mass spectra as a function of time. These spectra were recorded by Lara Turner, to whom thanks are given.

The analysis of the resulting 29 spectra was performed as follows. Let the probability of a D atom on an O site in the "partially deuterated" precursor site be x. It follows that:

$$P(\mathrm{H}) = 1-x$$
$$P(\mathrm{D_2O}) = x^2$$
$$P(\mathrm{H_2O}) = (1-x)^2$$
$$P(\mathrm{DOH,HOD}) = 2x(1-x)$$

The relative intensities of the lines in the mass spectra are noted and can be assigned as follows:

m/e	Fragment
16	O
17	OH
18	H_2O + OD
19	DOH + HOD
20	D_2O

The best way to analyse the D to H ratio is to consider the lines at 19 and 20 *m/e*, rather than 18 and 20 since that at *m/e* = 18 is due to fragments containing both H and D.

Let *r* be represent the ratio of intensities of the lines at 19 and 20 on the relative isotopic mass scale. The amount of D relative to H (*i.e. x*) can be derived from *r* as follows:

$$r = I(20) / I(19)$$
$$r = x^2 / (2x(1-x))$$
$$\textit{i.e. } \boldsymbol{x = 2r / (1+2r)}$$

The Electronic Appendix shows a spreadsheet with all the relative abundances and the 20/19 ratio as a function of spectrum number (time) and is re-displayed below. Ideally the curve would be flat i.e. a constant D to H ratio. However the early spectra were recorded just above room temperature and the presence of surface water gave rise to much lower ratios as expected. The final spectrum was a sign of the complete loss of H_2O or D_2O the precursor as the ratio began to fall to zero. The maximum value of the ratio was chosen and used in the above equation.

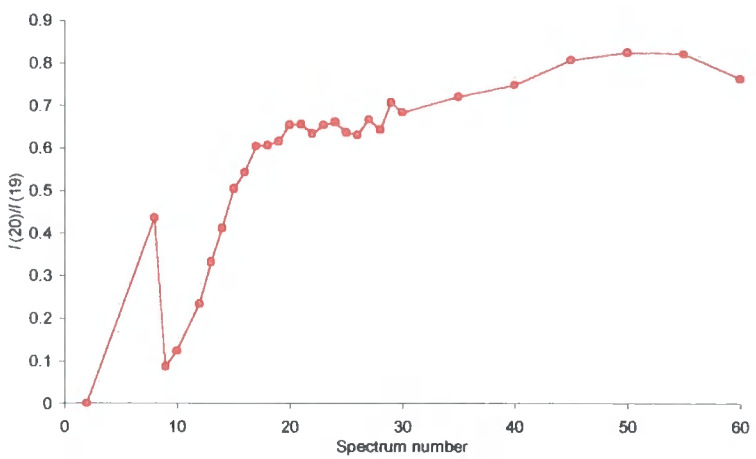

The maximum value of r from the above graph was 0.8229, which implies $x = 0.622$. This means the average formula is $D_{0.622}H_{0.378}O_{0.5}$. It is confirmed that D_2O in the material had partially exchanged with ambient H_2O, one cause of the large background in the neutron diffraction patterns shown in Section 2.2.6. The precursor can be more correctly written as $ZrMo_2O_7(OD)_{1.24}(OH)_{0.76}(D_2O)_{1.24}(H_2O)_{0.76}$ on average.

The neutron scattering length of D ($b_D = 0.6671$) had to be readjusted for the presence of H ($b_H = -0.3739$) using the relative abundances above. The resulting mean scattering length b_{av} is given by:

$$b_{av} = xb_D + (1-x)b_H$$
$$= 0.2736$$

The actual value used in the *TOPAS* input file is 0.410 (see e-Appendix). This is a rescaling of b_D *i.e.* $b_{av}/b_D = 0.2736 / 0.6671 = 0.410$, which is entirely equivalent. This scattering length adjustment improved quality of the Rietveld refinements considerably.

Appendix Two

A2.1 *TOPAS* Input File for Peak Fitting of Quench-annealed $ZrWMoO_8$

A seed input file created for the *TOPAS* refinement package is included below (see the e-Appendix for the electronic version). It was used to peak fit the first diffraction pattern collected in the variable time quench-anneal experiment of $ZrWMoO_8$ at *e.g.* 205 K (d8_01798). This seed file was then used to fit the same set of peaks at all other times in the experiment. Intensities were extracted and are displayed as a function of time in Figure 3.11. The whole experiment was repeated at 10 different temperatures and seed input files are included in the e-Appendix CD-R. The results of the peak fitting are available as a set of *Excel* spreadsheets in the e-Appendix.

```
'--------------------------------------------------
'ZrWMoO8 peak fitting input file for quench/anneal at 205K No LP factor required (just scales peaks down).
'--------------------------------------------------
'continue_after_convergence
randomize_on_errors
auto_sparse_CG
r_exp 20.672 r_exp_dash 30.067 r_wp 26.329 r_wp_dash 38.295 r_p 20.168 r_p_dash 33.682
weighted_Durbin_Watson 1.386 gof 1.274
iters 1000

'--------------------------------------------------
'put run number and ranges here – change " ' " markers later!
'--------------------------------------------------
#define TB

#ifdef TB
macro filename {d8_01798}
macro rangeuse {1}
#endif

RAW(filename)
range rangeuse

start_X 10
finish_X 46.5
Rp 217.5
Rs 217.5
CuKa1(0.001)
```

```
prm height -0.52925 min -1; max = 1; del 0.001  th2_offset = -2 57.2957795130823 (height) Cos(Th) /
Rs;

bkg @ 8.99102788 0.658707294 -3.40176887 2.77540619 1.09946579 -1.0060681 0.0797727148
1.05353266 1.01118547 -0.0928897409 0.250221862 -0.392499451

'------------------------------------------------
'peak fit macros here
'------------------------------------------------

prm acell 9.14553 min=9; max=9.3;


prm !lam 1.540596
macro get2th(h,k,l) {  (360/Pi) ArcSin((lam/(2*acell)) ((h)^2 + (k)^2 + (l)^2)^0.5)}
macro getthrad(h,k,l) {  ArcSin((lam/(2*acell)) ((h)^2 + (k)^2 + (l)^2)^0.5)}

'------------------------------------------------
'wider peaks fitted with fwhm + a * 2Th
'------------------------------------------------

macro peakmacro0(h,k,l,p1,v1,p3,v3) {xo_Is xo =get2th(h,k,l); peak_type pv pv_lor p1 v1 pv_fwhm =
fwhm_val0 + fwhm_th0 * get2th(h,k,l);   max = 0.35; I  p3  v3  val_on_continue=Rand(1,15); }

prm fwhm_val0 0.15359 min 0.01 max 0.5
prm !fwhm_th0 0.00 min 0.0 max 0.1
prm !fwhm_15deg = fwhm_val0 + fwhm_th0 * 15 ;:0.15359
prm !fwhm_30deg = fwhm_val0 + fwhm_th0 * 40 ;:0.15359

peakmacro0( 1, 1, 1,!lor,1,int111,0.0466406996)  '**
peakmacro0( 2, 2, 1,!lor,1,int221,2.4684765) '**
peakmacro0( 3, 0, 1,!lor,1,int301,0.905993103)  '**
peakmacro0( 4, 0, 1,!lor,1,int401,2.6299068)  '**

'------------------------------------------------
'narrow peaks fitted with fwhm + a * 2Th term
'------------------------------------------------

macro peakmacro1(h,k,l,p1,v1,p3,v3) {xo_Is xo =get2th(h,k,l); peak_type pv pv_lor p1 v1 pv_fwhm =
fwhm_val1 + fwhm_th1 * get2th(h,k,l);   max = 0.35; I  p3  v3  val_on_continue=Rand(1,15); }

prm fwhm_val1 0.06542 min 0.01 max 0.3
prm fwhm_th1 0.00048 min 0.0 max 0.1
prm !fwhm_30deg = fwhm_val1 + fwhm_th1 * 30 ;:0.07981


peakmacro1( 0, 0, 2,!lor,1,int002,6.4381976)
peakmacro1( 2, 0, 1,!lor,1,int201,61.9448717)
peakmacro1( 2, 1, 1,!lor,1,int211,60.5876105)
peakmacro1( 0, 2, 2,!lor,1,int022,26.840929)
peakmacro1( 3, 1, 1,!lor,1,int311,49.4955344)
peakmacro1( 2, 2, 2,!lor,1,int222,2.37532663)
peakmacro1( 0, 3, 2,!lor,1,int032,24.4384324)
peakmacro1( 2, 3, 1,!lor,1,int231,49.3852163)
peakmacro1( 4, 0, 0,!lor,1,int400,1.96933939)
peakmacro1( 3, 3, 0,!lor,1,int330,1.23255438)
peakmacro1( 3, 3, 1,!lor,1,int331,0.769312505)
peakmacro1( 4, 2, 0,!lor,1,int420,25.6290097)
peakmacro1( 4, 2, 1,!lor,1,int421,43.8509394)
```

```
'-------------------------------------------------
'output intensities here
'-------------------------------------------------
prm !sum1 = int111+int221+int301+int401;

out "search.res" append
Out(rangeuse,   " Range_number: %11.5f")
Out(sum1,    " %11.5f")
Out(int111,   " %11.5f")
Out(int221,   " %11.5f")
Out(int301,   " %11.5f")
Out(int401,   " %11.5f")
Out(int002,   " %11.5f")
Out(int201,   " %11.5f")
Out(int211,   " %11.5f")
Out(int022,   " %11.5f")
Out(int311,   " %11.5f")
Out(int222,   " %11.5f")
Out(int032,   " %11.5f")
Out(int231,   " %11.5f")
Out(int400,   " %11.5f")
Out(int330,   " %11.5f")
Out(int331,   " %11.5f")
Out(int420,   " %11.5f")
Out(int421,   " %11.5f")
'Out(alcell,    " %11.5f")
Out(height,   " %11.5f")
Out(fwhm_val0,   " %11.5f")
Out(fwhm_th0,   " %11.5f")
Out(fwhm_val1,   " %11.5f")
Out(fwhm_th1,   " %11.5f")
```

A2.2 Derivation of an Expression for the Rate Constant for β- to α-$ZrWMoO_8$ Via an Extent of Reaction Parameter

For a simple first order reaction, $X \rightarrow P$, the concentration as a function of time varies as follows:

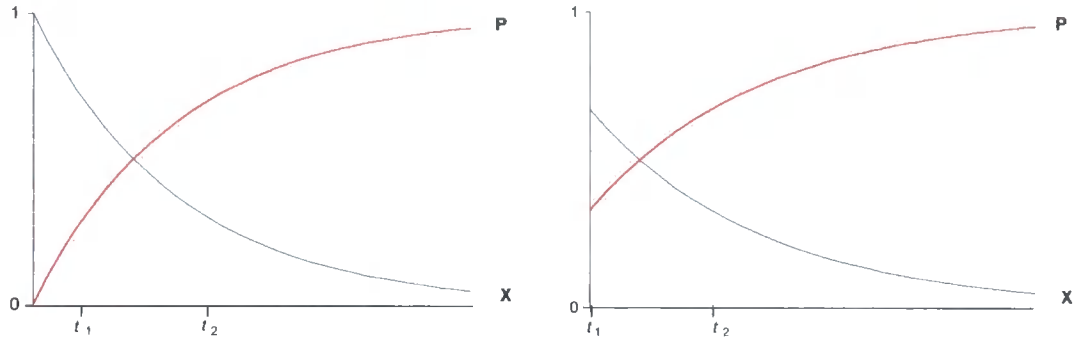

Let the concentration of P be α; the concentration of X at time t is,

$$\frac{d[X]}{dt} = -k_T[X] \Rightarrow [X]_t = [X]_0 \exp(-k_T t)$$

In the quench-warming experiments in Section 3.4.3, the β polymorph already begins to convert to the α-$ZrWMoO_8$ product during the quench, which is not infinitely rapid. Thus there is a non-zero concentration of the product even before any diffraction patterns are recorded during the subsequent slow warming phase of the experiment. The schematic plot shown above right is more applicable here; at time zero the concentration of P is non-zero. So,

$$[X]_t = [X]_{t1} \exp(-k_T t)$$

In a given time period $t_1 - t_2$, the loss in concentration of X is the gain in that of P:

$$\Delta\alpha_{t2} = [X]_{t1} - [X]_{t2} = [X]_{t1}\left(1 - \exp(-k_T t)\right)$$

The value of $[X]_{t1}$ is given by the amount present at time zero minus what has reacted so far, which itself is given by the sum of all the previous $\Delta\alpha$ values, *i.e.*

$$[X]_{t1} = 1 - \sum_{n=0}^{t1} \Delta\alpha_t$$

Substituting in gives,

$$\Delta\alpha_{t2} = \left(1 - \sum_{n=0}^{t1} \Delta\alpha_t\right)\left(1 - \exp(-k_T t)\right)$$

In Section 3.4.3, the extent of reaction is observed as a function of temperature (rather than time) so the following version of the above cumulative kinetic equation is employed there,

$$\Delta\alpha_T = \left(1 - \sum_{n=0}^{T-1} \Delta\alpha_T\right)\left(1 - \exp(-k_T t)\right)$$

The above expression relates the change in amount of product (alpha $ZrWMoO_8$) over a certain warming temperature range to the rate constant for the alpha to beta process.

Appendix Three

A3.1 *TOPAS* Input File for Trigonal $ZrMo_2O_8$

An example seed *TOPAS* input file that was created for Rietveld refinement is shown below. It was used to perform a room temperature refinement of trigonal $ZrMo_2O_8$ with a rigid tetrahedral MoO_4 body (Section 5.1.2). Similar input files were used for variable temperature refinements and are displayed in the e-Appendix CD-R. They contain an extra section which outputs the refined parameters, which can be read into *Excel* and their temperature dependence evaluated. *TOPAS* input files are very convenient as they simultaneously display values of all refined parameters. They are much quicker to edit and allow more user-functionality than the interface used in refinement packages such as *GSAS*.

```
'--------------------------------------------------
'trigonal ZrMo2O8 P-31c room temperature HTK1200 8 hr  run, with rigid tetrahedra
'--------------------------------------------------

#define phase1 'use phase 1 Trigonal-ZrMo2O8
#define phase2 'use phase 2 ZrO2

'--------------------------------------------------
'general refinement stuff
'--------------------------------------------------

auto_sparse_CG
r_exp 6.319 r_exp_dash 8.887 r_wp 10.599 r_wp_dash 14.906 r_p 7.906 r_p_dash 13.206
weighted_Durbin_Watson 0.777 gof 1.677
iters 1000

'--------------------------------------------------
'next section to control whether running tb (graphical) or tc (input file mode)
'information macro used to read temperature in from command line when using tc or supply from this
'file when running tb
'--------------------------------------------------

#define TB 'comment this line in or out if you're using TB (graphical) or TC (command line)

#ifdef TB
  macro filename {d8_01945}
  macro rangeuse { 1}
#endif

'--------------------------------------------------
'information about file, diffractometer, background, wavelength, etc
'--------------------------------------------------
```

```
RAW(filename)
range rangeuse
Monochromator_Fix_Biso(!mono,27.26,!fixb, -0.07)

start_X 10
finish_X 120.0
Rp 217.5
Rs 217.5
Simple_Axial_Model(!sam, 12)
Specimen_Displacement(height, -0.20562_0.00043)
bkg @ 121.559484_0.395566457 -72.4207469_0.677259628 46.7735534_0.62778169
-36.1459665_0.589777797 36.0857187_0.547235386 -19.4247894_0.533886155
12.4762229_0.48947707 -19.8370125_0.498349485 19.4697719_0.449793488
-13.5238563_0.450790248 11.3524305_0.382063471 -5.50757202_0.377243467
lam
 ymin_on_ymax  0.001
 la  1 lo  1.540596 lh  0.5

'--------------------------------------------------
'structural information for trigonal ZrMo2O8 from Auray et al.
'--------------------------------------------------
#ifdef phase1
        str
                r_bragg  2.60963031
                scale @ 0.0000422687_0.0000001135
                phase_name trigonal-ZrMo2O8
                MVW( 2466.604_0.000,vol 1043.0081_0.0172,percentphase1 97.419_0.233)
                space_group P-31c
                a lpa1 10.14097_0.00006 min 10.0; max 10.2;
                b lpa1 10.14097_0.00006 min 10.0; max 10.2;
                c lpc1 11.71111_0.00013 min 11.6; max 12.2;
                al  90
                be  90
                ga  120

PV_Peak_Type(pk1, 0.07549_0.01281,pk2, 0.09092_0.00730,pk3, 0.00010_0.01419,pk4,
0.29679_0.10397,pk5, 0.55836_0.06889,pk6, 0.00010_0.11798)

                macro F1(param,val) {x val }
                macro F2(param,val) {y val }
                macro F3(param,val) {z val }
                macro A3(param,v1,v2) {z  param v1  min=v2-0.1; max=v2+0.1; }
                macro R1(param,v1,v2) {x  v1  }
                macro R2(param,v1,v2) {y  v1  }
                macro R3(param,v1,v2) {z  v1  }

 site Zr1  F1(!xzr1, 0) F2(!yzr1, 0) F3(!zzr1, 0) occ Zr 1 beq bvalue1 2.3709_0.3552  min = -5; max = 15;
 site Zr2  F1(!xzr2, =1/3;) F2(!yzr2, =2/3;) A3(zzr2, 0.98256_0.00034,0.98132) occ Zr 1 beq bvalue2
1.5645_0.1314  min = -5; max = 15;
 site Mo1  R1(xmo1, 0.32929_0.00000,0.32871) R2(ymo1, 0.33757_0.00000,0.33891) R3(zmo1,
0.14917_0.00000,0.14900) occ Mo 1 beq bvalue3 1.6982_0.0327  min = -5; max = 15;
 site O1  R1(xo1, 0.33405_0.00000,0.17310) R2(yo1, 0.49347_0.00000,0.16640) R3(zo1,
0.07843_0.00000,0.10080) occ O  1 beq bvalue4 2.4007_0.4840  min = -5; max = 15;
 site O2  R1(xo2, 0.49731_0.00000,0.33230) R2(yo2, 0.33310_0.00000,0.49590) R3(zo2,
0.11847_0.00000,0.08140) occ O  1 beq bvalue5 3.2074_0.6203  min = -5; max = 15;
 site O3  R1(xo3, 0.17006_0.00000,0.49790) R2(yo3, 0.16698_0.00000,0.33640) R3(zo3,
0.10202_0.00000,0.08372) occ O  1 beq bvalue6 3.6488_0.9954  min = -5; max = 15;
 site O4  R1(xo4, 0.31631_0.00000,0.31890) R2(yo4, 0.35593_0.00000,0.35220) R3(zo4,
0.29153_0.00000,0.29230) occ O  1 beq bvalue7 2.5347_0.3037  min = -5; max = 15;
```

```
'------------------------------
'Rigid tetrahedral body macro
'------------------------------

macro Tet2(s0, s1, s2, s3, s4, r1, r2) 'tetrahedron with redefined ORIGIN at Mo not O-terminal.
{
    point_for_site s0 ux =  0.000000000000000  ; uy = 0.0000000000000000  ; uz=  0;
    point_for_site s1 ux = -0.816496580927726 r1; uy = 0.4714045207910317 r1;  uz =  -r1/3;
    point_for_site s2 ux =  0.816496580927726 r1; uy = 0.4714045207910317 r1;  uz =  -r1/3;
    point_for_site s3 uy = -0.942809041582063 r1; uz =  -r1/3;
    point_for_site s4 uz = r2;
}

  rigid
        Tet2(Mo1,O1,O2,O3,O4,1.764,1.690)   'a tetrahedron in +z direction
'    tet_on_general(Mo1,O1,O2,O3,O4,1.764)
    Rotate_about_axies(rotcon(rotxmo1,-6.43812_0.758918973 min -20; max 20;), rotcon(rotymo1,-
10.83304_0.387371095 min -20; max 20;), rotcon(rotzmo1,-29.25618_2.91099786 min -60; max 60;))
    Translate2(tet(xmo1,
0.32929_0.000955479928,0.33328),tet(ymo1,0.33757_0.000934360142,0.32926),tet(zmo1,0.14917_9.95
391744e-005,0.14264))

'All O coords redundant now, replaced with rotx,y,zmo1. Output below; see evidence for tet moving
towards c vector

'-----------------------------------------------
'Command to stop O moving too far from Mo or Zr
'-----------------------------------------------

box_interaction to_N 8  Zr* Mo*  zrmo = If( R < 3.4 , (R-3.4)^2, 0);
box_interaction to_N 8  O* O*  oo = If( R < 2.4 , (R-2.4)^2, 0);

box_interaction to_N 5  Zr* O*  oct = If(Or(R < 1.8,R > 2.3),(R-2.075)^2, 0);

'box_interaction to_N 0 Mo1 O1 !mo1o1dist = (R-1.764)^2;
'box_interaction to_N 0 Mo1 O2 !mo1o2dist = (R-1.764)^2;
'box_interaction to_N 0 Mo1 O3 !mo1o3dist = (R-1.764)^2;
'box_interaction to_N 0 Mo1 O4 !mo1o4dist = (R-1.69)^2;


box_interaction to_N 5 Zr1 O* !zr1odist = (R-2.086)^2;
box_interaction to_N 5 Zr2 O* !zr2odist = (R-2.086)^2;


penalty = zrmo + oo + oct + !zr1odist + !zr2odist ;


prm !zrmodist = zrmo ;:0.00000_0.00000
prm !oodist   = oo   ;:0.00000_0.00000
prm !zro6     = oct  ;:0.00000_0.00000



#endif
```

```
'------------------------------------------------------------
'ZrO2 by Smith et al.  a=5.145(5) b=5.2075(5) c=5.3107(5) beta=99.23(8)
'------------------------------------------------------------

#ifdef phase2

str
                r_bragg  8.70442752
                scale @ 0.0000415189_0.0000038742
                phase_name ZrO2
                MVW( 492.892_0.000, 140.7862_0.1362,percentphase2 2.581_0.233)
                space_group P21/c
                a @ 5.15933_0.00308
                b @ 5.20735_0.00302
                c @ 5.30922_0.00259
                be @ 99.24691_0.02670
                Crystallite_Size(crysize2, 56.45192_5.05402 min 30; max 1000;)

        site Zr1 x 0.27580 y 0.04110 z 0.20820  occ Zr 1 beq bvalue 5.2916_1.2750 min 0; max 10;
        site O1  x 0.07030 y 0.33590 z 0.34060  occ O 1 beq bvalue 5.2916_1.2750 min 0; max 10;
        site O2  x 0.44230 y 0.75490 z 0.47890 occ O 1 beq bvalue 5.2916_1.2750 min 0; max 10;

#endif

do_errors
```

List of Publications

The following literature articles were derived from studies presented in this thesis at the time of submission.

1. "Synthesis, Structure and Thermal Contraction of a New Low-temperature Polymorph of $ZrMo_2O_8$." S. Allen, N. R. Warmingham, R. K. B. Gover and J. S. O. Evans, *Chem. Mater.*, 2003, in press.

2. "Beyond Rietveld Refinement – Non Crystallographic Information from Powder Diffraction." S. Allen and J. S. O. Evans, *IUCr CPD Newsletter*, **29**, 2003, 11-14.

3. "Negative Thermal Expansion and Oxygen Disorder in Cubic $ZrMo_2O_8$." S. Allen and J. S. O. Evans, *Phys. Rev. B*, 2003, accepted.

4. "The Kinetics of Low Temperature Oxygen Migration in $ZrWMoO_8$." S. Allen and J. S. O. Evans, *J. Mater. Chem.*, 2003, submitted.

5. "A Second-order Phase Transition in Trigonal AMo_2O_8 (A = Zr, Hf)." R. J. Ward, S. Allen, J. S. O. Evans, in preparation.

List of Attended Lectures, Seminars, Courses and Conferences

1999

October 12 Dr. S. Beckett, Nestlé.
"Chocolate for the Next Millennium."

October 13 Prof. M. A. Spackman, University of New England, Australia.
"Towards a Pictoral Glossary of Intermolecular Interactions."

October 13 Prof. G. Fleet, University of Oxford.
"Sugar Lactone and Amino Acids."

October 19 Prof. K. Gloe, TU Dresden, Germany.
"Tailor Made Molecules for the Selective Binding of Metal Ions."

October 20 Prof. S. Lincoln, University of Adelaide.
"Aspects of Complexation and Supramolecular Chemistry."

October 25 Prof. S. Collins, University of Waterloo, Canada.
"Methacrylate Polymerization Using Zirconium Enolate Initiators: Polymerization Mechanisms and Control of Polymer Tacticity."

October 27 Dr. C. Braddock, Imperial College.
"Novel Catalysts for Atom Economic Transformations."

November 3 Prof. D.W. Smith, University of Waikato, New Zealand.
"The Strengths of C–C and C–H Bonds in Organic and Organometallic Molecules: Empirical, Semi-empirical and Ab Initio Calculations."

November 10 Dr. I. Samuel, University of Durham.
"Improving Organic Light Emitting Diodes by Molecular, Optical and Device Design."

November 16 Prof. A. Holmes.
"Conjugated Polymers for the Market Place."

November 18 Dr. G. Siligardi, Kings College, London.
"The Use of Circular Dichrosim to Detect and Characterise Biomolecular Interactions in Solution."

November 24 Prof. T. Jones, Imperial College.
"Atomic and Molecular Control of Inorganic and Organic Semiconductor Thin Films."

November 30 Rev. R. Lancaster.
"Fireworks: Principles and Practice."

December 8 Prof. D. Crout, University of Warwick.
"More than Simply Sweet: Carbohydrates in Medicine and Biology."

December 9 Prof. F. Palacio, University of Zaragoza.
"Induced Net Spontaneous Magnetisation by Non-magnetic Impurities in Low-anisotropy Antiferromagnets."

2000

January 12 Prof. D. Haddleton, University of Warwick.
"Atom Transfer Polymerisation - What's all the Hype About?"

January 25 Prof. B. Meijer.
"From Supramolecular Architecture Towards Functional Materials."

February 2 Dr. C. Wilson, ISIS.
"Examining Protons in Interesting Potential Wells - Variable Temperature (and Pressure) Neutron Diffraction Studies of Organic Single Crystals."

February 15 Prof. D. Phillips.
"A Little Light Relief."

March 7 Prof. Motherwell, University College, London.
"Curiosity and Simplicity - Essential Ingredients for the Discovery of New Reactions."

March 8 Prof. J. Courtieu, Université de Paris-Sud, Orsay.
"Chiral Recognition through NMR in Liquid Crystal Solvents: an Order Affair."

March 9 Dr. A. Fairbanks, Dyson-Perrins Laboratory, Oxford.
"Selectivity in Glycoside Formation."

March 20 Prof. S. Marder, University of Arizona.
"Design of Molecules for Two-Photon Absorption and Their Application to 3D Polymerization and Imaging."

April 3 - 5 BCA Spring Meeting, Heriot-Watt University.

May 3 Drs. C. Barnard and L. Slade, Johnson Matthey.
"High Throughput Screening - a Route to Customised Catalysis."

May 5 Professor R. Hochstrasser, University of Pennsylvania.
"Ultrafast Molecular and Protein Dynamics Seen Through Their Vibrations."

May 8 Prof. H. F. Koch, Ithaca College, USA.
"Do Carbon Acidities Predict Reactivites with Alkoxides?"

May 24 Dr. S. Shimada.
"Reactivities of Si–H Bond Towards Group 10 Metal Complexes: Isolation of Tetravalent and Hexavalent Silyl Group 10 Metal Complexes."

July 6 Prof. Roald Hoffman, Nobel Prize Winner 1981.
"Electron-rich Three-centre Bonding Across the Periodic Table."

October 11 Dr. V. Christou, Inorganic Chemistry Laboratory, Oxford.
"Recent Developments in Organic LED Technology: Organolanthanide Phosphors"

October 18 Prof. A. F. Hill, Imperial College.
"The Hydrometallation of Phospha-alkynes."

October 25 Prof. S. F. Campbell, Pfizer.
"Science, Art and Drug Discovery - A Personal Perspective."

November 7 Dr. C. Ludman, University of Durham.
"Explosions - a Demonstration Lecture."

November 28 Prof. G. Stewart, Heriot-Watt University.
"Processing Intensification in the Brewing Industry."

November 29 Prof. T. G. Truscott, University of Keele.
"Life, Death and the Carotenoids"

2001

January 17 Prof. K. Roberts, University of Leeds.
"Application of Polarised NEXAFS Spectroscopy to the Structural Characterisation of Soft Molecular Interfaces."

January 31 Dr. P. Wright, University of St. Andrews.
"Making Space for Molecules: Designed Synthesis of Novel Molecular Sieves."

February 14 Dr. S. T. Howard, Cardiff University.
"Analysis of Bonding Energy Distributions in Polyatomic Molecules."

February 27 G. Ferry.
"The Life and Work of Dorothy Hodgkin."

March 7 Dr. N. Norman, Bristol University.
"Recent Developments in Diborane(4) Chemistry."

March 14 Dr. D. Keen, ISIS.
"Probing Structural Disorder with Diffuse Neutron Scattering."

March 30 - April 6 BCA Intensive Course in Crystallography.

May 4 Prof. M. Brookhart, University of North Carolina.
"Catalysis Using Late Transition Metal Complexes."

May 9 Prof. R. Mukherjee, Indian Institute of Technology, Kanpur.
"Spin-state Regulation in Iron(II) and Iron (III) Complexes with Pyrazolylpyridine and Deprotonated Pyridine Amide Ligands."

June 14 Prof. T. Marder, University of Durham.
"Conjugated Rigid-rods as Multifunctional Materials: Applications in Photonics and Molecular and Nanoscale Electronics."

October 17 Prof. P. Knowles, University of Birmingham.
"Towards Accurate *ab initio* Electronic Structure for Large Molecules."

October 24 Prof. R. G. Denning, Inorganic Chemistry Laboratory, Oxford.
"Photonic Crystals."

November 19 Prof. P. W. Atkins, Physical Chemistry Laboratory, Oxford.
"A Century of Physical Chemistry."

2002

January 16 Prof. R. R. Schrock, Massachusetts Institute of Technology.
"Electronically Unsaturated Sterically Crowded Tetrahedral Catalysts for Asymmetric Ring-closing Metathesis and the Living Polymerisation of Ordinary Olefins."

January 31 Prof. P. Day, Royal Institution.
"Some Supramolecular Chemistry of Magnets and Superconductors."

March 15 Dr. G. Saunders, Queen's University, Belfast.
"Dehydrofluorinative Carbon-carbon Coupling as a Route to Complexes of Hybrid Cyclopentadienide- and Arene-Phosphine Ligands."

May 31 Prof. V. C. Gibson, Imperial College.
"Designing Catalysts for Polymer Synthesis."

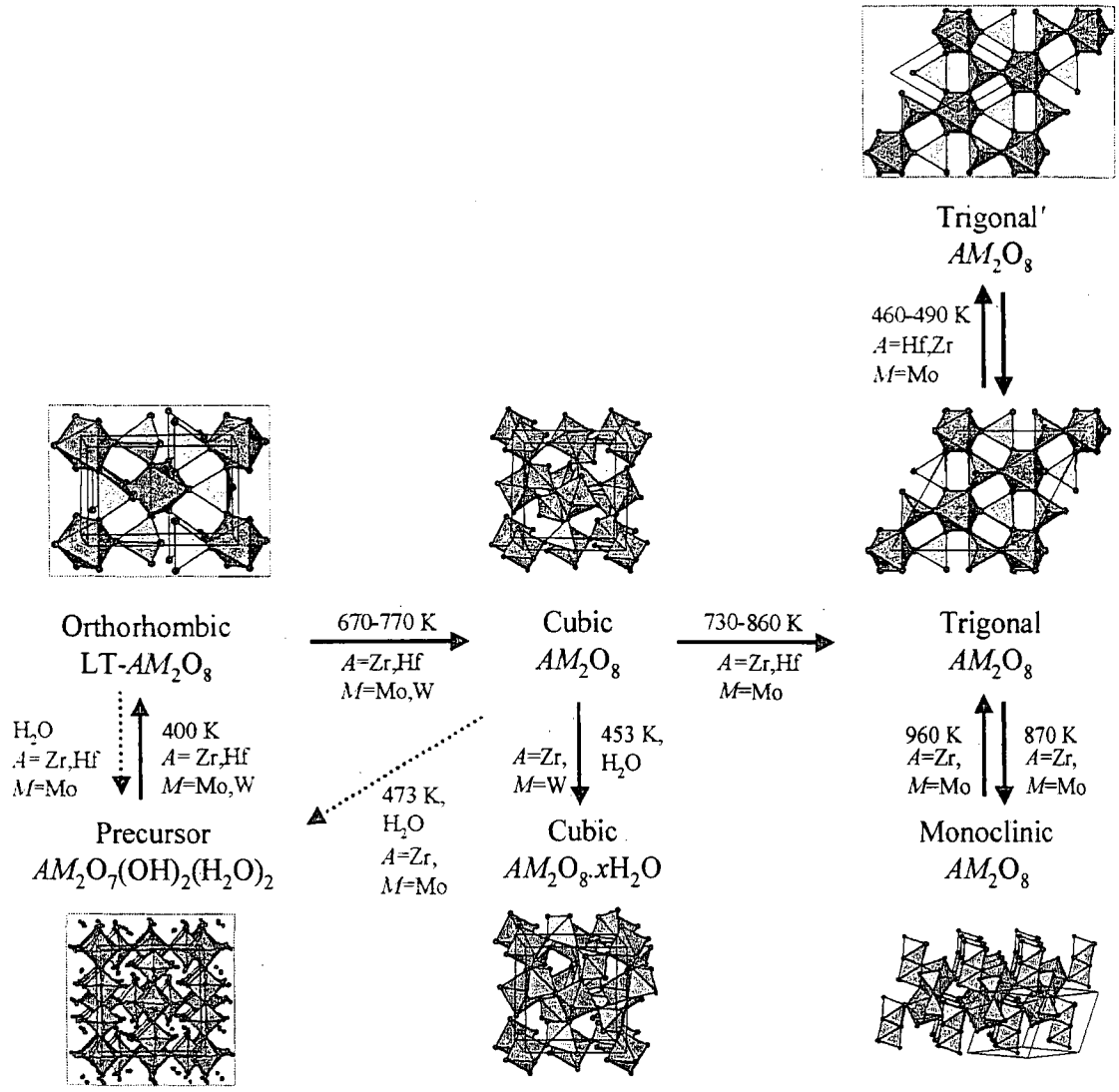

Quick Reference Figure: Summary of AM_2O_8 and related phases as a function of temperature at ambient pressure. Phases and relations highlighted in red are newly characterised in this thesis. Phases labeled in black show established phases from the literature.

October 24 Prof. R. G. Denning, Inorganic Chemistry Laboratory, Oxford.
"Photonic Crystals."

November 19 Prof. P. W. Atkins, Physical Chemistry Laboratory, Oxford.
"A Century of Physical Chemistry."

2002

January 16 Prof. R. R. Schrock, Massachusetts Institute of Technology.
"Electronically Unsaturated Sterically Crowded Tetrahedral Catalysts for Asymmetric Ring-closing Metathesis and the Living Polymerisation of Ordinary Olefins."

January 31 Prof. P. Day, Royal Institution.
"Some Supramolecular Chemistry of Magnets and Superconductors."

March 15 Dr. G. Saunders, Queen's University, Belfast.
"Dehydrofluorinative Carbon-carbon Coupling as a Route to Complexes of Hybrid Cyclopentadienide- and Arene-Phosphine Ligands."

May 31 Prof. V. C. Gibson, Imperial College.
"Designing Catalysts for Polymer Synthesis."

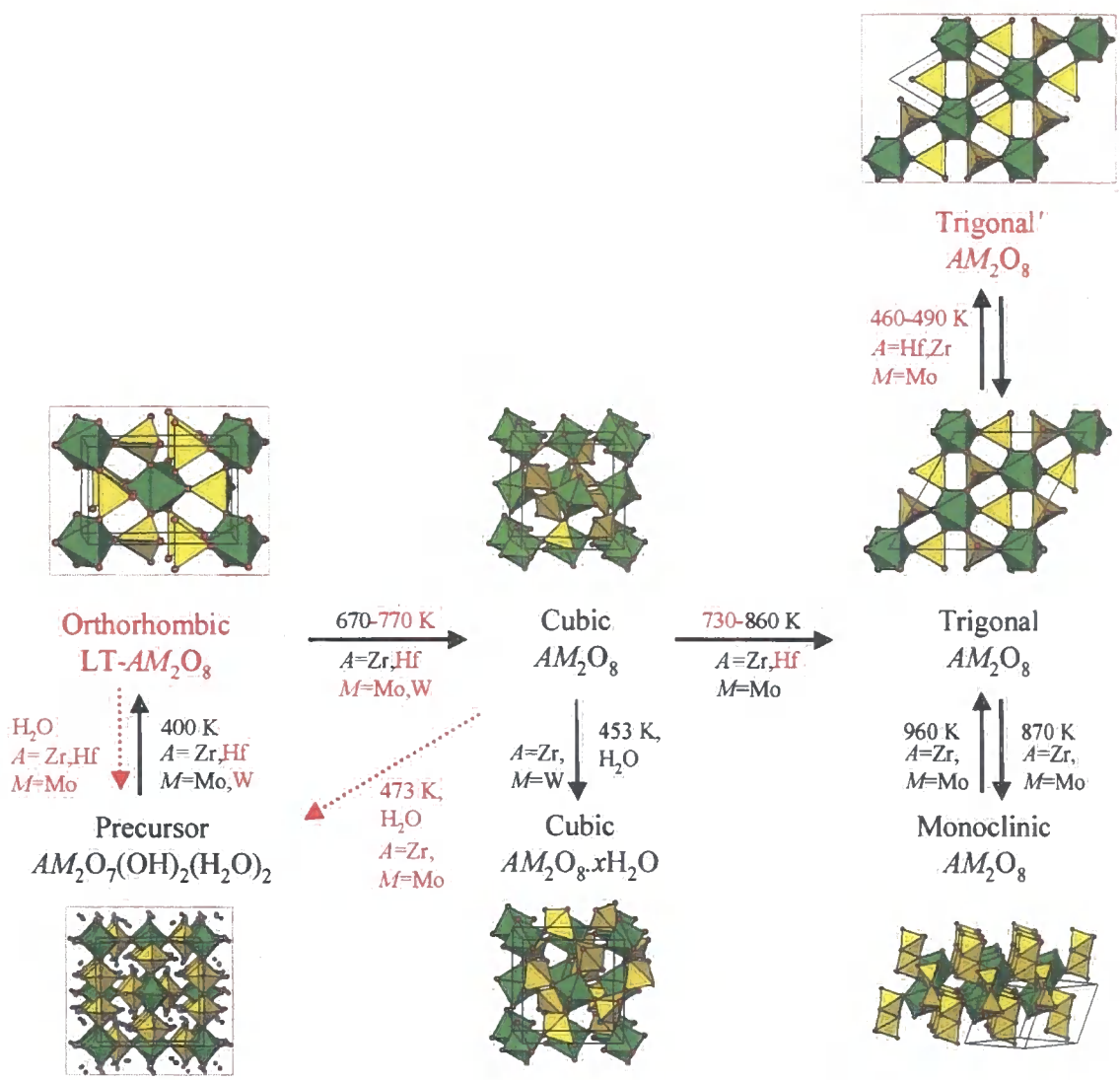

Quick Reference Figure: Summary of AM_2O_8 and related phases as a function of temperature at ambient pressure. Phases and relations highlighted in red are newly characterised in this thesis. Phases labeled in black show established phases from the literature.